POLYMER SOLAR CELLS: MOLECULAR DESIGN AND MICROSTRUCTURE CONTROL

EDITED BY: Kui Zhao, Ergang Wang and Jiangang Liu
PUBLISHED IN: Frontiers in Chemistry

frontiers Research Topics

frontiers

ISSN 1664-8714
ISBN 978-2-88966-194-7
DOI 10.3389/978-2-88966-194-7

About Frontiers

Frontiers is more than just an open-access publisher of scholarly articles: it is a pioneering approach to the world of academia, radically improving the way scholarly research is managed. The grand vision of Frontiers is a world where all people have an equal opportunity to seek, share and generate knowledge. Frontiers provides immediate and permanent online open access to all its publications, but this alone is not enough to realize our grand goals.

Frontiers Journal Series

The Frontiers Journal Series is a multi-tier and interdisciplinary set of open-access, online journals, promising a paradigm shift from the current review, selection and dissemination processes in academic publishing. All Frontiers journals are driven by researchers for researchers; therefore, they constitute a service to the scholarly community. At the same time, the Frontiers Journal Series operates on a revolutionary invention, the tiered publishing system, initially addressing specific communities of scholars, and gradually climbing up to broader public understanding, thus serving the interests of the lay society, too.

Dedication to Quality

Each Frontiers article is a landmark of the highest quality, thanks to genuinely collaborative interactions between authors and review editors, who include some of the world's best academicians. Research must be certified by peers before entering a stream of knowledge that may eventually reach the public - and shape society; therefore, Frontiers only applies the most rigorous and unbiased reviews.
Frontiers revolutionizes research publishing by freely delivering the most outstanding research, evaluated with no bias from both the academic and social point of view. By applying the most advanced information technologies, Frontiers is catapulting scholarly publishing into a new generation.

What are Frontiers Research Topics?

Frontiers Research Topics are very popular trademarks of the Frontiers Journals Series: they are collections of at least ten articles, all centered on a particular subject. With their unique mix of varied contributions from Original Research to Review Articles, Frontiers Research Topics unify the most influential researchers, the latest key findings and historical advances in a hot research area! Find out more on how to host your own Frontiers Research Topic or contribute to one as an author by contacting the Frontiers Editorial Office: researchtopics@frontiersin.org

POLYMER SOLAR CELLS: MOLECULAR DESIGN AND MICROSTRUCTURE CONTROL

Topic Editors:
Kui Zhao, Shaanxi Normal University, China
Ergang Wang, Chalmers University of Technology, Sweden
Jiangang Liu, Northwestern Polytechnical University, China

Citation: Zhao, K., Wang, E., Liu, J., eds. (2020). Polymer Solar Cells: Molecular Design and Microstructure Control. Lausanne: Frontiers Media SA. doi: 10.3389/978-2-88966-194-7

Table of Contents

frontiers in Chemistry

EDITORIAL
published: 06 October 2020
doi: 10.3389/fchem.2020.00697

Editorial: Polymer Solar Cells: Molecular Design and Microstructure Control

Jiangang Liu[1]*, *Ergang Wang*[2]* and *Kui Zhao*[3]*

[1] School of Electronics and Information, Northwestern Polytechnical University, Xi'an, China, [2] Department of Chemistry and Chemical Engineering, Chalmers University of Technology, Gothenburg, Sweden, [3] School of Materials Science and Engineering, Shaanxi Normal University, Xi'an, China

Keywords: solar cells, synthesis, microstructure, morphology, efficiency

Editorial on the Research Topic

Polymer Solar Cells: Molecular Design and Microstructure Control

Photovoltaic (PV) devices can directly convert sunlight into electricity, which enables a practical and facile solution to address the challenge of the ever-increasing energy demand in a sustainable way. Intensive research and development are searching for high efficiency solar cells with low-cost fabrication. So far PV devices based on various inorganic materials dominate the entire market, including silicon (Si), III-V group semiconductors, CIGS, and CdTe. However, partially due to the related environmental issues and high production cost, traditional PV technologies raise the obvious constraints on the further manufacturing capacity of system-cost, scale-up, and their wide adoption. Recently there has been an ever-growing interest in emerging polymer-based PV technology owing to synthetic variability and low-temperature solution-processing of organic semiconductors, and the capacity of lightweight, flexible, easy and low-cost manufacturing of devices. It is our great pleasure to propose this special issue entitled "Polymer Solar Cells: Molecular Design and Microstructure Control" for *Frontiers in Chemistry*. The issue highlights important aspects of structure-function relationship from both molecular design and microstructure control perspectives. We present a collection of 11 featured articles from this exciting field that covers molecular design of novel materials and microstructure control of the bulk heterojunction (BHJ) layer for high-performance polymer solar cells.

The microstructure of the active layer plays a critical role in photovoltaic outcome. It has been widely believed that percolation networks of both donor and acceptor enable efficient charge transport and collection. Yan et al. found that the weight average molecular weight (M_W) of polymer had a profound influence on the formation of the percolation network. When the M_W of N2200 is larger than 96 kDa, a percolation network structure is formed in the J51:N2200 blend film due to the chain tanglement and multi-chain aggregations, resulting in increased electron mobility and improved device performance (Yan et al.).

Domain sizes should be carefully controlled owing to exciton diffusion length of only 10–20 nm. While it still remains challenging to control the domain sizes as the film formation is more related to thermodynamic process, inhibiting the crystallization of the donor and/or acceptor could reduce the domain size effectively. Liu J. et al. synthesized random copolymers PNDI-Px by introducing porphyrin unit into NDI-based polymer. Due to the more flexible mainchain, the crystallinity of PNDI-Px was suppressed, achieving a finer phase separation structure (Liu J. et al.). In addition, Huang et al. developed a new strategy to control the polymer regiochemistry, which may be used as an effective method to control the crystallinity of polymers and further regulate the phase separation degree. Small molecules are often characterized by high crystallinity. Liu C. et al. synthesized a new small molecule donor with an acceptor-donor-acceptor structure, namely

OPEN ACCESS

Edited and reviewed by:
Bretislav Friedrich,
Fritz-Haber-Institut, Germany

***Correspondence:**
Jiangang Liu
jgliu@nwpu.edu.cn
Ergang Wang
ergang@chalmers.se
Kui Zhao
zhaok@snnu.edu.cn

Specialty section:
This article was submitted to Physical Chemistry and Chemical Physics, a section of the journal Frontiers in Chemistry

Received: *26 June 2020*
Accepted: *06 July 2020*
Published: *06 October 2020*

Citation:
Liu J, Wang E and Zhao K (2020) Editorial: Polymer Solar Cells: Molecular Design and Microstructure Control. Front. Chem. 8:697. doi: 10.3389/fchem.2020.00697

DRTB16-FT, having fluorine atoms on the thienyl substituent of the central benzodithiophene unit. It shows a low-lying HOMO energy level of −5.64 eV, which is beneficial for reducing energy loss when blending with an acceptor. However, the strong aggregation of DRTB16-FT induced the formation of large domain size, causing a low device performance (Liu C. et al.). Li et al. demonstrated that a propeller-like structure could prevent the small molecules from aggregating into undesired large crystals. They designed and synthesized three new propeller-like PDI derivatives with all-fused rigid structures, which showed a more suitable absorption range and charge transport abilities than that of unfused counterparts. Using PTB7-Th as donor and propeller-like PDI derivative as acceptor, micrometer-sized crystals which have been widely found in conventional PDI based solar cells were efficiently diminished (Li et al.).

The vertical phase separation also plays a crucial role in charge transport along the perpendicular direction. In an optimized vertical phase separation, the donor should be enriched at the anode and the acceptor should accumulate at the cathode. Shao et al. systematically examine how fluorine substituent impacts vertical phase separation. They found that the fluorination of a polymer enables better vertical phase separation in the blend film, which facilitates more efficient charge generation and extraction (Shao et al.). Nowadays the vertical phase separation is measured by non-*in-situ* methods, which exhibit high cost, complicated operation and low precision. Feng et al. proposed an *in-situ* measurement method in combination with a self-developed *in-situ* instrument. This diagnostic method is easily accessible and equipped in laboratories, which provides a convenient way to investigate the film-depth-dependent optical and electronic properties (Feng et al.).

The use of a ternary active layer, which is fabricated by introducing a second donor or acceptor into a binary D:A blend is emerging as a promising strategy to improve the device performance. The third component could not only broaden the absorption bandwidth but also regulate the morphology of the active layer. Zhang et al. introduced trifluoromethyl on a newly synthesized small molecular DTBO to strengthen hydrogen bonding between DTBO and the acceptor. The hydrogen bonding has a strong impact on electrostatic potential and benefits π-π stacking in the active layer, leading to superior charge extraction and low charge recombination (Zhang et al.). The addition of a third component also increased the hole mobility of active layer. Liu X. et al. incorporated a state-of-the-art narrow bandgap polymer (PTB7-Th) into the PBDT-TAZ:NOE10 binary system, which enhanced the photovoltaic performance and thermal stability of the device. The improved photovoltaic performance partly benefits from the improved hole mobility, resulting in more efficient charge generation, and balanced charge transport (Liu X. et al.). The photophysical processes of ternary solar cells are investigated by Yin et al. through introducing a small molecule donor BTR as a third component to the PCE-10:PC71BM binary system. It was shown that photocarrier losses via recombination are mitigated and the voltage losses are slightly suppressed in the ternary system, leading to improved performance (Li et al.).

This special issue thus represents the state-of-the-art in this challenging and fascinating scientific area. We are greatly indebted to all authors for their significant contributions and enthusiastic support. We also thank *Frontiers in Chemistry* for their great editorial support. We sincerely hope that this special issue can contribute to better understanding of the fundamental structure-function relationship in organic PV, and that the readers of *Frontiers in Chemistry* will find this special issue helpful and enjoy it!

AUTHOR CONTRIBUTIONS

JL collected the manuscript and was in charge of reviewing manuscript. KZ organized this issue and was in charge of reviewing manuscript. EW was in charge of reviewing manuscript. All authors contributed to the article and approved the submitted version.

FUNDING

This work was supported by the National Natural Science Foundation of China (51773203, 51903211, 61974085, and 51933010).

Conflict of Interest: The authors declare that the research was conducted in the absence of any commercial or financial relationships that could be construed as a potential conflict of interest.

frontiers in Chemistry

ORIGINAL RESEARCH
published: 11 February 2020
doi: 10.3389/fchem.2020.00021

Mediated Non-geminate Recombination in Ternary Organic Solar Cells Through a Liquid Crystal Guest Donor

Ao Yin[1], Dongyang Zhang[1], Jianqiu Wang[1], Huiqiong Zhou[2], Zhiqiang Fu[3] and Yuan Zhang[1]**

[1] School of Chemistry, Beijing Advanced Innovation Center for Biomedical Engineering, Beihang University, Beijing, China, [2] CAS Key Laboratory of Nanosystem and Hierachical Fabrication CAS Center for Excellence in Nanoscience, National Center for Nanoscience and Technology, Beijing, China, [3] School of Engineering and Technology, China University of Geosciences, Beijing, China

The approach via ternary blends prompts the increase of absorbed photon density and resultant photocurrent enhancement in organic solar cells (OSCs). In contrast to actively reported high efficiency ternary OSCs, little is known about charge recombination properties and carrier loss mechanisms in these emerging devices. Here, through introducing a small molecule donor BTR as a guest component to the PCE-10:$PC_{71}BM$ binary system, we show that photocarrier losses via recombination are mitigated with respect the binary OSCs, owing to a reduced bimolecular recombination. The gain of the fill factor in ternary devices are reconciled by the change in equilibrium between charge exaction and recombination in the presence of BTR toward the former process. With these modifications, the power conversion efficiency in ternary solar cells receives a boost from 8.8 (PCE-10:$PC_{71}BM$) to 10.88%. We further found that the voltage losses in the ternary cell are slightly suppressed, related to the rising charge transfer-state energy. These benefits brought by the third guest donor are important for attaining improvements on key photophysical processes governing the photovoltaic efficiencies in organic ternary solar cells.

Keywords: ternary solar cells, charge recombination, charge transfer states, small molecule donor, voltage loss

OPEN ACCESS

Edited by:
Jiangang Liu,
Shantou University, China

Reviewed by:
Jianyu Yuan,
Soochow University, China
Qiuju Liang,
Northwestern Polytechnical University, China

****Correspondence:***
Huiqiong Zhou
zhouhq@nanoctr.cn
Yuan Zhang
yuanzhang@buaa.edu.cn

Specialty section:
This article was submitted to Physical Chemistry and Chemical Physics, a section of the journal Frontiers in Chemistry

Received: *16 October 2019*
Accepted: *09 January 2020*
Published: *11 February 2020*

Citation:
Yin A, Zhang D, Wang J, Zhou H, Fu Z and Zhang Y (2020) Mediated Non-geminate Recombination in Ternary Organic Solar Cells Through a Liquid Crystal Guest Donor. Front. Chem. 8:21. doi: 10.3389/fchem.2020.00021

INTRODUCTION

The recent efforts on organic bulk heterojunction (BHJ-OSCs) solar cells have pushed forward this photovoltaic technology toward a meaningful solution for generating the electricity at lower expenses. An efficient strategy to further boost the photon-harvesting in BHJ-OSCs concerns ternary blends that are capable of capturing a larger portion of the solar spectrum. (Lu et al., 2014; Li et al., 2017). As a result, the power conversion efficiencies (PCE) have exceeded 10% (Kan et al., 2017) with PCEs > 14% using blends of two non-fullerene acceptors (Xiao et al., 2017). The general concept of ternary OSCs relies on addition of a third photo-absorber into the prime binary BHJ to achieve modulations on solar cell performance. A successful design for ternary OSCs involve introducing a small molecule (SM) donor into the polymer blends where the carrier transport profits from the high crystallinity of SM donors (Zhang et al., 2017a). Ternary blends with two co-blended SM-donors also have been reported showing enlarged PCEs (Baran et al., 2016).

Recently, there have emerged ternary blends comprising of two well-miscible acceptors with which the photocurrent can increase due to the complementary absorption of acceptor alloy (Jiang et al., 2017b). Given the intrinsic trade-off between short-circuit current (J_{sc}) and open-circuit voltage (V_{oc}) in organic BHJ-OSCs, implementation of a concurrent increase in these two parameters is yet of challenge. To this end, maximizing the gain of photocurrent while maintaining voltage losses (ΔV_{oc}) unchanged appears to be significant to reach the potential of ternary BHJ-OSCs.

In contrast to actively reported progressions in the PCE of ternary OSCs, fundamental insights into charge transport and recombination properties still lack for these devices. Although there has been a consensus on the general design rules for ternary BHJ-OSCs in terms of energetic level matching or morphology compatibility (Ye et al., 2012), questions including how the introduced third components impact charge recombination and carrier losses in ternary blends remain unclear. In previous studies based on fullerene binary OSCs, charge recombination has been identified as a major loss channel for the PCE (Julien et al., 2018). It is generally accepted that after interfacial exciton dissociation on charge transfer states (CTS) (Veldman et al., 2009), the fate of electron-hole (or polaron) pairs is mainly dictated by the competing processes of charge collection and recombination (Deibel et al., 2010). In addition to geminate losses at CTS, largely due to severe morphology reasons, non-geminate recombination tends to play a more critical role in ultimate photovoltaic characteristics (Hou et al., 2018). Non-geminate recombination often occurs via bimolecular paths (with insignificant charge trapping) which are subject to the encounter probability of the two carriers in the mutual coulombic field. In this scenario, the recombination rate (B) is given by (van der Poll Thomas et al., 2012).

$$B = \beta np, \tag{1}$$

where β is the recombination rate constant (or coefficient), and np is product of mobile electron and hole densities under irradiation. In binary BHJ-OSCs, the β has been found to deviate from the Langevin rate β_L, purely governed by the mobility of the two carriers as $\beta_L = (q/\varepsilon_0\varepsilon_r)(\mu_p+\mu_n)$ (here q is elementary charge, $\varepsilon_0\varepsilon_r$ is the dielectric constant and μ_p or μ_n is the hole or electron mobility) (Proctor Christopher et al., 2014). The reduction of recombination in BHJs leads to a so-called reduction factor (γ) defined as $\gamma = \beta/\beta_L$. Values of $\gamma < 1$ have been observed in binary OSCs with non-fullerene acceptors, which can be correlated to the transport balance in the BHJ film. In addition, the significance of recombination has been related to its impact on the device fill factor (FF). For example, the dependencies of B on irradiation intensity (Armin et al., 2016; Brus Viktor et al., 2016; Heiber et al., 2016) have been linked to the observed variation of photocurrent with applied bias, which basically describes the shape of photocurrent or FF in device. In rationally-designed ternary systems, the enlargement of photon densities related to the guest components should result in a boost of photocurrent. On the other hand, the increase of n (or p) tends to raise the encounter probability of photo-carriers, according to Equation 1. Therefore, attaining the control on β seems to be essential for efficient carrier sweepout such that the carriers can contribute to the photocurrents in ternary OSCs. In this context, it will be of interest to concern a guest molecular donor with a low recombination rate and examine how the recombination process in ternary blends is modulated in the presence of donor guest. So far, investigations in these aspects are rarely reported, which impedes further enhancement of PCEs in ternary OSCs.

In this article, we chose a ternary model system comprising a polymeric donor ([4,8-bis(5-(2-ethylhexyl)thiophen-2-yl)-benzo[1,2-b:4,5-b′]dithiophene-co-3-fluorothieno[3,4-b]-thiophene-2-carboxylate]) PCE-10 (Liao et al., 2013) blended with $PC_{71}BM$ as the prime binary BHJ and a liquid crystal benzodithiophene terthiophene rhodanine (BTR) (Sun et al., 2015) as the third SM-donor guest (see chemical structure of different components in **Figure 1A**). We show that the low recombination rate in the BTR:$PC_{71}BM$ binary OSC provides an opportunity for mediating recombination losses in the PCE-10:BTR:$PC_{71}BM$ ternary devices. Based on an optimal blend ratio (0.2:0.8 w/w for BTR:PCE-10), the enlargements of J_{sc} and FF in the ternary cell are found associated with a stronger reduction factor with regard to the polymer binary device. As a result, the recombination rate constant and recombination intensity are both weakened. The modified recombination is further manifested by the recombination kinetics with light intensity (P_{light})-dependent impedance spectroscopy. We observe longer-lived photo-carriers in the ternary cell over a wide range of P_{light}. The suppressed charge recombination in ternary devices leads to more efficient carrier extraction, which explains the simultaneously enhanced photocurrent and fill factor in the presence of BTR donor. Based on Fourier transform photocurrent spectroscopy, we gained insights into the voltage losses (ΔV_{oc}) in the ternary OSCs. The results suggest a slightly reduced non-radiative recombination loss but unchanged radiative recombination loss due to the rising of charge transfer-state energy. This work enriches our fundamental understandings on charge recombination properties in ternary OSCs which coupled with smart device design may prompt the improvement of photovoltaic efficiencies.

EXPERIMENT

Materials

PCE-10, and BTR were purchased from 1-Material Inc., and $PC_{71}BM$ was purchased from Lumtec Inc. and used as received.

Device Fabrication

Patterned indium-tin-oxide (ITO) glass substrates were cleaned sequentially in soap water and with socination using deionized water, acetone, and isopropanol. After drying with N_2, the ITO substrates were UV/ozone treated for 4 min. ZnO solutions were prepared by dissolving 0.2 g of zinc acetate dihydrate [$Zn(CH_3COO)_2{\cdot}2H_2O$, 99.9%, Afla] and 0.055 ml of ethanolamine ($NH_2CH_2CH_2OH$, 99.5%, Aladdin) in 2 mL of 2-methoxyethanol ($CH_3OCH_2CH_2OH$, 99.8%, Alfa). ZnO films were prepared by spin-coating the precursor solution on top of the ITO substrates (5,000 rpm) for 20s as the electron transport

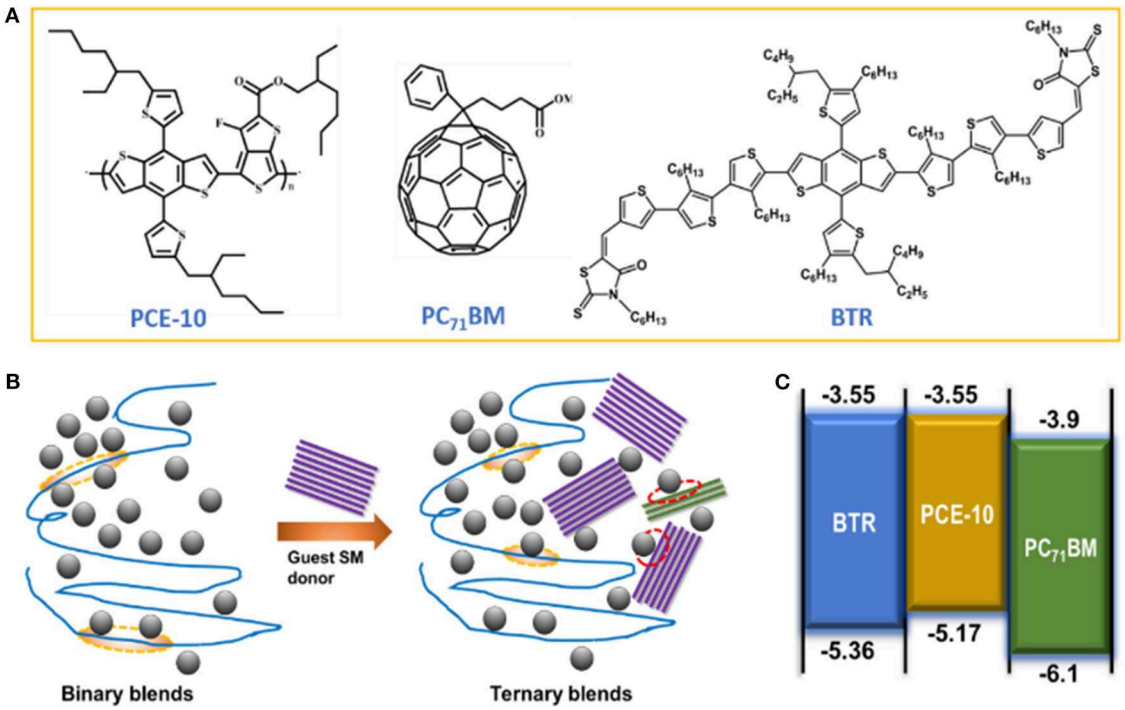

FIGURE 1 | (A) Chemical structures of used components in studied ternary blends. **(B)** Illustration of binary blends comprising of a polymer donor and fullerene acceptor alongside ternary blends with addition of a third small molecule (SM) acceptor. Also highlighted by ovals are the interfaces between polymer donor/$PC_{71}BM$ (orange) and SM-donor/$PC_{71}BM$ (red). **(C)** Energy diagram of ternary blends in this study.

layer followed by thermal annealing at 200°C for 30 min in air. The ZnO-coated ITO substrates were then transferred into a nitrogen-filled glovebox before use. PCE-10:$PC_{71}BM$ (1:1.1 weight ratio) and PCE-10:BTR:$PC_{71}BM$ (0.8:0.2:1.1 weight ratio) were solublized in chlorobenzene (15 mg/ml) with 2.5% DIO (v/v). The BTR:$PC_{71}BM$ (1:1.1 weight ratio) was dissolved in chloroform (15 mg/ml). The photoactive layers were attained by spin-coating the BHJ solutions pre-heated at 60°C over night at appropriate spin-rate, leading to typical film thickness of ∼200 nm. After deposition of the BHJ films, drops of chloroform were dripped into a small dish holding the BTR devices with waiting for 40s. Then MoO_x was evaporated on the active layer as hole transport layer at a pressure of $\sim 10^{-5}$ Pa. Finally, the Al cathode (∼80 nm) was thermally evaporated on MoO_x. The active area of the device was 4 mm^2, defined by shadow masks. Single carrier device: the active layers were prepared identically to the procedure for solar cells. The hole-only devices were fabricated with the structure of ITO/PEDOT:PSS/active layer/Au and the structure for electron-only devices was ITO/ZnO/active layer/PFN-Br/Al.

Characterization

J-V characteristics of solar cells was performed by using a Keithley 2400 Sourcemeter under AM 1.5G solar illumination at 100 mW/cm^2 provided by a Class AAA solar simulator along with a National Institute of Metrology (NIM, China) calibrated KG5-filtered silicon reference cells. Irradiation-dependent solar cell testing was performed by applying a filter wheel with designed optical densities between the samples and light source to obtain desired illumination intensities and calibrated by a NIM-certified silicon reference cell. Single carrier devices were characterized in a Lakeshore vacuum probe station by using a Keithley 4,200 semiconductor parameter analyzer in dark condition. PL spectroscopy of BHJ and neat films was measured by using a Horiba Jobin Yvon Nanolog fluorimeter under excitation of 580 nm.

RESULTS AND DISCUSSION

Figure 1B schematically illustrates the nanomorphology of PCE-10:$PC_{71}BM$ binary and ternary blends with the co-blended BTR SM-donor. As can be seen, additional interfaces at BTR/fullerene are introduced in the ternary blends which likely create increased recombination channels. The chosen liquid crystal BTR donor possesses a deeper-lying energy of the highest occupied molecular orbital (HOMO) at ∼5.36 eV and an absorption between 400 and 550 nm. This feature enables a complementary absorption to that of the PCE-10:$PC_{71}BM$ binary blends (see energy diagram of ternary blends in **Figure 1C**). Hereinafter, we focus on the analysis based on the optimal blend ratio at 0.8:0.2 (w/w) for PCE-10:BTR that yields the best PCE of 10.88%. (Chen et al., 2017) With non-optimal blend ratios (for PCE-10:BTR), more significant geminate losses may be present, which complicates our analyses on bimolecular recombination

properties. **Figure 2A** displays absorption spectra of the binary and ternary blend films normalized to respective absorption peaks. Upon addition of BTR, the ternary blend film exhibits a broader absorbance with a spectral range between 400 and 750 nm. This optical profile is expected to promote J_{sc} in the solar cell, which will be detailed below.

In addition to the broadened absorption, it is a prerequisite that the singlet excitons created in the guest donor of ternary blends can dissociate into mobile carriers to contribute to the photocurrent (Lu et al., 2014). In this regard, we examined the photoluminescence (PL) quenching efficiency (PL_{quench}) by which charge transfer in ternary BHJ films was assessed (Ameri et al., 2013). **Figure 2B** shows steady-state PL spectroscopy measured on thin films of neat donors, binary and ternary blends. As can be seen, the PCE-10:$PC_{71}BM$ binary and ternary bled films both display a strongly quenched PL at ∼760 nm originating from singlet excitons in the PCE-10 donor (Chen et al., 2017), corresponding to a PL_{quench} of 99.88% (PCE-10 blends) and 99.39% (ternary blends). The quenching of PL from BTR (∼708 nm) is also pronounced in the ternary blends, which is in contrast to the less significant quenching of the donor PL in BTR:$PC_{71}BM$ (**Figure 2B**) showing a PL_{quench} of 93%. This observation can be correlated to the reduced homogeneity in the SM binary blends, indicated by electron microscopy (Sun et al., 2011), pointing to a larger phase separation. To better assess charge transfers in the ternary blends, we also examined PL of co-blended donor films with the results shown in **Figure 2C**. With 20% of BTR, the PL of donor blends resembles that of neat PCE-10 and we cannot observe the emission from the SM donor (around 708 nm). The significant quenching of singlet excitons in BTR is suggestive of efficient hole transfers from the SM-donor toward PCE-10 polymer, which seems to be driven under the HOMO energy offset of ∼200 meV (see **Figure 1B**). The PL results provides evidence for the occurrence of electron transfers at the donor/$PC_{71}BM$ and hole transfers at the BTR/PCE-10 interfaces in the ternary blends.

Now we turn to biomolecular recombination in ternary devices. As test beds, we fabricated ternary and corresponding binary BHJ-OSCs with an inverted device architecture (see device structure in the inset of **Figure 3A**). **Figure 3A** shows photocurrent density vs. voltage (J-V) characteristics of binary and ternary solar cells (with the optimal blend ratio of 0.8:0.2 for PCE-10:BTR) and the extracted device parameters are summarized in **Table 1**. The PCE-10 and BTR binary solar cells produce a PCE of 8.8 and 6.92%, respectively at the optimized conditions (the D/A ratios are both of 1:1.1 for cells with the polymer and SM-donors). Upon addition 20% of BTR guest donor into the polymer binary blend, the ultimate PCE receives a considerable enhancement to 10.88%, showing an enhanced J_{sc} = 20.34 mA/cm^2 and FF = 69.02%. A slight increase in V_{oc} (22 meV) was found in the ternary device which can be ascribed to the deeper-lying HOMO in BTR. The V_{oc} result is in line with the general tendency in ternary solar cells where the V_{oc} takes advantage of the binary system having a larger effective band gap, defined by the energetic offset between donor HOMO and acceptor LUMO (Scharber et al., 2006).

To have more mechanistic understandings on the modified device performance, we examined charge transport in steady-state by single-carrier device measurements. It is noteworthy that charge carrier mobilities in organic

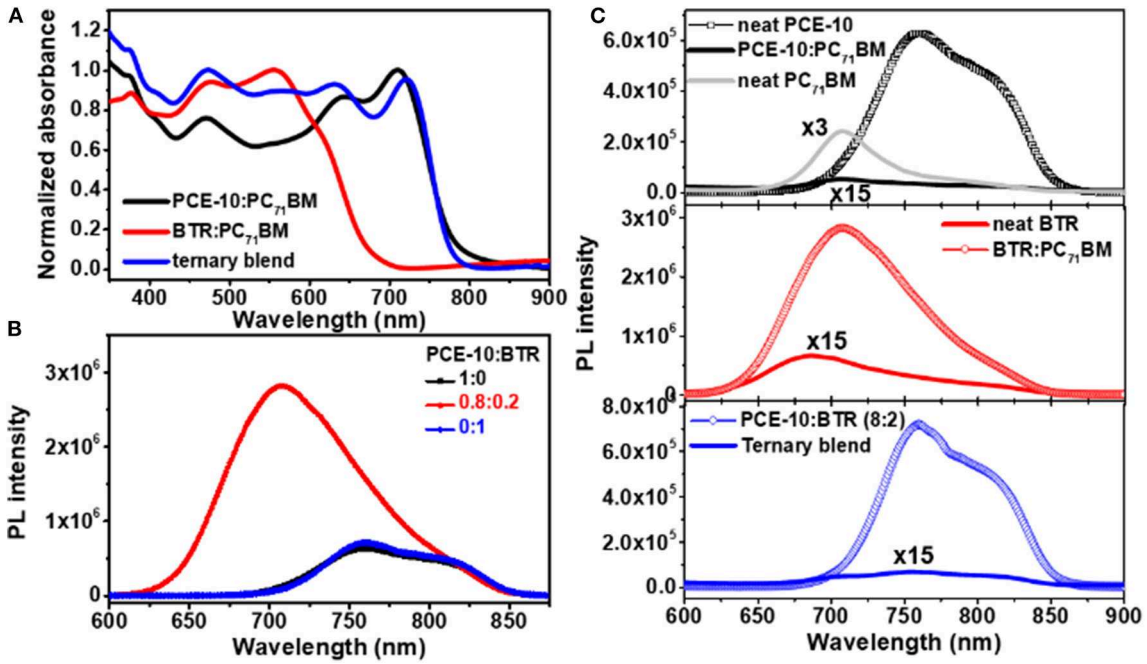

FIGURE 2 | (A) Normalized absorption spectroscopy of binary and ternary blend films. **(B)** Photoluminescence (PL) quenching based on neat donor(s) and binary (ternary) blend films. **(C)** PL spectroscopy of neat and co-blended donor films.

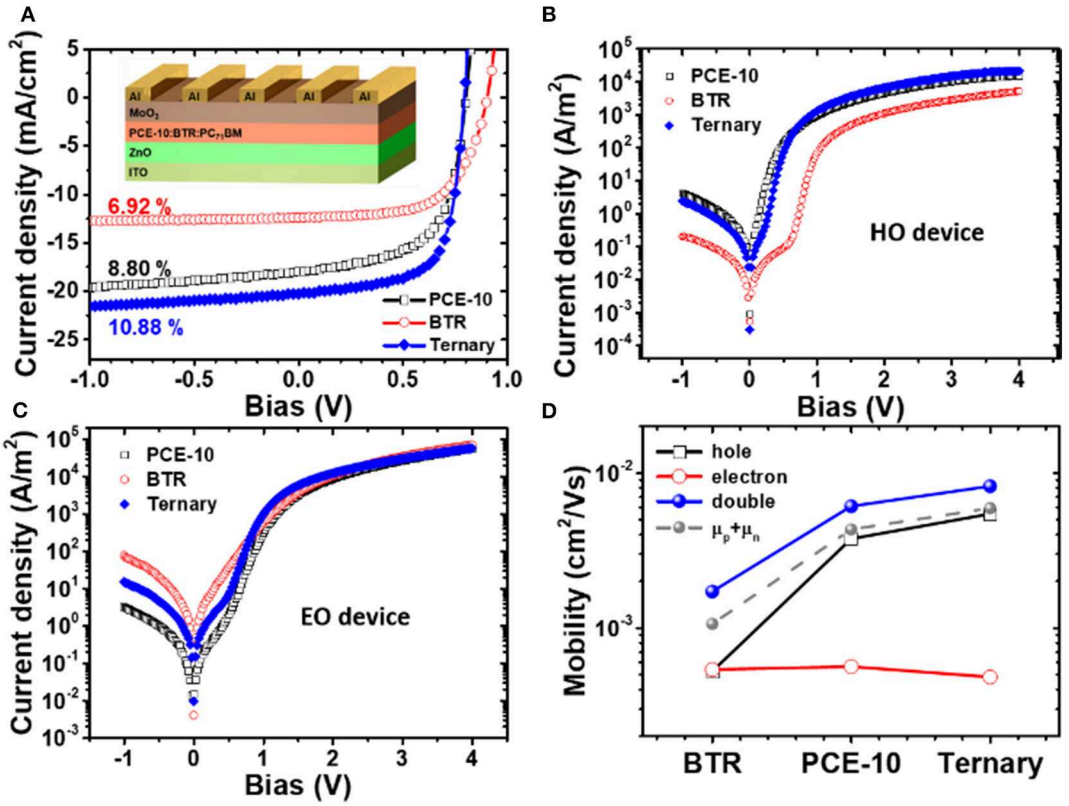

FIGURE 3 | (A) Current density vs. voltage (*J-V*) characteristics of BHJ-OSCs based on photo-active layers of PCE-10:$PC_{71}BM$, BTR:$PC_{71}BM$ binary blends, and PCE-10:BTR:$PC_{71}BM$ ternary blends. Dark *J-V* curves of **(B)** hole-only (HO) and **(C)** electron-only (EO) devices based on the same active layers of solar cells. **(D)** Carrier mobility of holes, electrons, and double carriers in BTR and PCE-10 binary, and ternary blends determined by single-carrier device measurements and solar cell dark current analysis. Also compared is the sum of electron and hole mobilities in single-carrier devices.

TABLE 1 | Photovoltaic parameters of PCE-10:$PC_{71}BM$ and BTR:$PC_{71}BM$ binary, and PCE-10:BTR:$PC_{71}BM$ ternary solar cells (blend ratio is 0.8:0.2:1) under 1.5 AM G solar irradiation (100 mW/cm^2).

BHJ	V_{oc} (V)	J_{sc} (mA/cm^2)	FF (%)	η (%)
PCE-10:BTR:$PC_{71}BM$	0.794	20.34	69.02	10.88
PCE-10:$PC_{71}BM$	0.772	17.62	64.52	8.80
BTR:$PC_{71}BM$	0.904	12.45	61.76	6.92

semiconductor devices can be determined either by transient, e.g., photo-CELIV (Yang et al., 2015) or steady-state opto-electrical methods (Nicolai et al., 2012). While the former techniques often require us to use thick films, the attained results may not truly reflect actual conditions in the solar cell with film thicknesses of active layer around 100 nm in some cases. Also, the dispersive transport in disorder systems tends to challenge reliable analyses on the transit time extracted from transient techniques, eventually complicating the mobility determination (Wetzelaer Gert-Jan et al., 2013). With these considerations, we simply adopted the well-established steady-state method with which the mobility in the space-charge limited current (SCLC) regime was assessed. **Figures 3B,C** show *J-V* characteristics in dark of hole- and electron-only devices based on active layers prepared identically to those in solar cells. The mobility of holes (μ_p) and electrons (μ_n) in blend films were determined through fitting the measurements to Mott-Gurney law. (Laquai et al., 2015) The results of μ_p and μ_n were averaged based on 10 devices in respective conditions and are shown in **Figure 3D**. As can be seen, the BTR has moderate carrier mobility with a balanced mobility ratio approaching 1. As will be addressed in follows, such transport feature can be connected to the low recombination rate in the BTR: $PC_{71}BM$ binary system with which the recombination in ternary devices are modulated.

Upon addition of the BTR donor, we observe opposite changes in the mobility of the two carriers, i.e., μ_p in the ternary blend increases with respect to μ_p in the two binary systems, while μ_n becomes slightly reduced. This result may be related to the distinct impacts of BTR on the charge transport networks involving the two carriers. Note that in our devices, the mobility imbalance (with the largest mobility ratio of 13.8) is not too severe and thus it may not cause the space-charge effect in photocurrents (Mihailetchi et al., 2005). This argument is supported by the absence of square-root dependent photocurrent on effective bias (see results in **Figure S1**) (Lenes et al., 2009). In a previous study based on the ITIC electron acceptor, we show that the imbalanced carrier mobility in BHJ solar cells does not necessarily cause an

enlargement of recombination, on the contrary it beneficially leads to a stronger reduction for bimolecular recombination (Zhang et al., 2017b). The presence of the recombination factor can be understood where faster carriers in the BHJ have to wait for their slower counterparts to recombine at the donor/acceptor interface, effectively weakening the encounter probability, and recombination intensity (Wehenkel et al., 2012). With this knowledge, the most imbalanced mobility in the ternary blends is implicative of a smaller reduction factor γ which in turn can mitigate recombination losses. To determine γ, we extracted the effective mobility of double carriers (μ_{sol}) based on the dark current of solar cells with Mott-Gurney law fittings. As shown in **Figure 3D**, the μ_{sol} of the ternary device is higher than both of μ_p and μ_n in the binary systems. In solar cells, μ_{sol} is subject to the co-existing processes of charge recombination and neutralization (Maurano et al., 2010). To this end, the μ_{sol} cannot be simply calculated by the sum of single carrier mobilities ($\mu_p+\mu_n$). A $\mu_{sol} = \mu_p+\mu_n$ only validates for double-carrier devices where the hole and electron transport independently within their own (non-percolated) networks (Heeger Alan, 2013) and never can meet with each other, resembling the operation of two back-connected single-carrier diodes (Wetzelaer Gert-Jan et al., 2013). Apparently this situation does not apply to the BHJ-OSCs featured with phase-separated and inter-percolated transport networks. As will be shown, that the μ_{sol} exceeds the value of $\mu_p+\mu_n$ mainly stems from the recombination current in the solar cell and the difference between these mobility values provides a quantification for γ based on a simple analytical model reported previously (Wetzelaer Gert-Jan et al., 2013).

To better correlate the steady-state transport to photovoltaic behaviors, we measured transient photocurrent (TPC) decay kinetics in the ternary and binary solar cells excited at 488 nm. The results of TPC at various biases are shown in **Figure 4A**. All the TPC trances are characteristics of a sharp rise in association with longer-lived decays extended to hundreds of nanoseconds. We note that the peak intensity reduces with incrementally varied forward bias, which results from the increased recombination current compensating the photocurrent at lower internal electrical fields (E_{int}). With an invariable recombination in the solar cell, the bias-dependent decay traces in **Figure 4A** should overlap on top of each other after normalization. While the decay becomes evidently slower at larger forward bias (see normalized TPC in **Figure S2**), confirming that the recombination indeed varies at different E_{int}.

Based on the mono-exponential decay model, we determined the extraction time for charges (τ_{ext}) in the solar cells. **Figure 4B** shows τ_{ext} vs. bias characteristics for solar cells with ternary and binary blends. All devices exhibit a relatively fast charge sweepout with the τ_{ext} falling in dozens of ns. We note that the order of τ_{ext} does not exactly follow that of the carrier mobility or balance. For example, the τ_{ext} for the BRT binary cell amounts to the lowest values, followed by that of the ternary device and lastly the binary blend system. This non-correlation is understood by that the τ_{ext} is subject to the combined result of charge collection and recombination and both processes will be promoted with increased mobility. The fast carrier extraction in the SM-binary solar cell may be linked to the smaller recombination rate associated with a very balanced mobility. Also, the τ_{ext} in the BTR binary device displays the least field-dependence compared to PCE-10 based binary and ternary devices. The different dependencies of τ_{ext} on E_{int} seems not to arise from a field-dependent mobility, as the current in single-carrier devices exhibit nearly perfect quadratic voltage dependence within a wide bias range (see *J-V* characteristics in **Figure S3**). On the other hand, field-dependent charge generation has been observed in a variety of BHJ-OSCs which was used to explain the poor fill factor (Albrecht et al., 2012). While in our case, geminate losses at low electric fields tend not to be a significant factor given the relatively high FF. To this end, the different dependencies of τ_{ext} on E_{int} (or bias) could be related to the field dependence of non-geminate recombination in our BHJ devices (Credgington et al., 2012; Foertig et al., 2013). An important indication

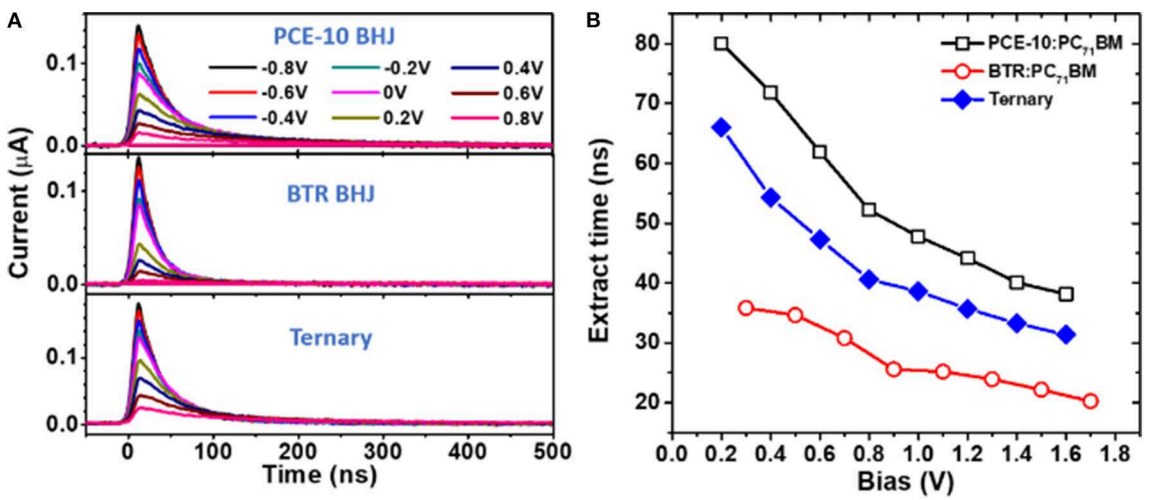

FIGURE 4 | (A) Transient photocurrent (TPC) decay kinetics of different BHJ-OSCs measured with applying different biases (excitation at 488 nm). **(B)** Extraction time of charges in operating solar cells as a function of bias determined by fittings with a mono-exponential decay model.

from the TPC measurements is that the introduced BTR donor promotes the efficiency for charge collection in the ternary solar cell in competition with recombination. As a result, the recombination losses with the increased density of photo-carriers can be suppressed.

The data so far, all point to reduced carrier losses in the ternary OSC with gains of J_{sc} and FF. To have a quantitative assessment on recombination, next we determined the recombination rate constant and reduction factor with the analytical model proposed by Wetzelaer Gert-Jan et al. (2013) which is written as,

$$\gamma = \frac{16\pi}{9}\frac{\mu_p\mu_n}{\mu_{sol}^2 - (\mu_p + \mu_n)^2} \quad (2)$$

The relevance of Equation 2 to solar cells is that the charge recombination parameters determined by transport measurements can mimic the situation in steady-state solar cell operation. **Figure 5A** shows the attained reduction factor γ for various solar cells. The γ displays a decreasing trend with the increase of mobility imbalance, e.g., the smallest value of 0.448 is found in the ternary with the largest mobility ratio. The correlation of γ to mobility ratio agrees with a recent study on PBDB-T:ITIC non-fullerene OSCs where the identified smaller γ is accompanied by a more severe mobility imbalance (Zhang et al., 2017b). A strong reduction in bimolecular recombination with respect to the Langevin process has been observed in non-fullerene binary OSCs with a large FF as well.

The Langevin rate constant β_L generally follows the relation,

$$\beta_L = \frac{q}{\varepsilon_o\varepsilon_s}(\mu_p + \mu_n) \quad (3)$$

where $\varepsilon_0\varepsilon_s$ is the dielectric constant of the BHJ film. Based on Equation 3, we are able to extract the recombination rate constant in the solar cell according to $\beta = \gamma\beta_L$. **Figure 5A** shows the determined β and the results are in line with typical values in BHJ-OSCs in the range of 10^{-10}–10^{-12} $cm^{-3}s^{-1}$ (Jiang et al., 2017a). Of importance: the recombination rate constant in the ternary reduces when compared to the β in the prime binary blends. These results can benefit from the introduced BTR donor with the lowest value of B in blend with $PC_{71}BM$. The modified bimolecular recombination in the ternary solar cell also is correlated to the π-π stacking in the ternary BHJ that was found to preferentially adapt to the out-of-plane direction with a small intermolecular d-space (~3.77 Å) (Zhang et al., 2015). The ternary BHJ with similar blend ratios have been identified with an improved domain purity with respect to

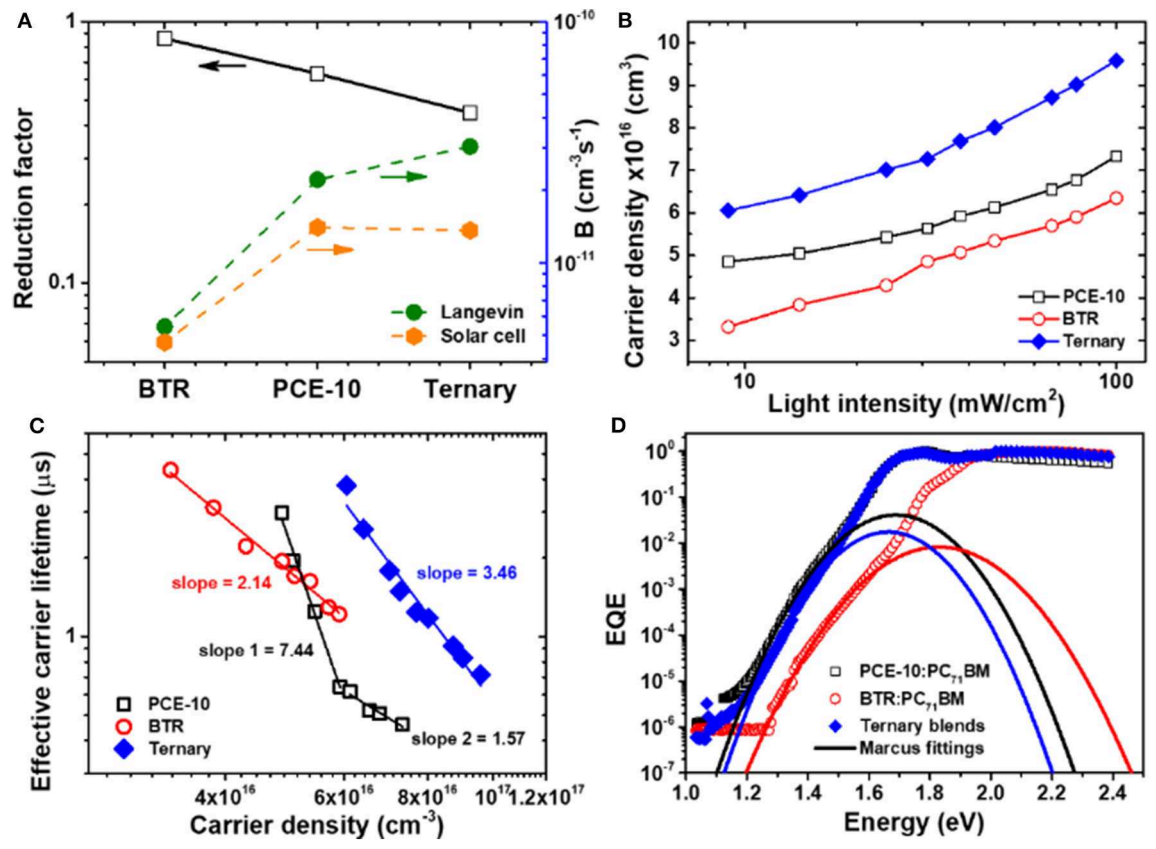

FIGURE 5 | (A) Reduction factor γ, recombination rate constant β and Langevin rate constant β_L determined on BHJ-OSCs with PCE-10 and BTR binary blends and PCE-10:BTR:$PC_{71}BM$ ternary blends. **(B)** Density of photocarriers as a function of light intensity in binary and ternary devices. **(C)** Effective carrier lifetime vs. carrier density characteristics of solar cells alongside linear fittings used to assess the recombination order. Inset texts: slopes of linear fittings. **(D)** Fourier transform photocurrent spectra (FTPS) of binary and ternary OSCs together with fittings with Marcus equation.

that in the PCE-10:$PC_{71}BM$ film (Ran Niva et al., 2015). As bimolecular recombination in BHJ-OSCs primarily occurs at the D/A interface (Janssen and Jenny, 2013), the reduction of mixed phases with higher domain purity helps lower the encounter probability for photo-carriers. This tendency is fully consistent with the identified reduction in the recombination rate constant in our ternary device.

It should be noted that the determined recombination parameters in **Figure 3A** extracted from steady-state transport only provides an approximation on the average rate of recombination (Peter et al., 2014). In actual solar cells under irradiation, the β may not necessarily be a constant, but change with carrier density (np). Carrier density-dependent β has been found in the canonical P3HT:PCBM system with a recombination order of 2 (Maurano et al., 2010). Rare examples for β being carrier-independent (constant) are found in polymer solar cells based on PIPCP:$PC_{61}BM$ (Garcia-Belmonte et al., 2010). Generally, the recombination rate B follows,

$$B = \frac{dn}{dt_{carr}} = \beta np \tag{4}$$

Through plotting np as a function of carrier lifetime t_{carr}, the dependence of β on carrier density can be assessed. We extracted the carrier lifetime t_{carr} and carrier density n (here assuming $n = p$) by irradiation intensity dependent on impedance spectroscopy at open-circuit condition. In this situation, the net current flow is zero because of the compensation of charge recombination. The values of n were attained by integrating the measured chemical capacitance C_μ over V_{oc} at different $P_{light,}$ and t_{carr} was extracted from the product of recombination resistance and C_μ (Yan et al., 2018). **Figure S4** shows Nyquist plots of impedance spectra measured on the solar cells at different P_{light}. Through equivalent circuit modeling (see utilized circuit in **Figure S5**), the determined n is plotted against P_{rad} in **Figure 5B**. The n was found to fall in the range of 10^{16}–10^{17} cm^{-3} at 1 sun (100 mW/cm^2) irradiation, exhibiting a quasi-exponential dependence on P_{light}. At 1 sun, the determined n in the binary solar cells roughly agrees with the value of $\sim 5\times10^{-16}$ cm^{-3} reported for other binary systems with similar band gaps (Yan et al., 2018). Consistently, the order of n follows the tendency of J_{sc} in device. It is noted that the n in the ternary device exhibits a sharper increase in the high light intensity regime (close to 1 sun), compared to the trend in binary devices. In a previous study, a saturation-like increase of n in DPP-containing SM-solar cells was found associated with more substantial carrier losses near 1 sun. (van der Poll Thomas et al., 2012) The trend in the ternary device in **Figure 5B** is suggestive of mitigated carrier losses near 1 sun irradiation. With the determined n and t_{carr}, the recombination kinetics were assessed through plotting these two parameters in logarithm scale. As seen from **Figure 5C**, under the same carrier density, the ternary device is indeed associated with longer-lived photo-carriers. Considering that the t_{carr} is only governed by recombination in the open-circuit condition without involving transport, the longer lifetime of carriers should be mainly attributed to the reduced recombination rate with smaller values of β near approaching 1 sun, according to Equation 1. In a theoretical study based on an array of BHJ-OSCs, it was shown that the ratio of charge extraction time to recombination lifetime denoted as Θ can significantly affect FFs in solar cell (Bartesaghi et al., 2015; Ran et al., 2017). Typical Θ values in OSCs range between 10^{-3} and 10^{-2}. Upon establishing an equilibrium between charge sweepout and recombination, increasing charge carrier mobility tends to shift the balance toward extraction. On this basis, a smaller value for the dimensionless parameter Θ can account for a higher FF. (Mozer et al., 2005) Based on the results of TPC and impedance spectroscopy, the Θ was determined to be 1.13×10^{-1} for the PCE-10:$PC_{71}BM$ binary device and 5.7×10^{-2} for the ternary device. Should be noted the Θ in operational solar cells may be even smaller as the charge extraction time determined by TPC was based on excitation with a laser pulse that has a much lower intensity than standard 1 sun irradiation. The reduced Θ in the ternary device reconciles the enhancement of FF, benefitting from the modified charge extraction and recombination balance.

The slopes in **Figure 5C** provide additional insights into the recombination order (RO). We found a slope of 2.14 in the BTR binary device, which resembles the value of P3HT:PCBM cells, pointing to roughly a 1st order recombination with RO roughly being 1. It suggests that the carrier density-dependence of β is weak in the SM-binary blends. The ternary device is associated with a slightly increased RO with a slope of 3.46, indicating a slight increase of the carrier dependence for β. Of interest, there appear two regimes with different slopes in the PCE-10 based binary cell. Variations of carrier density dependence or RO in different regimes of P_{light} have been found in previous (Maurano et al., 2010; van der Poll Thomas et al., 2012). A RO >1 is generally attributed to the effects of charge trapping/release, morphological traps, or spacial inhomogeneity in the distribution of photo-carriers (Andreas et al., 2011; Kirchartz and Nelson, 2012). These factors could play a role in our binary and ternary devices and further studies will be required to fully understand these observations.

With the identified impacts of recombination on the behaviors in ternary devices, at last we turn to the influence of BTR guest donor on V_{oc}. For this purpose, we measured energy of charge transfer-states (CTS) with which the V_{oc} losses are assessable. CTS are ubiquitously present in OSCs and the energy of CTS (E_{ct}, defined by the energetic distance from the ground states to the 1st excited states of CTS) sets an upper limit for experimentally achievable V_{oc} (Collins Samuel et al., 2015). As CTS are directly photo-excited, a commonly used method for determine E_{ct} involves measurements of the photocurrent arising from CTS absorption. **Figure 5D** shows Fourier transform photocurrent spectra (FTPS) of different solar cells. With the change of incident photon energy, we observe a wide range of photoresponse over orders of magnitudes. At the low energy regime, a sharp decrease of EQE is observed in association with an onset at 1.73 eV (PCE-10: $PC_{71}BM$), 1.97 eV (BTR:$PC_{71}BM$), and 1.72 eV (ternary). The difference in EQE onsets is consistent to that of the effective band gaps. The shoulder-like features are characteristics of the CTS absorption in fullerene based OSCs. The broad feature can be partially due to the relatively larger reorganization energy (λ) at CTS. (Perng et al., 1996; Vandewal et al., 2010) The values of E_{ct} and λ were determined through fittings of FTPS measurements

TABLE 2 | Fitting parameters for FTPS measurements in **Figure 5D** according to the Marcus theory.

BHJ	E_{ct} (eV)	λ (eV)	ΔV_{oc} (V)
PCE-10:BTR:$PC_{71}BM$	1.44	0.231	0.646
PCE-10:$PC_{71}BM$	1.44	0.256	0.668
BTR:$PC_{71}BM$	1.50	0.339	0.596

to Marcus equation (see lines in **Figure 5**) (Marcus, 1990). As summarized in **Table 2**, the E_{ct} of ternary device is identical to that of PCE-10 binary device, being 1.44 eV. The E_{ct} of the SM-binary cell increases to 1.5 eV, related to the deeper-lying HOMO in BTR. We estimated the V_{oc} losses (ΔV_{oc}) according to the relation, $\Delta V_{oc} = E_{ct}$-V_{oc} and the results are provided in **Supplementary Material**, SI. Among these BHJ solar cells, the least ΔV_{oc} (< 0.6 V) and the largest ΔV_{oc} ($= 0.668$ V) were found in the BTR and PCE-10 binary devices, respectively. It is of interest that the voltage losses become reduced in the ternary device, benefitting from the lower ΔV_{oc} in the BRT binary BHJ. This result points to the importance that the recombination losses for photo-carrier and voltage losses in the ternary solar cells can be simultaneously mitigated through the introducing the BTR guest with intrinsically a lower recombination and higher-lying E_{ct}, eventually leading to the enhanced PCE. Based on the fitting results (see **Table 2**), the ternary device displays the smallest reorganization energy ($\lambda = 0.231$ V). The value of λ provides a measure of the line width or energetic disorder in CTS (Thomas et al., 2015). Generally, the reduction of λ benefits the delocalization of charge wave functions and charge separation (Graham et al., 2014). From the results of FTPS, the ternary device presents a reduced energetic disorder at the interfacial CTS. The morphology origin for this phenomenon may be linked to the higher domain purity in the ternary blends (Mario et al., 2011). The energetic offset between CTS and excited states in donor constitutes the radiative losses in V_{oc} (Shenkun et al., 2018). Meanwhile, it serves the critical driving force for interfacial charge dissociation. On this basis, for the sake of attaining smaller ΔV_{oc}, it will be more realistic to suppress non-radiative losses in ternary devices without hampering charge generation and ultimate photocurrent. This may be implemented via control of transport balance and/or PL properties toward increases of electroluminescence efficiency in ternary BHJ films.

CONCLUSIONS

To summarize, we have comprehensively investigated the impacts of the introduced BTR small molecule guest to PCE-10:$PC_{71}BM$ binary blends on bimolecular recombination and photo-carrier losses in ternary solar cells. Strategically, we show that the reduction factor for recombination is modulated through co-blending the BTR donor with intrinsically a low recombination rate and balanced carrier mobility in blend with $PC_{71}BM$ acceptor. This leads to achieving a suppressed charge recombination and expedited charge sweepout in ternary devices. These modifications to some degree are correlated to charge transport characteristics in the ternary BHJ films, hinting that the mobility imbalance may not necessarily be a hindering factor. Based on the dimensionless parameter Θ that describes the ratio of charge extraction time to recombination time, the enhanced FF in the ternary solar cells is reconciled by the reduced Θ revealing the change of equilibrium between these two competing processes. By examination of recombination kinetics, we identify low recombination orders in the concerned BHJ systems, meaning a weak dependence of recombination rate constant on carrier density, possibly due to the specific nanomorphology in ternary blends. FTPS measurements indicate that the V_{oc} losses in the ternary cell are slightly mitigated upon addition of BTR, which originates from the rise of CT-state energy. The presented benefits in the presence of small molecule donor frame a useful guideline for future design of high efficiency ternary organic solar cells.

DATA AVAILABILITY STATEMENT

All datasets generated for this study are included in the article/**Supplementary Material**.

AUTHOR CONTRIBUTIONS

All authors listed have made a substantial, direct and intellectual contribution to the work, and approved it for publication.

FUNDING

This work was supported by the National Natural Science Foundation of China (Grant No. 21875012, 21674006, and 51275494) and the Chinese Academy of Sciences (100 Top Young Scientists Program). YZ thanks for the 111 project (B14009).

SUPPLEMENTARY MATERIAL

The Supplementary Material for this article can be found online at: https://www.frontiersin.org/articles/10.3389/fchem.2020.00021/full#supplementary-material

REFERENCES

Albrecht, S., Schindler, W., Kurpiers, J., Kniepert, J., Blakesley, J. C., Dumsch, I., et al. (2012). On the field dependence of free charge carrier generation and recombination in blends of PCPDTBT/PC70BM: influence of solvent additives. *J. Phys. Chem. Lett.* 3, 640–645. doi: 10.1021/jz3000849

Ameri, T., Khoram, P., Min, J., and Brabec Christoph, J. (2013). Organic ternary solar cells: a review. *Adv. Mater.* 25, 4245–4266. doi: 10.1002/adma.201300623

Andreas, B., Savenije, T., Martin, M. D. H., Vladimir, H., and Carsten, D. (2011). Influence of phase segregation on recombination dynamics in organic bulk-heterojunction solar cells. *Adv. Funct. Mater.* 21, 1687–1692. doi: 10.1002/adfm.201002358

Armin, A., Subbiah, J., Stolterfoht, M., Shoaee, S., Xiao, Z., Lu, S., et al. (2016). Reduced recombination in high efficiency molecular nematic liquid crystalline: fullerene solar cells. *Adv. Energy Mater.* 6:1600939. doi: 10.1002/aenm.201600939

Baran, D., Ashraf, R. S., Hanifi, D. A., Abdelsamie, M., Gasparini, N., Röhr, J. A., et al. (2016). Reducing the efficiency–stability–cost gap of organic photovoltaics with highly efficient and stable small molecule acceptor ternary solar cells. *Nat. Mater.* 16, 363–369. doi: 10.1038/nmat4797

Bartesaghi, D., Pérez, I., Kniepert, C. Roland, J., Turbiez, S., Neher, M. D., et al. (2015). Competition between recombination and extraction of free charges determines the fill factor of organic solar cells. *Nat. Commun.* 6:7083. doi: 10.1038/ncomms8083

Brus Viktor, V., Proctor Christopher, M., Ran Niva, A., and Nguyen, T. Q. (2016). Capacitance spectroscopy for quantifying recombination losses in nonfullerene small-molecule bulk heterojunction solar cells. *Adv. Energy Mater.* 6:1502250. doi: 10.1002/aenm.201502250

Chen, Y., Ye, P., Jia, X., Gu, W., Xu, X., Wu, X., et al. (2017). Tuning Voc for high performance organic ternary solar cells with non-fullerene acceptor alloys. *J. Mater. Chem.* 5, 19697–19702. doi: 10.1039/C7TA06237K

Collins Samuel, D., Proctor Christopher, M., Ran Niva, A., and Nguyen, T. Q. (2015). Understanding open-circuit voltage loss through the density of states in organic bulk heterojunction solar cells. *Adv. Energy Mater.* 6:1501721. doi: 10.1002/aenm.201501721

Credgington, D., Jamieson Fiona, C., Walker, B., Nguyen, T. Q., and Durrant James, R. (2012). Quantification of geminate and non-geminate recombination losses within a solution-processed small-molecule bulk heterojunction solar cell. *Adv. Mater.* 24, 2135–2141. doi: 10.1002/adma.201104738

Deibel, C., Strobel, T., and Dyakonov, V. (2010). Role of the charge transfer state in organic donor–acceptor solar cells. *Adv. Mater.* 22, 4097–4111. doi: 10.1002/adma.201000376

Foertig, A., Kniepert, J., Gluecker, M., Brenner, T., Dyakonov, V., Neher, D., et al. (2013). Nongeminate and geminate recombination in PTB7:PCBM solar cells. *Adv. Funct. Mater.* 24, 1306–1311. doi: 10.1002/adfm.201302134

Garcia-Belmonte, G., Boix, P. P., Bisquert, J., Sessolo, M., and Bolink, H. J. (2010). Simultaneous determination of carrier lifetime and electron density-of-states in P3HT:PCBM organic solar cells under illumination by impedance spectroscopy. *Solar Energy Mater. Solar Cells* 94, 366–375. doi: 10.1016/j.solmat.2009.10.015

Graham, K. R., Cabanetos, C., Jahnke, J. P., Idso, M. N., El Labban, A., Ngongang Ndjawa, G. O., et al. (2014). Importance of the donor: fullerene intermolecular arrangement for high-efficiency organic photovoltaics. *J. Am. Chem. Soc.* 136, 9608–9618. doi: 10.1021/ja502985g

Heeger Alan, J. (2013). 25th anniversary article: bulk heterojunction solar cells: understanding the mechanism of operation. *Adv. Mater.* 26, 10–28. doi: 10.1002/adma.201304373

Heiber, M. C., Nguyen, T.-Q., and Deibel, C. (2016). Charge carrier concentration dependence of encounter-limited bimolecular recombination in phase-separated organic semiconductor blends. *Phys. Rev. B* 93:205204. doi: 10.1103/PhysRevB.93.205204

Hou, J., Inganäs, O., Friend, R. H., and Gao, F. (2018). Organic solar cells based on non-fullerene acceptors. *Nat. Mater.* 17, 119–128. doi: 10.1038/nmat5063

Janssen, J. R. A., and Jenny, N. (2013). Factors limiting device efficiency in organic photovoltaics. *Adv. Mater.* 25, 1847–1858. doi: 10.1002/adma.201202873

Jiang, K., Zhang, G., Yang, G., Zhang, J., Li, Z., Ma, T., et al. (2017a). Multiple cases of efficient nonfullerene ternary organic solar cells enabled by an effective morphology control method. *Adv. Energy Mater.* 8:1701370. doi: 10.1002/aenm.201701370

Jiang, W., Yu, R., Liu, Z., Peng, R., Mi, D., Hong, L., et al. (2017b). Ternary nonfullerene polymer solar cells with 12.16% efficiency by introducing one acceptor with cascading energy level and complementary absorption. *Adv. Mater.* 30:1703005. doi: 10.1002/adma.201703005

Julien, G., Andreas, P., Fortunato, P., Jannic, W., Zhipeng, K., Federico, C., et al. (2018). From recombination dynamics to device performance: quantifying the efficiency of exciton dissociation, charge separation, and extraction in bulk heterojunction solar cells with fluorine-substituted polymer donors. *Adv. Energy Mater.* 8:1701678. doi: 10.1002/aenm.201701678

Kan, B., Feng, H., Wan, X., Liu, F., Ke, X., Wang, Y., et al. (2017). Small-molecule acceptor based on the heptacyclic benzodi (cyclopentadithiophene) unit for highly efficient nonfullerene organic solar cells. *J. Am. Chem. Soc.* 139, 4929–4934. doi: 10.1021/jacs.7b01170

Kirchartz, T., and Nelson, J. (2012). Meaning of reaction orders in polymer: fullerene solar cells. *Phys. Rev. B* 86:165201. doi: 10.1103/PhysRevB.86.165201

Laquai, F., Andrienko, D., Mauer, R., and Blom Paul, W. M. (2015). Charge carrier transport and photogeneration in P3HT: PCBM photovoltaic blends. *Macromol. Rapid Commun.* 36, 1001–1025. doi: 10.1002/marc.201500047

Lenes, M., Morana, M., Brabec Christoph, J., and Blom Paul, W. M. (2009). Recombination-limited photocurrents in low bandgap polymer/fullerene solar cells. *Adv. Funct. Mater.* 19, 1106–1111. doi: 10.1002/adfm.200801514

Li, H., Lu, K., and Wei, Z. (2017). Polymer/small molecule/fullerene based ternary solar cells. *Adv. Energy Mater.* 7:1602540. doi: 10.1002/aenm.201602540

Liao, S. H., Jhuo, H. J., Cheng, Y. S., and Chen, S. A. (2013). Fullerene derivative-doped zinc oxide nanofilm as the cathode of inverted polymer solar cells with low-bandgap polymer (PTB7-Th) for high performance. *Adv. Mater.* 25, 4766–4771. doi: 10.1002/adma.201301476

Lu, L., Xu, T., Chen, W., Landry, E. S., and Yu, L. (2014). Ternary blend polymer solar cells with enhanced power conversion efficiency. *Nat. Photonics* 8, 716–722. doi: 10.1038/nphoton.2014.172

Marcus, R. A. (1990). Theory of charge-transfer spectra in frozen media. *J. Phys. Chem.* 94, 4963–4966. doi: 10.1021/j100375a038

Mario, C., Matt, B., Daniele, F., Zhihua, C., Riccardo, D. P., Christopher, N., et al. (2011). Very low degree of energetic disorder as the origin of high mobility in an n-channel polymer semiconductor. *Adv. Funct. Mater.* 21, 3371–3381. doi: 10.1002/adfm.201100592

Maurano, A., Hamilton, R., Shuttle Chris, G., Ballantyne Amy, M., Nelson, J., O'Regan, B., et al. (2010). Recombination dynamics as a key determinant of open circuit voltage in organic bulk heterojunction solar cells: a comparison of four different donor polymers. *Adv. Mater.* 22, 4987–4992. doi: 10.1002/adma.201002360

Mihailetchi, V. D., Wildeman, J., and Blom, P. W. M. (2005). Space-charge limited photocurrent. *Phys. Rev. Lett.* 94:126602. doi: 10.1103/PhysRevLett.94.126602

Mozer, A. J., Sariciftci, N. S., Lutsen, L., Vanderzande, D., Österbacka, R., Westerling, M., et al. (2005). Charge transport and recombination in bulk heterojunction solar cells studied by the photoinduced charge extraction in linearly increasing voltage technique. *Appl. Phys. Lett.* 86:112104. doi: 10.1063/1.1882753

Nicolai, H. T., Kuik, M., Wetzelaer, G. A. H., de Boer, B., Campbell, C., Risko, C., et al. (2012). Unification of trap-limited electron transport in semiconducting polymers. *Nat. Mater.* 11, 882–887. doi: 10.1038/nmat3384

Perng, B. C., Newton, M. D., Raineri, F. O., and Friedman, H. L. (1996). Energetics of charge transfer reactions in solvents of dipolar and higher order multipolar character. I. Theory. *J. Chem. Phys.* 104, 7153–7176. doi: 10.1063/1.471431

Peter, Z., Martijn, K., Ran, N., Love, J. A., and Thuc-Quyen, N. (2014). Effects of processing conditions on the recombination reduction in small molecule bulk heterojunction solar cells. *Adv. Energy Mater.* 4:1400438. doi: 10.1002/aenm.201400438

Proctor Christopher, M., Albrecht, S., Kuik, M., Neher, D., and Nguyen, T. Q. (2014). Overcoming geminate recombination and enhancing extraction in solution-processed small molecule solar cells. *Adv. Energy Mater.* 4:1400230. doi: 10.1002/aenm.201400230

Ran N. A., Love John, A., Heiber Michael, C., Jiao, X., Hughes Michael, P., Karki, A., et al. (2017). Charge generation and recombination in an organic solar cell with low energetic offsets. *Adv. Energy Mater.* 8:1701073. doi: 10.1002/aenm.201701073

Ran Niva, A., Love John, A., Takacs Christopher, J., Sadhanala, A., Beavers Justin, K., Collins Samuel, D., et al. (2015). Harvesting the full potential of photons with organic solar cells. *Adv. Mater.* 28, 1482–1488. doi: 10.1002/adma.201504417

Scharber, M. C., Mühlbacher, D., Koppe, M., Denk, P., Waldauf, C., Heeger, A. J., et al. (2006). Design rules for donors in bulk-heterojunction solar cells—towards 10 % energy-conversion efficiency. *Adv. Mater.* 18, 789–794. doi: 10.1002/adma.200501717

Shenkun, X., Yuxin, X., Zhong, Z., Xuning, Z., Jianyu, Y., Huiqiong, Z., et al. (2018). Effects of nonradiative losses at charge transfer states and energetic disorder on the open-circuit voltage in nonfullerene organic solar cells. *Adv. Funct. Mater.* 28:1705659. doi: 10.1002/adfm.201705659

Sun, K., Xiao, Z., Lu, S., Zajaczkowski, W., Pisula, W., Hanssen, E., et al. (2015). A molecular nematic liquid crystalline material for high-performance organic photovoltaics. *Nat. Commun.* 6:6013. doi: 10.1038/ncomms7013

Sun, Y., Welch, G. C., Leong, W. L., Takacs, C. J., Bazan, G. C., and Heeger, A. J. (2011). Solution-processed small-molecule solar cells with 6.7% efficiency. *Nat. Mater.* 11, 44–48. doi: 10.1038/nmat3160

Thomas, H., Burke, T. M., Mateker, W. R., Sachs-Quintana, I. T., Vandewal, K., Brabec, C. J., et al. (2015). Disorder-induced open-circuit voltage losses in organic solar cells during photoinduced burn-in. *Adv. Energy Materials* 5:1500111. doi: 10.1002/aenm.201500111

van der Poll Thomas, S., Love John, A., Nguyen, T. Q., and Bazan Guillermo, C. (2012). Non-basic high-performance molecules for solution-processed organic solar cells. *Adv. Mater.* 24, 3646–3649. doi: 10.1002/adma.201201127

Vandewal, K., Tvingstedt, K., Gadisa, A., Inganäs, O., and Manca, J. V. (2010). Relating the open-circuit voltage to interface molecular properties of donor: acceptor bulk heterojunction solar cells. *Phys. Rev. B* 81:125204. doi: 10.1103/PhysRevB.81.125204

Veldman, D., Meskers Stefan, C. J., and Janssen Ren,é, A. J. (2009). The energy of charge-transfer states in electron donor–acceptor blends: insight into the energy losses in organic solar cells. *Adv. Funct. Mater.* 19, 1939–1948. doi: 10.1002/adfm.200900090

Wehenkel, D. J., Koster, L. J. A., Wienk, M. M., and Janssen, R. A. J. (2012). Influence of injected charge carriers on photocurrents in polymer solar cells. *Phys. Rev.* 85:125203. doi: 10.1103/PhysRevB.85.125203

Wetzelaer Gert-Jan, A. H., Van der Kaap Niels, J., Koster, L. J. A., and Blom Paul, W. M. (2013). Quantifying bimolecular recombination in organic solar cells in steady state. *Adv. Energy Mater.* 3, 1130–1134. doi: 10.1002/aenm.201300251

Xiao, Z., Jia, X., and Ding, L. (2017). Ternary organic solar cells offer 14% power conversion efficiency. *Sci. Bull.* 62, 1562–1564. doi: 10.1016/j.scib.2017.11.003

Yan, C., Barlow, S., Wang, Z., Yan, H., Jen, A. K. Y., Marder, S. R., et al. (2018). Non-fullerene acceptors for organic solar cells. *Nat. Rev. Mater.* 3:18003. doi: 10.1038/natrevmats.2018.3

Yang, Y., Chen, W., Dou, L., Chang, W.-H., Duan, H.-S., Bob, B., et al. (2015). High-performance multiple-donor bulk heterojunction solar cells. *Nat. Photonics* 9, 190–198 doi: 10.1038/nphoton.2015.9

Ye, L., Zhang, S., Ma, W., Fan, B., Guo, X., Huang, Y., et al. (2012). From binary to ternary solvent: morphology fine-tuning of D/A blends in PDPP3T-based polymer solar cells. *Adv. Mater.* 24, 6335–6341. doi: 10.1002/adma.201202855

Zhang, G., Zhang, K., Yin, Q., Jiang, X.-F., Wang, Z., Xin, J., et al. (2017a). High-performance ternary organic solar cell enabled by a thick active layer containing a liquid crystalline small molecule donor. *J. Am. Chem. Soc.* 139, 2387–2395. doi: 10.1021/jacs.6b11991

Zhang, J., Zhang, Y., Fang, J., Lu, K., Wang, Z., Ma, W., et al. (2015). Conjugated polymer–small molecule alloy leads to high efficient ternary organic solar cells. *J. Am. Chem. Soc.* 137, 8176–8183. doi: 10.1021/jacs.5b03449

Zhang, X., Zuo, X., Xie, S., Yuan, J., Zhou, H., and Zhang, Y. (2017b). Understanding charge transport and recombination losses in high performance polymer solar cells with non-fullerene acceptors. *J. Mater. Chem.* 5, 17230–17239. doi: 10.1039/C7TA05865A

Conflict of Interest: The authors declare that the research was conducted in the absence of any commercial or financial relationships that could be construed as a potential conflict of interest.

frontiers in Chemistry

ORIGINAL RESEARCH
published: 05 March 2020
doi: 10.3389/fchem.2020.00144

Impact of Polymer Backbone Fluorination on the Charge Generation/Recombination Patterns and Vertical Phase Segregation in Bulk Heterojunction Organic Solar Cells

Yanqiu Shao[1], Yuying Chang[1,2], Suju Zhang[1], Mingyue Bi[1], Shengjian Liu[3], Daliang Zhang[4], Shirong Lu[5] and Zhipeng Kan[5]**

[1] School of Chemistry and Chemical Engineering, Mudanjiang Normal University, Mudanjiang, China, [2] Heilongjiang Province Key Laboratory of New Carbon-Base Functional and Superhard Material, Mudanjiang, China, [3] Guangzhou Key Laboratory of Materials for Energy Conversion and Storage, Guangdong Provincial Engineering Technology Research Center for Materials for Energy Conversion and Storage, School of Chemistry, South China Normal University (SCNU), Guangzhou, China, [4] Institute of Advanced Interdisciplinary Studies, Chongqing University, Chongqing, China, [5] Organic Semiconductor Research Center, Chongqing Institute of Green and Intelligent Technology, Chinese Academy of Sciences, Chongqing, China

OPEN ACCESS

Edited by:
Ergang Wang,
Chalmers University of Technology, Sweden

Reviewed by:
Lei Ying,
South China University of Technology, China
Hua Tan,
Xiangtan University, China

***Correspondence:**
Yanqiu Shao
shaoyanqiu1969@163.com
Zhipeng Kan
kanzhipeng@cigit.ac.cn

Specialty section:
This article was submitted to Physical Chemistry and Chemical Physics, a section of the journal Frontiers in Chemistry

Received: 16 December 2019
Accepted: 17 February 2020
Published: 05 March 2020

Citation:
Shao Y, Chang Y, Zhang S, Bi M, Liu S, Zhang D, Lu S and Kan Z (2020) Impact of Polymer Backbone Fluorination on the Charge Generation/Recombination Patterns and Vertical Phase Segregation in Bulk Heterojunction Organic Solar Cells. Front. Chem. 8:144. doi: 10.3389/fchem.2020.00144

Incorporating fluorine (–F) substituents along the main-chains of polymer donors and acceptors is an effective strategy toward efficient bulk-heterojunction (BHJ) solar cells. Specifically, F-substituted polymers often exhibit planar conformations, leading to favorable packing, and electronic coupling. However, the effects of fluorine substituents on the charge generation and recombination characteristics that determine the overall efficiency of BHJ active layers remain critically important issues to examine. In this report, two PBDT[2X]T polymer analogs –poly[4,8-bis((2-ethylhexyl)oxy)benzo[1,2-*b*:4,5-*b'*]dithiophene-thiophene] [PBDT[2H]T] and its F-substituted counterpart poly[4,8-bis((2-ethylhexyl)oxy)benzo[1,2-*b*:4,5-*b'*]dithiophene-3,4-difluoro-thiophene] [PBDT[2F]T]—are studied to systematically examine how –F substituents impact the blend morphology, charge generation, carrier recombination and extraction in BHJ solar cells. Considering the large efficiency differences between PBDT[2H]T- and PBDT[2F]T-based BHJ devices, significant emphasis is given to characterizing the out-of-plane morphology of the blend films as vertical phase-separation characteristics are known to have dramatic effects on charge transport and carrier extraction in polymer-fullerene BHJ solar cells. Herein, we use electron energy loss spectroscopy (EELS) in tandem with charge transport characterization to examine PBDT[2X]T-fullerene blend films. Our analyses show that PBDT[2H]T and PBDT[2F]T possess very different charge generation, recombination and extraction characteristics, resulting from distinct aggregation, and phase-distribution within the BHJ blend films.

Keywords: bulk heterojunction, polymer backbone fluorination, charge generation and recombination, vertical phase segregation, organic solar cells

INTRODUCTION

The substitution of π-conjugated polymer chains with fluorine (–F) substituents is an effective strategy in the design of polymer donors and acceptors for efficient bulk-heterojunction (BHJ) solar cells (Li et al., 2019). Of all considered benefits, recent studies have shown that F-substituted polymers are prone to adopt planar conformations, and favorable packing and electronic coupling patterns (Do et al., 2016; Tang et al., 2020) broader consensus emphasizes their propensity for higher backbone rigidity and a more pronounced tendency to aggregate on going from solutions to thin-film (Li et al., 2014, 2020; Fei et al., 2015) compared to their counterparts without –F substituents –material properties that can be taken advantage of in BHJ solar cell optimization processes (Liu et al., 2014).

In spite of the significant experimental work pursued to describe the correlations between –F substitutions in polymer main-chains and polymer performance in actual BHJ solar cells, direct connections between material structure and device efficiency are often difficult to make. Considering F-substituted polymers, some important questions remain, in particular with regard to how molecular scale effects directed by –F substituents can impact mesoscale morphologies, charge generation, and recombination patterns in BHJ thin films (Eisner et al., 2019). Since experimental methods are lacking to directly probe how functional group substitutions affect polymer main-chain packing and aggregation, computational methodologies must be employed to provide this level of description (Do et al., 2017). Quantum mechanical calculations can describe intrinsic *inter*-monomer torsion profiles, which govern the main-chain dihedral distribution in the bulk; whereas molecular dynamics (MD) simulations can provide information on main-chain packing arrangements in the bulk, and the propensity to form ordered π-π aggregates (Li et al., 2020). To further molecular-scale insights and qualitatively describe the types of aggregates that prevail in the bulk, solid-state nuclear magnetic resonance (SS-NMR) spectroscopy can be used to complement computational methodologies, providing an experimental analysis of the conformational landscape defined by the polymer main-chains in the bulk (Do et al., 2016). Based on this methodology, both theoretical and experimental studies on the influence of –F substitutions on *intra-* and *inter*-molecular interactions have shown that the higher polymer backbone planarity and rigidity are at the origin of local packing effects (to which relate binding energies and electronic coupling between neighboring chains), and that these result in distinct aggregation and charge transport patterns (Do et al., 2016). As an example, in poly(3-alkyl-4-fluoro)thiophenes (F-P3AT) (Fei et al., 2015) –F substitutions have been shown to raise the melting temperature and crystallization enthalpy of the P3AT analogs –variations in intrinsic material properties that are consistent with backbone planarization effects, inducing main-chain rigidity, and higher propensity for aggregation in the solid state. In turn, employing F-P3AT, field-effect transistor mobilities increased by a factor of 5 compared to P3AT-based transistors (Fei et al., 2015).

In polymer-based BHJ solar cells, –F substitutions of monomer units including: thiophenes (Jo et al., 2014; Wolf et al., 2015), carbazoles (Kim et al., 2014), thienothiophenes (Chen et al., 2009; Carsten et al., 2011), benzothiadiazole (Stuart et al., 2013; Yang et al., 2013; Kim et al., 2014), benzotriazoles (Price et al., 2011; Chen et al., 2019), benzodithiophenes (Chen et al., 2009; Jo et al., 2014; Wolf et al., 2015), indacenodithiophenes (Schroeder et al., 2012), and anthradithiophenes (Gundlach et al., 2008) have resulted in improved device efficiencies. Due to the strong inductive electron-withdrawing nature of –F substituents (element of highest electronegativity), F-substituted polymer donors possess lower-lying highest occupied molecular orbital (HOMO) energy levels than their counterparts without –F substituents –leading to higher open-circuit voltages (V_{OC}) in BHJ solar cells (Chen et al., 2009, 2019). Setting aside their important effect on the electronic properties of both polymer donors (Chen et al., 2009; Price et al., 2011; Schroeder et al., 2012; Stuart et al., 2013; Yang et al., 2013; Jo et al., 2014; Kim et al., 2014; Li et al., 2014; Wolf et al., 2015; Do et al., 2016; Kawashima et al., 2016) and acceptors (Liu et al., 2016, 2017), –F substitutions may also affect the preferential orientation of polymer aggregates relative to device substrates, impacting device performance in some instances (Stuart et al., 2013), although here we note that those effects are not well-understood to date, and there were reports with opposite conclusions (Kawashima et al., 2016). Most systematic studies of the effect of F-substituents in polymers (comparing F-substituted vs. unsubstituted, analogous model systems) have converged to the idea that device performance can vary dramatically when either donor or acceptor contain F-substituents in their main-chain (Jo et al., 2014; Wolf et al., 2015; Kawashima et al., 2016). Along those lines, several reports have shown that concurrent synthetic and device optimizations of fluorinated polymers can yield significant improvements in BHJ thin films as carrier mobilities increase, and that those improvements result in direct BHJ solar cell efficiency increments (Jo et al., 2014; Wolf et al., 2015). Using pump probe ultrafast spectroscopy, Gorenflot et al. (2018) reported the exciton dissociation, charge separation, and extraction in BHJ solar cells with fluorine substituents, and it was found that in the fluorinated polymer BHJ solar cells, the charge generation is about 40% higher than that of the non-fluorinated polymer BHJ solar cells, resulting from improved exciton diffusion to the heterojunction, in conjunction with more efficient charge separation and reduced geminate recombination losses (Gorenflot et al., 2018). However, the effects of the presence of F-substituted polymers on the charge generation and recombination characteristics in BHJ solar cells, and how those effects translate into practical device efficiency variations, remain critically important issues to examine. In addition, significant emphasis is given to characterize the "out-of-plane" morphology of the blend films, because vertical phase-separation characteristics are known to have dramatic effects on charge transport and carrier extraction in polymer-fullerene BHJ solar cells.

In this report, we examine the charge generation and recombination in two analogous model systems in BHJ solar cells: poly[4,8-bis((2-ethylhexyl)oxy)benzo[1,2-*b*:4,5-*b*']dithiophene-thiophene] [PBDT[2H]T] and its F-substituted counterpart poly[4,8-bis((2-ethylhexyl)oxy)benzo[1,2-*b*:4,5-*b*']dithiophene-3,4-difluoro-thiophene [PBDT[2F]T]. (**Chart 1**)

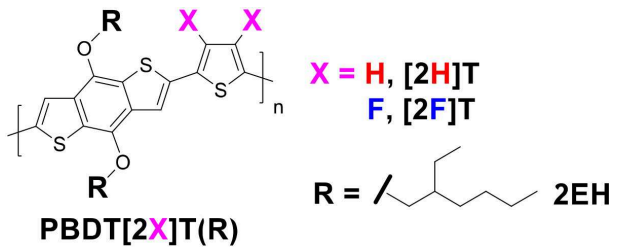

CHART 1 | Chemical structures of the PBDT[2X]T polymers (with X = H or F).

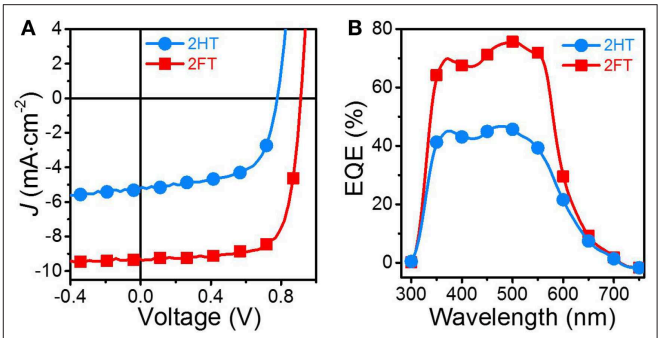

FIGURE 1 | (A) *J-V* curves and **(B)** EQE spectra for optimized 2HT- (blue) and 2FT-based (red) BHJ solar cells with $PC_{71}BM$ as the acceptor; AM1.5G solar illumination (100 mW/cm^2).

The PBDT[2X]T polymers dispersion index and molecular weight are shown in **Table S3**. Specifically, we systematically characterize carrier transport, recombination, and extraction across the BHJ devices and turn to morphological studies to establish a fuller understanding of how aggregation and vertical phase distributions impact the carrier dynamics, and in turn, BHJ solar cell efficiency.

RESULTS AND DISCUSSION

Optimized BHJ solar cells with direct device architecture were fabricated and tested under AM1.5G solar illumination (100 mW/cm^2). The PBDT[2X]T:$PC_{71}BM$ blend solutions (ratio: 1:1.5, wt/wt) were cast from a hot chlorobenzene (CB; *ca.* 90°C) solution with 5 vol% 1-chloronaphthalene (CN) (cf. details in the SI; film thicknesses in the range 80–90 nm). The energy level diagram of PBDT[2H]T, PBDT[2F]T and $PC_{71}BM$ in **Figure S2**. **Figure S3** accounts for the relative thin-film absorbance and solution absorption coefficients of the PBDT[2H]T and PBDT[2F]T. As shown in **Figure 1A** and **Table 1**, the optimized PBDT[2H]T:$PC_{71}BM$ (2HT-based) and PBDT[2F]T:$PC_{71}BM$ (2FT-based) BHJ solar cells achieved very distinct efficiencies and device statistics including standard deviations are provided in the Supplementary Information (**Tables S1**, **S2**; **Figure S1**). While the optimized 2HT-based devices achieved V_{OC} of *ca.* 0.77 V, modest J_{SC} of *ca.* 5.2 mA/cm^2, and fill-factors (*FF*s) of 60.1%, the 2FT-based counterpart yields a substantially higher J_{SC} of *ca.* 9.3 mA/cm^2, and a concurrently improved *FF* (73.3%) and V_{OC} (*ca.* 0.89 V). Overall, 2FT-based devices achieve a power conversion efficiency (PCE) improvement of more than two-fold, reaching up to 6.2% (*avg.* 6.1%) under the same film-casting conditions.

The large differences in J_{SC} values between 2HT- and 2FT-based BHJ solar cells (**Table 1**) are shown in the *J-V* curves provided in **Figure 1A**, and are consistent with the integrated current from the external quantum efficiency (EQE) spectra shown in **Figure 1B** (± 6%). In **Figure 1B**, 2FT-based devices show the most prominent spectral response in the range 350–600 nm, with EQE values reaching *ca.* 75% at 500 nm (EQE >60% in the range 350–580 nm). In comparison, EQE values in 2HT-based devices remain below 50% across the visible spectrum –observations implying that the substitution pattern in PBDT[2X]T correlates with significant variations in BHJ solar cell performance.

TABLE 1 | PV performance of the 2HT- and 2FT-based BHJ solar cells[a,b].

	V_{OC} (V)	J_{SC} (mA/cm^2)	*FF* (%)	Avg. PCE (%)	Max. PCE (%)
2HT	0.77	5.2	60.1	2.4	2.7
2FT	0.89	9.3	73.3	6.1	6.2

[a]*Average values across >10 devices across 3 substrates.* [b]*Device statistics in the Supplementary Information,* ***Table S1****.*

The competition between charge recombination and extraction governs the *FF* in BHJ solar cells and in turn device PCE. Meanwhile, both the loss of photogenerated carriers by recombination and charge extraction processes are limited by the carrier mobilities of the blend film for holes and electrons. To estimate the electron and hole mobilities in optimized PBDT[2X]T:$PC_{71}BM$ blend films, we measured the dark current density-voltage characteristics of single-carrier devices (see experimental details in the SI) and then fitted the data using the space-charge-limited current (SCLC) (Giulianini et al., 2010) model described by the Mott-Gurney law (with a small field dependent term), as in following equation (Mihailetchi et al., 2005).

$$J(V) = \frac{9}{8}\varepsilon_0\varepsilon_r\mu_0 \exp\left(0.89\beta\sqrt{\frac{V - V_{bi}}{L}}\right)\frac{(V - V_{bi})^2}{L^3} \quad (1)$$

where ε_0 and ε_r are the dielectric permittivity of a vacuum and the active layer, L is the thickness of the active layer, V is the applied voltage, V_{bi} is the built-in voltage, μ_0 is the zero-field mobility, and β is the field-activation factor.

Figure 2 shows the dark *J-V* characteristics of the electron-only diode in the configuration ITO/Al/2XT:$PC_{71}BM$/Al (**Figure 2A**) and that for the hole-only diode with the architecture ITO/MoO_3/2XT:$PC_{71}BM$/MoO_3/Ag (**Figure 2B**) (cf. additional details in the Supplementary Information, **Figure S4**). The fitting to the experimental results (solid lines in **Figure 2**; the parameters used in the fitting and films with other thickness are detailed in the Supplementary Information, **Figure S4**, **Tables S4** and **S5**) indicate that the electron mobility in the BHJ blend films with the 2HT and 2FT polymers is comparable: *ca.* 6.2 ×

10^{-4} cm^2 V^{-1}s^{-1} and 6.8 × 10^{-4} cm^2 V^{-1}s^{-1}, respectively. In contrast, the hole mobility in the 2HT- and 2FT-based blend films are an order of magnitude different: *ca.* 4.4 × 10^{-6} vs. 3.5 × 10^{-5} cm^2 V^{-1}s^{-1}, respectively. As a result, the carrier mobilities are significantly more balanced in 2FT-based devices –which represents an important parameter in explaining the performance differences observed between 2HT- and 2FT-based BHJ solar cells.

The charge collection probability, P_c (I, V), is defined as the ratio between J_{SC} and saturated photocurrent density $J_{ph.sat.}$ at reversed biases when the current density becomes independent of the applied voltage (cf. details in the Supplementary Information, **Figures S5**, **S6**) (Cowan et al., 2010; Mori et al., 2014).

Figure 3A shows the P_c $(I, -2V)$ for the 2HT- and 2FT-based BHJ solar cells as a function of incident light intensity I. In both cases, the P_c values were almost independent of incident light intensity over the range 0.17–1.20 suns, yielding *ca.* 80% for 2HT-based devices and 95% for their 2FT counterparts. When the charge carrier density increases with increasing light intensity, the magnitude of the bimolecular recombination rate should also increase and the P_c should decrease at higher values of I if the device suffers non-negligible bimolecular recombination at short-circuit. Therefore, the independence of P_c on I suggests that neither 2HT- nor 2FT-based devices suffer from bimolecular recombination under the short-circuit conditions.

To further examine whether carrier recombination was limiting device efficiency to a different extent in 2HT- and 2FT-based devices, we turned to a characterization of J_{SC} and V_{OC} as a function of incident light intensity. **Figure 3B** provides the dependence of J_{SC} as a function of incident light intensity plotted in a log-log scale and fitted to a power law (solid lines). As reported in earlier work, a power law dependence of J_{SC}on incident light intensity I in BHJ solar cells is described by $J_{sc} \propto I^{\alpha}$ (Cowan et al., 2010; Koster et al., 2011; Kyaw et al., 2013). An exponential factor of $\alpha = 1$ (or near unity) is indicative of efficient carrier extraction prior to recombination at short-circuit. For 2HT-based devices, the power law fit to the J_{SC} vs. I data yields an α value of 0.94 ± 0.01, while for 2FT-based devices, the J_{SC} vs. I data fit yields an α value of 0.99 ± 0.01, indicating that carrier extraction proceeds with more recombination losses in 2HT-based BHJ solar cells. Therefore, through the analysis of P_c and the J_{SC} dependence on incident light intensity, 2HT-based devices suffer from two major losses channels thus far: (i) a relatively poor charge generation pattern reflected in the low J_{SC} (6 mA/cm^{-2}) and (ii) non-negligible recombination losses prior to extraction.

In parallel, **Figure 3C** depicts the variation of V_{OC} vs. I in a natural log-linear scale and fitted to $V_{oc} \propto n\frac{kT}{q}\ln(I)$ (Cowan et al., 2010; Kyaw et al., 2013), where k, T, and q are the Boltzmann constant, temperature in Kelvin, and the elementary charge, respectively. The parameter n (usually in the range of 1–2) accounts for the presence of carrier traps across the active layers or interfaces with the electrodes, and any deviations from $n = 1$ (trap-free condition) reflects the existence of trap-assisted recombination. As shown in **Figure 3C**, $n = 1.24$ and 1.27 were inferred for 2HT- and 2FT-based BHJ solar cells, respectively –implying that both 2HT- and 2FT-based devices suffer from trap-assisted recombination at open-circuit. To further our understanding of the charge recombination and extraction patterns in 2HT- and 2FT-based BHJ solar cells, we turned to transient photovoltage and photocurrent analyses.

Transient photovoltage (TPV) measurements and their analysis provide information regarding the non-geminate

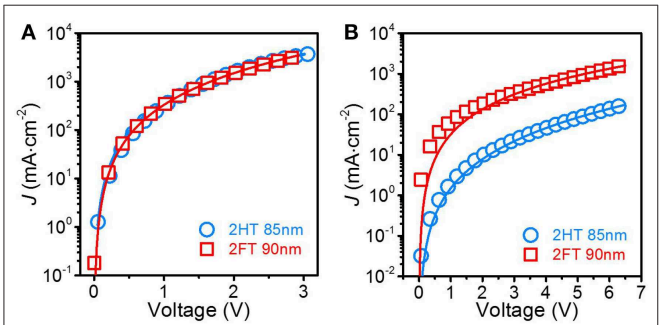

FIGURE 2 | Dark current density-voltage characteristics for **(A)** electron-only (ITO/Al/active layer/Al) and **(B)** hole-only (ITO/MoO_3/active layer/MoO_3/Ag) diodes with optimized PBDT[2X]T:PC_{71}BM active layers.

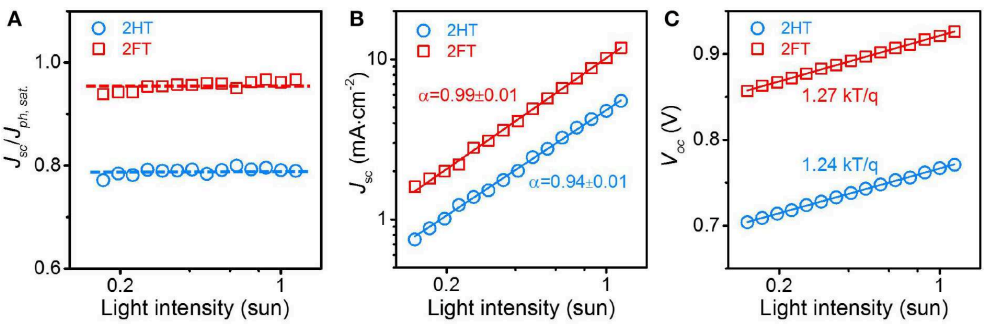

FIGURE 3 | (A) Charge collection probability P_c as a function of incident light intensity in linear-log scale, **(B)** J_{SC} as a function of incident light intensity in log-log scale, and **(C)** V_{OC} as a function of incident light intensity for the 2HT- and 2FT-based BHJ solar cells in linear-log scale. The solid lines in **(B,C)** correspond to fits to the data based on the equations $J_{sc} \propto I^{\alpha}$ and $V_{oc} \propto n\frac{kT}{q}\ln(I)$, respectively.

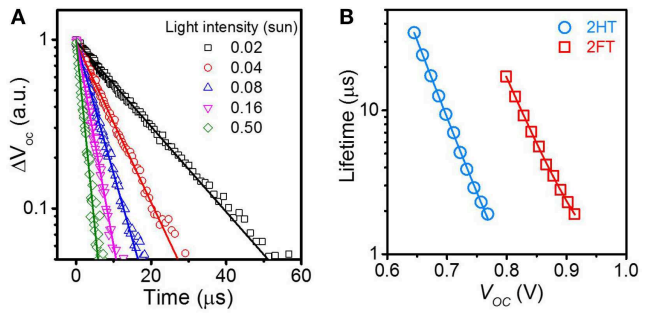

FIGURE 4 | (A) Normalized transient photovoltage perturbation from 2FT-based BHJ solar cells under various light intensities at open-circuit. **(B)** Carriers lifetime as a function of V_{OC} from the best performed device. The solid lines in both figure subsets are mono-exponential fits (cf. fitting details in the SI).

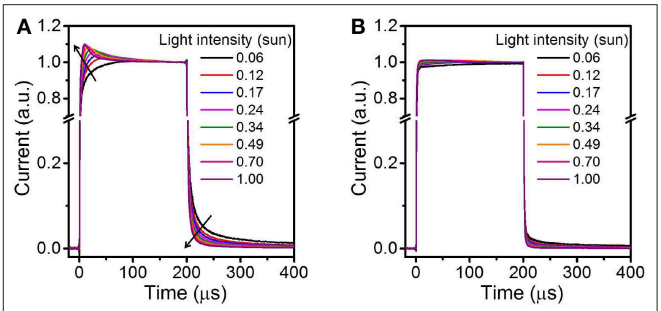

FIGURE 5 | Transient photocurrent (normalized) in response to a 200 μs white light (LED) pulse for **(A)** 2HT- and **(B)** 2FT-based BHJ solar cells. The legend in **(A)** provides the various light intensities (in equivalent suns). The black arrows emphasize the dependence of the photocurrent as a function of light intensity (after pulse excitation) and light intensities (cf. details in the SI).

recombination of charges within devices. TPV measurements record the voltage decay transient of a device held at open-circuit under continuous illumination after being subject to a short perturbative light pulse; the photovoltage decay can be used as a direct measure of charge recombination kinetics in BHJ solar cells at open-circuit. One or two time constants, representative of carrier lifetime, can be obtained by fitting the decay kinetics with mono- or bi-exponential equations, suggesting that one or two recombination routes can co-exist, that can generally be assigned to either bimolecular or/and trap-assisted recombination (Li et al., 2011; Liang et al., 2018). TPV measurements were performed on the 2HT- and 2FT-based BHJ solar cells to characterize the non-geminate recombination profile in the two systems.

In both 2HT- and 2FT- based BHJ solar cells, mono-exponential fits to the experimental kinetics data were found to be appropriate fitting equations. **Figure 4A** shows the normalized TPV responses for a 2FT-based device subjected to several incident light intensities (Data fitting details reported in the Supplementary Information, see **Figure S7**). The single carrier lifetime figure derived from the TPV fitting of 2HT- and 2FT-based devices correlate with a single carrier recombination loss channel, here trap-assisted recombination as determined from the variation of V_{OC} with illumination intensity discussed in the previous section. **Figure 4B** plots the carrier lifetime as a function of V_{OC} for the 2HT- and 2FT-based BHJ solar cells. As expected, the carrier lifetime decreases with increasing V_{OC}, and the carrier lifetime at 1 sun is estimated as 2.3 and 2.0 μs (comparable) for 2HT- and 2FT-based devices, respectively.

Carrier transport and extraction across BHJ active layers can be examined via transient photocurrent (TPC) measurements (Hwang et al., 2009; McNeill et al., 2009; Li and McNeill, 2011; Li et al., 2011, 2013; Gao et al., 2014; Tremolet de Villers et al., 2014; Liang et al., 2019); analyses that are particularly relevant to the study of carrier traps and trap-assisted recombination in BHJ solar cells. In these analyses, the occurrence and extent of carrier traps across the active layer and/or at the interfaces between the BHJ blend film and the electrodes are reflected in the dependence of device current response and shape on light intensity. Instances of carrier traps concentrated at BHJ active layer/electrode interfaces and impinging on charge extraction have been discussed in recent studies (Hwang et al., 2009; McNeill et al., 2009; Li and McNeill, 2011; Tremolet de Villers et al., 2014). For example, in direct BHJ device configurations, fullerenes accumulating at the anode induce transient current peaks, greatly surpassing the steady-state current during rise events. Using concurrent experimental results and theoretical models, it has been shown that fullerenes act as hole-blocking layers, hindering hole extraction at the anode and, in turn, lowering BHJ solar cell efficiency (Tremolet de Villers et al., 2014). Here, we examine the turn-on and turn-off dynamics of the 2HT- and 2FT-based devices using long light pulse excitations (200 μs; cf. details in the SI), allowing the current density to reach steady-state conditions.

Figure 5 depicts the normalized transient photocurrent for optimized 2HT- and 2FT-based devices (cf. conditions given in **Table 1**); supplementary data can be found in the Supplementary Information (**Figure S8**). **Figure 6B** shows that the fast dynamics of the 2FT-based devices contrast with that for 2HT-based devices in **Figure 6A**. The rise/fall times on the order of 2 μs (i.e., the time required to reach 90% of the maximum current from an initial 10%) obtained from 2FT-based active layers (**Figure 6B**) are practically independent of light intensity. In comparison, the TPC curves for the 2HT-based devices show a significant dependence on light intensity, with a fast-initial transient photocurrent peak at higher light intensities followed by a second, slower photocurrent decay component leveling off at the steady-state current (at short-circuit) within *ca.* 150 μs (**Figure 6A**). Comparing the turn-off dynamics of the 2HT- and 2FT-based devices: the fast *ca.* 2 μs decay and the absence of pronounced photocurrent tail observed in 2FT-based active layers contrast with the persistent, light-intensity-dependent photocurrent tail observed in 2HT-based active layers, which suggests that carrier collection is delayed by deep traps for as long as 200 μs in the 2HT-based devices. In general, the slower dynamic component (beyond 205 μs, **Figures 5A,B**) becomes less prominent as light intensity increases, suggesting that the traps are filled at higher light intensities and, as a result, their impact on charge transport becomes less pronounced (McNeill et al., 2009; Li and McNeill, 2011). Based on earlier discussions and prior reports (Heumueller et al., 2014; Tremolet de Villers

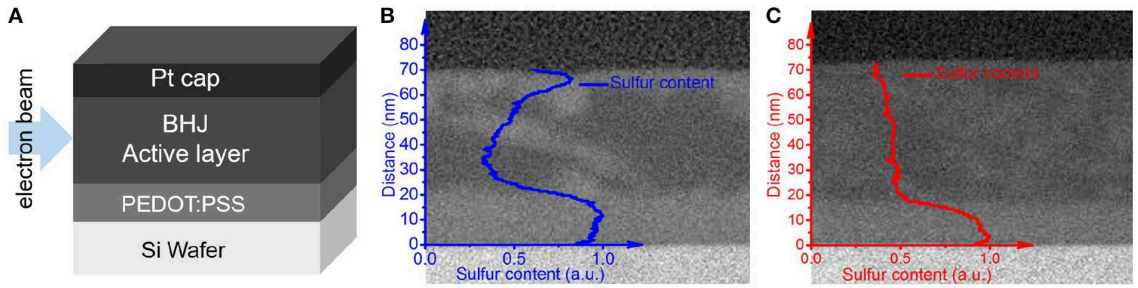

FIGURE 6 | (A) Schematic of the samples prepared for the cross-sectional TEM and EELS analyses. TEM cross-section images of the **(B)** 2HT- and **(C)** 2FT-based BHJ active layers cast on PEDOT:PSS and superimposed core-level sulfur analyses for the phase ratio mapping of polymer-rich (brighter regions) and fullerene-rich (darker regions) phases in the BHJ cross-section. The sulfur-content lines vs. distance from the substrate represented in subsets **(B,C)** capture the sulfur distribution averaged across the whole film cross section, and the distances are reported from the surface of the Si wafer (brightest layer) to the Pt capping layer (black).

et al., 2014; Pearson et al., 2016), the transient peak observed in 2HT-based devices may be the result of morphological effects buried within the active layer or occurring at the electrode interfaces. To probe those effects and provide a qualitative, macroscopic insight into the vertical distribution of polymer- and fullerene-rich domains across the optimized BHJ solar cells, we turned to electron energy loss spectroscopy (EELS) analyses performed from cross-sections of the BHJ thin films imaged by transmission electron microscopy (TEM) (cf. experimental details provided in the SI).

Figure 6 provides the EELS profiles collected from the cross-sections of BHJ thin films (cast from optimized conditions, see **Table 1**) with PBDT[2H]T (**Figure 6B**) and PBDT[2F]T (**Figure 6C**). Obtained from core-level sulfur analyses, the superimposed plots provide relative phase ratio mapping for the sulfur-rich—i.e., polymer-rich—and sulfur-deficient—i.e., fullerene-rich—regions in the BHJ cross-section. Here, we note that PEDOT:PSS interlayers were cast between the Si wafer (substrate) and the BHJ active layer to reproduce the morphology of the photoactive layers as obtained in actual BHJ solar cells; the high sulfur contents observed in the first *ca.* 20 nm distance from the Si wafer are thus consistent with the presence of the PEDOT:PSS. Beyond the PEDOT:PSS interface, the sulfur maps show two distinct phase distribution patterns for optimized 2HT- and 2FT-based BHJ active layers. On the one hand, **Figure 6B** suggests the existence of a gradient of polymer-rich phases across 2HT-based active layers on going from the PEDOT:PSS interface (anode) to the top interface (cathode in an actual BHJ device), with an apparent peak indicative of an accumulation of the polymer donor 2HT near the top interface (cathode). On the other hand, **Figure 6C** reflects a relatively uniform concentration profile of polymer and fullerene throughout the depth of the BHJ active layer. If supported by a more quantitative analysis of the vertical phase distribution in the BHJ active layers, the polymer-rich phase concentrated near the top interface (cathode) in 2HT-based active layers can hinder electron extraction by forming an electron-blocking layer. Concurrently, the apparently fullerene-rich phase concentrated near the PEDOT:PSS interface (anode) in 2HT-based active layers (**Figure 6B**) may be detrimental to hole extraction (hole-blocking layer).

CONCLUSION

To summarize, we systematically characterized the charge generation and recombination patterns in BHJ solar cells with PBDT[2H]T and its F-substituted counterpart PBDT[2F]T, and used EELS in tandem with charge transport characterization to examine PBDT[2X]T-fullerene blend films. The reduction in microsecond transient photocurrent allowed us to attribute the recombination losses in the 2HT-based BHJ solar cells to the hole extraction barrier/traps. However, the fluorinated polymer donor 2FT- based photoactive layer had a more uniformly distributed polymer/fullerene blend throughout most of the depth of the film with a thin fullerene accumulation layer at the anode, without showing the reduction in photocurrent. Thus, 2FT-based BHJ solar cells showed more efficient charge generation, extraction, and higher hole mobility compared with those of the 2HT-based BHJ solar cells, leading to higher V_{OC}, J_{SC}, FF, and overall device performance. The vertical phase segregation features of the 2HT- and 2FT-based BHJ solar cells were confirmed with EELS (sulfur mapping). The –F substituents impacted the polymer packing, which translates to the difference in aggregations from solution to film, thus the differences in polymer-fullerene phase mixing/composition in BHJ thin films. Our results provide an insight into the fluorination effects on the thin film BHJ compositions, especially the vertical phase, thus the device efficiency, providing a direct evidence of benefits from fluorination of polymers.

DATA AVAILABILITY STATEMENT

All datasets generated for this study are included in the article/supplementary material.

AUTHOR CONTRIBUTIONS

ZK, YS, YC, and SLu proposed the idea of this paper and contributed to analize the experiment results and wring the paper. YC and ZK contributed to the fabrication of the solar cells and characterization. DZ conducted the TEM. SLi contributed to the synthesis of the donor. SZ and MB conducted SCLC.

FUNDING

This work was financially supported by the National Natural Science Foundation of China (No. 61805245, 2180509), CAS Pioneer Hundred Talents Program (Y82A060Q10, Y92A160Q10), Recruitment Program of Global Experts (R52A199Z10), Higher education teaching reform of Heilongjiang Province of China (SJGY20190688), Heilongjiang Provincial Department of Education's Scientific Research Project (1352MSYYB006), Natural Science Foundation of Chongqing (cstc2015jcyjB0628 and cstc2017rgzn-zdyfX0030), the Guangdong Natural Science Foundation (No. 2016A030310428), and Guangzhou Science and Technology Foundation (No. 201904010361). Science and Technology Innovation Project of Mudanjiang Normal University (kjcx2019-22mdjnu).

SUPPLEMENTARY MATERIAL

The Supplementary Material for this article can be found online at: https://www.frontiersin.org/articles/10.3389/fchem.2020.00144/full#supplementary-material

REFERENCES

Carsten, B., Szarko, J. M., Son, H. J., Wang, W., Lu, L., He, F., et al. (2011). Examining the effect of the dipole moment on charge separation in donor–acceptor polymers for organic photovoltaic applications. *J. Am. Chem. Soc.* 133, 20468–20475. doi: 10.1021/ja208642b

Chen, H.-Y., Hou, J., Zhang, S., Liang, Y., Yang, G., Yang, Y., et al. (2009). Polymer solar cells with enhanced open-circuit voltage and efficiency. *Nat Photon* 3, 649–653. doi: 10.1038/nphoton.2009.192

Chen, Y., Zhang, Q., Du, M., Li, G., Li, Z., Huang, H., et al. (2019). Benzotriazole-based p-type polymers with thieno [3, 2-b] thiophene π-bridges and fluorine substituents to realize high Voc. *ACS Publ.* 1, 906–913. doi: 10.1021/acsapm.9b00156

Cowan, S. R., Roy, A., and Heeger, A. J. (2010). Recombination in polymer-fullerene bulk heterojunction solar cells. *Phys. Rev. B* 82:245207. doi: 10.1103/PhysRevB.82.245207

Do, K., Ravva, M. K., Wang, T., and Bredas, J.-L. (2017). Computational methodologies for developing structure–morphology–performance relationships in organic solar cells: a protocol review. *Chem. Mater.* 29, 346–354. doi: 10.1021/acs.chemmater.6b03111

Do, K., Saleem, Q., Ravva, M. K., Cruciani, F., Kan, Z., Wolf, J., et al. (2016). Impact of fluorine substituents on π-conjugated polymer main-chain conformations, packing, and electronic couplings. *Adv. Mater.* 28, 8197–8205. doi: 10.1002/adma.201601282

Eisner, F. D., Azzouzi, M., Fei, Z., Hou, X., Anthopoulos, T. D., Dennis, T. J. S., et al. (2019). Hybridization of local exciton and charge-transfer states reduces nonradiative voltage losses in organic solar cells. *J. Am. Chem. Soc.* 141, 6362–6374. doi: 10.1021/jacs.9b01465

Fei, Z., Boufflet, P., Wood, S., Wade, J., Moriarty, J., Gann, E., et al. (2015). Influence of backbone fluorination in regioregular poly (3-alkyl-4-fluoro) thiophenes. *J. Am. Chem. Soc.* 137, 6866–6879. doi: 10.1021/jacs.5b02785

Gao, F., Li, Z., Wang, J., Rao, A., Howard, I. A., Abrusci, A., et al. (2014). Trap-induced losses in hybrid photovoltaics. *ACS Nano* 8, 3213–3221. doi: 10.1021/nn501185h

Giulianini, M., Waclawik, E. R., Bell, J. M., and Motta, N. (2010). Temperature and electric field dependent mobility in poly (3-hexylthiophene) diodes. *J. Appl. Phys.* 108:014512. doi: 10.1063/1.3460111

Gorenflot, J., Paulke, A., Piersimoni, F., Wolf, J., Kan, Z., Cruciani, F., et al. (2018). From recombination dynamics to device performance: quantifying the efficiency of exciton dissociation, charge separation, and extraction in bulk heterojunction solar cells with fluorine-substituted polymer donors. *Adv. Energy Mater.* 8:1701678. doi: 10.1002/aenm.201701678

Gundlach, D. J., Royer, J. E., Park, S. K., Subramanian, S., Jurchescu, O. D., Hamadani, B. H., et al. (2008). Contact-induced crystallinity for high-performance soluble acene-based transistors and circuits. *Nat. Mater.* 7, 216–221. doi: 10.1038/nmat2122

Heumueller, T., Mateker, W. R., Sachs-Quintana, I. T., Vandewal, K., Bartelt, J. A., Burke, T. M., et al. (2014). Reducing burn-in voltage loss in polymer solar cells by increasing the polymer crystallinity. *Energy Environ. Sci.* 7, 2974–2980. doi: 10.1039/C4EE01842G

Hwang, I., McNeill, C. R., and Greenham, N. C. (2009). Drift-diffusion modeling of photocurrent transients in bulk heterojunction solar cells. *J. Appl. Phys.* 106:094506. doi: 10.1063/1.3247547

Jo, J. W., Jung, J. W., Wang, H.-W., Kim, P., Russell, T. P., and Jo, W. H. (2014). Fluorination of polythiophene derivatives for high performance organic photovoltaics. *Chem. Mater.* 26, 4214–4220. doi: 10.1021/cm502229k

Kawashima, K., Fukuhara, T., Suda, Y., Suzuki, Y., Koganezawa, T., Yoshida, H., et al. (2016). Implication of fluorine atom on electronic properties, ordering structures, and photovoltaic performance in naphthobisthiadiazole-based semiconducting polymers. *J. Am. Chem. Soc.* 138, 10265–10275. doi: 10.1021/jacs.6b05418

Kim, J., Yun, M. H., Kim, G.-H., Lee, J., Lee, S. M., Ko, S.-J., et al. (2014). Synthesis of PCDTBT-based fluorinated polymers for high open-circuit voltage in organic photovoltaics: towards an understanding of relationships between polymer energy levels engineering and ideal morphology control. *ACS Appl. Mater. Interfaces* 6, 7523–7534. doi: 10.1021/am500891z

Koster, L. J., Kemerink, M., Wienk, M. M., Maturová, K., and Janssen, R. A. (2011). Quantifying bimolecular recombination losses in organic bulk heterojunction solar cells. *Adv. Mater. Weinheim.* 23, 1670–1674. doi: 10.1002/adma.201004311

Kyaw, A. K., Wang, D. H., Gupta, V., Leong, W. L., Ke, L., Bazan, G. C., et al. (2013). Intensity dependence of current-voltage characteristics and recombination in high-efficiency solution-processed small-molecule solar cells. *ACS Nano* 7, 4569–4577. doi: 10.1021/nn401267s

Li, M., Bin, H., Jiao, X., Wienk, M. M., Yan, H., and Janssen, R. A. (2020). Controlling the microstructure of conjugated polymers in high-mobility monolayer transistors via the dissolution temperature. *Angew. Chem. Int. Ed.* 59, 846–852. doi: 10.1002/anie.201911311

Li, W., Albrecht, S., Yang, L., Roland, S., Tumbleston, J. R., McAfee, T., et al. (2014). Mobility-controlled performance of thick solar cells based on fluorinated copolymers. *J. Am. Chem. Soc.* 136, 15566–15576. doi: 10.1021/ja5067724

Li, W., Xiao, Z., Smith, J. A., Cai, J., Li, D., Kilbride, R. C., et al. (2019). Enhancing the efficiency of PTB7-Th: CO i 8DFIC-based ternary solar cells with versatile third components. *Appl. Phys. Rev.* 6:041405. doi: 10.1063/1.5125438

Li, Z., Gao, F., Greenham, N. C., and McNeill, C. R. (2011). Comparison of the operation of polymer/fullerene, polymer/polymer, and polymer/nanocrystal solar cells: a transient photocurrent and photovoltage study. *Adv. Funct. Mater.* 21, 1419–1431. doi: 10.1002/adfm.201002154

Li, Z., Lakhwani, G., Greenham, N. C., and McNeill, C. R. (2013). Voltage-dependent photocurrent transients of PTB7:PC70BM solar cells: experiment and numerical simulation. *J. Appl. Phys.* 114:034502. doi: 10.1063/1.4813612

Li, Z., and McNeill, C. R. (2011). Transient photocurrent measurements of PCDTBT:PC70BM and PCPDTBT:PC70BM solar cells: evidence for charge trapping in efficient polymer/fullerene blends. *J. Appl. Phys.* 109:074513. doi: 10.1063/1.3573394

Liang, R. Z., Babics, M., Seitkhan, A., Wang, K., Geraghty, P. B., Lopatin, S., et al. (2018). Additive-morphology interplay and loss channels in "all-small-molecule" bulk-heterojunction (BHJ) solar cells with the nonfullerene acceptor IDTTBM. *Adv. Funct. Mater.* 28:1705464. doi: 10.1002/adfm.201705464

Liang, R. Z., Zhang, Y., Savikhin, V., Babics, M., Kan, Z., Wohlfahrt, M., et al. (2019). Higher mobility and carrier lifetimes in solution-processable small-molecule ternary solar cells with 11% efficiency. *Adv. Energy Mater.* 9:1802836. doi: 10.1002/aenm.201802836

Liu, S., Kan, Z., Thomas, S., Cruciani, F., Brédas, J. L., and Beaujuge, P. M. (2016). Thieno [3, 4-c] pyrrole-4, 6-dione-3, 4-difluorothiophene polymer acceptors for efficient all-polymer bulk heterojunction solar cells. *Angew. Chem.* 128, 13190–13194. doi: 10.1002/ange.201604307

Liu, S., Song, X., Thomas, S., Kan, Z., Cruciani, F., Laquai, F., et al. (2017). Thieno [3, 4-c] pyrrole-4, 6-dione-based polymer acceptors for high open-circuit voltage all-polymer solar cells. *Adv. Energy Mater.* 7:1602574. doi: 10.1002/aenm.201602574

Liu, X., Gu, L., Zhang, Q., Wu, J., Long, Y., and Fan, Z. (2014). All-printable band-edge modulated ZnO nanowire photodetectors with ultra-high detectivity. *Nat. Commun.* 5, 1–9. doi: 10.1038/ncomms5007

McNeill, C. R., Hwang, I., and Greenham, N. C. (2009). Photocurrent transients in all-polymer solar cells: trapping and detrapping effects. *J. Appl. Phys.* 106:024507. doi: 10.1063/1.3177337

Mihailetchi, V. D., Wildeman, J., and Blom, P. W. (2005). Space-charge limited photocurrent. *Phys. Rev. Lett.* 94:126602. doi: 10.1103/PhysRevLett.94.126602

Mori, D., Benten, H., Okada, I., Ohkita, H., and Ito, S. (2014). Highly efficient charge-carrier generation and collection in polymer/polymer blend solar cells with a power conversion efficiency of 5.7%. *Energy Environ. Sci.* 7, 2939–2943. doi: 10.1039/C4EE01326C

Pearson, A. J., Hopkinson, P. E., Couderc, E., Domanski, K., Abdi-Jalebi, M., and Greenham, N. C. (2016). Critical light instability in CB/DIO processed PBDTTT-EFT:PC71BM organic photovoltaic devices. *Org. Electron.* 30, 225–236. doi: 10.1016/j.orgel.2015.12.024

Price, S. C., Stuart, A. C., Yang, L., Zhou, H., and You, W. (2011). Fluorine substituted conjugated polymer of medium band gap yields 7% efficiency in polymer–fullerene solar cells. *J. Am. Chem. Soc.* 133, 4625–4631. doi: 10.1021/ja1112595

Schroeder, B. C., Huang, Z., Ashraf, R. S., Smith, J., D'Angelo, P., Watkins, S. E., et al. (2012). Silaindacenodithiophene-based low band gap polymers – the effect of fluorine substitution on device performances and film morphologies. *Adv. Funct. Mater.* 22, 1663–1670. doi: 10.1002/adfm.201102941

Stuart, A. C., Tumbleston, J. R., Zhou, H., Li, W., Liu, S., Ade, H., et al. (2013). Fluorine substituents reduce charge recombination and drive structure and morphology development in polymer solar cells. *J. Am. Chem. Soc.* 135, 1806–1815. doi: 10.1021/ja309289u

Tang, H., Yan, C., Karuthedath, S., Yin, H., Gao, Y., Gao, J., et al. (2020). Deciphering the role of fluorination: morphological manipulation prompts charge separation and reduces carrier recombination in all-small-molecule photovoltaics. *Solar RRL*. 2020:1900528. doi: 10.1002/solr.201900528

Tremolet de Villers, B. J., MacKenzie, R. C. I., Jasieniak, J. J., Treat, N. D., and Chabinyc, M. L. (2014). Linking vertical bulk-heterojunction composition and transient photocurrent dynamics in organic solar cells with solution-processed MoOx contact layers. *Adv. Energy Mater.* 4:1301290. doi: 10.1002/aenm.201301290

Wolf, J., Cruciani, F., El Labban, A., and Beaujuge, P. M. (2015). Wide band-gap 3,4-difluorothiophene-based polymer with 7% solar cell efficiency: an alternative to P3HT. *Chem. Mater.* 27, 4184–4187. doi: 10.1021/acs.chemmater.5b01520

Yang, L., Tumbleston, J. R., Zhou, H., Ade, H., and You, W. (2013). Disentangling the impact of side chains and fluorine substituents of conjugated donor polymers on the performance of photovoltaic blends. *Energy Environ. Sci.* 6, 316–326. doi: 10.1039/C2EE23235A

Conflict of Interest: The authors declare that the research was conducted in the absence of any commercial or financial relationships that could be construed as a potential conflict of interest.

frontiers in Chemistry

CORRECTION
published: 08 April 2020
doi: 10.3389/fchem.2020.00267

Corrigendum: Impact of Polymer Backbone Fluorination on the Charge Generation/Recombination Patterns and Vertical Phase Segregation in Bulk Heterojunction Organic Solar Cells

Yanqiu Shao[1], Yuying Chang[1,2], Suju Zhang[1], Mingyue Bi[1], Shengjian Liu[3], Daliang Zhang[4], Shirong Lu[5] and Zhipeng Kan[5]**

[1] School of Chemistry and Chemical Engineering, Mudanjiang Normal University, Mudanjiang, China, [2] Heilongjiang Province Key Laboratory of New Carbon-Base Functional and Superhard Material, Mudanjiang, China, [3] Guangzhou Key Laboratory of Materials for Energy Conversion and Storage, Guangdong Provincial Engineering Technology Research Center for Materials for Energy Conversion and Storage, School of Chemistry, South China Normal University (SCNU), Guangzhou, China, [4] Institute of Advanced Interdisciplinary Studies, Chongqing University, Chongqing, China, [5] Organic Semiconductor Research Center, Chongqing Institute of Green and Intelligent Technology, Chinese Academy of Sciences, Chongqing, China

Keywords: bulk heterojunction, polymer backbone fluorination, charge generation and recombination, vertical phase segregation, organic solar cells

OPEN ACCESS

Approved by:
Frontiers Editorial Office, Frontiers Media SA, Switzerland

****Correspondence:***
Yanqiu Shao
shaoyanqiu1969@163.com
Zhipeng Kan
kanzhipeng@cigit.ac.cn

Specialty section:
This article was submitted to Physical Chemistry and Chemical Physics, a section of the journal Frontiers in Chemistry

Received: *12 March 2020*
Accepted: *18 March 2020*
Published: *08 April 2020*

Citation:
Shao Y, Chang Y, Zhang S, Bi M, Liu S, Zhang D, Lu S and Kan Z (2020) Corrigendum: Impact of Polymer Backbone Fluorination on the Charge Generation/Recombination Patterns and Vertical Phase Segregation in Bulk Heterojunction Organic Solar Cells. Front. Chem. 8:267. doi: 10.3389/fchem.2020.00267

A Corrigendum on

Impact of Polymer Backbone Fluorination on the Charge Generation/Recombination Patterns and Vertical Phase Segregation in Bulk Heterojunction Organic Solar Cells
by Shao, Y., Chang, Y., Zhang, S., Bi, M., Lu, S., Zhang, D., et al. (2020). Front. Chem. 8:144. doi: 10.3389/fchem.2020.00144

In the published article, there was an error regarding the affiliations for Yuying Chang. As well as having affiliation(s) 1, they should also have "**Heilongjiang Province Key Laboratory of New Carbon-Base Functional and Superhard Material, Mudanjiang, China**."

The authors apologize for this error and state that this does not change the scientific conclusions of the article in any way. The original article has been updated.

frontiers in Chemistry

ORIGINAL RESEARCH
published: 24 March 2020
doi: 10.3389/fchem.2020.00190

Introducing Trifluoromethyl to Strengthen Hydrogen Bond for High Efficiency Organic Solar Cells

*Hao Zhang, Xiaoyang Du, Yunhan Tang, Xi Lu, Lei Zhou, Caijun Zheng, Hui Lin and Silu Tao**

School of Optoelectronic Science and Engineering, University of Electronic Science and Technology of China (UESTC), Chengdu, China

Nowadays, the ternary strategy has become a common way to improve the power conversion efficiency (PCE) of organic solar cells (OSCs). The intermolecular interaction between the third component and donor or acceptor plays a key role in achieving a high performance. However, hydrogen bond as a strong intermolecular interaction is rarely considered in ternary OSCs. In this work, we introduce trifluoromethyl on a newly synthesized small molecular DTBO to strength hydrogen bonds between DTBO and IEICO-4F. Due to the existence of hydrogen bonds has a strong impact on electrostatic potential (ESP) and benefits π-π stacking in the active layer, the ternary OSCs show superior charge extraction and low charge recombination. In DTBO, PTB7-Th and IEICO-4F based ternary devices, the PCE increases from 11.02 to 12.48%, and short-circuit current density (J_{SC}) increases from 24.94 to 26.43 mA/cm^2 compared with typical binary devices. Moreover, the addition of DTBO can realize an energy transfer from DTBO to PTB7-Th and broaden the absorption spectrum of blend films. Grazing-incidence wide-angle X-ray scattering (GIWAXS) patterns show that the π-π stacking distance of IEICO-4F decreased after adding 10 wt% DTBO. The effect of the hydrogen bond is also achieved in the PM6: Y6 system, showing 16.64% efficiency by comparison to the 15.49% efficiency of binary system. This work demonstrates that introduce trifluoromethyl to enhance hydrogen bond which improve π-π stacking can achieve higher performance in OSCs.

Keywords: organic solar cells, ternary devices, hydrogen bond, π-π stacking, energy transfer

OPEN ACCESS

Edited by:
Jiangang Liu,
Shantou University, China

Reviewed by:
Fujun Zhang,
Beijing Jiaotong University, China
Xao-Tao Hao,
Shandong University, China

****Correspondence:***
Silu Tao
silutao@uestc.edu.cn

Specialty section:
This article was submitted to Physical Chemistry and Chemical Physics, a section of the journal Frontiers in Chemistry

Received: *03 February 2020*
Accepted: *28 February 2020*
Published: *24 March 2020*

Citation:
Zhang H, Du X, Tang Y, Lu X, Zhou L, Zheng C, Lin H and Tao S (2020) Introducing Trifluoromethyl to Strengthen Hydrogen Bond for High Efficiency Organic Solar Cells. Front. Chem. 8:190. doi: 10.3389/fchem.2020.00190

INTRODUCTION

Solar energy is a promising alternative energy for future renewable energy. OSCs are the research focus in photovoltaic industry due to their superiority of low cost, flexibility and lightweight (Rossander et al., 2017; Dong et al., 2019; Jeong et al., 2019; Yan et al., 2019). Synthesis of novel acceptors has contributed to increase the power conversion efficiency (PCE). The state-of-the-art binary OSCs with single-junction structure have made a great improvement in PCE, which is up to 15% (Yuan et al., 2019). Nevertheless, it is a great challenge to further improve PCE. Many researchers have made much effort and got outcomes by adding solvent additives (Lee et al., 2008; Liang et al., 2010; Moon et al., 2010), incorporating the third material in the active layer (Bi et al., 2018; Nian et al., 2018), designing new device structure (Meng et al., 2018) and interface engineering (He et al., 2015). To date, ternary OSCs (containing a second donor or a second

acceptor) has become one of the main strategies to elevate the PCE (Bi and Hao, 2019), the highest PCE of ternary devices is over 16% (Pan et al., 2019; Yan et al., 2019; Du et al., 2020).

In OSCs, π-π stacking plays a key role in device performance, which is extremely important for the charge transfer and transport (Ran et al., 2017; Hou et al., 2018). In addition, molecular aggregation is crucial to the exciton dissociation efficiency, high charge extraction, and low charge carrier recombination, leading to a better carrier mobility and domain purity (Zhang et al., 2017, 2018). Hence, incorporating a third component can achieve a better impact on π-π stacking and molecular aggregation, resulting in a better charge carrier transport channel and a better device performance.

To date, non-fullerene acceptors have shown remarkable performance. But one of the main challenges for non-fullerene acceptor is how to maintain efficient π-π interactions (Kang et al., 2016; Lee et al., 2016; Hou et al., 2018). Therefore, non-fullerene acceptors are the perfect materials to study the impact of the third component on the π-π stacking. Meanwhile, in ternary OSCs, incorporating a third material can broaden the absorption spectrum, resulting in enhanced photon harvesting ability and increased short-circuit current density (J_{SC}) (Ameri et al., 2013; Yao et al., 2017; Jiang et al., 2018). To date, OSCs with very common donor PTB7-Th and narrow band gap non-fullerene acceptor IEICO-4F can easily achieve a high J_{SC} over 25 mA/cm^2 (Song et al., 2019; Zhu et al., 2019). Since the fluorine atom has a strong electronegative property which can easily form hydrogen bonds with N-H group, IEICO-4F is an ideal non-fullerene acceptor to study the impact of hydrogen bonds on π-π stacking and obtain a good performance.

In this work, we designed and synthesized a novel small molecule with a simple structure, DTBO (7-(dibutylamino)-3-(6-(trifluoromethyl)-1H-benzo[d]imidazol-2-yl)-2H-chromen-2-one), via introducing trifluoromethyl on a previously reported small molecule Coumarin 7 (3-(1H-benzo[d]imidazol-2-yl)-7-(diethylamino)-2H-chromen-2-one) (Du et al., 2018). Due to the poor performance in ternary non-fullerene OSCs, we introduce trifluoromethyl on Coumarin 7 to strengthen the hydrogen bond with the non-fullerene acceptor in order to obtain a great impact on the acceptor. This small molecule was added to a PTB7-Th: IEICO-4F binary system as a nonvolatile additive to fabricate ternary OSCs. Because of strong electronegative of F atom in IEICO-4F, DTBO can easily form a hydrogen bond with IEICO-4F, which can be testified by Fourier transform infrared (FT-IR). Due to strong electron pulling effect of trifluoromethyl, theoretical predictions demonstrate that the hydrogen bond between DTBO and IEICO-4F is much stronger than that between Coumarin 7 and IEICO-4F. The existence of hydrogen bonds enhances the electrostatic potential (ESP) of IEICO-4F which promotes the charge transfer between the donor and acceptor. The intermolecular interactions between DTBO and IEICO-4F decreases the π-π stacking distance, leading to significant improvement charge extraction, and low charge recombination in comparison to the binary film. Moreover, DTBO has complementary absorption spectrum compared with PTB7-Th and IEICO-4F, which enhances photon harvesting ability of ternary blend. As a result, after adding 10 wt% DTBO, PCE, FF, and J_{SC} of the PTB7-Th: IEICO-4F based OSCs increased from 11.02 to 12.48%, 64.97 to 67.64% and 24.94 to 26.43 mA/cm^2, respectively. On the contrary, owing to weak hydrogen bonds between Coumarin 7 and IEICO-4F, the performance of the ternary device is not as good as DTBO. This result suggests us that enhance intermolecular interactions is an effective way to achieve a high PCE. Recently, many non-fullerene acceptors have shown excellent performance. To further prove this strategy's universality in other non-fullerene acceptors which have an end group like that of IEICO-4F, we also use PM6: Y6 as the host system to fabricate ternary OSCs with DTBO, and the final PCE improved from 15.49 to 16.64%.

RESULTS AND DISCUSSION

Characterization

The chemical structures of DTBO, PTB7-Th, IEICO-4F are shown in **Figure 1A**. The synthetic procedures and synthetic scheme of DTBO are shown in the Supporting Information. The 1H NMR spectra, 13C NMR spectra and IR spectra are shown in **Figures S10–S13**. Since fluorine is the most electronegative atom in the periodic table of the elements, the N-H group in Coumarin 7 can easily form a hydrogen bond with the fluorine atom in IEICO-4F. In order to strengthen the hydrogen bond between DTBO and IEICO-4F, trifluoromethyl was introduced into DTBO. Due to strong electron pulling effect of trifluoromethyl, the hydrogen atom in N-H group shows higher ESP than Coumarin 7 which benefits hydrogen bond strength.

Fourier Transform infrared spectroscopy (FT-IR) was used to determine whether hydrogen bonds formed (Du et al., 2019). In **Figure 1B**, the pure DTBO film has a sharp wave trough at 3,356 cm^{-1} which is the characteristic wave trough of N-H bond, when adding different molar ratios of IEICO-4F the wave trough gradually moved to 3,338 cm^{-1}. For the reason that there is no N-H group in IEICO-4F, IEICO-4F does not show any wave trough at 3,000 to 3,500 cm^{-1}. As we known, the wave trough of N-H group will move to small wavenumber when a hydrogen bond is formed. The shift of FT-IR implied that the intermolecular hydrogen bonds existed (Steiner, 2003).

Hydrogen bond is essentially electrostatic interactions. Therefore, the molecular electrostatic potential was calculated by density functional theory (DFT) with the B3LYP/6-31G (d, p) basis set, based on the ground state geometries of Coumarin 7, DTBO and IEICO-4F. The calculations were performed by Gaussian 09 and the ESP statistics of each atom were conducted by Multifwn (Lu and Chen, 2012) The ESP distribution of DTBO and Coumarin 7 are illustrated in **Figure 1C**, the atom labels in these two molecules are shown in **Figure S1**, and the average ESP values on the atoms were calculated and summarized in **Figure S2**. The result suggests that the surface of hydrogen atom in N-H group shows strong electropositive. As for DTBO, the incorporation of trifluoromethyl group shows notable influence on the ESP. In N-H group of DTBO and Coumarin 7, the ESP of DTBO around the hydrogen atom increases to 30.99 kcal/mol compared with Coumarin 7 (26.57 kcal/mol), the improvement of ESP will enhance the strength of hydrogen bond. Furthermore, we calculated the binding energy of hydrogen bond, the binding

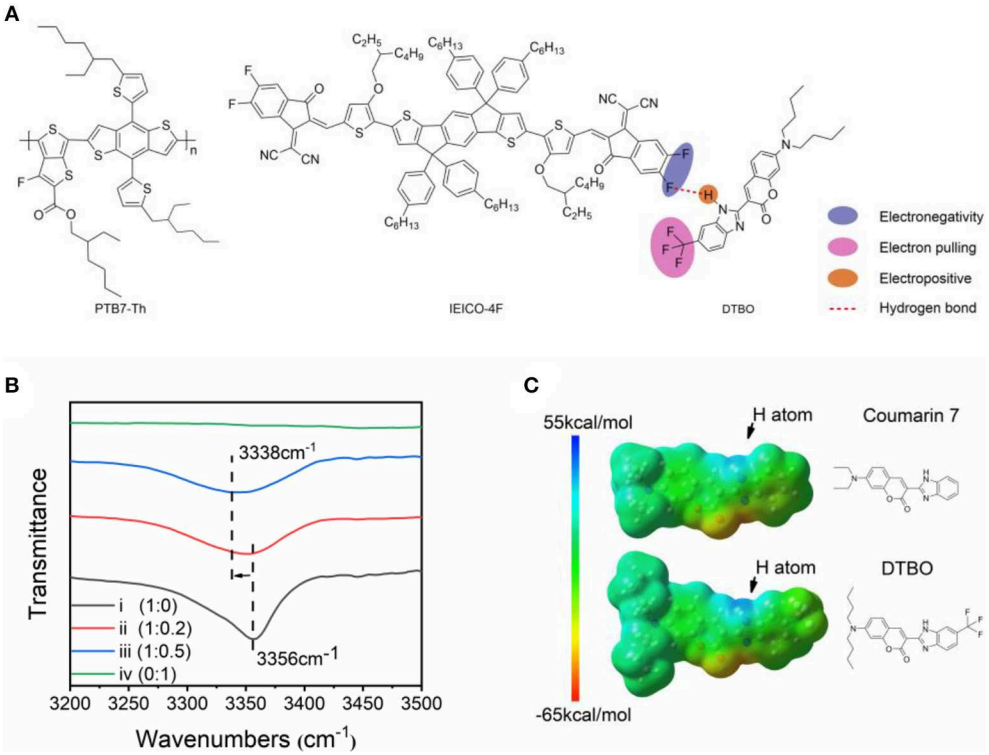

FIGURE 1 | (A) Chemical structure of PTB7-Th, IEICO-4F and DTBO; **(B)** FT-IR spectra of DTBO: IEICO-4F blend films with different molar ratios: (i) DTBO: IEICO-4F = 1: 0, (ii) DTBO: IEICO-4F = 1: 0.2, (iii) DTBO: IEICO-4F = 1: 0.5, (iv) DTBO: IEICO-4F = 0: 1; **(C)** ESP maps of DTBO and Coumarin 7.

energy between DTBO and IEICO-4F (6.40 kcal/mol) is higher than that between Coumarin 7 and IEICO-4F (5.57 kcal/mol), which means DTBO and IEICO-4F have much more stable intermolecular interaction.

To further clarify the influence of intermolecular hydrogen bonds on charge distribution, the ESP maps of hydrogen bond linked IEICO-4F: Coumarin 7 system and IEICO-4F: DTBO system were calculated respectively. **Figures 2A,B** and **Figure S3A** are the ESP maps of IEICO-4F and hydrogen-bond-linked IEICO-4F, **Figures S3B–D** are the ESP area distributions. As shown in **Figure 2D**, for the IEICO-4F, the proportion of positive surface area is 67.89%, the maximal value of ESP is 24.26 kcal/mol. Notably, the proportion of positive surface area increased to 70.59% in hydrogen-bond-linked IEICO-4F: Coumarin 7 system, the maximal value of ESP increased to 30.14 kcal/mol. For the hydrogen-bond-linked IEICO-4F: DTBO system, the proportion of positive surface area did not change too much (70.91%), but the maximal value of ESP kept growing to 38.09 kcal/mol, which means the electrostatic attraction between the hydrogen-bond-linked IEICO-4F and PTB7-Th will be stronger than that between pure IEICO-4F and PTB7-Th. According to pervious report, acceptor has high and positive ESP on the most part of its surface while donor has negative ESP. The different ESP can produce an intermolecular electric field (IEF) between acceptor and donor, which facilitates the charge generation (Yao et al., 2018, 2019). In no-fullerene acceptor, the electron deficient end-capping units forms π-π interactions with the polymer donor in the blend film. As shown in **Figure 2C**, the existence of hydrogen bond increases the ESP of end group in IEICO-4F. As a result, the larger difference of ESP between IEICO-4F and PTB7-Th will induce a larger IEF, the larger IEF at the D-A interface facilitates the charge transfer more efficiency. Our results show that hydrogen-bond-linked IEICO-4F has a higher proportion of positive surface area, the donor and acceptor would show a larger potential difference in the ternary OSC, which is beneficial to charge generation and transfer.

The UV vis absorption spectra of neat films are shown in **Figure 3A**. The highest occupied molecular orbital (HOMO) and lowest unoccupied molecular orbital (LUMO) energy levels are shown in **Figure 3B**. The absorption peak of Coumarin 7 is at 398 nm, while the DTBO has a red-shift of ∼40 nm corresponding to an optical band gap (*Eopt g*) of 2.46 eV. From the cyclic voltammetry (CV) plots (**Figure S5**), we can determine that the HOMO level and the LUMO are down-shifted for DTBO compared to the values for Coumarin 7, which is consistent with the theoretical calculation (**Figure S4**). Since the absorption band of DTBO is located in the short-wave region and PTB7-Th: IEICO-4F have strong absorption in the long-wave region, the ternary system absorbs more solar photons than binary system, resulting in an increased J_{SC} (Jiang et al., 2018).

The absorption spectra of blend films with different DTBO content were measured and shown in **Figure 3C**. The weight ratio

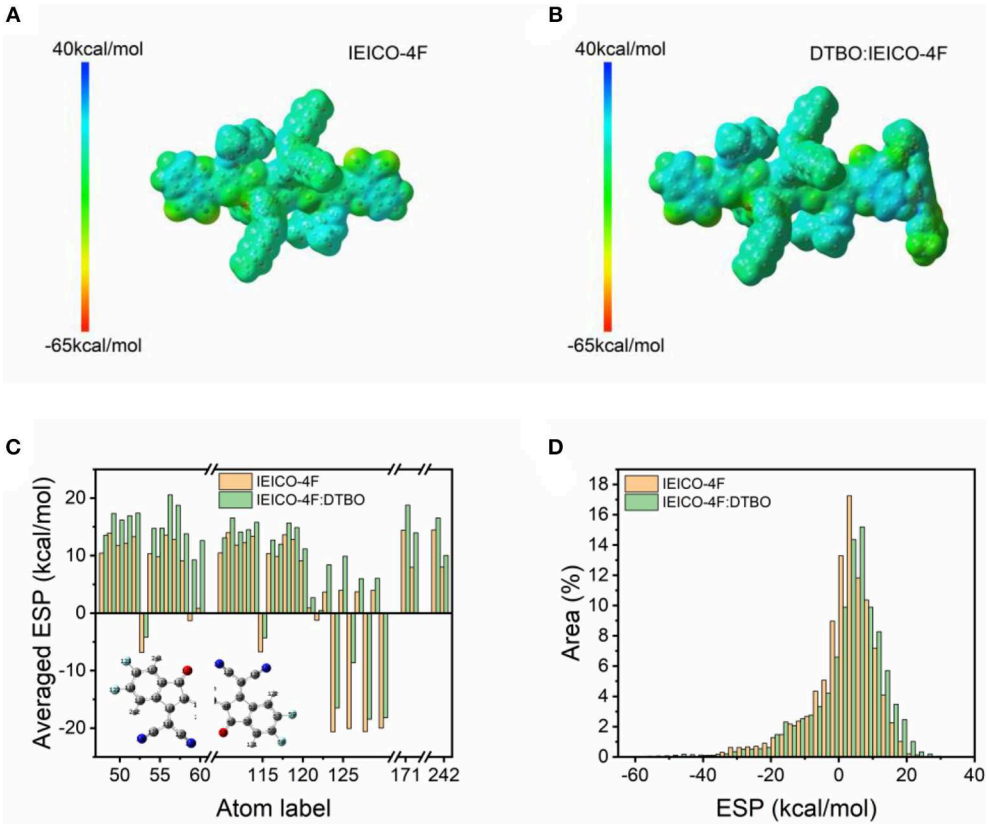

FIGURE 2 | ESP maps of **(A)** IEICO-4F and **(B)** hydrogen-bond-linked IEICO-4F: DTBO; **(C)** Average ESP statistics of each atom in end group; **(D)** ESP area distributions of the molecules.

of PTB7-Th and IEICO-4F is 1: 1.5, and DTBO was added to the binary system as the third compound with different PTB7-Th: DTBO weight ratios. Obviously, the absorption from 400 to 500 nm enhanced by introducing DTBO into the binary films. Because of the enhancement of absorption, a moderate amount of DTBO can boost the photon harvesting. In addition, there is a little increase in absorption spectra from 600 to 900 nm when blending DTBO, suggesting that the crystallization and arrangement of donor and accepter were changed.

According to the previous research (Yang et al., 2013; Gupta et al., 2015; An et al., 2016; Li et al., 2018), Förster-type energy transfer occurs when the absorption spectrum of one compound overlaps the emission spectrum of another compound. **Figure 3D** shows photoluminescence (PL) spectrum of neat DTBO film. It shows that the PTB7-Th has a strong absorption from 550 to 750 nm, and the maximum PL emission peak of DTBO is located at 553 nm, therefore the ternary films have the basic conditions for the energy transfer. In **Figure 3E**, as the content of DTBO increases gradually, the PL intensity of PTB7-Th: DTBO films gradually increases, implying the energy transfer from DTBO to PTB7-Th (Gao et al., 2020; Ma et al., 2020a). This phenomenon will boost PTB7-Th to produce more excitons which dissociate at the PTB7-Th: IEICO-4F interfaces, resulting an increased J_{SC} (Zhao F. et al., 2017). To further explore the effect of this small molecule on PTB7-Th, devices with only DTBO and PTB7-Th were fabricated to investigate the charge transfer or exciton dissociation between PTB7-Th and DTBO. The *J-V* curves were measured under AM 1.5G illumination with light intensity of 100 mW/cm^2 (**Figure 3F**). The J_{SC} of DTBO based device is $<4 \times 10^{-6}$ mA/cm^2. The J_{SC} of DTBO and PTB7-Th based devices is between DTBO based devices and PTB7-Th based devices. This result shows us that there is no charge transfer or exciton dissociation at DTBO/PTB7-Th interfaces. Based the analysis above, the exciton generated by DTBO transfer its energy to PTB7-Th by energy transfer process and then dissociated at PTB7-Th/IEICO-4F interface. The photon-generated carriers will be transported to electrode through the channel formed by IEICO-4F or PTB7-Th induced increased J_{SC} in ternary devices.

Since DTBO can change the ESP of IEICO-4F, it is reasonable to use GIWAXS to check the impact of DTBO on the molecular packing and crystallization of donor and accepter (Collins et al., 2012; Tumbleston et al., 2014). The 2-D diffraction patterns and line-cut profiles are shown in **Figure 4** and **Figure S6**. Obviously, the molecular packing of both binary and ternary samples show a favored face-on orientation relative to the substrate, and exhibit strong π-π stacking signal in the out-of-plane (OP) direction (Rivnay et al., 2012). To further analyze the details of line cuts

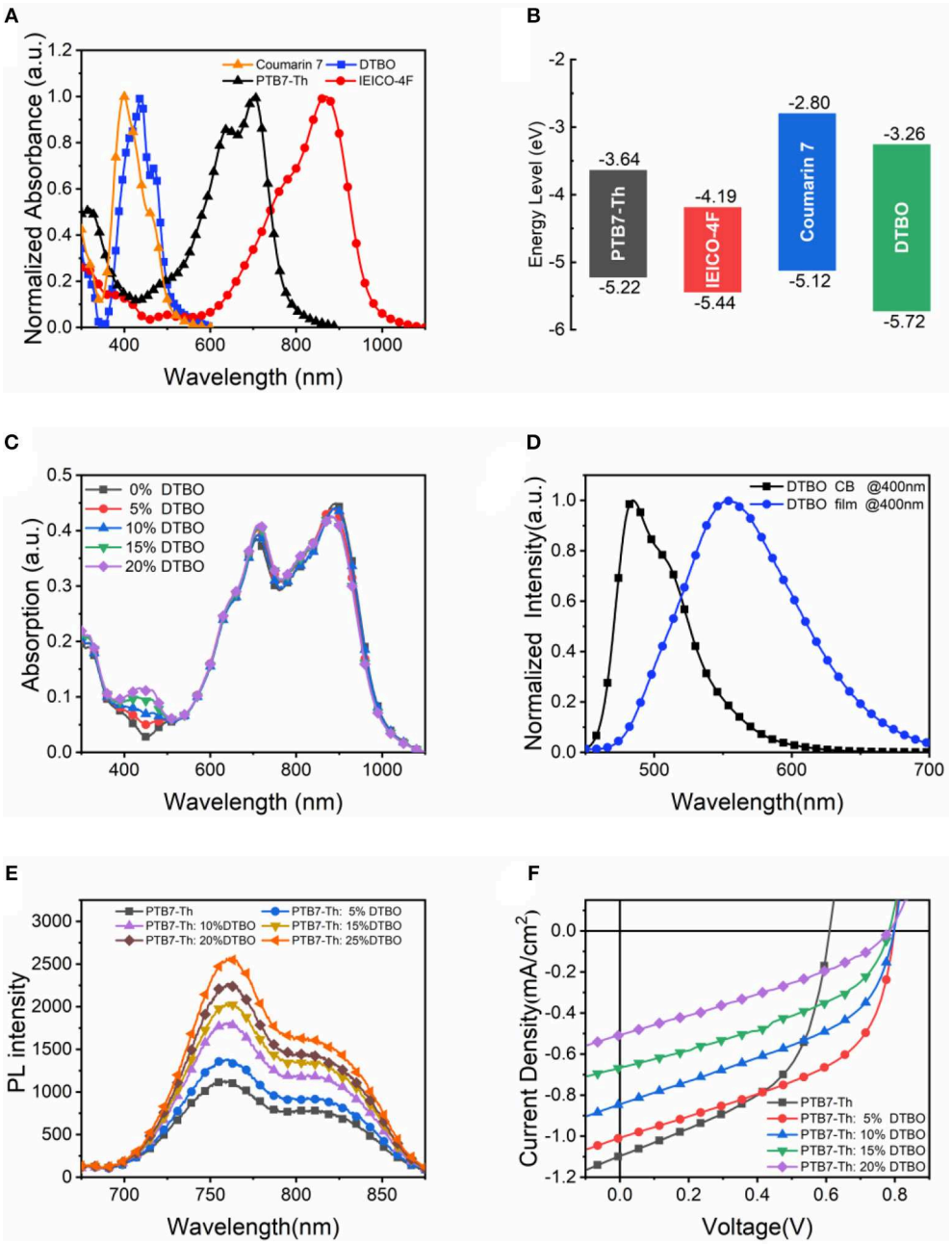

FIGURE 3 | (A) UV vis absorption spectra of neat films; **(B)** HOMO and LUMO energy levels; **(C)** Absorption spectra of ternary films with different DTBO content; **(D)** PL spectra of DTBO in chlorobenzene solution and neat DTBO film under 400 nm light excitation; **(E)** PL spectra of PTB7-Th and DTBO blend films under 450 nm light excitation; **(F)** *J-V* curves of PTB7-Th and DTBO based devices.

from the GIWAXS patterns, peak fit analysis was used in this study (Liu et al., 2014; Zhao et al., 2016). As seen from **Figure 4B**, pure IEICO-4F showed a strong (010) π-π stacking at about 18.28 nm^{-1} in the OP direction. When blended with 10% DTBO, the (010) diffraction peak shifted from 18.28 to 18.64 nm^{-1} and the d-spacing changed from 3.44 to 3.37 Å. As for pure PTB7-Th (**Figure S6C**), the OP (010) π-π stacking peak is observed at 16.33 nm^{-1}. However, the position of (010) π-π stacking peak in PTB7-Th: 10% DTBO (16.33 nm^{-1}) film did not change. This phenomenon may cause by intermolecular interactions between DTBO and IEICO-4F.

The coherence length (L_C) was calculated by Scherrer equation from the full width at half-maximum (FWHM) of OP π-π stacking peaks. For the PTB7-Th: IEICO-4F binary film at high q region, according to peak fitting analysis, the blend film exhibits two diffraction peaks at 17.15 nm^{-1} (PTB7-Th),

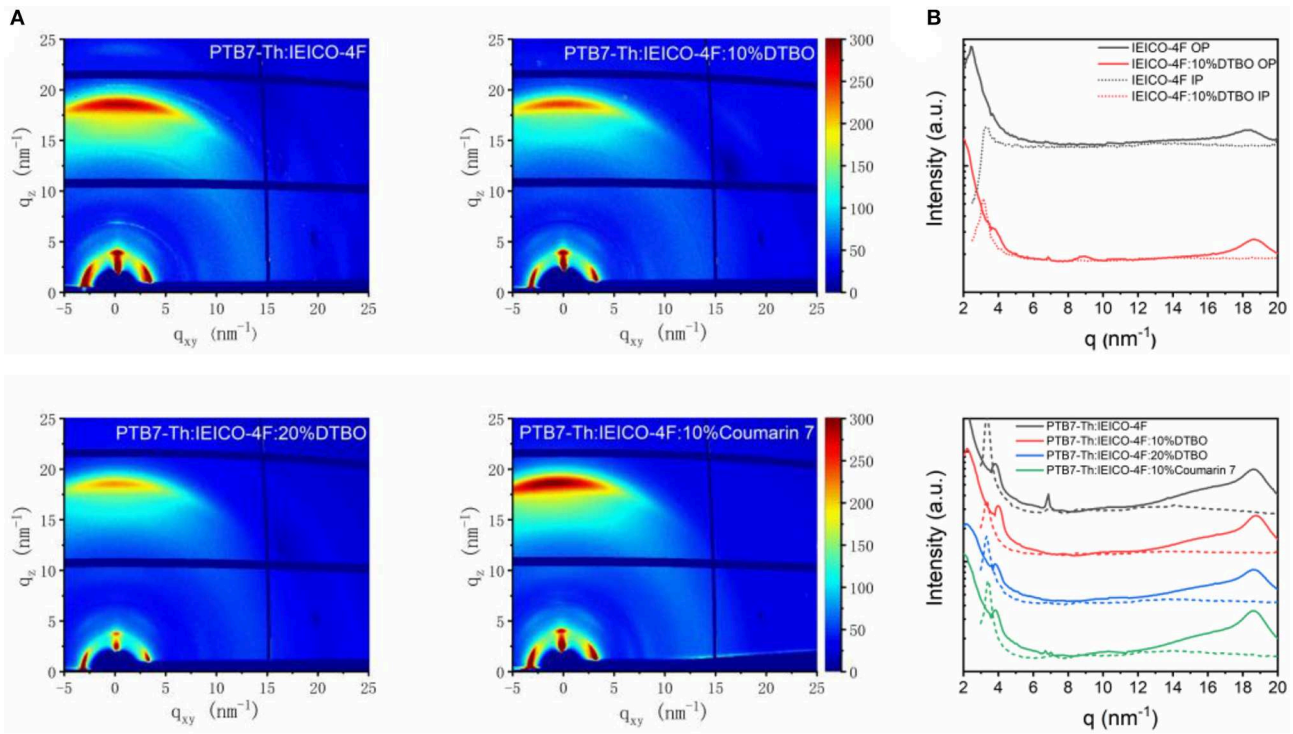

FIGURE 4 | (A) 2-D GIWAXS X-ray scattering pattern; **(B)** line-cut profiles of binary and ternary films.

18.66 nm^{-1} (IEICO-4F), and the L_C of PTB7-Th and IEICO-4F are 1.25 nm, and 4.60 nm, respectively. With addition of 10% DTBO, the diffraction peaks of PTB7-Th (17.17 nm^{-1}) did not change, while the peak of IEICO-4F changed to 18.81 nm^{-1}. As a result, the d-spacing of IEICO-4F changed from 3.37 to 3.34 Å. The level of crystallinity along OP direction influences the charge transport of the blend film. The crystallinity of IEICO-4F along OP direction in ternary film slightly decreased from 4.60 to 4.49 nm when adding 10% DTBO which is harmful in devices. But the J_{SC} of 10% addition ternary devices increased may contribute by the decreased of d-spacing (Mukherjee et al., 2016; Ran et al., 2018) When adding more DTBO (20%) in the ternary blend, the d-spacing of PTB7-Th (3.70 Å) and the L_C of IEICO-4F (4.15 nm) are reduced a lot compared with binary and ternary (10% DTBO) films. π-π stacking is vital to the charge transport, the decreased d-spacing and similar L_C indicate that the addition of 10% DTBO is an optimal choice. Just like ternary blend with 20% DTBO, the ternary blend with 10% Coumarin 7 show increased d-spacing and reduced L_C compared with 10% DTBO, indicating that addition of Coumarin 7 is not good as the 10% DTBO ternary blend.

Device Performance

In order to prove the previous analysis is correct, ternary solar cells were fabricated with inverted (ITO/ZnO/active layer/MoO_3/Ag) architectures (**Figure 5D**). The weight ratio of PTB7-Th to IEICO-4F was kept at 1:1.5 (8 mg/ml for PTB7-Th), and PTB7-Th: DTBO weight ratios are 1:0, 1:0.05, 1:0.1, 1:0.15, and 1:0.2 in this study. Each active layer thickness was maintained at ≈100 nm. Typical *J-V* curves of inverted ternary OSCs are illustrated in **Figure 5A**, with the corresponding PCE metrics summarized in **Table 1**.

The PTB7-Th: IEICO-4F binary control devices exhibit an average PCE of 11.02% (best 11.39%) with a V_{OC} of 0.68 V, a J_{SC} of 24.94 mA/cm^2 and FF of 64.97%. Adding 10% of DTBO into the PTB7-Th: IEICO-4F blend dramatically increases the J_{SC} to 26.43 mA/cm^2 and FF to 67.64%, resulting in a promising average PCE of 12.48% (best 12.88%). Further addition of DTBO (15 and 20%) led to a decrease in the J_{SC} and FF. These results show that using a small molecule to form hydrogen bonds with acceptor can dramatically improve the ternary device performance. However, the ternary OSCs based on PTB7-Th: Coumarin 7: IEICO-4F showed a poor performance (**Table S1**). This result confirms previous predictions that the stronger intermolecular interaction can achieve higher performance in OSCs.

External quantum efficiency (EQE) measurements were conducted to confirm the J_{SC} of the OSCs. The J_{SC} calculated from the EQE spectra were coincident with those acquired from *J-V* measurements, with <5% difference between the two methods. As shown in **Figure 5B**, blending various amounts of DTBO (5–15%), the ternary OSCs show enhancement compared with the binary OSCs, contributing to the increased J_{SC} value. Notably, due to the enhanced absorption after doping DTBO, the EQE increased from 400 to 500 nm, which means that DTBO is contributing to the photon harvesting charge generation. The ΔEQE ($EQE_{binary} - EQE_{ternary}$)

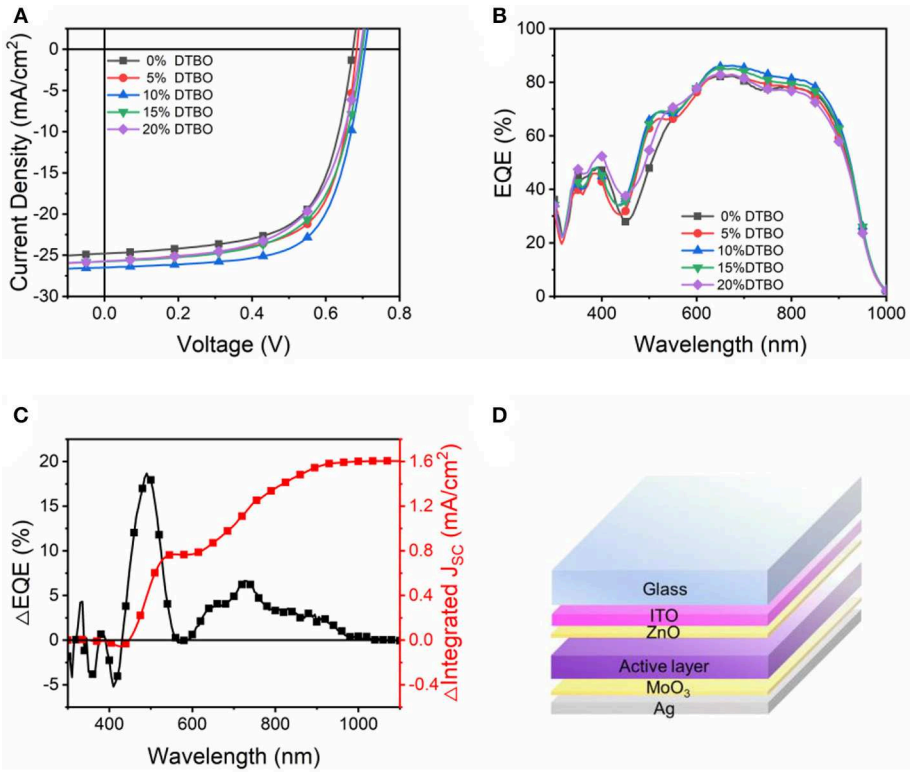

FIGURE 5 | (A) *J–V* curve of OSCs devices; **(B)** EQE curves of the devices with different DTBO content in the PTB7-Th: IEICO-4F systems; **(C)** ΔEQE for 10% DTBO ternary blends; **(D)** Inverted OSCs architectures used in this study.

(Zhao W. et al., 2017; Ma et al., 2018; Song et al., 2019) was calculated to analyze the optimal ternary device. In **Figure 5C**, the increased ΔEQE from 400 to 600 nm caused by the absorption of DTBO. DTBO absorbed the photons and transferred the energy of the photons to PTB7-Th through Förster resonance process, leading to an increased current. However, the energy transfer only contributes half of increased J_{SC}, the increased EQE from 600 to 1,000 nm also contribute by the better π-π stacking between PTB7-Th and IEICO-4F, which benefit for the charge transfer between donor and acceptor leading an increased EQE from longwave. Moreover, the improved charge carrier collection and reduced recombination contribute to the enhanced EQE values which will be discussed below.

The charge carrier mobility was measured by using the space-charge-limited-current (SCLC) method (**Figure S7**) (Mihailetchi et al., 2005). The hole-only devices and electron-only devices were fabricated by using the device architectures ITO/PEDOT: PSS/active layer/MoO_3/Au and ITO/ZnO/active layer/LiF/Al, respectively. The hole and electron mobility are calculated the slopes of $J^{0.5}$-V curves by modeling the dark current in the SCLC region. All detailed data are summarized in **Figure 6A**, **Table S2**. Notably, for the ternary films, with the increase of DTBO content, electron mobility increased, while hole mobility decreased. The increased electron mobility and the decreased hole mobility contributed to a more balanced charge carrier mobility, leading to a better FF for the device, especially for the device with 10% DTBO content (Bartesaghi et al., 2015).

TABLE 1 | The photovoltaic parameters for binary and ternary OSCs under AM 1.5 G illumination (100 mW/cm^2).

Third compound	V_{oc}[a] (V)	J_{sc}[a] (mA/cm^2)	J_{calc}[b] (mA/cm^2)	FF[a] (%)	PCE[a, c] (%)
0% DTBO	0.68	24.94	24.06	64.97	11.02 (11.39)
5% DTBO	0.69	25.66	24.48	66.08	11.65 (12.15)
10% DTBO	0.70	26.43	25.66	67.64	12.48 (12.88)
15% DTBO	0.69	25.78	25.29	63.90	11.30 (11.66)
20% DTBO	0.70	25.86	24.51	61.60	11.10 (11.41)
10% Coumarin 7	0.69	26.25	24.91	66.53	12.06 (12.33)

[a]*All average values were calculated from 10 devices.* [b]J_{sc}*integrated from the EQE spectrum.* [c]*Best PCE in brackets.*

To understand the charge recombination mechanisms in the devices, the V_{OC} and J_{SC} dependence on light intensity was plotted in **Figures 6B,C**. In general, bimolecular recombination can be investigated by the function of $J_{SC} \propto P_{light}^{\alpha}$, where P_{light} is the light intensity and α is the exponential factor. If bimolecular recombination is insignificant, the α will close to 1, since all generated excitons are swept out prior to recombination (Kyaw et al., 2013; Lu et al., 2015). The fitting α values are 0.982, 0.988, 0.986, 0.986, and 0.985 for binary OSCs and the ternary

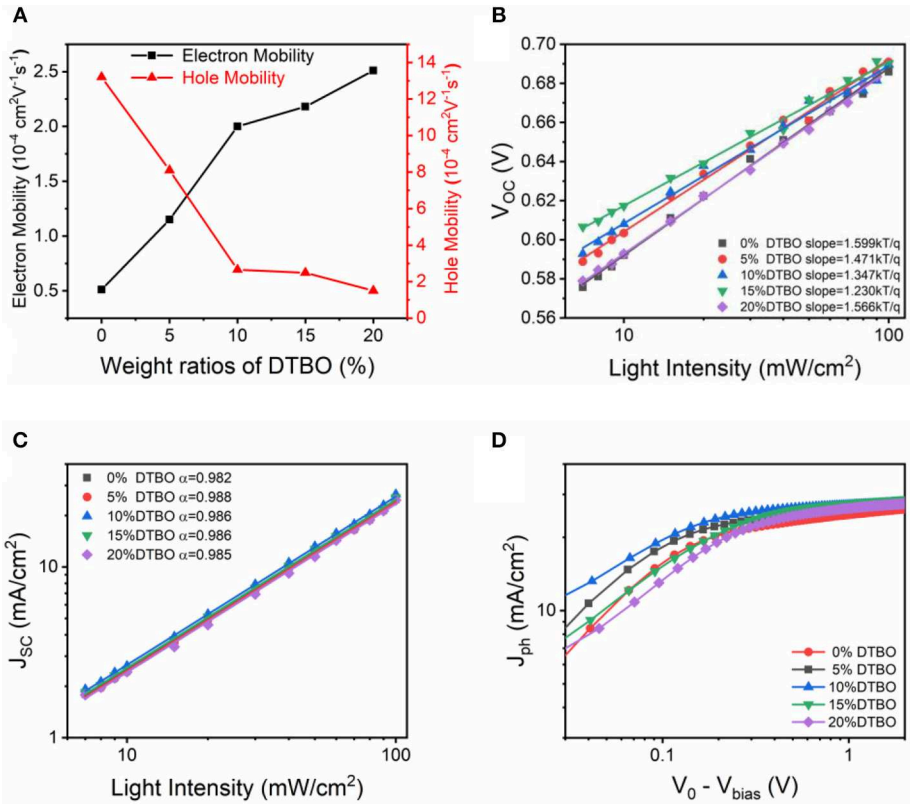

FIGURE 6 | (A) Charge mobility of the PTB7-Th: IEICO-4F with different content of DTBO. **(B)** V_{OC} and **(C)** J_{SC} dependence on light illumination intensity curves of OSCs devices. **(D)** Photocurrent density (J_{ph}) vs. effective voltage ($V_0 - V_{bias}$) characteristics.

OSCs containing 5, 10, 15, and 20% DTBO, suggesting that the bimolecular recombination can be reduced in the optimized ternary OSCs. In the plot of V_{OC} vs. the natural logarithm of the light intensity, non-geminate recombination can be analyzed by the slope of nKT/q (where k is Boltzmann constant, T is the absolute temperature, and q is elementary charge) (Cowan et al., 2010). In general, a slope close to KT/q means that the bimolecular recombination is the main reason for the loss mechanism in OSCs, when the trap-assisted recombination is involved, the slope is gradually increased to $2KT/q$. The slope of binary OSCs is 1.599 KT/q, by addition of 10% DTBO, the trap-assisted recombination is greatly reduced (1.347 KT/q). Which means moderate amount of DTBO can reduce trap-assisted recombination to get a higher FF and better performance in ternary device. Meanwhile, adding more DTBO (>15%) has an adverse effect on suppressing trap-assisted recombination resulting in poor device performance.

The charge generation and extraction properties were analyzed by the photocurrent density (J_{ph}). The J_{ph} as a function of the effective voltage (V_{eff}) is plotted in **Figure 6D**. The J_{ph} is defined as $J_{ph} = J_L - J_D$, where J_L and J_D are the current density under AM 1.5G and dark current density, respectively. The V_{eff} is defined as $V_{eff} = V_0 - V_{bias}$, where V_0 is the voltage at $J_{ph} = 0$ and V_{bias} is the applied voltage (Blom et al., 2007). Under high V_{eff} ($V_{eff} > 2V$), all photon-generated excitons are considered completely dissociated and all photogenerated charge are considered completely extracted by the individual electrode, the saturation current density (J_{sat}) is only limited by the photons harvesting of active layers. In this situation, J_{sat} can be described as a function of $J_{sat} = G_{\max}Lq$, where L and q are the thickness of active layers and elementary charge, G_{max} is the maximum rate of free charge carrier generation. The calculated G_{max} of binary and ternary (10, 20%) OSCs are 1.63×10^{22}, 1.74×10^{22}, 1.72×10^{22} cm^{-3} s^{-1}, respectively, which change in the same trend as the J_{SC} value (Li et al., 2016; Xu et al., 2017). Exciton dissociation efficiency was calculated by J_{SC}/J_{sat} (Lu et al., 2014). The J_{SC}/J_{sat} was increased from 91.3 to 95.9% when adding 10% DTBO, suggesting that optimized ternary OSCs has enhanced exciton dissociation. In fact, photocurrent generation also can be limited by charge collection efficiency (η_{coll}) (Ma et al., 2020b). The high charge collection efficiency can increase the FF and J_{SC}. As for the ternary devices, the incorporation of DTBO also improved the charge collection efficiency. In general, the maximal power output of OSCs usually occurs at the low V_{eff} regime (<0.5 V). Under the maximal power output condition, all η_{coll} values obtained from the optimal ternary device (70.3% at 0.1 V, 86.2% at 0.2 V, and 94.9% at 0.5 V) exceeded those from the binary device (60.2% at 0.1 V, 78.1% at 0.2 V, and 88.8% at 0.5 V) and ternary device with 20% DTBO (48.3% at 0.1 V, 69.9% at 0.2 V, and 88.9% at 0.5 V). This demonstrates the improved

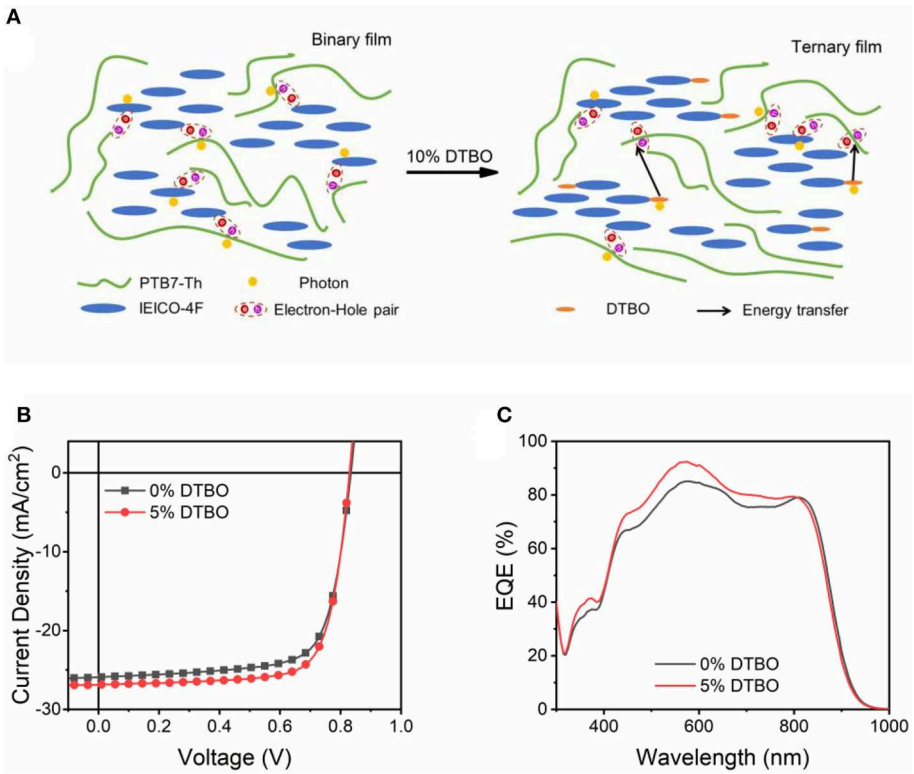

FIGURE 7 | (A) Scheme of energy transfer in DTBO based ternary device; **(B)** *J-V* curve of binary and ternary OSCs based PM6: Y6 system; **(C)** EQE curves of OSCs with 0%, 5% DTBO in the PM6: Y6 systems.

charge collection efficiency in the optimal ternary device (10% DTBO) (Liu et al., 2019). These results agree with the increase of J_{SC} in OSCs devices, proving that addition of 10% of DTBO promotes charge dissociation and extraction, leading to enhanced FF and J_{SC} for ternary solar cells.

Up to now, non-fullerene acceptor with the end group like IEICO-4F show great potential to achieve high PCE. **Figure 7A** is the scheme of energy transfer in DTBO based ternary device. In order to prove the test this strategy works in other non-fullerene acceptors, we choose the PM6: Y6 as the host system. As shown in **Figure S8**, the end group of Y6 is the same as that of IEICO-4F, which means the same effect may occur in Y6. The absorption spectra and energy levels of PM6, Y6 are shown in **Figure S9**. We fabricated devices based inverted architectures, the final PCE increased from 15.49 to 16.64%, and J_{SC} increased to 26.88 mA/cm^2 (**Table 2**). The EQE curves are shown in **Figure 7C**, which is consist with the change of J_{SC} (**Figure 7B**).

TABLE 2 | The photovoltaic parameters for PM6: DTBO: Y6 OSCs under AM 1.5 G illumination (100 mW/cm^2).

Third compound	V_{oc}[a] (V)	J_{sc}[a] (mA/cm^2)	J_{calc}[b] (mA/cm^2)	FF[a] (%)	PCE[a, c] (%)
0% DTBO	0.83	25.49	24.52	73.17	15.49 (15.85)
5% DTBO	0.83	26.88	25.59	74.92	16.64 (17.07)

[a]*All average values were calculated from 10 devices.* [b]J_{SC} *integrated from the EQE spectrum.* [c]*Best PCE in brackets.*

CONCLUSION

In conclusion, we report a novel small molecule DTBO, which could form hydrogen bonds with the acceptor to achieve the increased J_{SC} and PCE in ternary OSCs. We proved the existence of intermolecular hydrogen bonds between DTBO and IEICO-4F by infrared spectroscopy. The existence of hydrogen bonds can change the ESP of IEICO-4F to promote a better π-π stacking between donor and acceptor which is beneficial for charge transfer. GIWAXS was also used to demonstrate the impact of hydrogen bonds on molecular packing, proving that the hydrogen bonds have a small effect on PTB7-Th, while they have a large effect on IEICO-4F which benefits charge transport. Meanwhile, adding the third component to the binary system not only broadens the absorption spectrum, but also achieves the energy transfer from DTBO to PTB7-Th, leading to a higher J_{SC}. Incorporating DTBO in ternary OSCs also benefits charge generation and extraction, which makes contributions to J_{SC}. The balanced charge carrier mobility in ternary OSCs is the reason why FF increased. In comparison, the ternary OSCs containing Coumarin 7 show poor performance, even though Coumarin 7 and DTBO have a similar structure. Since Coumarin 7 formed a weak hydrogen bond with IEICO-4F, the

intermolecular interaction is weaker than that between DTBO and IEICO-4F, resulting in a weak impact on π-π stacking and low PCE. What's more, the strategy is also effective for other non-fullerene acceptors like Y6. Overall, these results may provide a strategy to achieve high OSCs performance by introducing intermolecular hydrogen bond in ternary OSCs to improve the π-π stacking in the active layer, thus achieving better performance.

DATA AVAILABILITY STATEMENT

All datasets generated for this study are included in the article/**Supplementary Material**.

AUTHOR CONTRIBUTIONS

HZ synthesized DTBO, fabricated, and tested OSCs devices (PTB7-Th:IEICO-4F system). XD designed DTBO and helped design experimental protocols. YT carried out GIWAXS measurements and analysis. XL and LZ fabricated and tested OSCs devices (PM6:Y6 system). CZ and HL calculated ESP with DFT. ST conceived and directed the project. HZ wrote the paper.

FUNDING

This work was supported by the National Natural Science Foundation of China (NSFC Grant Nos. 61775029, 61604035, and 51533005), International Cooperation and Exchange Project of Science and Technology Department of Sichuan Province (Grant No. 2019YFH0059).

SUPPLEMENTARY MATERIAL

The Supplementary Material for this article can be found online at: https://www.frontiersin.org/articles/10.3389/fchem.2020.00190/full#supplementary-material

REFERENCES

Ameri, T., Khoram, P., Min, J., and Brabec, C. J. (2013). Organic ternary solar cells: a review. *Adv. Mater.* 25, 4245–4266. doi: 10.1002/adma.201300623

An, Q., Zhang, F., Zhang, J., Tang, W., Deng, Z., and Hu, B. (2016). Versatile ternary organic solar cells: a critical review. *Energy Environ. Sci.* 9, 281–322. doi: 10.1039/C5EE02641E

Bartesaghi, D., Pérez, I. C., Kniepert, J., Roland, S., Turbiez, M., Koster, L. J. A. (2015). Competition between recombination and extraction of free charges determines the fill factor of organic solar cells. *Nat. Commun.* 6:7083. doi: 10.1038/ncomms8083

Bi, P., and Hao, X. (2019). Versatile ternary approach for novel organic solar cells: a review. *Solar RRL* 3:1800263. doi: 10.1002/solr.201800263

Bi, P., Xiao, T., Yang, X., Niu, M., Wen, Z., Zhang, K., et al. (2018). Regulating the vertical phase distribution by fullerene-derivative in high performance ternary organic solar cells. *Nano Energy* 46, 81–90. doi: 10.1016/j.nanoen.2018.01.040

Blom, P. W. M., Mihailetchi, V. D., Koster, L. J. A., and Markov, D. E. (2007). Device physics of polymer:fullerene bulk heterojunction solar cells. *Adv. Mater.* 19, 1551–1566. doi: 10.1002/adma.200601093

Collins, B. A., Cochran, J. E., Yan, H., Gann, E., Hub, C., Fink, R., et al. (2012). Polarized X-ray scattering reveals non-crystalline orientational ordering in organic films. *Nat. Mater.* 11, 536–543. doi: 10.1038/nmat3310

Cowan, S. R., Roy, A., and Heeger, A. J. (2010). Recombination in polymer-fullerene bulk heterojunction solar cells. *Phys. Rev. B* 82:245207. doi: 10.1103/PhysRevB.82.245207

Dong, S., Zhang, K., Xie, B., Xiao, J., Yip, H.-L., Yan, H., et al. (2019). High-performance large-area organic solar cells enabled by sequential bilayer processing via nonhalogenated solvents. *Adv. Energy Mater.* 9:1802832. doi: 10.1002/aenm.201802832

Du, X., Lu, X., Zhao, J., Zhang, Y., Li, X., Lin, H., et al. (2019). Hydrogen bond induced green solvent processed high performance ternary organic solar cells with good tolerance on film thickness and blend ratios. *Adv. Funct. Mater.* 29:1902078. doi: 10.1002/adfm.201902078

Du, X., Tao, S., Li, L., Wang, W., Zheng, C., Lin, H., et al. (2018). Hydrogen-bonding strategy to optimize charge distribution of PC 71 BM and enable a high efficiency of 12.45% for organic solar cells. *Solar RRL* 2:1800038. doi: 10.1002/solr.201800038

Du, X., Yuan, Y., Zhou, L., Lin, H., Zheng, C., Luo, J., et al. (2020). Delayed fluorescence emitter enables near 17% efficiency ternary organic solar cells with enhanced storage stability and reduced recombination energy loss. *Adv. Funct. Mater.* 1909837. doi: 10.1002/adfm.201909837

Gao, J., Gao, W., Ma, X., Hu, Z., Xu, C., Wang, X., et al. (2020). Over 14.5% efficiency and 71.6% fill factor of ternary organic solar cells with 300 nm thick active layers. *Energy Environ. Sci.* doi: 10.1039/C9EE04020J. [Epub ahead of print].

Gupta, V., Bharti, V., Kumar, M., Chand, S., and Heeger, A. J. (2015). Polymer–Polymer förster resonance energy transfer significantly boosts the power conversion efficiency of bulk-heterojunction solar cells. *Adv. Mater.* 27, 4398–4404. doi: 10.1002/adma.201501275

He, Z., Xiao, B., Liu, F., Wu, H., Yang, Y., Xiao, S., et al. (2015). Single-junction polymer solar cells with high efficiency and photovoltage. *Nat. Photonics.* 9, 174–179. doi: 10.1038/nphoton.2015.6

Hou, J., Inganäs, O., Friend, R. H., and Gao, F. (2018). Organic solar cells based on non-fullerene acceptors. *Nat. Mater.* 17, 119–128. doi: 10.1038/nmat5063

Jeong, E. G., Jeon, Y., Cho, S. H., and Choi, K. C. (2019). Textile-based washable polymer solar cells for optoelectronic modules: toward self-powered smart clothing. *Energy Environ. Sci.* 12, 1878–1889. doi: 10.1039/C8EE03271H

Jiang, W., Yu, R., Liu, Z., Peng, R., Mi, D., Hong, L., et al. (2018). Ternary nonfullerene polymer solar cells with 12.16% efficiency by introducing one acceptor with cascading energy level and complementary absorption. *Adv. Mater.* 30:1703005. doi: 10.1002/adma.201703005

Kang, H., Lee, W., Oh, J., Kim, T., Lee, C., and Kim, B. J. (2016). From fullerene–polymer to all-polymer solar cells: the importance of molecular packing, orientation, and morphology control. *Acc. Chem. Res.* 49, 2424–2434. doi: 10.1021/acs.accounts.6b00347

Kyaw, A. K. K., Wang, D. H., Gupta, V., Leong, W. L., Ke, L., Bazan, G. C., et al. (2013). Intensity dependence of current–voltage characteristics and recombination in high-efficiency solution-processed small-molecule solar cells. *ACS Nano* 7, 4569–4577. doi: 10.1021/nn401267s

Lee, J., Singh, R., Sin, D. H., Kim, H. G., Song, K. C., and Cho, K. (2016). A nonfullerene small molecule acceptor with 3D interlocking geometry enabling efficient organic solar cells. *Adv. Mater.* 28, 69–76. doi: 10.1002/adma.201504010

Lee, J. K., Ma, W. L., Brabec, C. J., Yuen, J., Moon, J. S., Kim, J. Y., et al. (2008). Processing additives for improved efficiency from bulk heterojunction solar cells. *J. Am. Chem. Soc.* 130, 3619–3623. doi: 10.1021/ja710079w

Li, S., Ye, L., Zhao, W., Zhang, S., Mukherjee, S., Ade, H., et al. (2016). Energy-level modulation of small-molecule electron acceptors to achieve over 12% efficiency in polymer solar cells. *Adv. Mater.* 28, 9423–9429. doi: 10.1002/adma.201602776

Li, W., Yan, Y., Gong, Y., Cai, J., Cai, F., Gurney, R. S., et al. (2018). Contrasting effects of energy transfer in determining efficiency improvements in ternary polymer solar cells. *Adv. Funct. Mater.* 28:1704212. doi: 10.1002/adfm.201704212

Liang, Y., Xu, Z., Xia, J., Tsai, S.-T., Wu, Y., Li, G., et al. (2010). For the bright future—bulk heterojunction polymer solar cells with power conversion efficiency of 7.4%. *Adv. Mater.* 22, E135–8. doi: 10.1002/adma.200903528

Liu, T., Luo, Z., Chen, Y., Yang, T., Xiao, Y., Zhang, G., et al. (2019). A nonfullerene acceptor with a 1000 nm absorption edge enables ternary organic solar cells with improved optical and morphological properties and efficiencies over 15%. *Energy Environ. Sci.* 12, 2529–2536. doi: 10.1039/C9EE01030K

Liu, Y., Zhao, J., Li, Z., Mu, C., Ma, W., Hu, H., et al. (2014). Aggregation and morphology control enables multiple cases of high-efficiency polymer solar cells. *Nat. Commun.* 5:5293. doi: 10.1038/ncomms6293

Lu, L., Chen, W., Xu, T., and Yu, L. (2015). High-performance ternary blend polymer solar cells involving both energy transfer and hole relay processes. *Nat. Commun.* 6:7327. doi: 10.1038/ncomms8327

Lu, L., Xu, T., Chen, W., Landry, E. S., and Yu, L. (2014). Ternary blend polymer solar cells with enhanced power conversion efficiency. *Nat. Photonics.* 8, 716–722. doi: 10.1038/nphoton.2014.172

Lu, T., and Chen, F. (2012). Multiwfn: a multifunctional wavefunction analyzer. *J. Comput. Chem.* 33, 580–592. doi: 10.1002/jcc.22885

Ma, X., An, Q., Ibraikulov, O. A., Lévêque, P., Heiser, T., Leclerc, N., et al. (2020a). Efficient ternary organic photovoltaics with two polymer donors by minimizing energy loss. *J. Mater. Chem. A* 8, 1265–1272. doi: 10.1039/C9TA12025D

Ma, X., Mi, Y., Zhang, F., An, Q., Zhang, M., Hu, Z., et al. (2018). Efficient ternary polymer solar cells with two well-compatible donors and one ultranarrow bandgap nonfullerene acceptor. *Adv. Energy Mater.* 8:1702854. doi: 10.1002/aenm.201702854

Ma, X., Wang, J., An, Q., Gao, J., Hu, Z., Xu, C., et al. (2020b). Highly efficient quaternary organic photovoltaics by optimizing photogenerated exciton distribution and active layer morphology. *Nano Energy* 70:104496. doi: 10.1016/j.nanoen.2020.104496

Meng, L., Zhang, Y., Wan, X., Li, C., Zhang, X., Wang, Y., et al. (2018). Organic and solution-processed tandem solar cells with 17.3% efficiency. *Science* 361, 1094–1098. doi: 10.1126/science.aat2612

Mihailetchi, V. D., Wildeman, J., and Blom, P. W. M. (2005). Space-charge limited photocurrent. *Phys. Rev. Lett.* 94:126602. doi: 10.1103/PhysRevLett.94.126602

Moon, J. S., Takacs, C. J., Cho, S., Coffin, R. C., Kim, H., Bazan, G. C., et al. (2010). Effect of processing additive on the nanomorphology of a bulk heterojunction material. *Nano Lett.* 10, 4005–4008. doi: 10.1021/nl101923m

Mukherjee, S., Jiao, X., and Ade, H. (2016). Charge creation and recombination in multi-length scale polymer:fullerene BHJ solar cell morphologies. *Adv. Energy Mater.* 6:1600699. doi: 10.1002/aenm.201600699

Nian, L., Kan, Y., Wang, H., Gao, K., Xu, B., Rong, Q., et al. (2018). Ternary non-fullerene polymer solar cells with 13.51% efficiency and a record-high fill factor of 78.13%. *Energy Environ. Sci.* 11, 3392–3399. doi: 10.1039/C8EE01564C

Pan, M.-A., Lau, T.-K., Tang, Y., Wu, Y.-C., Liu, T., Li, K., et al. (2019). 16.7%-efficiency ternary blended organic photovoltaic cells with PCBM as the acceptor additive to increase the open-circuit voltage and phase purity. *J. Mater. Chem. A* 7, 20713–20722. doi: 10.1039/C9TA06929A

Ran, N. A., Love, J. A., Heiber, M. C., Jiao, X., Hughes, M. P., Karki, A., et al. (2018). Charge generation and recombination in an organic solar cell with low energetic offsets. *Adv. Energy Mater.* 8:1701073. doi: 10.1002/aenm.201701073

Ran, N. A., Roland, S., Love, J. A., Savikhin, V., Takacs, C. J., Fu, Y.-T., et al. (2017). Impact of interfacial molecular orientation on radiative recombination and charge generation efficiency. *Nat. Commun.* 8:79. doi: 10.1038/s41467-017-00107-4

Rivnay, J., Mannsfeld, S. C. B., Miller, C. E., Salleo, A., and Toney, M. F. (2012). Quantitative determination of organic semiconductor microstructure from the molecular to device scale. *Chem. Rev.* 112, 5488–5519. doi: 10.1021/cr3001109

Rossander, L. H., Dam, H. F., Carlé, J. E., Helgesen, M., Rajkovic, I., Corazza, M., et al. (2017). In-line, roll-to-roll morphology analysis of organic solar cell active layers. *Energy Environ. Sci.* 10, 2411–2419. doi: 10.1039/C7EE01900A

Song, X., Gasparini, N., Nahid, M. M., Paleti, S. H. K., Wang, J.-L., Ade, H., et al. (2019). Dual sensitizer and processing-aid behavior of donor enables efficient ternary organic solar cells. *Joule* 3, 846–857. doi: 10.1016/j.joule.2019.01.009

Steiner, T. (2003). C–H···O hydrogen bonding in crystals. *Crystallogr. Rev.* 9, 177–228. doi: 10.1080/08893110310001621772

Tumbleston, J. R., Collins, B. A., Yang, L., Stuart, A. C., Gann, E., Ma, W., et al. (2014). The influence of molecular orientation on organic bulk heterojunction solar cells. *Nat. Photonics.* 8, 385–391. doi: 10.1038/nphoton.2014.55

Xu, X., Bi, Z., Ma, W., Wang, Z., Choy, W. C. H., Wu, W., et al. (2017). Highly efficient ternary-blend polymer solar cells enabled by a nonfullerene acceptor and two polymer donors with a broad composition tolerance. *Adv. Mater.* 29:1704271. doi: 10.1002/adma.201704271

Yan, T., Song, W., Huang, J., Peng, R., Huang, L., and Ge, Z. (2019). 16.67% rigid and 14.06% flexible organic solar cells enabled by ternary heterojunction strategy. *Adv. Mater.* 31:1902210. doi: 10.1002/adma.201902210

Yang, L., Yan, L., and You, W. (2013). Organic solar cells beyond one pair of donor–acceptor: ternary blends and more. *J. Phys. Chem. Lett.* 4, 1802–1810. doi: 10.1021/jz400723u

Yao, H., Cui, Y., Qian, D., Ponseca, C. S., Honarfar, A., Xu, Y., et al. (2019). 14.7% efficiency organic photovoltaic cells enabled by active materials with a large electrostatic potential difference. *J. Am. Chem. Soc.* 141, 7743–7750. doi: 10.1021/jacs.8b12937

Yao, H., Cui, Y., Yu, R., Gao, B., Zhang, H., and Hou, J. (2017). Design, synthesis, and photovoltaic characterization of a small molecular acceptor with an ultra-narrow band gap. *Angew. Chem. Int. Ed.* 56, 3045–3049. doi: 10.1002/anie.201610944

Yao, H., Qian, D., Zhang, H., Qin, Y., Xu, B., Cui, Y., et al. (2018). Critical role of molecular electrostatic potential on charge generation in organic solar cells. *Chin. J. Chem.* 36, 491–494. doi: 10.1002/cjoc.201800015

Yuan, J., Zhang, Y., Zhou, L., Zhang, G., Yip, H.-L., Lau, T.-K., et al. (2019). Single-junction organic solar cell with over 15% efficiency using fused-ring acceptor with electron-deficient core. *Joule* 3, 1140–1151. doi: 10.1016/j.joule.2019.01.004

Zhang, H., Wang, X., Yang, L., Zhang, S., Zhang, Y., He, C., et al. (2017). Improved domain size and purity enables efficient all-small-molecule ternary solar cells. *Adv. Mater.* 29:1703777. doi: 10.1002/adma.201703777

Zhang, J., Tan, H. S., Guo, X., Facchetti, A., and Yan, H. (2018). Material insights and challenges for non-fullerene organic solar cells based on small molecular acceptors. *Nat. Energy* 3, 720–731. doi: 10.1038/s41560-018-0181-5

Zhao, F., Li, Y., Wang, Z., Yang, Y., Wang, Z., He, G., et al. (2017). Combining energy transfer and optimized morphology for highly efficient ternary polymer solar cells. *Adv. Energy Mater.* 7:1602552. doi: 10.1002/aenm.201602552

Zhao, J., Li, Y., Yang, G., Jiang, K., Lin, H., Ade, H., et al. (2016). Efficient organic solar cells processed from hydrocarbon solvents. *Nat. Energy* 1:15027. doi: 10.1038/nenergy.2015.27

Zhao, W., Li, S., Zhang, S., Liu, X., and Hou, J. (2017). Ternary polymer solar cells based on two acceptors and one donor for achieving 12.2% efficiency. *Adv. Mater.* 29:1604059. doi: 10.1002/adma.201604059

Zhu, Y., Gadisa, A., Peng, Z., Ghasemi, M., Ye, L., Xu, Z., et al. (2019). Rational strategy to stabilize an unstable high-efficiency binary nonfullerene organic solar cells with a third component. *Adv. Energy Mat.* 9:1900376. doi: 10.1002/aenm.201900376

Conflict of Interest: The authors declare that the research was conducted in the absence of any commercial or financial relationships that could be construed as a potential conflict of interest.

frontiers in Chemistry

ORIGINAL RESEARCH
published: 07 April 2020
doi: 10.3389/fchem.2020.00211

In situ Measuring Film-Depth-Dependent Light Absorption Spectra for Organic Photovoltaics

Xiang Feng[1,2†], *Yuheng Wang*[1,2†], *Tong Xiao*[1,2], *Zichao Shen*[1,2], *Yurong Ren*[1,2], *Guanghao Lu*[1,2] *and Laju Bu*[1,2*]

[1] *Frontier Institute of Science and Technology, and School of Science, Xi'an Jiaotong University, Xi'an, China,* [2] *State Key Laboratory of Electrical Insulation and Power Equipment, Xi'an Jiaotong University, Xi'an, China*

Organic donor–acceptor bulk heterojunction are attracting wide interests for solar cell applications due to solution processability, mechanical flexibility, and low cost. The photovoltaic performance of such thin film is strongly dependent on vertical phase separation of each component. Although film-depth-dependent light absorption spectra measured by non-*in situ* methods have been used to investigate the film-depth profiling of organic semiconducting thin films, the *in situ* measurement is still not well-resolved. In this work, we propose an *in situ* measurement method in combination with a self-developed *in situ* instrument, which integrates a capacitive coupled plasma generator, a light source, and a spectrometer. This *in situ* method and instrument are easily accessible and easily equipped in laboratories of the organic electronics, which could be used to conveniently investigate the film-depth-dependent optical and electronic properties.

Keywords: organic photovoltaics, organic solar cells, bulk heterojunction, depth profiling, light absorption spectroscopy

OPEN ACCESS

Edited by:
Kui Zhao,
Shaanxi Normal University, China

Reviewed by:
Jianyu Yuan,
Soochow University, China
Zicheng Ding,
Shaanxi Normal University, China
Liyang Yu,
Sichuan University, China

***Correspondence:**
Laju Bu
laju2014@mail.xjtu.edu.cn

† These authors have contributed equally to this work

Specialty section:
This article was submitted to Physical Chemistry and Chemical Physics, a section of the journal Frontiers in Chemistry

Received: *26 January 2020*
Accepted: *05 March 2020*
Published: *07 April 2020*

Citation:
Feng X, Wang Y, Xiao T, Shen Z, Ren Y, Lu G and Bu L (2020) In situ Measuring Film-Depth-Dependent Light Absorption Spectra for Organic Photovoltaics. Front. Chem. 8:211. doi: 10.3389/fchem.2020.00211

INTRODUCTION

As one of the effective approaches to utilize solar energy converting energy, photovoltaics have received extensive attention. Achieving high-efficiency, large-area manufacture, and excellent environmental stability are the goals (Liu et al., 2015; Niu et al., 2018; Fan et al., 2019; Xu et al., 2019a,b; Zhu et al., 2019; Zhang et al., 2020). Especially, organic photovoltaic devices (OPVs) using solution-processible donor–acceptor bulk heterojunction (BHJ) as photon-harvesting active layer are attractive for next-generation flexible photovoltaic modules (Li et al., 2012, 2018; Lin et al., 2012; Heeger, 2014; Dong et al., 2019). With the development of organic optoelectronic materials, device structures, and fabrication processes, device performance has been fundamentally optimized, and power conversion efficiency (PCE) of single-junction OPV has exceeded 18% until now (Lin et al., 2015, 2019; Zhao et al., 2015, 2017; Liu et al., 2016, 2020; Meng et al., 2018; Cheng et al., 2019; Yan T. et al., 2019; Yuan et al., 2019). As compared with organic films deposited upon vacuum evaporation, during the BHJ films deposition from solution, the phase evolution of binary or ternary blends usually induces vertical phase separation, leading to film-depth-dependent distribution of both composition and morphology (Xu et al., 2009; Yan et al., 2017; Bi et al., 2018; Huang et al., 2018; Adil et al., 2019; Yan H. et al., 2019). To study the vertical distribution characteristics of film, many methods have been developed. However, the inherent disadvantages of these technologies

limit further application, such as high cost, complicated operation, low preciseness, etc. For example, sputter combined with dynamic secondary ion mass spectroscopy is a universal method to study vertical component distribution by measuring element distribution in depth profile. However, this method is rather expensive. Additionally, high energy sputter treatment may damage the film, and primary ions also cause the surface state to change. Neutron reflectivity requires expensive equipment, namely, accelerator, which is not immediately accessible. The result accuracy of variable-angle spectroscopic ellipsometry is closely related to the fitting model, which requires multiple measurements to reduce errors. As for the three-dimensional imaging transmission electron microscope, the sample preparation process is complicated. Therefore, it is necessary to develop a simple and efficient method to study the film-depth-dependent characteristics.

BHJ solar cells are actually composed of anode/cathode, hole/electron transport layers, and photo-response active layer. Owing to light interferences among these layers, which have different refractive indices and extinction coefficients, the photon-harvesting profile is non-linear along vertical direction (Gusain et al., 2019). On the one hand, vertical phase separation between the donor and acceptor makes this photon-harvesting scenario more complicated, pointing to the importance of film-depth optical variations. After fission of exciton, the hole and electron need to transport along different pathways, i.e., donor and acceptor phases, toward anode and cathode, respectively. Therefore, the film-depth-dependent distribution of donor and acceptor plays an important role in device performance. On the other hand, the UV–visible (UV-vis) light absorption is caused by the transition of valence electrons to the conductance band, while thus formed hole–electron pair has a so-called binding energy. Consequently, for organic semiconductors, the light absorption spectra could roughly reflect the electronic properties of organic materials. By this way, we can indirectly investigate the charge behavior in the active layer (Bredas, 2014a,b). Therefore, UV-vis light absorption spectroscopy is a commonly used characterization method for optical and electronic properties of BHJ photovoltaic layers. Although depth profiling upon film-depth-dependent light absorption spectra (FLAS) has been previously developed by us and successfully applied in polymer solar cells and organic thin-film transistors (Bu et al., 2016a,b; Wang J. et al., 2018; Liang et al., 2019), the non-*in situ* measurement is time consuming, less precise, and difficult to be integrated with other measurements.

In this work, we propose an *in situ* measurement method in combination with an *in situ* instrument that integrates a capacitive coupled plasma generator, a light source, and a spectrometer to *in situ* measure FLAS. The *in situ* FLAS of organic BHJ active layer could be measured more immediately within a few minutes, with improved film depth resolution on the scale of nanometer, as compared with non-*in situ* measurements. Subsequently, these *in situ* FLAS are used to investigate vertical distribution of composition and aggregation, the photon harvesting profile along film-depth direction, and film-depth-dependent charge transport behavior.

MATERIALS AND METHODS

Materials

The indium tin oxide (ITO) glass substrates with sheet resistance of $\leq$15 Ω sq^{-1} were purchased from South China Science& Technology Co., Ltd. The poly{(2,6-(4,8-bis(5-(2-ethylhexyl)thiophen-2-yl)-benzo[1,2-b:4,5-b′]dithiophene))-alt-(5,5-(1′,3′-di-2-thienyl-5′,7′-bis(2-ethylhexyl)benzo[1′,2′-c:4′,5′-c′]dithiophene-4,8-dione))} (PBDB-T) was purchased from Organtec Ltd. The 3,9-bis{2-methylene-[3-(1,1-dicyanomethylene)-indanone]}-5,5,11,11-tetrakis(4-hexylphenyl)-dithieno[2,3-d:2′,3′-d′]-s-indaceno[1,2-b:5,6-b′]dithiophene (ITIC) was purchased from Solarmer Materials Inc. The zinc acetate dihydrate [$Zn(CH_3COO)_2{\cdot}2H_2O$], ethanolamine ($NH_2CH_2CH_2OH$), 2-methoxyethanol ($CH_3OCH_2CH_2OH$), and polystyrene (PS) were purchased from Sigma-Aldrich Inc. The molecular weight of PS was 2,000 K with polymer dispersity index of 1.3. The molybdenum trioxide (MoO_3) was purchased from Adamas Reagent Co., Ltd. The poly(3,4-ethylenedioxythiophene):poly(styrenesulfonate) (PEDOT:PSS) was purchased from Xi'an Polymer Light Technology Corp.

Fabrication and Measurement of BHJ Devices

The device structure was ITO/ZnO/active layer/MoO_3/Al. The ITO substrates were ultrasonically cleaned by detergent, deionized water, acetone, and isopropanol for 15 min, respectively. After being dried with nitrogen, the substrates were treated with UV ozone for 30 min. The zinc oxide (ZnO) precursor solution was obtained by dissolving 1 g $Zn(CH_3COO)_2{\cdot}2H_2O$ and 0.28 g $NH_2CH_2CH_2OH$ into 10 ml $CH_3OCH_2CH_2OH$, and then spin coated at 3,000 rpm. The ITO substrates were baked at 150°C for 15 min to form the ZnO layer (30 nm) and then transferred to nitrogen glove box. The PBDB-T and ITIC (w/w = 1:1) were dissolved in chlorobenzene at the concentration of 20 mg/ml. The active layer solution was spin coated on the ZnO layer at 2,000 rpm. In the end, hole transport layer MoO_3 (10 nm) and electrode Al (100 nm) were deposited by vacuum evaporation, respectively. The device effective area was 0.04 cm^2. The AM 1.5G solar simulator (light intensity, 100 mW/cm^2) was used as the light source for J–V characteristic measurement.

Fabrication of Bilayer Configuration Films

The bilayer configurations of PBDB-T/ITIC and ITIC/PBDB-T were fabricated through layer-by-layer transferring method. The ITO substrates were ultrasonically cleaned by detergent, deionized water, acetone, and isopropanol for 15 min, respectively. The PBDB-T and ITIC were dissolved in chlorobenzene at the concentration of 20 mg/ml, respectively. To facilitate the transfer of ITIC film, the blend solution of ITIC and PS (w/w = 2:1) was obtained in chlorobenzene at the concentration of 20 mg/ml. As for PBDB-T/ITIC film, PEDOT:PSS was spin coated on the substrate at 5,000 rpm; then, PBDB-T solution was spin coated at 2,000 rpm. The substrate was put into deionized water slowly, and PBDB-T film could

float due to the water solubility of PEDOT:PSS. The floated PBDB-T film was transferred onto the substrate with spin-coated ITIC film at 2,000 rpm. The fabrication of ITIC/PBDB-T film was almost similar, and the difference was that blend solution of ITIC and PS was spin coated on the PEDOT:PSS layer.

Film-Depth-Dependent Light Absorption Spectra Measurement

The FLAS measurement uses the instrument setup by our laboratory, which will be described in detail in the following parts. The sample was put into the capacitive coupled plasma generator (PT-5S, Shenzhen Sanwa Boda Mechanical & Electrical Technology Co., Ltd.), and the vacuum pump (2XZ-4, Shenzhen Sanwa Boda Mechanical & Electrical Technology Co., Ltd.) evacuated to ∼3 Pa. Then, oxygen entered into vacuum discharge chamber, and plasma was generated by capacitive coupling discharge etching the film. The spectrometer (PG2000-Pro, Ideaoptics) collected the *in situ* spectrum information of film after each etching. Each etching time is almost identical (∼20 s).

RESULTS AND DISCUSSION

In situ Instrument and *in situ* Spectra Measurement

As shown in **Figure 1A**, the *in situ* instrument is mainly composed of a power supply, a light source, a capacitive coupled plasma generator, a spectrometer, and a computer. The power supply can provide the stable constant current to ensure the continuous work of light source. The light source is a xenon lamp (150 W), and its spectrum is from ultraviolet to near infrared. To reduce the impact of output power density loss and ensure the constant output, light intensity is adjustable and output characteristics of power supply are required. The stable current can be adjusted in the range of 7–9 A; meanwhile, the current instability is limited to 0.05%. The spectrometer provides balanced sensitivity and high resolution within the spectrum of 200–1,100 nm. The Morpho, as spectrometer analysis software, displays the spectra in real time.

The integration of plasma etching and *in situ* spectra measurement is realized by introducing the optical path into the capacitive coupled plasma generator. The plasma generator selects a sealed low dielectric vacuum discharge chamber made of aluminum alloy to approximate the total reflection integrating sphere. The optical fiber is tightly connected to the upper and lower sides of vacuum discharge chamber by fastener to ensure the vacuum degree and avoid the movement that may deteriorate the focus of optical path. When the *in situ* instrument works, the divergent light from xenon lamp becomes parallel through a plano-convex lens and enters the optical fiber after gathering. The light is irradiated to the sample through optical fiber above the vacuum chamber and then enters the spectrometer through optical fiber below the vacuum chamber. After light is processed by a spectrometer and spectrum analysis software, the absorption spectrum is obtained. The sample is always fixed at the same position during etching and measurement and continuously thinned by the oxygen plasma. Considering the effect of different etching rate, this *in situ* measurement method is suitable for organic film with small phase separation scale and surface roughness. To achieve outstanding device performance, most organic optoelectronic films are eligible. Additionally, due to the low etching power and short treatment time, temperature in the vacuum chamber does not rise too much, and it is just slightly higher than room temperature during the entire etching process, which cannot cause film nanostructure to evolve.

Previous research has proven that the plasma can selectively etch the organic film without damaging the materials below the surface at low pressure (<30 Pa) (Bu et al., 2016a). Hence, we can etch the film with low-pressure plasma and measure the *in situ* absorption spectra to investigate the film-depth-dependent characteristics. The theoretical basis for obtaining the FLAS is based on Lambert–Beer law. As follows:

$$A = -\log \frac{I}{I_0 - I_R} \tag{1}$$

$$I = (I_0 - I_R)10^{-A} \tag{2}$$

where A is the absorbance; I_0, I, and I_R are the incident, transmitted, and reflected light intensity, respectively. It is obvious that the proportion of light absorption by equal thickness layer is identical regardless of incident light intensity. In this case, if the active layer is assumed to be divided into n sublayers, and the absorbance of each sublayer is A_i ($i = 1, 2, 3,..., n$) (**Figure 1B**), then the transmitted light intensity is

$$I = (I_0 - I_R)\prod_{i=1}^{n} 10^{-A_i} = (I_0 - I_R)10^{-\sum_i^n A_i} \tag{3}$$

$$A_{\text{active layer}} = A_1 + A_2 + \ldots + A_n \tag{4}$$

It can be seen that the absorption spectrum of film can be considered as a linear superposition of the sublayers. Thus, the FLAS can be obtained by subtracting the absorption spectrum of etching film layer by layer.

As the most important part of entire instrument, we focus on the capacitive coupled plasma generator. It mainly includes three parts: radio frequency (RF) power supply part, system control part, and vacuum and gas circuit part. Owing to the small RF power, the parts of RF power supply and system control can be assembled to save room and simplified the operation. **Figure 2A** shows the system working flow chart of capacitive coupled plasma generator. With the set vacuum degree, the circuit system starts the RF source to generate a 40-kHz RF pulse (offset is <0.2 kHz), and then, RF pulse is amplified to the output stage. To ensure that it has enough energy to excite the high-voltage plate and generate plasma, the role of output stage is 3-fold: isolation, boost, and matching.

The RF power is adjusted by changing the width of RF pulse, which can be set in the system or manual control, and it is generally 300 W during the measurement. The ideal RF pulse output does not consider the loss of components and magnetic materials, but the actual RF pulse waveform is distorted. When the distortion is severe, the effective power output can be greatly reduced. In addition, excessive harmonic

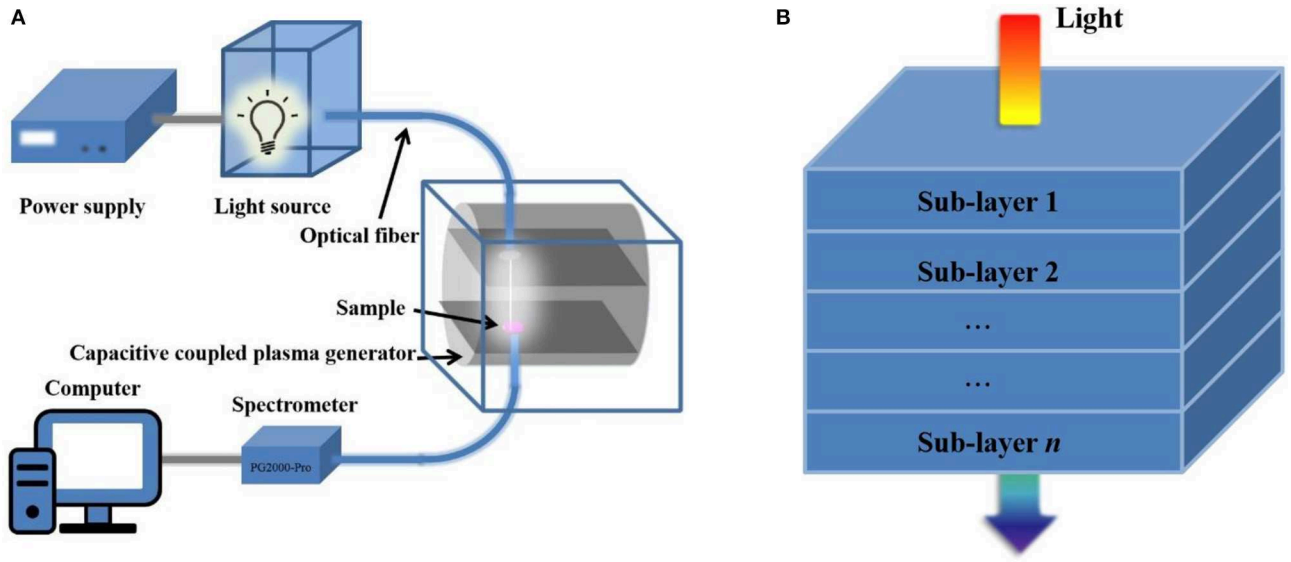

FIGURE 1 | Schemes of instrument and analytical principle for *in situ* measuring FLAS. **(A)** Components of the instrument. **(B)** Schematic diagram showing the layer is composed of *n* sublay.

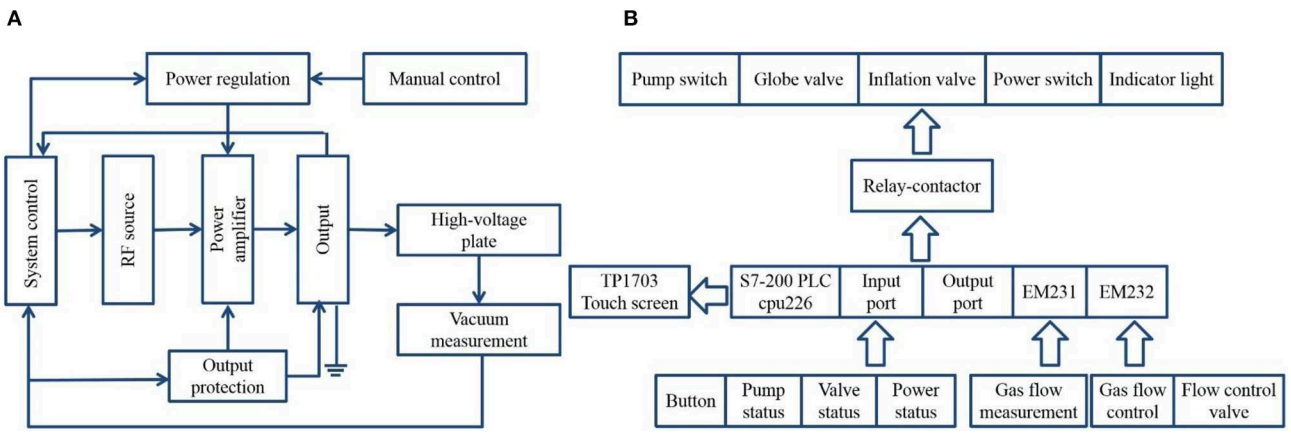

FIGURE 2 | Control principles of capacitive coupled plasma generator. **(A)** System working flow chart. **(B)** Programmable logic controller (PLC) control system framework.

pulse can also reduce the RF efficiency, which can not only cause abnormal plasma generation but also burn the equipment. Thus, the technical demands for RF power are required. **Figure 2B** shows the frame of control system. According to the control requirements of capacitive coupled plasma generator, the S7-200 series programmable logic controller (PLC) with 24 digital input terminals, 16 digital output terminals, and 2 RS485 communication/programming ports is selected, which has compact structure, strong scalability, and rich instruction. The analog input (EM231) and analog output (EM232) modules are expanded to control and detect the gas flow. The TP170B touch screen can realize the etching parameter setting, process monitoring, and display functions of entire system. The gas inlet and outlet ports are set at the back of capacitive coupled plasma generator. The two gas inlet ports are connected to gas source, and the gas outlet port is connected to vacuum pump. The type and mixing ratio of gas can be selected through the touch screen. To control pressure of vacuum discharge chamber, gas flow can be adjusted by the pressure reducing valve of gas cylinder and flow meter.

Glow Discharge Emission Spectra at Different Oxygen Plasma Pressures

The discharge mode of plasma generator is RF glow discharge with capacitive coupling. Compared with traditional direct current glow discharge, RF glow discharge can process insulated samples (Conrads and Schmidt, 2000). At low pressure, gas is ionized in an alternating electric field between the high-voltage

plates. The charged ions are accelerated to continuously collide with molecules, and the plasma is generated. At the same time, the unstable excited-state atoms can return to ground states and emit photons in a short time, releasing energy in the form of light to form the glow. According to different gas categories, colorful visible light from blue to deep purple can be emitted, and the material processing temperature is close to room temperature. The selected gas source is oxygen, and the color of oxygen plasma glow discharge is purple (**Figure 3A**). Oxygen plasma contains a variety of reactive components, including O^{2+}, O^{2-}, O_3, O, O^+, O^-, ionized ozone, etc. These highly active particles interact with the treated surface to get the etched surface modification (Chan et al., 1996).

As we have known, gas pressure can affect the intensity of glow discharge and further affect the etching rate. We study the oxygen plasma glow discharge spectra at different pressures. Owing to the complex plasma composition, emission spectra include the emission of molecules and atoms. The sharp emission peaks are mainly at 842 nm [OI (3p3P−3s3S)] and 774 nm [OI (3p5P−3s5S)] (Vandsburger et al., 2013). The emission band at 300–400 nm mainly comes from the emission of O [OII (3p−3s) at 423 nm and OIII (3d−3p) at 332 nm], OH, and N2 as a result of the presence of air. As shown in **Figure 3B**, the lower the pressure, the stronger the intensity of glow discharge spectrum, which means the faster the etching rate. Generally, the etching pressure is maintained at ∼3 Pa to ensure that the material below the surface is not damaged. At the same time, the etching rate is maintained at a fast level.

Device Performance and Film-Depth-Dependent Light Absorption Spectra

The inverted device structure studied in this work is ITO/ZnO/Active layer/MoO_3/Al (**Figure 4A**), with PBDB-T as donor and ITIC as acceptor. Compared with standard structure, the air stability of inverted structure is better. **Figure 4B** shows the molecular structures of PBDB-T and ITIC. **Figure 4C** shows the energy levels of individual layers in OPVs from the literature (Li et al., 2019).

Figure 4D shows the absorption spectra of neat PBDB-T film, neat ITIC film, and blend film. The absorption spectrum of PDBD-T is mainly at 500–700 nm, and the absorption spectrum of ITIC ranges from 550 to 800 nm. The absorption spectrum of blend film is from 500 to 800 nm.

As a classic system, lots of work were devoted to performance optimization and mechanism research of PBDB-T/ITIC devices (Zhao W. et al., 2016; Zhao W. C. et al., 2016; Pan et al., 2017; An et al., 2018; Bi et al., 2018; Liang et al., 2018). Here, we mainly study the film-depth-dependent optical and electrical properties by the *in situ* instrument. Without additive and annealing treatment, the as-cast devices show good device performance. From the *J*–*V* characteristic curve of BHJ device (**Figure 5A**), the PCE of 9.65% was achieved, with the open circuit voltage (V_{oc}) of 0.92 V, short circuit current density (J_{sc}) of 16.80 mA/cm^2, and fill factor (FF) of 62.4%. The UV-vis absorption spectra are sensitive to chain conformation and aggregation structure of conjugated organic material. As for PBDB-T /ITIC, the π–π stacking between molecular chains leads to the delocalization of π electrons, which reduces the optical gap. In other words, the red shift of absorption peak means more ordered molecular aggregation. From the FLAS of BHJ (**Figure 5B**), the first sublayer shows red shift compared to the second sublayer, indicating the better molecular packing at the top surface of the film. The difference in aggregate structure along the vertical direction is strongly correlated with the solvent evaporation process.

To demonstrate the validity of measurement, bilayer configuration films were prepared for comparison. We prepared two kinds of structures: one is PBDB-T/ITIC, and the other is ITIC/PBDB-T from top to bottom. The thickness of single-layer films were ∼100 nm, so the thickness of bilayer configuration films were ∼200 nm. As for ITIC/PBDB-T structure, little PS was added to the ITIC solution to facilitate the transfer of small molecule ITIC film. In addition, the absorption peak of PS is at 190 nm, which do not affect the absorption spectrum of ITIC. We did not measure the performance of bilayer configuration devices because the films made by this method were rough, resulting in poor device performance. As shown in **Figures 5C**, **D**, the FLAS of bilayer configuration films show significant stratification. As for PBDB-T/ITIC film, the FLAS on the top mainly show the peak of PBDB-T, while the FLAS on the bottom mainly show the peak of ITIC. The ITIC/PBDB-T film is just the opposite. Moreover, due to structural difference, donor and acceptor materials are etched by oxygen plasma at different rates, but the difference is not so great.

Film-Depth-Dependent Optical and Electronic Properties

Numerical simulation is an effective method to research the physical mechanism and predict the theoretical limit efficiency of OPVs (Zhao et al., 2011; Kirchartz and Nelson, 2014). Utilizing the FLAS, we can investigate the film-depth-dependent optical and electronic properties of organic film by appropriate models and further apply to device performance optimization. Comparing the pure composition absorption spectra and FLAS, we fit the thickness and composition distribution of each sublayer along film-depth direction by least squares method. As shown in **Figure 6A**, the active layer forms vertical phase separation. The donor aggregates on the top and the acceptor aggregates on the bottom, which is beneficial to the inverted device. After exciton dissociation, the holes and electrons can be quickly collected by anode and cathode, respectively.

The transfer matrix method, considering the interference of light between multilayer film, has been widely used in the optical simulation of OPVs to investigate photoelectric field and exciton generation rate distribution (Pettersson et al., 1999; Xia et al., 2019). In this model, complex refractive index, $N = n + ik$, is the main optical constant, where n is the refractive index and k is the extinction coefficient. The refractive index n has little effect on the light absorption, and the refractive index of polymer is almost 2, so it can be directly taken as 2 to simplify calculation. The extinction coefficient is obtained from the FLAS according to

$$A = -\lg\left(e^{-\frac{4\pi kd}{\lambda}}\right) \quad (5)$$

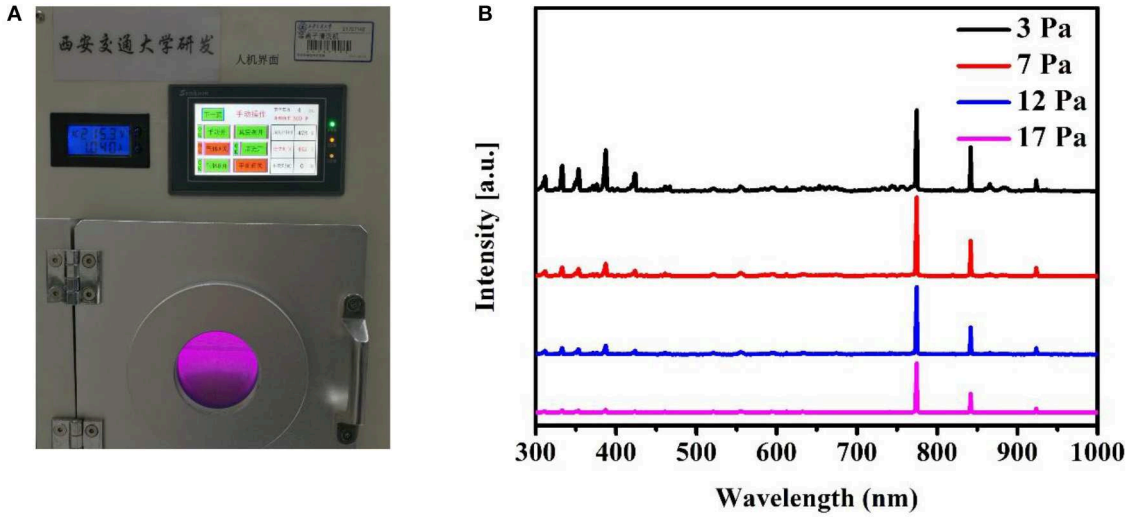

FIGURE 3 | Glow discharge generating plasma. **(A)** A photo of the *in situ* film-depth-dependent light absorption spectra (FLAS) instrument during the oxygen plasma generation. The purple area in the photo shows oxygen plasma glow discharge. **(B)** Emission spectra of oxygen plasma during glow discharge at different oxygen plasma pressures. The spectra are shifted along the vertical direction for clarity.

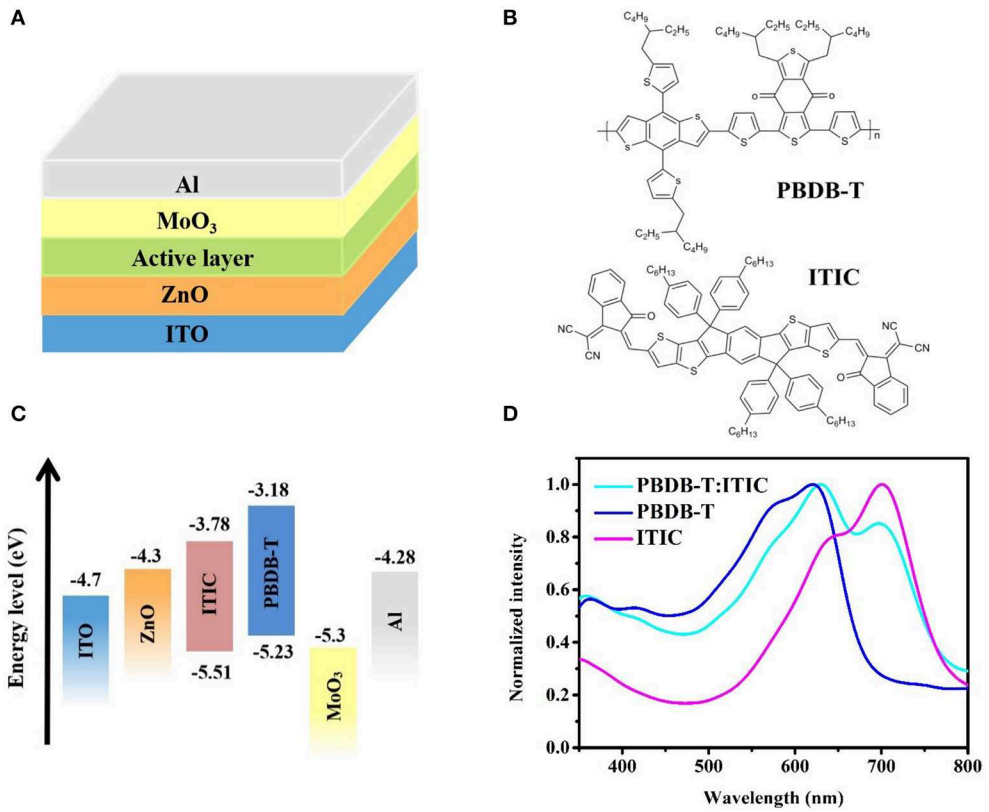

FIGURE 4 | (A) Inverted device structure of organic photovoltaic devices (OPVs) studied in this work. **(B)** Molecular structures of poly{(2,6-(4,8-bis(5-(2-ethylhexyl)thiophen-2-yl)-benzo[1,2-b:4,5-b′]dithiophene))-alt-(5,5-(1′,3′-di-2-thienyl-5′,7′-bis(2-ethylhexyl)benzo[1′,2′-c:4′,5′-c′]dithiophene-4,8-dione))} (PBDB-T) and 3,9-bis{2-methylene-[3-(1,1-dicyanomethylene)-indanone]}-5,5,11,11-tetrakis(4-hexylphenyl)-dithieno[2,3-d:2′,3′-d′]-s-indaceno[1,2-b:5,6-b′]dithiophene (ITIC). **(C)** Energy level diagram of individual layers in OPVs. **(D)** Normalized absorption spectra of neat PBDB-T, neat ITIC, and PBDB-T:ITIC blend film.

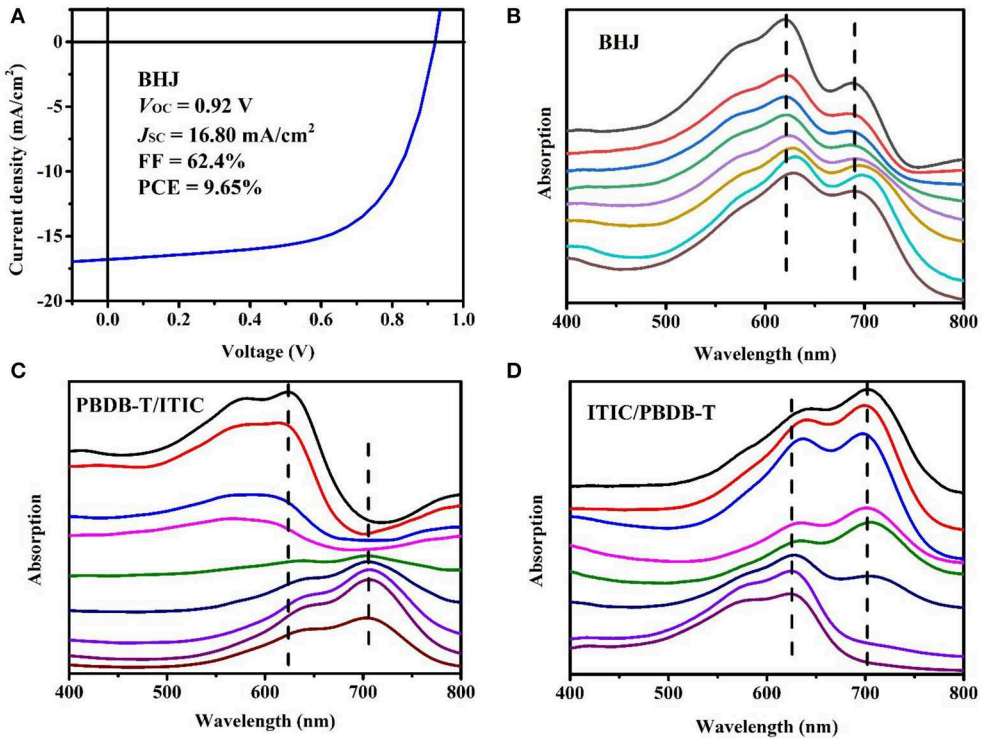

FIGURE 5 | Device performance and film-depth-dependent light absorption spectra (FLAS). **(A)** *J–V* characteristic curve of bulk heterojunction (BHJ) device under illumination of solar simulator (AM 1.5G, 100 mW/cm^2). **(B–D)** FLAS of BHJ and bilayer. **(B)** Poly{(2,6-(4,8-bis(5-(2-ethylhexyl)thiophen-2-yl)-benzo[1,2-b:4,5-b′] dithiophene))-alt-(5,5-(1′,3′-di-2-thienyl-5′,7′-bis(2-ethylhexyl)benzo[1′,2′-c:4′,5′-c′]dithiophene-4,8-dione))}:3,9-bis{2-methylene-[3-(1,1-dicyanomethylene)-indanone]}-5,5,11,11-tetrakis(4-hexylphenyl)-dithieno[2,3-d:2′,3′-d′]-s-indaceno[1,2-b:5,6-b′]dithiophene (PBDB-T:ITIC) (1:1) BHJ. The dashed lines show that the absorption peak varies with film depth. **(C)** PBDB-T/ITIC bilayer configuration with PBDB-T layer at the top and ITIC layer at the bottom, as prepared by layer-by-layer transferring method. **(D)** ITIC/PBDB-T bilayer configuration with ITIC layer at the top and PBDB-T layer at the bottom. ITIC was blended with some polystyrene to warrant the film transferring. The upper sublayer spectrum corresponds to the top of film, and the lower sublayer spectrum corresponds to the bottom of film. The spectra are shifted along the vertical direction for clarity. The sublayer thickness corresponding to each spectrum is ∼12–13 nm.

where d is the calculated sublayer thickness, and λ is the wavelength. Considering the vertical distribution of composition, we divide the active layer into multiple sublayers. Each sublayer takes a different extinction coefficient, and its interior is considered to be uniform (Wang Y. et al., 2018). Then, the exciton generation contour is obtained (**Figure 6B**), and exciton generation profile is calculated by integrating the wavelengths from the exciton generation contour (**Figure 6C**). The positions of exciton generation are mainly located in the middle of active layer, and sunlight with the range from 500 to 800 nm contributes the most, which is consistent with the absorption spectra of donor and acceptor. It is beneficial that excitons are generated and separated in the middle of the active layer for OPVs. In this way, the distance of charge transport to electrode is short, which means a smaller probability of recombination, resulting in higher PCE.

Owing to the complex molecular conformation and chain orientation of conjugated polymer, the energy band structure is significantly different from that of inorganic material (Gregg and Hanna, 2003). The energy levels for charge transport are closely associated with highest occupied molecular orbital (HOMO) and lowest unoccupied molecular orbital (LUMO) levels. Because of vertical phase separation, the molecular aggregation along the film-depth direction is different, further causing fluctuation of energy band (Blakesley and Neher, 2011). **Figure 6D** shows film-depth-dependent energy levels (HOMO of PBDB-T and LUMO of ITIC) extracted from FLAS. As follows:

$$E_{\mathrm{LUMO}} = E_{A-\mathrm{LUMO}} + \left(\frac{1,240}{\lambda_{\mathrm{A-FLAS}}} - \frac{1,240}{\lambda_{\mathrm{A}}}\right) \quad (6)$$

$$E_{\mathrm{HOMO}} = E_{\mathrm{D-HOMO}} + \left(\frac{1,240}{\lambda_{\mathrm{D-FLAS}}} - \frac{1,240}{\lambda_{\mathrm{D}}}\right) \quad (7)$$

where $E_{\mathrm{A-LUMO}}$ and $E_{\mathrm{D-HOMO}}$ are the LUMO of acceptor and HOMO of donor, respectively. λ_{A} and λ_{D} are the wavelengths corresponding to absorption peaks of acceptor and donor neat film, respectively. $\lambda_{\mathrm{A-FLAS}}$ and $\lambda_{\mathrm{D-FLAS}}$ are the wavelengths corresponding to absorption peaks of acceptor and donor FLAS, respectively. As we all know, the fluctuation of energy band is easy to form traps and leads to the recombination of carriers, which is detrimental to the device performance. Furthermore,

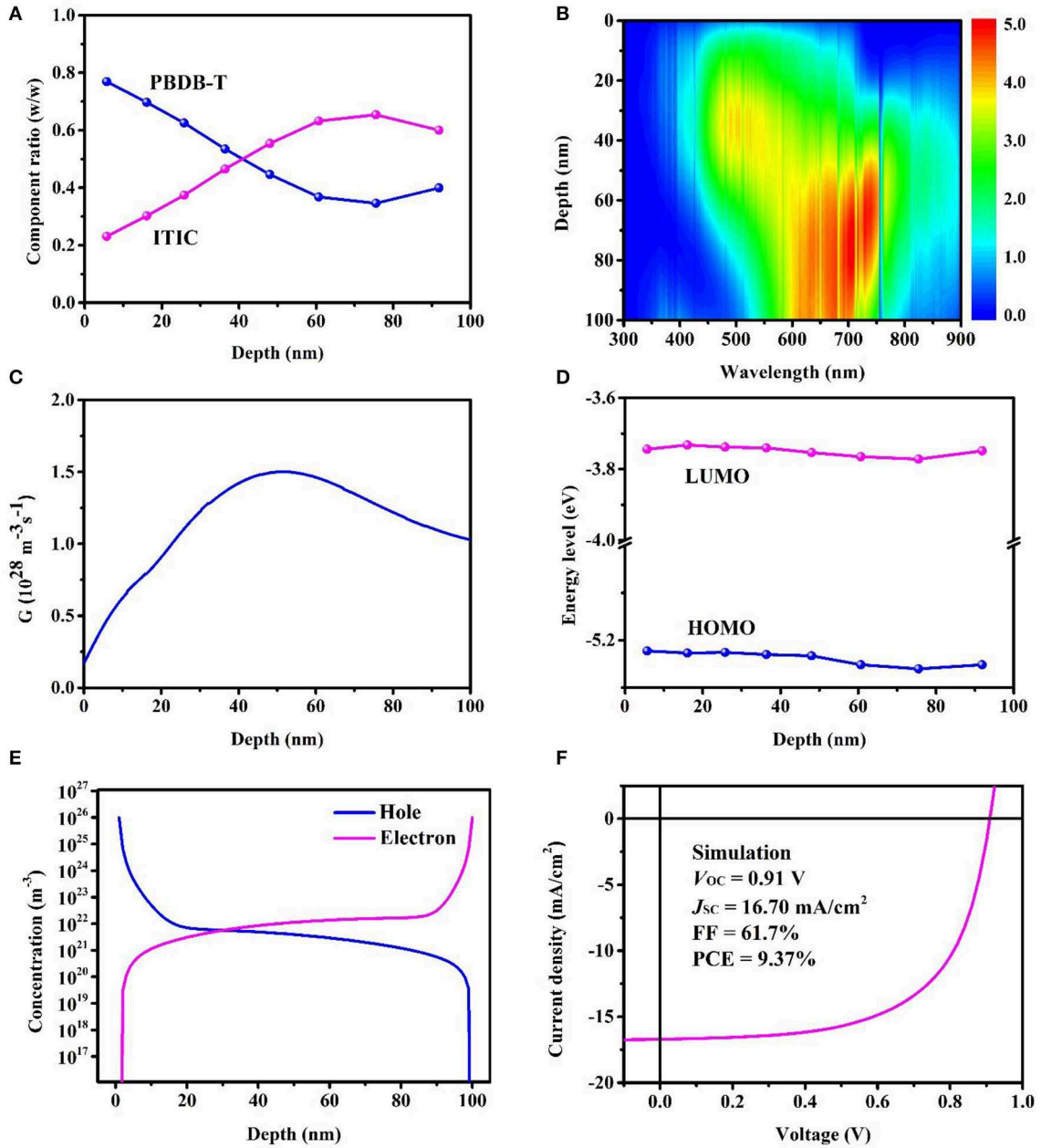

FIGURE 6 | Film-depth-dependent optical and electronic properties of bulk heterojunction (BHJ) devices; 0 and 100 nm refer to active layer/MoO_3 and ZnO/active layer interfaces, respectively. **(A)** Composition distribution profiles of donor and acceptor, as extracted from film-depth-dependent light absorption spectra (FLAS). **(B)** Exciton generation contour at wavelength and film depth direction (unit, 10^{25} m^{-3} s^{-1} nm^{-1}). The noise-like vertical lines are caused by the fluctuation of real solar spectrum (AM 1.5G). **(C)** Exciton generation profile at film depth direction calculated from **(B)**. **(D)** Film-depth-dependent energy levels {highest occupied molecular orbital (HOMO) of Poly{(2,6-(4,8-bis(5-(2-ethylhexyl)thiophen-2-yl)-benzo[1,2-b:4,5-b′]dithiophene))-alt-(5,5-(1′,3′-di-2-thienyl-5′,7′-bis(2-ethylhexyl)benzo[1′,2′-c:4′, 5′-c′]dithiophene-4,8-dione))} (PBDB-T) and lowest unoccupied molecular orbital (LUMO) of 3,9-bis{2-methylene-[3-(1,1-dicyanomethylene) -indanone]}-5,5,11,11-tetrakis(4-hexylphenyl)-dithieno[2,3-d:2′,3′-d′]-s-indaceno[1,2-b:5,6-b′]dithiophene (ITIC)}, as approximately obtained from FLAS. **(E)** Simulated film-depth-dependent carrier concentration distribution. **(F)** Simulated *J-V* characteristic curve, using film-depth-dependent optical **(B)** and electronic **(D)** properties, both of which are extracted from FLAS.

based on drift-diffusion model, the effect of band fluctuation is introduced into potential term (Scheunemann et al., 2019; Wang et al., 2019; Xiao et al., 2020). The carrier concentration distribution is calculated (**Figure 6E**). Carriers gather in the middle of the active layer and deplete within a few nanometers at both interfaces. We also simulate the *J–V* curve of BHJ device, which is in good agreement with the experimental result (**Figure 6F**).

CONCLUSIONS

In this work, we propose an *in situ* measurement method in combination with an *in situ* instrument that integrates a capacitive coupled plasma generator, a light source, and a spectrometer. This *in situ* method and instrument are easily accessible and easily equipped in laboratories. Subsequently, the *in situ* FLAS are used to investigate vertical distribution of composition and aggregation, photon harvesting contour along film-depth direction, and film-depth-dependent charge transport behavior. The *in situ* measurement and simulation contribute to the optimization of photovoltaic devices. This work provides a general method for *in situ* film-depth profiling, which could be used to conveniently investigate the film-depth-dependent optical and electronic properties.

DATA AVAILABILITY STATEMENT

All datasets generated for this study are included in the article/supplementary material.

AUTHOR CONTRIBUTIONS

XF performed the glow discharge spectra and FLAS measurement, simulated the optical and electronic properties of OPVs, and wrote the manuscript. YW and TX conducted the instrument construction and numerical model building. ZS fabricated the BHJ devices. YR revised the manuscript. LB and GL supervised the project and contributed to the writing of manuscript.

FUNDING

This work was financially supported by the National Natural Science Foundation of China (Grant Nos. 21973072, 51873172, 51907148, and 51473132), the Fundamental Research Funds for the Central Universities (xjh012019023), the Natural Science Basic Research Plan in Shaanxi Province of China (2019JQ-070), and the Youth Fund of the State Key Laboratory of Electrical Insulation and Power Equipment (Grant No. EIPE19308).

REFERENCES

Adil, M. A., Zhang, J., Wang, Y., Yu, J., Yang, C., Lu, G., et al. (2019). Regulating the phase separation of ternary organic solar cells via 3D architectured AIE molecules. *Nano Energy* 68:104271. doi: 10.1016/j.nanoen.2019.104271

An, Q. S., Zhang, F. J., Gao, W., Sun, Q. Q., Zhang, M., Yang, C. L., et al. (2018). High-efficiency and air stable fullerene-free ternary organic solar cells. *Nano Energy* 45, 177–183. doi: 10.1016/j.nanoen.2017.12.050

Bi, P., Xiao, T., Yang, X., Niu, M., Wen, Z., Zhang, K., et al. (2018). Regulating the vertical phase distribution by fullerene-derivative in high performance ternary organic solar cells. *Nano Energy* 46, 81–90. doi: 10.1016/j.nanoen.2018.01.040

Blakesley, J. C., and Neher, D. (2011). Relationship between energetic disorder and open-circuit voltage in bulk heterojunction organic solar cells. *Phys. Rev. B* 84:075210. doi: 10.1103/PhysRevB.84.075210

Bredas, J.-L. (2014a). Mind the gap! *Mater. Horiz.* 1, 17–19. doi: 10.1039/C3MH00098B

Bredas, J. L. (2014b). When electrons leave holes in organic solar cells. *Science* 343, 492–493. doi: 10.1126/science.1249230

Bu, L., Gao, S., Wang, W., Zhou, L., Feng, S., Chen, X., et al. (2016a). Film-depth-dependent light absorption and charge transport for polymer electronics: a case study on semiconductor/insulator blends by plasma etching. *Adv. Electron. Mater.* 2:1600359. doi: 10.1002/aelm.201600359

Bu, L., Qiu, Y., Wei, P., Zhou, L., Lu, W., Li, S., et al. (2016b). Manipulating transistor operation via nonuniformly distributed charges in a polymer insulating electret layer. *Phys. Rev. Appl.* 6:054022. doi: 10.1103/PhysRevApplied.6.054022

Chan, C. M., Ko, T. M., and Hiraoka, H. (1996). Polymer surface modification by plasmas and photons. *Surf. Sci. Rep.* 24, 1–54. doi: 10.1016/0167-5729(96)80003-3

Cheng, X. F., Li, M. M., Guo, Z. Q., Yu, J. D., Lu, G. H., Bu, L. J., et al. (2019). "Twisted" conjugated molecules as donor materials for efficient all-small-molecule organic solar cells processed with tetrahydrofuran. *J. Mater. Chem. A* 7, 23008–23018. doi: 10.1039/C9TA07760J

Conrads, H., and Schmidt, M. (2000). Plasma generation and plasma sources. *Plasma Sources Sci. Technol.* 9, 441–454. doi: 10.1088/0963-0252/9/4/301

Dong, S., Zhang, K., Xie, B., Xiao, J., Yip, H.-L., Yan, H., et al. (2019). High-performance large-area organic solar cells enabled by sequential bilayer processing via nonhalogenated solvents. *Adv. Energy Mater.* 9:1802832. doi: 10.1002/aenm.201802832

Fan, Y. Y., Fang, J. J., Chang, X. M., Tang, M. C., Barrit, D., Xu, Z., et al. (2019). Scalable ambient fabrication of high-performance CsPbI2Br Solar Cells. *Joule* 3, 2485–2502. doi: 10.1016/j.joule.2019.07.015

Gregg, B. A., and Hanna, M. C. (2003). Comparing organic to inorganic photovoltaic cells: theory, experiment, and simulation. *J. Appl. Phys.* 93, 3605–3614. doi: 10.1063/1.1544413

Gusain, A., Faria, R. M., and Miranda, P. B. (2019). Polymer solar cells-interfacial processes related to performance issues. *Front. Chem.* 7:61. doi: 10.3389/fchem.2019.00061

Heeger, A. J. (2014). 25th anniversary article: bulk heterojunction solar cells: understanding the mechanism of operation. *Adv. Mater.* 26, 10–27. doi: 10.1002/adma.201304373

Huang, L., Wang, G., Zhou, W., Fu, B., Cheng, X., Zhang, L., et al. (2018). Vertical stratification engineering for organic bulk-heterojunction devices. *ACS Nano* 12, 4440–4452. doi: 10.1021/acsnano.8b00439

Kirchartz, T., and Nelson, J. (2014). Device modelling of organic bulk heterojunction solar cells. *Top. Curr. Chem.* 352, 279–324. doi: 10.1007/128_2013_473

Li, G., Zhu, R., and Yang, Y. (2012). Polymer solar cells. *Nat. Photonics* 6, 153–161. doi: 10.1038/nphoton.2012.11

Li, Q., Wang, L. M., Liu, S., Zhan, X., Zhu, T., Cao, Z., et al. (2019). Impact of donor-acceptor interaction and solvent additive on the vertical composition distribution of bulk heterojunction polymer solar cells. *ACS Appl. Mater. Interfaces* 11, 45979–45990. doi: 10.1021/acsami.9b15753

Li, Y. W., Xu, G. Y., Cui, C. H., and Li, Y. F. (2018). Flexible and semitransparent organic solar cells. *Adv. Energy Mater.* 8:1701791. doi: 10.1002/aenm.201701791

Liang, Q., Jiao, X., Yan, Y., Xie, Z., Lu, G., Liu, J., et al. (2019). Separating crystallization process of P3HT and O-IDTBR to construct highly crystalline interpenetrating network with optimized vertical phase separation. *Adv. Funct. Mater.* 29:1807591. doi: 10.1002/adfm.201807591

Liang, Q. J., Han, J., Song, C. P., Yu, X. H., Smilgies, D. M., Zhao, K., et al. (2018). Reducing the confinement of PBDB-T to ITIC to improve the crystallinity of PBDB-T/ITIC blends. *J. Mater. Chem. A* 6, 15610–15620. doi: 10.1039/C8TA05892J

Lin, Y., Adilbekova, B., Firdaus, Y., Yengel, E., Faber, H., Sajjad, M., et al. (2019). 17% Efficient organic solar cells based on liquid exfoliated WS2 as a replacement for PEDOT:PSS. *Adv. Mater.* 31:1902965. doi: 10.1002/adma.201902965

Lin, Y., Li, Y., and Zhan, X. (2012). Small molecule semiconductors for high-efficiency organic photovoltaics. *Chem. Soc. Rev.* 41, 4245–4272. doi: 10.1039/c2cs15313k

Lin, Y., Wang, J., Zhang, Z. G., Bai, H., Li, Y., Zhu, D., et al. (2015). An electron acceptor challenging fullerenes for efficient polymer solar cells. *Adv. Mater.* 27, 1170–1174. doi: 10.1002/adma.201404317

Liu, F., Ferdous, S., Schaible, E., Hexemer, A., Church, M., Ding, X. D., et al. (2015). Fast printing and *in situ* morphology observation of organic photovoltaics using slot-die coating. *Adv. Mater.* 27, 886–891. doi: 10.1002/adma.201404040

Liu, Q., Jiang, Y., Jin, K., Qin, J., Xu, J., Li, W., et al. (2020). 18% Efficiency organic solar cells. *Sci. Bull.* 65, 272–275. doi: 10.1016/j.scib.2020.01.001

Liu, T., Guo, Y., Yi, Y., Huo, L., Xue, X., Sun, X., et al. (2016). Ternary organic solar cells based on two compatible nonfullerene acceptors with power conversion efficiency. *Adv. Mater.* 28, 10008–10015. doi: 10.1002/adma.201602570

Meng, L. X., Zhang, Y. M., Wan, X. J., Li, C. X., Zhang, X., Wang, Y. B., et al. (2018). Organic and solution-processed tandem solar cells with 17.3% efficiency. *Science* 361, 1094–1098. doi: 10.1126/science.aat2612

Niu, T. Q., Lu, J., Tang, M. C., Barrit, D., Smilgies, D. M., Yang, Z., et al. (2018). High performance ambient-air-stable FAPbI(3) perovskite solar cells with molecule-passivated Ruddlesden-Popper/3D heterostructured film. *Energy Environ. Sci.* 11, 3358–3366. doi: 10.1039/C8EE02542H

Pan, Q. Q., Li, S. B., Duan, Y. C., Wu, Y., Zhang, J., Geng, Y., et al. (2017). Exploring what prompts ITIC to become a superior acceptor in organic solar cell by combining molecular dynamics simulation with quantum chemistry calculation. *Phys. Chem. Chem. Phys.* 19, 31227–31235. doi: 10.1039/C7CP05938H

Pettersson, L. A. A., Roman, L. S., and Inganäs, O. (1999). Modeling photocurrent action spectra of photovoltaic devices based on organic thin films. *J. Appl. Phys.* 86, 487–496. doi: 10.1063/1.370757

Scheunemann, D., Wilken, S., Sandberg, O. J., Österbacka, R., and Schiek, M. (2019). Effect of imbalanced charge transport on the interplay of surface and bulk recombination in organic solar cells. *Phys. Rev. Appl.*11:054090. doi: 10.1103/PhysRevApplied.11.054090

Vandsburger, L., Coulombe, S., and Meunier, J. L. (2013). Degradation of carbon nanotubes in oxygen glow discharges. *Carbon* 57, 248–258. doi: 10.1016/j.carbon.2013.01.071

Wang, J., Zhang, J., Xiao, Y., Xiao, T., Zhu, R., Yan, C., et al. (2018). Effect of isomerization on high-performance nonfullerene electron acceptors. *J. Am. Chem. Soc.* 140, 9140–9147. doi: 10.1021/jacs.8b04027

Wang, Y., Zhang, Y., Lu, G., Feng, X., Xiao, T., Xie, J., et al. (2018). Reconstructing space- and energy-dependent exciton generation in solution-processed inverted organic solar cells. *ACS Appl. Mater. Interfaces* 10, 13741–13747. doi: 10.1021/acsami.7b14698

Wang, Z., Hu, Y., Xiao, T., Zhu, Y., Chen, X., Bu, L., et al. (2019). Correlations between performance of organic solar cells and film-depth-dependent optical and electronic variations. *Adv. Opt. Mater.* 7:1900152. doi: 10.1002/adom.201900152

Xia, R., Gu, H., Liu, S., Zhang, K., Yip, H.-L., and Cao, Y. (2019). Optical analysis for semitransparent organic solar cells. *Sol. RRL* 3:1800270. doi: 10.1002/solr.201800270

Xiao, T., Wang, J., Yang, S., Zhu, Y., Li, D., Wang, Z., et al. (2020). Film-depth-dependent crystallinity for light transmission and charge transport in semitransparent organic solar cells. *J. Mater. Chem. A* 8, 401–411. doi: 10.1039/C9TA11613C

Xu, Y., Yuan, J., Liang, S., Chen, J.-D., Xia, Y., Larson, B. W., et al. (2019a). Simultaneously improved efficiency and stability in all-polymer solar cells by a P–i–N architecture. *ACS Energy Lett.* 4, 2277–2286. doi: 10.1021/acsenergylett.9b01459

Xu, Y., Yuan, J., Zhou, S., Seifrid, M., Ying, L., Li, B., et al. (2019b). Ambient processable and stable all-polymer organic solar cells. *Adv. Funct. Mater.* 29:1806747. doi: 10.1002/adfm.201806747

Xu, Z., Chen, L.-M., Yang, G., Huang, C.-H., Hou, J., Wu, Y., et al. (2009). Vertical phase separation in poly(3-hexylthiophene): fullerene derivative blends and its advantage for inverted structure solar cells. *Adv. Funct. Mater.* 19, 1227–1234. doi: 10.1002/adfm.200801286

Yan, H., Tang, Y., Meng, X., Xiao, T., Lu, G., and Ma, W. (2019). Achieving high doping concentration by dopant vapor deposition in organic solar cells. *ACS Appl. Mater. Interfaces* 11, 4178–4184. doi: 10.1021/acsami.8b16162

Yan, T., Song, W., Huang, J., Peng, R., Huang, L., and Ge, Z. (2019). 16.67% Rigid and 14.06% flexible organic solar cells enabled by ternary heterojunction strategy. *Adv. Mater.* 31:1902210. doi: 10.1002/adma.201902210

Yan, Y., Liu, X., and Wang, T. (2017). Conjugated-polymer blends for organic photovoltaics: rational control of vertical stratification for high performance. *Adv. Mater.* 29:1601674. doi: 10.1002/adma.201601674

Yuan, J., Zhang, Y., Zhou, L., Zhang, G., Yip, H.-L., Lau, T.-K., et al. (2019). Single-junction organic solar cell with over 15% efficiency using fused-ring acceptor with electron-deficient core. *Joule* 3, 1140–1151. doi: 10.1016/j.joule.2019.01.004

Zhang, Q., Yuan, X., Feng, Y., Larson, B. W., Su, G. M., Maung Maung, Y., et al. (2020). Understanding the interplay of transport-morphology-performance in PBDB-T-based polymer solar cells. *Sol. RRL* 4:1900524. doi: 10.1002/solr.201900524

Zhao, J. B., Li, Y. K., Lin, H. R., Liu, Y. H., Jiang, K., Mu, C., et al. (2015). High-efficiency non-fullerene organic solar cells enabled by a difluorobenzothiadiazole-based donor polymer combined with a properly matched small molecule acceptor. *Energy Environ. Sci.* 8, 520–525. doi: 10.1039/C4EE02990A

Zhao, W., Li, S., Yao, H., Zhang, S., Zhang, Y., Yang, B., et al. (2017). Molecular optimization enables over 13% efficiency in organic solar cells. *J. Am. Chem. Soc.* 139, 7148–7151. doi: 10.1021/jacs.7b02677

Zhao, W., Zhang, S., and Hou, J. (2016). Realizing 11.3% efficiency in fullerene-free polymer solar cells by device optimization. *Sci. China Chem.* 59, 1574–1582. doi: 10.1007/s11426-016-0198-0

Zhao, W. C., Qian, D. P., Zhang, S. Q., Li, S. S., Inganas, O., Gao, F., et al. (2016). Fullerene-free polymer solar cells with over 11% efficiency and excellent thermal stability. *Adv. Mater.* 28, 4734–4739. doi: 10.1002/adma.201600281

Zhao, X., Mi, B., Gao, Z., and Huang, W. (2011). Recent progress in the numerical modeling for organic thin film solar cells. *Sci. China Phys. Mech. Astron.* 54, 375–387. doi: 10.1007/s11433-011-4248-6

Zhu, L., Zhong, W., Qiu, C., Lyu, B., Zhou, Z., Zhang, M., et al. (2019). Aggregation-induced multilength scaled morphology enabling 11.76% efficiency in all-polymer solar cells using printing fabrication. *Adv. Mater.* 31:1902899. doi: 10.1002/adma.201902899

Conflict of Interest: The authors declare that the research was conducted in the absence of any commercial or financial relationships that could be construed as a potential conflict of interest.

frontiers in Chemistry

ORIGINAL RESEARCH
published: 21 April 2020
doi: 10.3389/fchem.2020.00302

Ternary All-Polymer Solar Cells With 8.5% Power Conversion Efficiency and Excellent Thermal Stability

Xi Liu[1,2], Chaohong Zhang[3,4], Shuting Pang[2], Ning Li[3,5], Christoph J. Brabec[3,5], Chunhui Duan[2]*, Fei Huang[2]* and Yong Cao[2]*

[1] School of Textile Materials and Engineering, Wuyi University, Jiangmen, China, [2] State Key Laboratory of Luminescent Materials and Devices, Institute of Polymer Optoelectronic Materials and Devices, South China University of Technology, Guangzhou, China, [3] Institute of Materials for Electronics and Energy Technology (i-MEET), Friedrich-Alexander-Universität Erlangen-Nürnberg, Erlangen, Germany, [4] SUSTech Academy for Advanced Interdisciplinary Studies, Southern University of Science and Technology, Shenzhen, China, [5] Helmholtz Institute Erlangen-Nürnberg for Renewable Energy (HI ERN), Erlangen, Germany

OPEN ACCESS

Edited by:
Jiangang Liu,
Shantou University, China

Reviewed by:
Erjun Zhou,
National Center for Nanoscience and Technology (CAS), China
Yuxiang Li,
Xi'an University of Science and Technology, China

***Correspondence:**
Xi Liu
liuxi_wyu@163.com
Chunhui Duan
duanchunhui@scut.edu.cn
Fei Huang
msfhuang@scut.edu.cn

Specialty section:
This article was submitted to Physical Chemistry and Chemical Physics, a section of the journal Frontiers in Chemistry

Received: 09 February 2020
Accepted: 26 March 2020
Published: 21 April 2020

Citation:
Liu X, Zhang C, Pang S, Li N, Brabec CJ, Duan C, Huang F and Cao Y (2020) Ternary All-Polymer Solar Cells With 8.5% Power Conversion Efficiency and Excellent Thermal Stability. Front. Chem. 8:302. doi: 10.3389/fchem.2020.00302

All-polymer solar cells (all-PSCs) composed of polymer donors and acceptors have attracted widespread attention in recent years. However, the broad and efficient photon utilization of polymer:polymer blend films remains challenging. In our previous work, we developed NOE10, a linear oligoethylene oxide (OE) side-chain modified naphthalene diimide (NDI)-based polymer acceptor which exhibited a power conversion efficiency (PCE) of 8.1% when blended with a wide-bandgap polymer donor PBDT-TAZ. Herein, we report a ternary all-PSC strategy of incorporating a state-of-the-art narrow bandgap polymer (PTB7-Th) into the PBDT-TAZ:NOE10 binary system, which enables 8.5% PCEs within a broad ternary polymer ratio. We further demonstrate that, compared to the binary system, the improved photovoltaic performance of ternary all-PSCs benefits from the combined effect of enhanced photon absorption, more efficient charge generation, and balanced charge transport. Meanwhile, similar to the binary system, the ternary all-PSC also shows excellent thermal stability, maintaining 98% initial PCE after aging for 300 h at 65°C. This work demonstrates that the introduction of a narrow-bandgap polymer as a third photoactive component into ternary all-PSCs is an effective strategy to realize highly efficient and stable all-PSCs.

Keywords: all-polymer solar cells, ternary solar cells, power conversion efficiency, thermal stability, Förster resonant energy transfer

INTRODUCTION

Bulk-heterojunction (BHJ) polymer solar cells (PSCs) are a promising solar-energy technology due to their low cost, easy fabrication, light weight, and mechanical flexibility (Yu et al., 1995; Thompson and Fréchet, 2008; Brabec et al., 2010; Andersen et al., 2014; Lu et al., 2015b; Huang et al., 2019). In recent years, PSCs have achieved power conversion efficiencies (PCEs) of over 16% via the development of novel photoactive materials, optimized morphological control, and improved interface and device engineering (Meng et al., 2018; An Q. et al., 2019; Chang et al., 2019; Fan et al., 2019a; Li K. et al., 2019; Yan et al., 2019; Yuan et al., 2019; Yu et al., 2019). Specifically, one important effort has been the creation of novel photoactive acceptors beyond fullerene-based acceptors, aiming to mitigate the drawbacks of fullerene-based materials such as their expensive

synthetic cost, weak optical absorption, finited bandgap, and morphological instability (Hummelen et al., 1995; Wienk et al., 2003; Cheng and Zhan, 2016). Therefore, there is increasing interest in developing and comprehending non-fullerene acceptors (Brabec et al., 2010; Nielsen et al., 2015; Kang et al., 2016; Cheng et al., 2018; Hou et al., 2018; Liu et al., 2018a; Yan et al., 2018; Yang et al., 2019b). Among these non-fullerene acceptors, polymeric electron acceptors were reported to have tunable absorption, modulable energy levels, and stable BHJ morphology (Li et al., 2014; Jung et al., 2015, 2016; Dou et al., 2016; Kang et al., 2016; Wang et al., 2017; Liu et al., 2018b; An N. et al., 2019; Yang et al., 2019a). Thus, all-polymer solar cells (all-PSCs) consisting of a polymeric donor and acceptor have attracted more and more attention and are promising for use in realizing highly efficient and stable solar cells (Kim et al., 2015; Kang et al., 2016; Liu et al., 2016, 2018b; Long et al., 2016; Wang et al., 2017; Zhang et al., 2017). Encouragingly, all-PSCs have recently achieved over 10% PCEs (Fan et al., 2017a,b, 2018, 2019b; Li et al., 2017a; Zhang et al., 2017; Chen et al., 2018; Kolhe et al., 2019; Li Z. et al., 2019; Meng et al., 2019; Yao et al., 2019; Zhu et al., 2019; Zhao et al., 2020). To date, highly efficient all-PSCs are mostly based on naphthalene diimide (NDI) polymer acceptors, because of their high electron mobility, suitable energy levels, and tunable BHJ morphology (Gao et al., 2016; Li et al., 2016; Fan et al., 2017a,b; Liu et al., 2018b). For example, poly[[*N*, *N*′-bis(2-octyldodecyl)-naphthalene-1,4,5,8-bis(dicarboximide)-2,6-diyl]-*alt*-5,5′-(2,2′-bithiophene)], is a state-of-the-art polymer acceptor with the commercial name N2200 (Yan et al., 2009; Fan et al., 2017b). However, the relatively weak absorption coefficient in near-infrared wavelengths of N2200 or its analogs prevents devices from attaining higher photocurrent responses and short-circuit current densities (J_{sc}) (Fan et al., 2017a,b; Liu et al., 2018b). State-of-the-art all-PSCs usually exhibit lower than 40% external quantum efficiencies (EQEs) in the 700–800 nm wavelength range, which offered by N2200, seriously limiting further improvement of their J_{sc} and PCE values (Fan et al., 2017a,b; Liu et al., 2018b).

Ternary all-PSCs are based on the incorporation of a third polymer component into a binary polymer: polymer blend, thereby effectively improving device efficiencies via extending and/or enhancing light absorption, manipulating energy levels, and regulating active layer morphology (Huang et al., 2017; Fu et al., 2018; Xu and Gao, 2018; Yu et al., 2018; Gasparini et al., 2019; Lee et al., 2019). Jenekhe et al. developed a ternary all-PSC with a PCE of 3.2% composed of a polymer donor and two polymer acceptors (Hwang et al., 2015). Using the same ternary approach, Ito et al. (Benten et al., 2016), Li et al. (Su et al., 2016), and Wang et al. (Li et al., 2017a) constructed efficient ternary all-PSCs by combining wide-bandgap polymers (PCDTBT, PBDD-ff4T, and PBDTTS-FTAZ, respectively), with the narrow-bandgap PTB7-Th:N2200 blend, where the wide-bandgap polymers contributed to complementary absorption and improved photocurrent, resulting in steadily increased PCEs of 6.7, 7.2, and 9.0%, respectively. Recently, Ying et al. realized several ternary all-PSCs, which achieved PCEs over 10%; the high efficiencies of these ternary all-PSCs were attributed to the complementary absorption, enhanced photo-harvesting, improved charge-carrier transportation, and inhibited recombination (Fan et al., 2018, 2019b; Li Z. et al., 2019).

Considering the future practical applications of PSCs, device stability is a significant issue beyond its contribution to high photovoltaic efficiency. Specifically, device stability issues include the oxidation of electrodes, degradation of interface layers, and intrinsic instability of photoactive layer morphology under light and thermal aging (Jørgensen et al., 2012; Cheng and Zhan, 2016; Holliday et al., 2016; Baran et al., 2017; Kim et al., 2017; Mateker and McGehee, 2017; Zhang et al., 2018b; Hu et al., 2019; Speller et al., 2019). The ternary strategy has displayed potential as a useful approach for achieving stable solar cells (Kim et al., 2017; Zhang et al., 2019b). For example, the research groups of McCulloch (Baran et al., 2017), Kim (Kim et al., 2017), and Ade (Hu et al., 2019) all demonstrated small molecule acceptor-based ternary systems with excellent thermal stabilities, mainly due to controlled crystallization and miscibility achieved through the incorporation of a third component. Moreover, we and others have demonstrated the excellent long-term and thermal stabilities of binary or tandem all-PSCs through effective material design and device engineering (Li et al., 2017b; Liu et al., 2018b; Zhang et al., 2018a,c). However, ternary all-PSCs with high efficiencies and excellent thermal stabilities have not been widely investigated (Li et al., 2017a).

Previously, we have reported a linear oligoethylene oxide (OE) side-chain modified NDI-based polymer acceptor (NOE10) which offered a high efficiency (PCE of 8.1%) and excellent long-term stability when blended with a wide-bandgap polymer donor (PBDT-TAZ) to form binary all-PSCs (Liu et al., 2018b). In this work, we further improved the efficiency of all-PSCs through the ternary strategy while maintaining excellent thermal stability beyond that of binary all-PSCs. Specifically, the ternary all-PSCs were constructed by combining a state-of-the-art narrow-bandgap polymer (PTB7-Th) into the PBDT-TAZ:NOE10 binary blend. The ternary all-PSCs enable a PCE of 8.5% within a broad ternary polymer ratio, representing an 18% improvement over the corresponding binary all-PSCs. The enhanced device performance of the ternary all-PSCs stem from the combined effects of improved photon absorption, the generation of more free charges through simultaneous charge and energy transfer, and balanced charge transport. More importantly, the ternary all-PSCs exhibit excellent thermal stability, maintaining 98% of their initial PCE after aging for 300 h at 65°C. This work demonstrates that the introduction of the state-of-the-art narrow-bandgap polymer PTB7-Th as a third photoactive component positions ternary PBDT-TAZ:PTB7-Th:NOE10 all-PSCs as highly efficient and stable all-PSCs. Further, the high performances of ternary all-PSCs within broad ternary polymer ratios offer benefits for future large-scale technological applications.

RESULTS AND DISCUSSION

Polymer Selection and Characterization

The acceptor polymer NOE10 is a linear oligoethylene oxide (OE) side-chain modified naphthalene diimide (NDI)-based polymer reported by our group previously and presented in

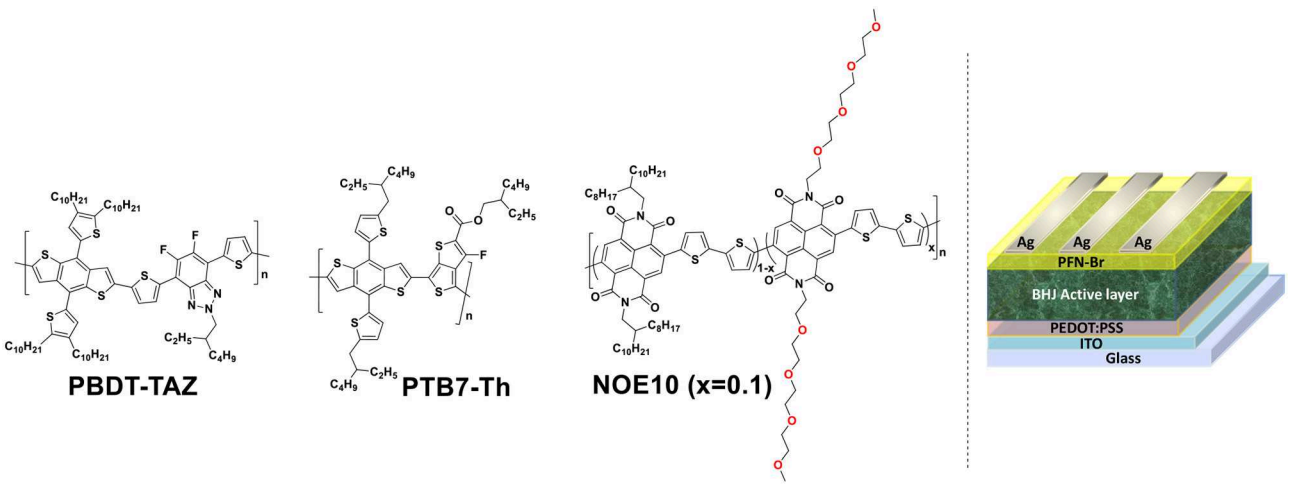

FIGURE 1 | Chemical structures of photoactive layer polymers (PBDT-TAZ, PTB7-Th, and NOE10) and the device architecture schematic diagram.

Figure 1. It can achieve a high PCE of ≈8% when used in a PBDT-TAZ:NOE10-based all-PSC due to its optimal photoactive layer morphology (Liu et al., 2018b). The donor polymer PBDT-TAZ is a wide-bandgap conjugated polymer derived from a benzodithiophene (BDT) building block and a difluorobenzotriazole (TAZ) unit with a bandgap >1.9 eV; PBDT-TAZ and its analogs have been widely applied in efficient all-PSCs demonstrated by our group and others (Li et al., 2016, 2017a; Duan et al., 2018; Liu et al., 2018b; Pang et al., 2019). Though the PBDT-TAZ:NOE10-based binary all-PSC showed a high PCE of 8.1% in our previous work, the binary blend shows weak absorption in the range of 600–800 nm, which restricts the further improvement of its quantum efficiency, J_{sc}, and PCE. The state-of-the-art narrow-bandgap polymer PTB7-Th offers high absorption coefficient in the 600–800 nm range, and is a reasonable candidate for application as the third component in a binary PBDT-TAZ:NOE10 blend to improve long-wavelength absorption. Thus, PBDT-TAZ:PTB7-Th:NOE10 blends with different ratios were applied as the photoactive layer in a ternary all-PSCs system. The ratio of PBDT-TAZ:NOE10 was fixed at 1.5:1, while the PTB7-Th content was varied to optimize the polymer ratios.

The optical absorption spectra of the photoactive layer polymers (PBDT-TAZ, PTB7-Th, and NOE10) and the corresponding blended films were shown in **Figure 2A**. The wide-bandgap donor polymer PBDT-TAZ exhibits absorption coefficients over 8×10^4 cm^{-1} in the 500–600 nm range, whereas acceptor polymer NOE10 shows relatively weak absorption coefficients in the 600–850 nm range, which limits the light-harvesting efficiency of the PBDT-TAZ:NOE10 binary blend. The narrow-bandgap polymer PTB7-Th shows high absorption coefficient in the range of 600–760 nm with a maximal absorption coefficient of 1.05×10^5 cm^{-1} at 705 nm, which complements the absorption of the binary system. The absorption spectra of the ternary blends representing different polymer ratios are shown in **Figure 2B**. As PTB7-Th content increases, the corresponding ternary blends clearly exhibit significantly enhanced absorption coefficient in the range of 650–760 nm. These results demonstrate that the introduction of PTB7-Th could improve the absorption of the ternary blend.

The electrochemical characteristic curves of the photoactive layer polymers were recorded using cyclic voltammetry (CV). Relevant CV curves are depicted in **Figure 2C**, and the calculated energy diagrams are shown in **Figure 2D**. The lowest unoccupied molecular orbital (LUMO) levels of PBDT-TAZ, PTB7-Th, and NOE10 are −2.99, −3.26, and −3.91 eV, respectively, which provide a cascading alignment for electron transfer. Meanwhile, the highest occupied molecular orbital (HOMO) levels of PBDT-TAZ, PTB7-Th, and NOE10 are −5.38, −5.29, and −5.81 eV, respectively, which indicates that the HOMO and LUMO levels of PTB7-Th fall between the HOMO and LUMO levels of PBDT-TAZ. The slightly increased HOMO level of PTB7-Th suggests that the partial holes generated from PBDT-TAZ may ultimately be transferred to the HOMO of PTB7-Th before extraction.

Photovoltaic Properties

BHJ all-PSCs based on the photoactive layer polymers PBDT-TAZ, PTB7-Th, and NOE10 were fabricated with a device structure of ITO/PEDOT:PSS/photoactive layer/PFN-Br/Ag. As shown in **Table 1**, **Figure S1** and **Table S1**, the ternary blend was optimized in terms of its detailed ternary ratio to maximize the PCE. The optimal ternary blended film was fabricated with a PBDT-TAZ:PTB7-Th:NOE10 weight ratio of 1.5:x:1 (x was set to be 0.1–1). Current density–voltage (J–V) characteristic curves and EQE curves of the champion devices using each ternary blend are exhibited in **Figures 3A,B**, and the corresponding photovoltaic parameters are listed in **Table 1**. There are a few notable results. First, the open-circuit voltage (V_{oc}) gradually decreased as the PTB7-Th content increased from 0 to 100%. The linear dependence of V_{oc} on the loading of PTB7-Th indicates that the partial holes generated from PBDT-TAZ may ultimately be transferred to the HOMO of PTB7-Th before extraction.

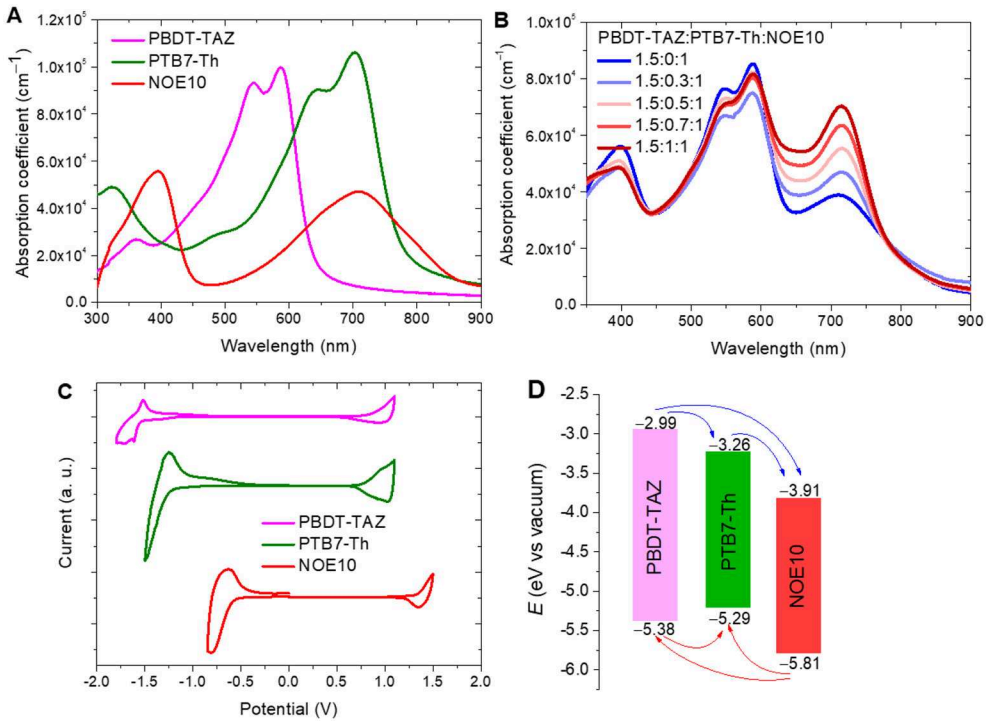

FIGURE 2 | (A) The absorption spectra of the neat polymers films (PBDT-TAZ, PTB7-Th, and NOE10); **(B)** absorption spectra of the corresponding blend films; **(C)** cyclic voltammetry curves of PBDT-TAZ, PTB7-Th, and NOE10; **(D)** calculated energy level diagram of the polymers.

Wang et al. presented a similar ternary system but reported a nearly constant V_{oc}, which may be attributable to the high weight ratio of PTB7-Th in the corresponding ternary blends (Li et al., 2017a). Second, there was a steady increase in J_{sc} as the PTB7-Th content increased from 0 to 80%, and forming a J_{sc} platform at 60–80% of PTB7-Th containing. These trends are consistent with absorption and EQE curves of the corresponding blends. The decreased J_{sc} of the 1.5:1:1 ternary ratio-based device should be due to the blend's unbalanced charge transport, which is discussed in the following sections. Third, the fill factor (FF) of the corresponding device decreased slightly with an increase of PTB7-Th, meanwhile, FF remains at a high level above 0.70 in 1.5:0:1–1.5:0.5:1 ternary ratio-based device. Our results indicate that the overall PCE can exceed 8% under a wide range of ternary ratios from 1.5:0.3:1 to 1.5:0.8:1; moreover, ternary all-PSCs with efficiency of 8.5% can be achieved with ternary ratios ranging from 1.5:0.5:1 to 1.5:0.7:1. Thus, these results suggest that the PBDT-TAZ:PTB7-Th:NOE10 ternary blend is a promising photoactive layer for use in high efficiency all-PSCs; furthermore, such ternary polymer-blend systems do not require precisely controlled ternary ratios, which increases the potential of ternary all-PSCs for use in large-scale commercial applications.

The EQE curves of the ternary all-PSCs are exhibited in **Figure 3B**. EQE responses of the corresponding ternary all-PSCs combined with absorption of the blends reflect the impact of the photoactive layer polymers on J_{sc}. Compared to all-PSCs with a ternary ratio of 1.5:0:1, the EQE response of ternary all-PSCs including PTB7-Th is significantly improved within the range of 450 to 780 nm. In particular, the all-PSCs with ternary ratios of 1.5:0.5:1, 1.5:0.7:1, and 1.5:1:1 exhibit ≈60% EQE values at 450–750 nm. The specific EQE response indicates that the PBDT-TAZ:PTB7-Th:NOE10 ternary blend offers efficient electron and hole transfer.

TABLE 1 | The detail photovoltaic properties of the devices.

D1:D2:A[a]	V_{oc} [V]	J_{sc} [mA cm^{-2}]	FF	PCE [%][b]
1.5:0:1	0.843	11.9	0.72	7.2 (7.0 ± 0.2)
1.5:0.2:1	0.821	13.1	0.73	7.8 (7.6 ± 0.2)
1.5:0.3:1	0.814	14.1	0.71	8.2 (8.1 ± 0.1)
1.5:0.4:1	0.810	14.2	0.70	8.1 (8.0 ± 0.2)
1.5:0.5:1	0.805	15.1	0.70	8.5 (8.5 ± 0.1)
1.5:0.6:1	0.803	15.5	0.68	8.4 (8.3 ± 0.2)
1.5:0.7:1	0.801	15.7	0.68	8.5 (8.5 ± 0.1)
1.5:0.8:1	0.796	15.6	0.66	8.2 (8.0 ± 0.2)
1.5:1:1	0.792	14.8	0.62	7.3 (7.2 ± 0.1)

[a]*D1 (PBDT-TAZ), D2 (PTB7-Th), A (NOE10);* [b]*the average values and standard deviations of statistics from the eight devices are given in parentheses.*

Charge Generation, Transport, and Recombination

Photoluminescence (PL) tests were conducted to analyze exciton dissociation efficiency and the energy transfer mechanism in blended films. As shown in **Figure 4A**, the PBDT-TAZ:NOE10

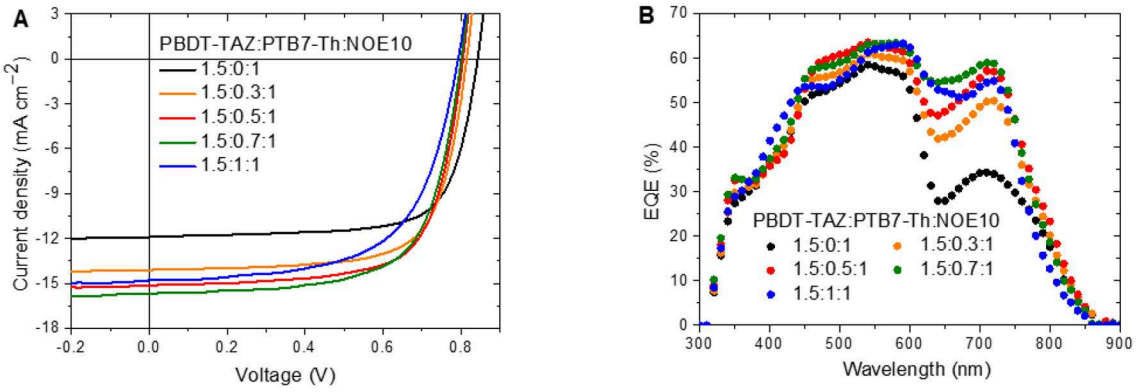

FIGURE 3 | (A) *J–V* curves of the all-PSC devices; **(B)** EQE curves of the corresponding devices.

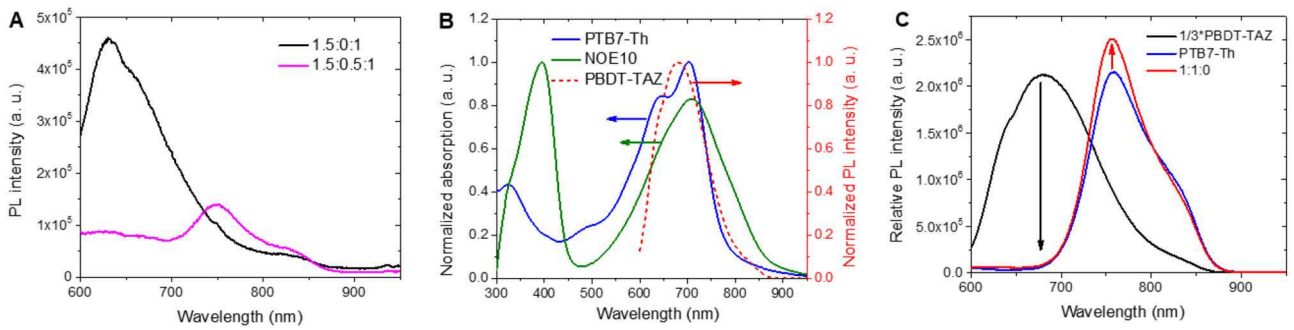

FIGURE 4 | (A) The films PL curves excited at 500 nm; **(B)** absorption spectra of pure PTB7-Th and NOE10 films, and PL curve of pure PBDT-TAZ film excited at 500 nm; **(C)** PL spectra of pure PBDT-TAZ, pure PTB7-Th, and PBDT-TAZ:PTB7-Th blended film excited at 500 nm.

binary blend (1.5:0:1) shows a PL peak at 625 nm; however the PL is completely quenched in the 600–700 nm range of the 1.5:0.5:1 ternary blend, and the slight PL signals at 700–850 nm contributed from the incomplete quenching of PTB7-Th (**Figure S2A**). This suggests that the incorporation of PTB7-Th improves exciton dissociation in the 1.5:0.5:1 ternary blend as compared to that in the 1.5:0:1 binary blend. Furthermore, to explain the more efficient exciton dissociation process in the ternary blends, we investigated the energy transfer mechanisms in the blended films with their corresponding PL spectra. As exhibited in **Figure 4B**, the PL spectrum of PBDT-TAZ strongly overlaps with the absorption range of PTB7-Th and NOE10, providing sufficient spectral overlap between the emission of the energy donor (PBDT-TAZ) and the absorption of the energy acceptor (PTB7-Th and NOE10) according to the Förster resonant energy transfer (FRET) theory, suggesting that FRET was realized from PBDT-TAZ to PTB7-Th and NOE10 (Huang et al., 2013). We further confirmed the existence of FRET of PBDT-TAZ and PTB7-Th through a PL experiment comparing pure PBDT-TAZ and PTB7-Th film with PBDT-TAZ:PTB7-Th blended film. When excited at 500 nm, the PBDT-TAZ:PTB7-Th blend exhibits a clearly higher PL peak intensity at 755 nm compared to the pure PTB7-Th film, while PBDT-TAZ's PL peak at 675 nm completely disappears in the blend (**Figure 4C**). In contrast, when excited at 700 nm, the PTB7-Th and PBDT-TAZ:PTB7-Th blended films exhibit similar PL spectra (**Figure S2B**). The PL responses evident at two different excitation wavelengths demonstrate that a FRET process occurs from PBDT-TAZ to PTB7-Th. It should be noted that there is competition between the energy transfer from PBDT-TAZ to PTB7-Th and the charge transfer from PBDT-TAZ to NOE10 in the BHJ ternary blends. As reported for several ternary solar cells, the energy and charge transfer processes often exhibit concurrency and intertwining (Lu et al., 2015a; Li et al., 2017a).

We further studied the exciton dissociation probability $P(E, T)$ of the all-PSCs (Koster et al., 2005). **Figure 5A** exhibits the photocurrent density (J_{ph}) vs. the effective voltage (V_{eff}) of the all-PSCs. The $P(E, T)$ is defined by normalizing J_{ph} with the saturation photocurrent density (J_{sat}) (Koster et al., 2005). Under the short-circuit conditions, the all-PSCs with ternary ratios of 1.5:0:1, 1.5:0.5:1, and 1.5:1:1 show $P(E, T)$ values of 93.6, 95.3, and 94.5%, respectively. The all-PSC with a ternary ratio of 1.5:0.5:1 exhibits the highest $P(E, T)$ value, further signifying that the inclusion of PTB7-Th as the third component promotes exciton dissociation in ternary devices, which is in agreement with the corresponding J_{sc} and EQE spectra.

Device photovoltaic properties, especially J_{sc} and FF values, can also be greatly impacted on charge transport properties. The

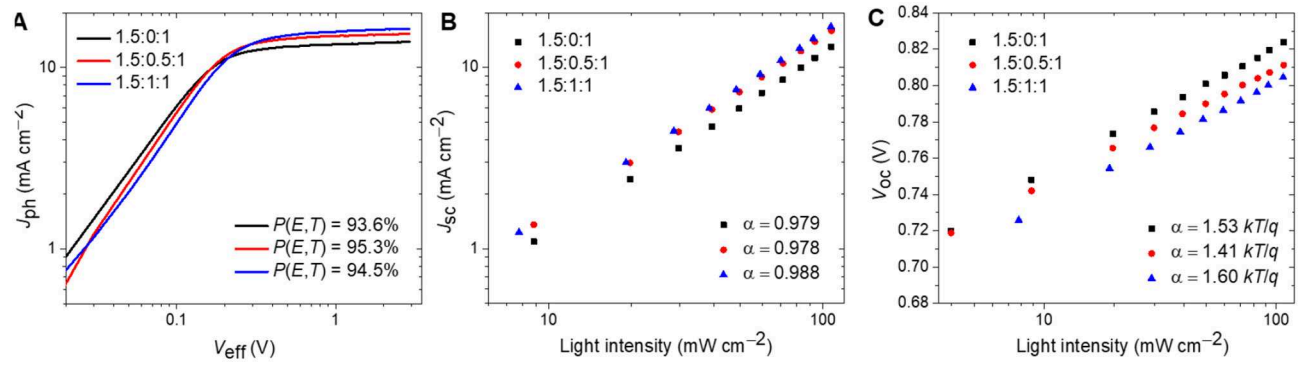

FIGURE 5 | (A) J_{ph}-V_{eff} curves of the devices; **(B)** J_{sc}-ln(P_{light}) properties of the devices; **(C)** V_{oc}-ln(P_{light}) properties of the devices.

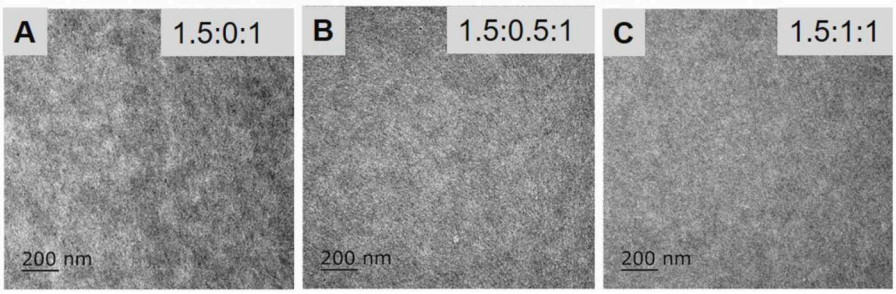

FIGURE 6 | TEM images of the blend films with PBDT-TAZ:PTB7-Th:NOE10 ternary ratios of 1.5:0:1 **(A)**, 1.5:0.5:1 **(B)**, and 1.5:1:1 **(C)**.

mobilities of the three different ternary-blended film ratios was tested and shown in **Figure S3**. The results are listed in **Table S2**. The devices with ternary ratios of 1.5:0:1, 1.5:0.5:1, and 1.5:1:1 show electron mobilities (μ_e) of 3.6×10^{-4}, 3.3×10^{-4}, and 2.4×10^{-4} cm^2 V^{-1} s^{-1}, respectively. The hole mobilities (μ_h) of these blended films are 1.9×10^{-4}, 3.2×10^{-4}, and 4.3×10^{-4} cm^2 V^{-1} s^{-1}, respectively. Correspondingly, the μ_e/μ_h ratios for blended films with ternary ratios of 1.5:0:1, 1.5:0.5:1, and 1.5:1:1 are 1.9, 1.0, and 0.6, respectively. The PBDT-TAZ:PTB7-Th:NOE10 blend with a ternary ratio of 1.5:0.5:1 offers optimally balanced electron/hole transport along with high FF (0.70) and J_{sc} (15.1 mA cm^{-2}) in all-PSCs.

Charge recombination mechanisms of the devices were investigated through measurements of the light intensity dependence of the J_{sc} and V_{oc} values. The correlation of J_{sc} and light intensity (P_{light}) obeys the power-law $J_{sc} \propto P_{light}^{\alpha}$, where α is an exponential factor that should equal 1 when all charge carriers are extracted before recombination (Cowan et al., 2010). As exhibited in **Figure 5B**, the α values of the fitted line for all-PSCs with ternary ratios of 1.5:0:1, 1.5:0.5:1, and 1.5:1:1 are 0.979, 0.978, and 0.988, respectively, indicating the negligible bimolecular recombination in these devices. The slope of the V_{oc} vs. ln(P_{light}) curve reveals the charge recombination at open circuit conditions. Trap-assisted recombination or monomolecular recombination is dominant when the slope is 2.0 kT/q, while the slope value would be equal to 1.0 kT/q when only bimolecular recombination occurs (Cowan et al., 2010). As shown in **Figure 5C**, the all-PSCs with ternary ratios of 1.5:0:1, 1.5:0.5:1, and 1.5:1:1 show a slope of 1.53 kT/q, 1.41 kT/q, and 1.60 kT/q, respectively. The all-PSC with a ternary ratio of 1.5:0.5:1 exhibits the lowest slope, suggesting the low trap-assisted recombination or monomolecular recombination of that ternary ratio device. These results are consistent with the exciton dissociation measurements, charge transport analysis, and devices photovoltaic properties.

Morphology

The morphology of the BHJ blend films was tested using transmission electron microscopy (TEM). The TEM images of the blended films with three different PTB7-Th polymer-content ratios are shown in **Figure 6**. The blended films with ternary ratios of 1.5:0:1 and 1.5:0.5:1 exhibit similarly aligned fibrillar structures which improve charge separation and transport. Meanwhile, the near-uniform film of the 1.5:1:1 blend reveals an intimately mixed nanostructure without noteworthy phase aggregation and separation. With such morphology, charge separation and transport in the 1.5:1:1 blend are impeded, resulting relatively lower J_{sc} and FF in solar cells. These morphologies may be associated with the weak crystallinity of PTB7-Th; thus, the excessive loading of PTB7-Th may obstruct BHJ morphology. Overall, the microstructural morphologies of the blended films are consistent with the J_{sc} and FF variations of

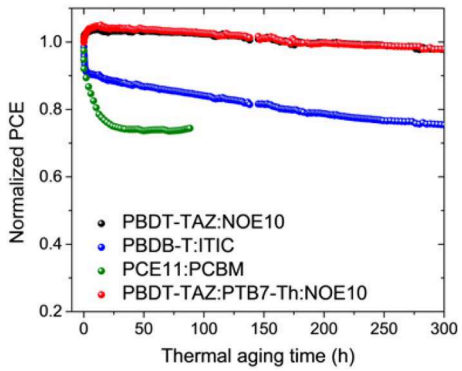

FIGURE 7 | Normalized device PCE based on PBDT-TAZ:PTB7-Th:NOE10, PBDT-TAZ:NOE10, PBDB-T:ITIC, and PCE11:PCBM over the 65°C thermal aging time.

the corresponding all-PSCs, and the J_{sc} values can be improved and the FF values maintained when the PBDT-TAZ:PTB7-Th:NOE10 ternary ratio is approximately 1.5:0.5:1.

Device Stability

In our previous work, we demonstrated the excellent long-term storage capacity and thermal stability of the PBDT-TAZ:NOE10-based binary all-PSC system (Liu et al., 2018b). Herein, we further investigated the device stability of a PBDT-TAZ:PTB7-Th:NOE10 (1.5:0.5:1)-based ternary all-PSC under continuous thermal aging and compared it with the stability of a binary all-PSC (PBDT-TAZ:NOE10) and other two highly efficient solar cells [PCE11:PCBM (Liu et al., 2014) and PBDB-T:ITIC (Zhao et al., 2016)]. The normalized performances of the devices under 65°C thermal aging are exhibited in **Figure 7**, while detailed device photovoltaic properties (V_{oc}, J_{sc}, and FF) are depicted in **Figure S4**. After 300 h of continuous thermal aging at 65°C, the ternary all-PSC (PBDT-TAZ:PTB7-Th:NOE10) device holds 98% initial PCE without burn-in efficiency loss. However, the PCE11:PCBM and PBDB-T:ITIC devices exhibit obvious burn-in efficiency losses within 10–20 h of thermal aging, and these devices exhibit markedly lower long-term stabilities, including <80% initial PCE retention for PBDB-T:ITIC devices after 300 h of aging and ≈70% initial PCE retention for PCE11:PCBM devices after 25 h of aging, which could be attributed to the instability of their BHJ microstructure morphology (Li N. et al., 2017; Du et al., 2019; Zhang et al., 2019a). As in the PBDT-TAZ:NOE10 binary devices, the burn-in-free feature of the ternary devices can be attributed to the stable blend morphology (Li N. et al., 2017). All-PSCs based on NOE10 polymer acceptors, including both binary and ternary systems, show excellent long-term thermal stability. This demonstrates that NOE10 shows significant promise as an electron acceptor for practical applications in the field of PSCs.

CONCLUSION

In conclusion, we have demonstrated an efficient approach to ternary all-PSCs construction by incorporating a state-of-the-art narrow-bandgap polymer, PTB7-Th, as the third component within a PBDT-TAZ:NOE10 binary system. The ternary all-PSCs achieve 8.5% PCEs within broad PTB7-Th-content ratios, representing an 18% improvement over binary all-PSCs. Compared to the binary system, the improved photovoltaic performance of ternary all-PSCs reflect the combined strengths of enhanced photon absorption, increased free charges generated through simultaneous charge and energy transfer, and balanced charge transport. Moreover, like the binary system, the ternary all-PSCs also show excellent thermal stability, maintaining 98% of their initial PCE after aging for 300 h at 65°C. This work demonstrates that the introduction of PTB7-Th as the third photoactive component in ternary PBDT-TAZ:PTB7-Th:NOE10 all-PSC construction is an effective strategy for realizing highly efficient and stable all-PSCs. It also suggests the strong potential of NOE10 as an acceptor polymer for future large-scale technological applications in both binary and ternary all-PSCs.

DATA AVAILABILITY STATEMENT

All datasets generated for this study are included in the article/**Supplementary Material**.

AUTHOR CONTRIBUTIONS

XL conceived the idea, synthesized and characterized the polymer acceptor, performed the fabrication of solar cells and data analysis, and collected TEM images. CZ performed the thermal stability experiments of the devices supervised by NL and CB. SP performed the SCLC experiments. XL and CD prepared the manuscript. All authors commented on the manuscript. CD, FH, and YC supervised the project.

FUNDING

This work was supported by the Ministry of Science and Technology (2019YFA0705900 and 2017YFA0206600), the National Natural Science Foundation of China (21875072 and 21520102006), and the Fundamental Research Funds for Central Universities of South China University of Technology. This work was also financially supported by the scientific research startup funds for high-level talents of Wuyi University (AL2019003), the Natural Science Foundation of Guangdong Province (nos. 2019A1515110944 and 2019A1515010848), and the Youth Innovation Talent Project for the Universities of Guangdong Province (Grant: 2019KQNCX161). NL and CB gratefully acknowledge the financial support through the Aufbruch Bayern initiative of the state of Bavaria (EnCN and Solar Factory of the Future), the Bavarian Initiative Solar Technologies go Hybrid (SolTech) and the SFB 953 (DFG, project No. 182849149).

SUPPLEMENTARY MATERIAL

The Supplementary Material for this article can be found online at: https://www.frontiersin.org/articles/10.3389/fchem.2020.00302/full#supplementary-material

REFERENCES

An, N., Ran, H., Geng, Y., Zeng, Q., Hu, J., Yang, J., et al. (2019). Exploring a fused 2-(thiophen-2-yl)thieno[3, 2-b]thiophene (T-TT) building block to construct n-type polymer for high-performance all-polymer solar cells. *ACS Appl. Mater. Interfaces* 11, 42412–42419. doi: 10.1021/acsami.9b12814

An, Q., Ma, X., Gao, J., and Zhang, F. (2019). Solvent additive-free ternary polymer solar cells with 16.27% efficiency. *Sci. Bull.* 64, 504–506. doi: 10.1016/j.scib.2019.03.024

Andersen, T. R., Dam, H. F., Hösel, M., Helgesen, M., Carlé, J. E., Larsen-Olsen, T. T., et al. (2014). Scalable, ambient atmosphere roll-to-roll manufacture of encapsulated large area, flexible organic tandem solar cell modules. *Energy Environ. Sci.* 7, 2925–2933. doi: 10.1039/c4ee01223b

Baran, D., Ashraf, R. S., Hanifi, D. A., Abdelsamie, M., Gasparini, N., Röhr, J. A., et al. (2017). Reducing the efficiency–stability–cost gap of organic photovoltaics with highly efficient and stable small molecule acceptor ternary solar cells. *Nat. Mater.* 16, 363–369. doi: 10.1038/nmat4797

Benten, H., Nishida, T., Mori, D., Xu, H., Ohkita, H., and Ito, S. (2016). High-performance ternary blend all-polymer solar cells with complementary absorption bands from visible to near-infrared wavelengths. *Energy Environ. Sci.* 9, 135–140. doi: 10.1039/c5ee03460d

Brabec, C. J., Gowrisanker, S., Halls, J. J., Laird, D., Jia, S., and Williams, S. P. (2010). Polymer–fullerene bulk-heterojunction solar cells. *Adv. Mater.* 22, 3839–3856. doi: 10.1002/adma.200903697

Chang, Y., Lau, T. K., Pan, M. A., Lu, X., Yan, H., and Zhan, C. (2019). The synergy of host–guest nonfullerene acceptors enables 16%-efficiency polymer solar cells with increased open-circuit voltage and fill-factor. *Mater. Horiz.* 6, 2094–2102. doi: 10.1039/c9mh00844f

Chen, D., Yao, J., Chen, L., Yin, J., Lv, R., Huang, B., et al. (2018). Dye-incorporated polynaphthalenediimide acceptor for additive-free high-performance all-polymer solar cells. *Angew. Chem. Int. Ed.* 57, 4580–4584. doi: 10.1002/anie.201800035

Cheng, P., Li, G., Zhan, X., and Yang, Y. (2018). Next-generation organic photovoltaics based on non-fullerene acceptors. *Nat. Photon.* 12, 131–142. doi: 10.1038/s41566-018-0104-9

Cheng, P., and Zhan, X. (2016). Stability of organic solar cells: challenges and strategies. *Chem. Soc. Rev.* 45, 2544–2582. doi: 10.1039/c5cs00593k

Cowan, S. R., Roy, A., and Heeger, A. J. (2010). Recombination in polymer-fullerene bulk heterojunction solar cells. *Phys. Rev. B* 82:245207. doi: 10.1103/PhysRevB.82.245207

Dou, C., Long, X., Ding, Z., Xie, Z., Liu, J., and Wang, L. (2016). An electron-deficient building block based on the B←N unit: an electron acceptor for all-polymer solar cells. *Angew. Chem. Int. Ed.* 55, 1436–1440. doi: 10.1002/anie.201508482

Du, X., Heumueller, T., Gruber, W., Classen, A., Unruh, T., Li, N., et al. (2019). Efficient polymer solar cells based on non-fullerene acceptors with potential device lifetime approaching 10 years. *Joule* 3, 215–226. doi: 10.1016/j.joule.2018.09.001

Duan, C., Li, Z., Pang, S., Zhu, Y. L., Lin, B., Colberts, F. J., et al. (2018). Improving performance of all-polymer solar cells through backbone engineering of both donors and acceptors. *Sol. RRL* 2:1800247. doi: 10.1002/solr.201800247

Fan, B., Ying, L., Wang, Z., He, B., Jiang, X. F., Huang, F., et al. (2017a). Optimisation of processing solvent and molecular weight for the production of green-solvent-processed all-polymer solar cells with a power conversion efficiency over 9%. *Energy Environ. Sci.* 10, 1243–1251. doi: 10.1039/c7ee00619e

Fan, B., Ying, L., Zhu, P., Pan, F., Liu, F., Chen, J., et al. (2017b). All-polymer solar cells based on a conjugated polymer containing siloxane-functionalized side chains with efficiency over 10%. *Adv. Mater.* 29:1703906. doi: 10.1002/adma.201703906

Fan, B., Zhang, D., Li, M., Zhong, W., Zeng, Z., Ying, L., et al. (2019a). Achieving over 16% efficiency for single-junction organic solar cells. *Sci. China Chem.* 62, 746–752. doi: 10.1007/s11426-019-9457-5

Fan, B., Zhong, W., Ying, L., Zhang, D., Li, M., Lin, Y., et al. (2019b). Surpassing the 10% efficiency milestone for 1-cm^2 all-polymer solar cells. *Nat. Commun.* 10:4100. doi: 10.1038/s41467-019-12132-6

Fan, B., Zhu, P., Xin, J., Li, N., Ying, L., Zhong, W., et al. (2018). High-performance thick-film all-polymer solar cells created via ternary blending of a novel wide-bandgap electron-donating copolymer. *Adv. Energy Mater.* 8:1703085. doi: 10.1002/aenm.201703085

Fu, H., Wang, Z., and Sun, Y. (2018). Advances in non-fullerene acceptor based ternary organic solar cells. *Sol. RRL* 2:1700158. doi: 10.1002/solr.201700158

Gao, L., Zhang, Z. G., Xue, L., Min, J., Zhang, J., Wei, Z., et al. (2016). All-polymer solar cells based on absorption-complementary polymer donor and acceptor with high power conversion efficiency of 8.27%. *Adv. Mater.* 28, 1884–1890. doi: 10.1002/adma.201504629

Gasparini, N., Salleo, A., McCulloch, I., and Baran, D. (2019). The role of the third component in ternary organic solar cells. *Nat. Rev. Mater.* 4:229. doi: 10.1038/s41578-019-0093-4

Holliday, S., Ashraf, R. S., Wadsworth, A., Baran, D., Yousaf, S. A., Nielsen, C. B., et al. (2016). High-efficiency and air-stable P3HT-based polymer solar cells with a new non-fullerene acceptor. *Nat. Commun.* 7:11585. doi: 10.1038/ncomms11585

Hou, J., Inganäs, O., Friend, R. H., and Gao, F. (2018). Organic solar cells based on non-fullerene acceptors. *Nat. Mater.* 17, 119–128. doi: 10.1038/nmat5063

Hu, H., Ye, L., Ghasemi, M., Balar, N., Rech, J. J., Stuard, S. J., et al. (2019). Highly efficient, stable, and ductile ternary non-fullerene organic solar cells from a two-donor polymer blend. *Adv. Mater.* 31:1808279. doi: 10.1002/adma.201808279

Huang, F., Bo, Z. S., Geng, Y. H., Wang, X. H., Wang, L. X., Ma, Y. G., et al. (2019). Study on optoelectronic polymers: an overview and outlook. *Acta Polym. Sin.* 50, 988–1046. doi: 10.11777/j.issn1000-3304.2019.19110

Huang, H., Yang, L., and Sharma, B. (2017). Recent advances in organic ternary solar cells. *J. Mater. Chem. A* 5, 11501–11517. doi: 10.1039/c7ta00887b

Huang, J. S., Goh, T., Li, X., Sfeir, M. Y., Bielinski, E. A., Tomasulo, S., et al. (2013). Polymer bulk heterojunction solar cells employing förster resonance energy transfer. *Nat. Photonics* 7, 479–485. doi: 10.1038/nphoton.2013.82

Hummelen, J. C., Knight, B. W., LePeq, F., Wudl, F., Yao, J., and Wilkins, C. L. (1995). Preparation and characterization of fulleroid and methanofullerene derivatives. *J. Org. Chem.* 60, 532–538. doi: 10.1021/jo00108a012

Hwang, Y. J., Courtright, B. A., and Jenekhe, S. A. (2015). Ternary blend all-polymer solar cells: enhanced performance and evidence of parallel-like bulk heterojunction mechanism. *MRS Commun.* 5, 229–234. doi: 10.1557/mrc.2015.36

Jørgensen, M., Norrman, K., Gevorgyan, S. A., Tromholt, T., Andreasen, B., and Krebs, F. C. (2012). Stability of polymer solar cells. *Adv. Mater.* 24, 580–612. doi: 10.1002/adma.201104187

Jung, J., Lee, W., Lee, C., Ahn, H., and Kim, B. J. (2016). Controlling molecular orientation of naphthalenediimide-based polymer acceptors for high performance all-polymer solar cells. *Adv. Energy Mater.* 6:1600504. doi: 10.1002/aenm.201600504

Jung, J. W., Jo, J. W., Chueh, C. C., Liu, F., Jo, W. H., Russell, T. P., et al. (2015). Fluoro-substituted n-type conjugated polymers for additive-free all-polymer bulk heterojunction solar cells with high power conversion efficiency of 6.71%. *Adv. Mater.* 27, 3310–3317. doi: 10.1002/adma.201501214

Kang, H., Lee, W., Oh, J., Kim, T., Lee, C., and Kim, B. J. (2016). From fullerene–polymer to all-polymer solar cells: the importance of molecular packing, orientation, and morphology control. *Acc. Chem. Res.* 49, 2424–2434. doi: 10.1021/acs.accounts.6b00347

Kim, T., Choi, J., Kim, H. J., Lee, W., and Kim, B. J. (2017). Comparative study of thermal stability, morphology, and performance of all-polymer, fullerene–polymer, and ternary blend solar cells based on the same polymer donor. *Macromolecules* 50, 6861–6871. doi: 10.1021/acs.macromol.7b00834

Kim, T., Kim, J. H., Kang, T. E., Lee, C., Kang, H., Shin, M., et al. (2015). Flexible, highly efficient all-polymer solar cells. *Nat. Commun.* 6:8547. doi: 10.1038/ncomms9547

Kolhe, N. B., Tran, D. K., Lee, H., Kuzuhara, D., Yoshimoto, N., Koganezawa, T., et al. (2019). New random copolymer acceptors enable additive-free processing of 10.1% efficient all-polymer solar cells with near-unity internal quantum efficiency. *ACS Energy Lett.* 4, 1162–1170. doi: 10.1021/acsenergylett.9b00460

Koster, L. J., Smits, E. C. P., Mihailetchi, V. D., and Blom, P. W. M. (2005). Device model for the operation of polymer/fullerene bulk heterojunction solar cells. *Phys. Rev. B* 72:085205. doi: 10.1103/PhysRevB.72.085205

Lee, J., Lee, S. M., Chen, S., Kumari, T., Kang, S. H., Cho, Y., et al. (2019). Organic photovoltaics with multiple donor–acceptor pairs. *Adv. Mater.* 31:1804762. doi: 10.1002/adma.201804762

Li, K., Wu, Y., Tang, Y., Pan, M. A., Ma, W., Fu, H., et al. (2019). Ternary blended fullerene-free polymer solar cells with 16.5% efficiency enabled with a higher-LUMO-level acceptor to improve film morphology. *Adv. Energy Mater.* 9:1901728. doi: 10.1002/aenm.201901728

Li, N., Perea, J. D., Kassar, T., Richter, M., Heumueller, T., Matt, G. J., et al. (2017). Abnormal strong burn-in degradation of highly efficient polymer solar cells caused by spinodal donor-acceptor demixing. *Nat. Commun.* 8:14541. doi: 10.1038/ncomms14541

Li, W., Roelofs, W. C., Turbiez, M., Wienk, M. M., and Janssen, R. A. (2014). Polymer solar cells with diketopyrrolopyrrole conjugated polymers as the electron donor and electron acceptor. *Adv. Mater.* 26, 3304–3309. doi: 10.1002/adma.201305910

Li, Z., Xu, X., Zhang, W., Meng, X., Genene, Z., Ma, W., et al. (2017a). 9.0% power conversion efficiency from ternary all-polymer solar cells. *Energy Environ. Sci.* 10, 2212–2221. doi: 10.1039/c7ee01858d

Li, Z., Xu, X., Zhang, W., Meng, X., Ma, W., Yartsev, A., et al. (2016). High performance all-polymer solar cells by synergistic effects of fine-tuned crystallinity and solvent annealing. *J. Am. Chem. Soc.* 138, 10935–10944. doi: 10.1021/jacs.6b04822

Li, Z., Zhang, W., Xu, X., Genene, Z., di Carlo Rasi, D., Mammo, W., et al. (2017b). High-performance and stable all-polymer solar cells using donor and acceptor polymers with complementary absorption. *Adv. Energy Mater.* 7:1602722. doi: 10.1002/aenm.201602722

Li, Z., Zhong, W., Ying, L., Liu, F., Li, N., Huang, F., et al. (2019). Morphology optimization via molecular weight tuning of donor polymer enables all-polymer solar cells with simultaneously improved performance and stability. *Nano Energy*. 64:103931. doi: 10.1016/j.nanoen.2019.103931

Liu, S., Kan, Z., Thomas, S., Cruciani, F., Brédas, J. L., and Beaujuge, P. M. (2016). Thieno[3, 4-c]pyrrole-4, 6-dione-3, 4-difluorothiophene polymer acceptors for efficient all-polymer bulk heterojunction solar cells. *Angew. Chem. Int. Ed.* 55, 12996–13000. doi: 10.1002/anie.201604307

Liu, X., Xie, B., Duan, C., Wang, Z., Fan, B., Zhang, K., et al. (2018a). A high dielectric constant non-fullerene acceptor for efficient bulk-heterojunction organic solar cells. *J. Mater. Chem. A* 6, 395–403. doi: 10.1039/c7ta10136h

Liu, X., Zhang, C., Duan, C., Li, M., Hu, Z., Wang, J., et al. (2018b). Morphology optimization via side chain engineering enables all-polymer solar cells with excellent fill factor and stability. *J. Am. Chem. Soc.* 140, 8934–8943. doi: 10.1021/jacs.8b05038

Liu, Y., Zhao, J., Li, Z., Mu, C., Ma, W., Hu, H., et al. (2014). Aggregation and morphology control enables multiple cases of high-efficiency polymer solar cells. *Nat. Commun.* 5:5293. doi: 10.1038/ncomms6293

Long, X., Ding, Z., Dou, C., Zhang, J., Liu, J., and Wang, L. (2016). Polymer acceptor based on double B←N bridged bipyridine (BNBP) unit for high-efficiency all-polymer solar cells. *Adv. Mater.* 28, 6504–6508. doi: 10.1002/adma.201601205

Lu, L., Kelly, M. A., You, W., and Yu, L. (2015a). Status and prospects for ternary organic photovoltaics. *Nat. Photonics* 9, 491–500. doi: 10.1038/nphoton.2015.128

Lu, L., Zheng, T., Wu, Q., Schneider, A. M., Zhao, D., and Yu, L. (2015b). Recent advances in bulk heterojunction polymer solar cells. *Chem. Rev.* 115, 12666–12731. doi: 10.1021/acs.chemrev.5b00098

Mateker, W. R., and McGehee, M. D. (2017). Progress in understanding degradation mechanisms and improving stability in organic photovoltaics. *Adv. Mater.* 29:1603940. doi: 10.1002/adma.201603940

Meng, L., Zhang, Y., Wan, X., Li, C., Zhang, X., Wang, Y., et al. (2018). Organic and solution-processed tandem solar cells with 17.3% efficiency. *Science* 361, 1094–1098. doi: 10.1126/science.aat2612

Meng, Y., Wu, J., Guo, X., Su, W., Zhu, L., Fang, J., et al. (2019). 11.2% Efficiency all-polymer solar cells with high open-circuit voltage. *Sci. China Chem.* 62, 845–850. doi: 10.1007/s11426-019-9466-6

Nielsen, C. B., Holliday, S., Chen, H. Y., Cryer, S. J., and McCulloch, I. (2015). Non-fullerene electron acceptors for use in organic solar cells. *Acc. Chem. Res.* 48, 2803–2812. doi: 10.1021/acs.accounts.5b00199

Pang, S., Zhang, R., Duan, C., Zhang, S., Gu, X., Liu, X., et al. (2019). Alkyl chain length effects of polymer donors on the morphology and device performance of polymer solar cells with different acceptors. *Adv. Energy Mater.* 9:1901740. doi: 10.1002/aenm.201901740

Speller, E. M., Clarke, A. J., Luke, J., Lee, H. K. H., Durrant, J. R., Li, N., et al. (2019). From fullerene acceptors to non-fullerene acceptors: prospects and challenges in the stability of organic solar cells. *J. Mater. Chem. A* 7, 23361–23377. doi: 10.1039/C9TA05235F

Su, W., Fan, Q., Guo, X., Guo, B., Li, W., Zhang, Y., et al. (2016). Efficient ternary blend all-polymer solar cells with a polythiophene derivative as a hole-cascade material. *J. Mater. Chem. A* 4, 14752–14760. doi: 10.1039/c6ta05932e

Thompson, B. C., and Fréchet, J. M. (2008). Polymer–fullerene composite solar cells. *Angew. Chem. Int. Ed.* 47, 58–77. doi: 10.1002/anie.200702506

Wang, Y., Yan, Z., Guo, H., Uddin, M. A., Ling, S., Zhou, X., et al. (2017). Effects of bithiophene imide fusion on the device performance of organic thin-film transistors and all-polymer solar cells. *Angew. Chem. Int. Ed.* 56, 15304–15308. doi: 10.1002/anie.201708421

Wienk, M. M., Kroon, J. M., Verhees, W. J., Knol, J., Hummelen, J. C., van Hal, P. A., et al. (2003). Efficient methano [70]fullerene/MDMO-PPV bulk heterojunction photovoltaic cells. *Angew. Chem. Int. Ed.* 42, 3371–3375. doi: 10.1002/anie.200351647

Xu, W., and Gao, F. (2018). The progress and prospects of non-fullerene acceptors in ternary blend organic solar cells. *Mater. Horiz.* 5, 206–221. doi: 10.1039/c7mh00958e

Yan, C., Barlow, S., Wang, Z., Yan, H., Jen, A. K. Y., Marder, S. R., et al. (2018). Non-fullerene acceptors for organic solar cells. *Nat. Rev. Mater.* 3:18003. doi: 10.1038/natrevmats.2018.3

Yan, H., Chen, Z., Zheng, Y., Newman, C., Quinn, J. R., Dötz, F., et al. (2009). A high-mobility electron-transporting polymer for printed transistors. *Nature* 457, 679-689. doi: 10.1038/nature07727

Yan, T., Song, W., Huang, J., Peng, R., Huang, L., and Ge, Z. (2019). 16.67% rigid and 14.06% flexible organic solar cells enabled by ternary heterojunction strategy. *Adv. Mater.* 31:1902210. doi: 10.1002/adma.201902210

Yang, J., An, N., Sun, S., Sun, X., Nakano, M., Takimiya, K., et al. (2019a). The effect of alkyl chain branching positions on the electron mobility and photovoltaic performance of naphthodithiophene diimide (NDTI)-based polymers. *Sci. China Chem.* 62, 1649–1655. doi: 10.1007/s11426-019-9645-1

Yang, J., Xiao, B., Tang, A., Li, J., Wang, X., and Zhou, E. (2019b). Aromatic-diimide-based n-type conjugated polymers for all-polymer solar cell applications. *Adv. Mater.* 31:1804699. doi: 10.1002/adma.201804699

Yao, H., Bai, F., Hu, H., Arunagiri, L., Zhang, J., Chen, Y., et al. (2019). Efficient all-polymer solar cells based on a new polymer acceptor achieving 10.3% power conversion efficiency. *ACS Energy Lett.* 4, 417–422. doi: 10.1021/acsenergylett.8b02114

Yu, G., Gao, J., Hummelen, J. C., Wudl, F., and Heeger, A. J. (1995). Polymer photovoltaic cells: enhanced efficiencies via a network of internal donor-acceptor heterojunctions. *Science* 270, 1789–1791. doi: 10.1126/science.270.5243.1789

Yu, R., Yao, H., Cui, Y., Hong, L., He, C., and Hou, J. (2019). Improved charge transport and reduced nonradiative energy loss enable over 16% efficiency in ternary polymer solar cells. *Adv. Mater.* 31:1902302. doi: 10.1002/adma.201902302

Yu, R., Yao, H., and Hou, J. (2018). Recent progress in ternary organic solar cells based on nonfullerene acceptors. *Adv. Energy Mater.* 8:1702814. doi: 10.1002/aenm.201702814

Yuan, J., Zhang, Y., Zhou, L., Zhang, G., Yip, H. L., Lau, T. K., et al. (2019). Single-junction organic solar cell with over 15% efficiency using fused-ring acceptor with electron-deficient core. *Joule* 3, 1140–1151. doi: 10.1016/j.joule.2019.01.004

Zhang, C., Heumueller, T., Gruber, W., Almora, O., Du, X., Ying, L., et al. (2019a). Comprehensive investigation and analysis of bulk-heterojunction microstructure of high-performance PCE11: PCBM solar cells. *ACS Appl. Mater. Interfaces* 11, 18555–18563. doi: 10.1021/acsami.8b22539

Zhang, C., Heumueller, T., Leon, S., Gruber, W., Burlafinger, K., Tang, X., et al. (2019b). A top-down strategy identifying molecular phase stabilizers to overcome microstructure instabilities in organic solar cells. *Energy Environ. Sci.* 12, 1078–1087. doi: 10.1039/C8EE03780A

Zhang, K., Xia, R., Fan, B., Liu, X., Wang, Z., Dong, S., et al. (2018a). 11.2% all-polymer tandem solar cells with simultaneously improved efficiency and stability. *Adv. Mater.* 30:1803166. doi: 10.1002/adma.201803166

Zhang, L., Lin, B., Hu, B., Xu, X., and Ma, W. (2018b). Blade-cast nonfullerene organic solar cells in air with excellent morphology, efficiency, and stability. *Adv. Mater.* 30:1800343. doi: 10.1002/adma.201800343

Zhang, Y., Xu, Y., Ford, M. J., Li, F., Sun, J., Ling, X., et al. (2018c). Thermally stable all-polymer solar cells with high tolerance on blend ratios. *Adv. Energy Mater.* 8:1800029. doi: 10.1002/aenm.201800029

Zhang, Z. G., Yang, Y., Yao, J., Xue, L., Chen, S., Li, X., et al. (2017). Constructing a strongly absorbing low-bandgap polymer acceptor for high-performance all-polymer solar cells. *Angew. Chem. Int. Ed.* 56, 13503–13507. doi: 10.1002/anie.201707678

Zhao, R., Wang, N., Yu, Y., and Liu, J. (2020). Organoboron polymer for 10% efficiency all-polymer solar cells. *Chem. Mater.* 3, 1308–1314. doi: 10.1021/acs.chemmater.9b04997

Zhao, W., Qian, D., Zhang, S., Li, S., Inganäs, O., Gao, F., et al. (2016). Fullerene-free polymer solar cells with over 11% efficiency and excellent thermal stability. *Adv. Mater.* 28, 4734–4739. doi: 10.1002/adma.201600281

Zhu, L., Zhong, W., Qiu, C., Lyu, B., Zhou, Z., Zhang, M., et al. (2019). Aggregation-induced multilength scaled morphology enabling 11.76% efficiency in all-polymer solar cells using printing fabrication. *Adv. Mater.* 31:1902899. doi: 10.1002/adma.201902899

Conflict of Interest: The authors declare that the research was conducted in the absence of any commercial or financial relationships that could be construed as a potential conflict of interest.

frontiers in Chemistry

ORIGINAL RESEARCH
published: 28 April 2020
doi: 10.3389/fchem.2020.00329

All-Small-Molecule Organic Solar Cells Based on a Fluorinated Small Molecule Donor With High Open-Circuit Voltage of 1.07 V

Chunyan Liu[1], Nailiang Qiu[1], Yanna Sun[2], Xin Ke[2], Hongtao Zhang[2], Chenxi Li[2], Xiangjian Wan[2]* and Yongsheng Chen[2]*

[1] Department of Chemistry and Chemical Engineering, Jining University, Qufu, China, [2] The Centre of Nanoscale Science and Technology and Key Laboratory of Functional Polymer Materials, Renewable Energy Conversion and Storage Center (RECAST), College of Chemistry, Nankai University, Tianjin, China

OPEN ACCESS

Edited by:
Ergang Wang,
Chalmers University of Technology, Sweden

Reviewed by:
Zhiguo Zhang,
Beijing University of Chemical Technology, China
Erjun Zhou,
National Center for Nanoscience and Technology (CAS), China

***Correspondence:**
Nailiang Qiu
nlqiu@jnxy.edu.cn
Xiangjian Wan
xjwan@nankai.edu.cn

Specialty section:
This article was submitted to Physical Chemistry and Chemical Physics, a section of the journal Frontiers in Chemistry

Received: 11 February 2020
Accepted: 31 March 2020
Published: 28 April 2020

Citation:
Liu C, Qiu N, Sun Y, Ke X, Zhang H, Li C, Wan X and Chen Y (2020) All-Small-Molecule Organic Solar Cells Based on a Fluorinated Small Molecule Donor With High Open-Circuit Voltage of 1.07 V. Front. Chem. 8:329. doi: 10.3389/fchem.2020.00329

A new small molecule donor with an acceptor-donor-acceptor (A-D-A) structure, namely DRTB-FT, has been designed and synthesized for all-small-molecule organic solar cells (ASM-OSCs). By introducing fluorine atoms on the thienyl substituent of the central benzodithiophene unit, DRTB-FT shows a low-lying highest occupied molecular orbital (HOMO) energy level of −5.64 eV. Blending with an A-D-A type acceptor F-2Cl, DRTB-FT based ASM-OSCs gave a power conversion efficiency (PCE) of 7.66% with a high open-circuit voltage (V_{OC}) of 1.070 V and a low energy loss of 0.47 eV. The results indicate that high V_{OC} of ASM-OSC devices can be obtained through careful donor molecular optimization.

Keywords: all-small-molecule organic solar cell, small molecule donor, small molecule acceptor, high open-circuit voltage, energy level control

INTRODUCTION

With the advantages of flexibility, light weight, roll to roll production and etc., bulk heterojunction (BHJ) organic solar cells (OSCs) have drawn extensive attention (Heeger, 2010; Qiu et al., 2017; Zhao F. et al., 2017; Cheng et al., 2018; Sun Y. et al., 2019). Significant progress has been obtained in the past decade, benefiting from the efforts in new material design and device optimization (Zhang Q. et al., 2014; He et al., 2015; Kan et al., 2015; Li Y. et al., 2018). Recently, non-fullerene acceptors (NFAs), especially acceptor-donor-acceptor (A-D-A) type small molecule acceptors, have demonstrated great success in OSCs due to the merits of facile synthesis, controllable absorption and fine-tuned energy levels (Lin et al., 2016; Zhao W. et al., 2017; Li T. et al., 2018; Zhang et al., 2018; Cui et al., 2019; Yuan et al., 2019).

From the perspective of donor materials, NFA based OSCs consist of polymer solar cells and small-molecule solar cells. Using polymer donor materials, both single junction and tandem OSCs have achieved the impressive power conversion efficiencies (PCEs) of 15–18% (Meng et al., 2018; An et al., 2019; Fan et al., 2019; Jiang et al., 2019; Lin et al., 2019; Sun H. et al., 2019; Wu Y. et al., 2019; Xiong et al., 2019; Yan et al., 2019). So far, all-small-molecule OSCs (ASM-OSCs), i.e., devices based on both small molecule donor and acceptor, have shown relatively lower performance compared with that of polymer donor based devices (Zhang Q. et al., 2014; Kan et al., 2015; Badgujar et al., 2016; Yang et al., 2017; Privado et al., 2018; Wang et al., 2018a; Duan et al., 2019). Nevertheless, with the advantages of versatile molecules design, less variation among

different batches and thus easiness of property control for small molecules, ASM-OSCs are strongly believed to have the potential to achieve and even surpass the performance of polymer donor counterparts (Chen et al., 2013). To date, with the extensive study of small molecular design and device optimization for ASM-OSCs, the PCEs over 10% have been achieved (Bin et al., 2018; Wang et al., 2018a,b; Chen et al., 2019; Cheng et al., 2019; Gao et al., 2019; Ge et al., 2019; Wu H. et al., 2019; Yue et al., 2019; Zhou et al., 2019). Notably, a PCE over 14% has been obtained just recently by Wei et al. indicating the great potential of ASM-OSCs (Zhou et al., 2019).

Presently, compared with the comprehensive study of small molecule NFA, less attention has been paid to small molecule donors, which in fact play a vital role same as acceptors in OSCs. Among many properties that should be considered for designing active layer materials, matched energy levels between donor and acceptor not only contribute to charge transfer and exciton separation, but also have great influence on the open-circuit voltage (V_{oc}) of OSC devices (Tang et al., 2017, 2019). Therefore, it is important to efficiently tune energy levels for designing active layer molecules. Among various strategies for tuning the energy level, introducing fluorine atoms into the designing molecule has been proved to be a simple way to downshift the frontier molecular orbital energy level, which has been used successfully in molecular design (Tang et al., 2018; Chen et al., 2019; Ge et al., 2019; Wu H. et al., 2019; Yue et al., 2019), e.g., PM6, a well-known polymer donor synthesized by Hou's group (Li W. et al., 2018). Recently, we have reported an ASM-OSC based on a non-fluorinated donor DRTB-T and an acceptor F-2Cl, showing a PCE of 10.76%, but a relatively lower V_{oc} of 0.969 V compared with other ASM-OSCs (Wang et al., 2018b). With these considerations, we have designed and synthesized a new small molecule donor with an A-D-A structure, namely DRTB-FT (as shown in **Figure 1A**), in which fluorine atoms are introduced on the thienyl substituent of central benzodithiophene (BDT) unit (Zhang and Li, 2014). As expected, DRTB-FT shows a lower highest occupied molecular orbital (HOMO) energy level of −5.64 eV in contrast to DRTB-T (−5.51 eV) (Yang et al., 2017). Notably, DRTB-FT has nearly the same solid film absorption ranging from 300 to 600 nm compared with that of DRTB-T, which is well complementary to that of an A-D-A type acceptor F-2Cl (500–800 nm). Thus, ASM-OSC based on DRTB-FT:F-2Cl gave a PCE of 7.66% with a high V_{oc} of 1.070 V and a low energy loss (E_{loss}) of 0.47 eV. The results indicate that high V_{oc} of ASM-OSC device can be obtained through careful donor molecular optimization. The moderate performance was mainly attributed to the low FF (0.532) and J_{sc} (-13.46 mA cm^{-2}) owing to the unmatched charge carrier mobilities and unfavorable active layer morphology.

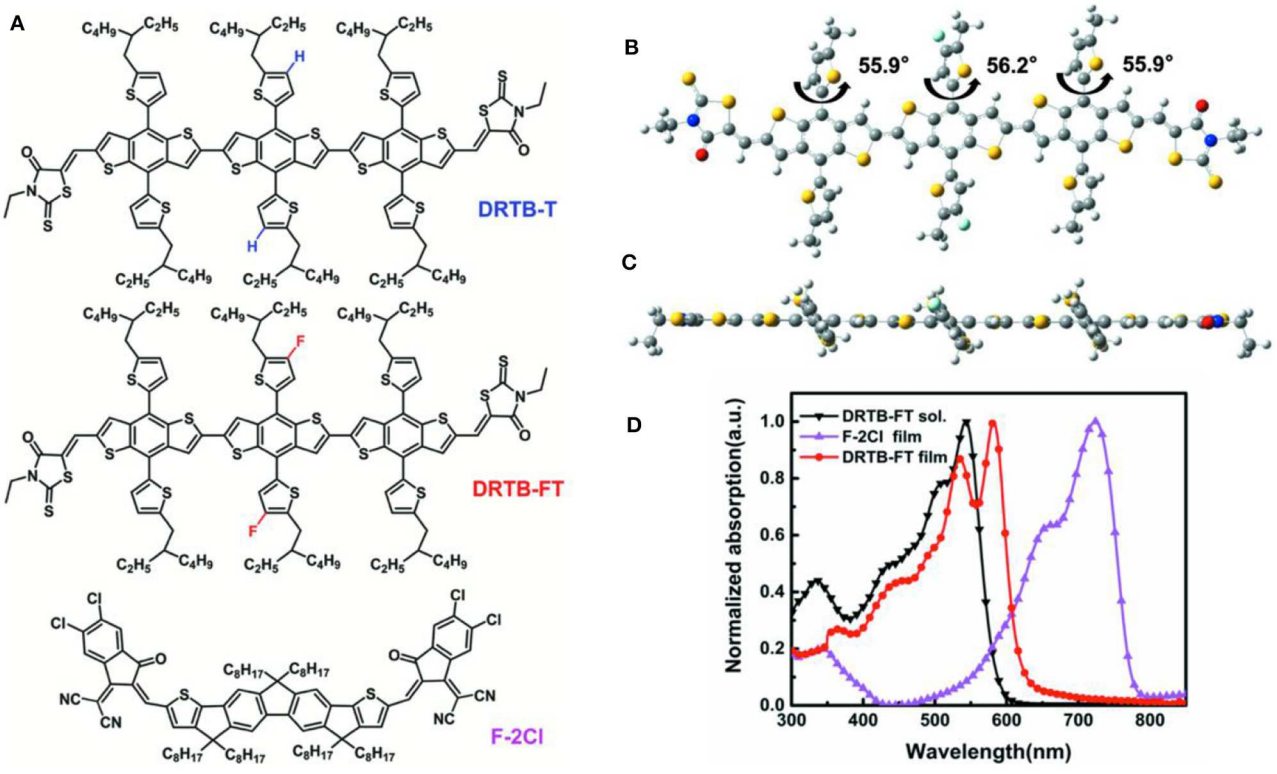

FIGURE 1 | (A) Chemical structures of DRTB-T, DRTB-FT, and F-2Cl; **(B)** Top view and **(C)** Side view of the optimized molecular geometries of DRTB-FT at B3LYP/6-31G*; **(D)** Absorption spectra of DRTB-FT and F-2Cl.

EXPERIMENTAL SECTION

Materials and Synthesis

DRTB-FT was synthesized following the procedure in **Scheme 1**. F-2Cl was prepared according to the reported procedure (Wang et al., 2018b). The materials were commercially available and used without further purification. All manipulations and reactions were carried out following the standard Schlenk technique under argon protection.

Compound 3. Under argon protection, the weighed compound 1 (0.40 g, 0.425 mmol) and 2 (0.64 g, 0.936 mmol) were dissolved in toluene(15 mL). Subsequently, $Pd(PPh_3)_4$ (50 mg) was added as catalyst. The solution was stirred under dark condition, keeping the temperature at 110°C for 20 h. After removing the solvent, compound 3 was obtained as a red solid by silica gel chromatography (PE/CH_2Cl_2 = 1:2 as eluent) (0.59 g, 76%). ^{1}H NMR (400 MHz, $CDCl_3$), δ (ppm): 9.71 (s, 2H), 8.10 (s, 2H), 7.51 (s, 2H), 7.47 (s, 2H), 7.30 (d, 2H), 7.19 (d, 4H), 6.93 (d, 4H), 2.94–2.90 (m, 12H), 1.77-1.72 (m, 6H), 1.48–1.38 (m, 48H), 1.04–0.95 (m, 36H) (**Figure S1**). ^{13}C NMR (100 MHz, $CDCl_3$), δ(ppm): 183.74, 155.61, 153.11, 146.94, 146.47, 143.13, 141.48, 139.26, 138.90, 138.52, 137.77, 137.08, 135.78, 135.46, 133.95, 133.57, 133.48, 128.33, 126.07, 125.64, 125.51, 124.36, 123.06, 122.75, 122.57, 120.83, 118.14, 117.89, 41.35, 40.71, 34.38, 32.63, 32.59, 29.68, 29.53, 28.93, 25.86, 25.71, 23.06, 14.18, 10.87. MALDI-TOF MS: calcd for $C_{104}H_{120}F_2O_2S_{12}$ [M^+], 1824.84; found: 1824.77.

Compound DRTB-FT. Compound 3 (150 mg, 0.082 mmol) and 3-ethyl-rhodanine (133 mg, 0.82 mmol) were added in $CHCl_3$ (20 mL). Under stirring the solution was deoxygenated using argon gas for 10 min. Subsequently, piperidine (0.1 mL) was added by syringe. After stirring at 60°C for 12 h, water (100 mL) was added and the product was extracted using $CHCl_3$ (2 × 80 mL). The combined $CHCl_3$ solution was washed twice using water and then dried by anhydrous Na_2SO_4. After removal of solvent, the crude product was chromatographied by silica gel (PE/CH_2Cl_3 = 1:3 as eluent), obtaining a powdery dark purple solid (142 mg, 82%). ^{1}H NMR (400 MHz, $CDCl_3$), δ (ppm): 7.66 (s, 2H), 7.43 (s, 2H), 7.34 (s, 2H), 7.30 (s, 2H), 7.26–7.23 (m, 4H), 7.16 (s, 2H), 6.94-6.92 (m, 4H), 4.02–4.00 (m, 4H), 2.96-2.87 (m, 12H), 1.81–1.78 (m, 6H), 1.57–1.42 (m, 48H), 1.19-1.16 (t, 6H), 1.06–0.92 (m, 36H). ^{13}C NMR (100 MHz, $CDCl_3$), δ (ppm): 189.92, 164.84, 153.75, 151.21, 144.84, 144.50, 139.73, 136.68, 136.43, 136.06, 135.62, 135.52, 134.92, 134.35, 133.98, 131.78, 129.46, 126.51, 126.25, 123.64, 123.28, 122.73, 121.82, 121.09, 120.87, 120.68, 120.50, 118.85, 118.69, 116.27, 115.99, 39.52, 39.43, 38.78, 37.74, 32.60, 32.54, 30.88, 30.77, 27.77, 27.14, 27.08, 26.99, 23.98, 23.91, 23.81, 23.17, 21.29, 21.25, 12.38, 12.31, 10.39, 9.15, 8.99 (**Figure S2**). MALDI-TOF MS: calcd for $C_{114}H_{130}F_2N_2O_2S_{16}$ [M^+], 2111.30; found: 2110.65 (**Figure S3**).

Measurements and Instruments

The ^{1}H and ^{13}C nuclear magnetic resonance (NMR) spectra were taken on by the Bruker AV400 Spectrometer. Matrix assisted laser desorption/ionization time-of-flight (MALDI-TOF) mass were measured using a Bruker Autoflex III instrument. X-ray diffraction (XRD) experiments were carried out with a Bruker Model D8 FOCUS X-ray diffractometer with Cu Kα radiation (λ = 1.5406 Å) at a current of 40 mA and a generator voltage of 40 kV. The UV-vis spectra were performed on a JASCO V-570 spectrophotometer. Cyclic voltammetry (CV) experiments were carried out using a LK98B II Microcomputer-based Electrochemical Analyzer and a conventional three-electrode configuration with a saturated calomel electrode (SCE) as the reference electrode, a Pt wire as the counter electrode, and a glassy carbon electrode as the working electrode at room temperature. The measurement was carried out employing acetonitrile solution of tetrabutylammonium phosphorus hexafluoride (n-Bu_4NPF_6, 0.1 M) as the supporting electrolyte with the scan rate of 100 mV s^{-1}. The LUMO (lowest unoccupied molecular orbital) and HOMO values were obtained following the formula $E_{LUMO} = -(4.80 + E_{re}^{onset})$ and $E_{HOMO} = -(4.80 + E_{ox}^{onset})$, where E_{re}^{onset} and E_{ox}^{onset} can be estimated from the CV curves, respectively. The geometry structures of DRTB-FT was optimized through Density functional theory (DFT) calculations (B3LYP/6-31G*) according to Gaussian 16 (Lee et al., 1988; Frisch et al., 2016).

The current density-voltage (J-V) characteristics of ASM-OSC devices were measured with a Keithley 2400 source-measure unit. Using a SAN-EI XES-70S1 AAA class solar simulator, photocurrent was performed under illumination with simulated 100 mW cm^{-2} AM 1.5G irradiation. The external quantum efficiency (EQE) curve was obtained by a QE-R Solar Cell Spectral Response Measurement System.

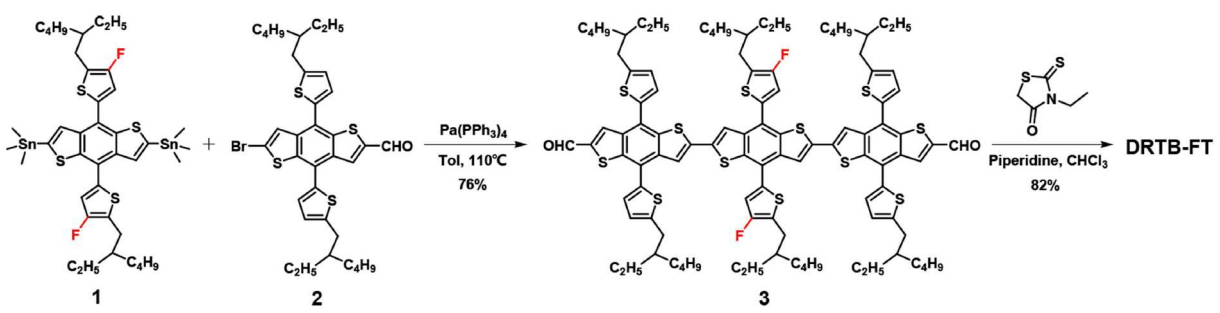

SCHEME 1 | Synthetic route of DRTB-FT.

Atomic force microscope (AFM) and Transmission electron microscopy (TEM) images were obtained on a Bruker MultiMode 8 in tapping mode and Philips Technical G2 F20 at 200 kV, respectively. Space charge limited current (SCLC) mobility was performed by a diode configuration of glass/ZnO/active layer/Al for electron mobility and ITO/PEDOT:PSS/active layer/Au for hole mobility, respectively. The results were fitted via a space charge limited form, being described as the equation:

$$J = \frac{9\varepsilon_0\varepsilon_r\mu_0 V^2}{8L^3}\exp\left(0.89\beta\sqrt{\frac{V}{L}}\right)$$

where J is the current density, ε_0 is the permittivity of free space (8.85×10^{-12} F m^{-1}), ε_r is the relative dielectric constant of the transport medium, μ_0 is the hole or electron mobility, V ($= V_{appl} - V_{bi}$) is the internal voltage in the device, where V_{appl} is the applied voltage to the device and V_{bi} is the built-in voltage due to the relative work function difference of the two electrodes, L is the film thickness of the active layer.

Fabrication of OSC Devices

ASM-OSC devices were fabricated using a conventional structure of glass/ITO/PEDOT:PSS/Donor:Acceptor/PDINO/Al, in which the electronic transport material PDINO was designed by Zhang et al. (2014). As a common procedure: the cleaned ITO-coated glasses were treated by ultraviolet-ozone for 15 min and spin-coated with PEDOT:PSS solution at 4,800 rpm for 20 s. Subsequently, the glasses were baked at 150°C for 20 min and transferred into the glove box with argon gas. Chloroform solution of both donor and acceptor was spin-coated on the PEDOT:PSS at 1,700 rpm for 20 s. Afterward, PDINO was spin-coated on the active layer at 3,000 rpm for 20 s with the concentration of 1.0 mg/ml using EtOH as solvent. Finally, under the high vacuum, a cathode material Al was deposited for 50 nm onto PDINO layer. The work area of each device is about 0.04 cm^2.

RESULTS AND DISCUSSION

Materials Synthesis and Characterization

The synthesis of DRTB-FT is illustrated in **Scheme 1**. By Stille coupling reaction between compound 1 and 2, two commercially available BDT derivatives, compound 3 was synthesized. Subsequent Knoevenagel condensation reaction between compound 3 and 3-ethylrhodanine gave the final product in high yield. As shown in the experimental section above, DRTB-FT was characterized through NMR spectroscopy and MALDI-TOF MS. DRTB-FT exhibits good solubility in common organic solvents such as chlorobenzene, dichloromethane and chloroform. As shown in **Figures 1B,C**, the optimized geometry of DRTB-FT based on DFT (B3LYP/6-31G*) displays a good coplanar conformation. The structural ordering of pristine DRTB-FT and DRTB-T film was investigated by XRD analysis. According to the XRD results (**Figure S4**), a weak diffraction peak (100) at 4.44 (2θ) was observed for the DRTB-T film. In contrast, DRTB-FT film exhibits a strong diffraction peak (100) at 4.46 (2θ), indicating stronger stacking and crystallinity than DRTB-T.

TABLE 1 | Optical and electrochemical data of DRTB-T and DRTB-FT.

Molecules	UV-vis			CV		
	λ_{max}^{sol} (nm)	λ_{max}^{film} (nm)	E_g^{opt} (eV) [a]	HOMO (eV)	LUMO (eV)	E_g^{cv} (eV)
DRTB-T[b]	545	545, 585	2.00	−5.51	−3.34	2.17
DRTB-FT	547	544, 587	1.99	−5.64	−3.61	2.03

[a] *Optical bandgap was obtained from the onset wavelength of the film.* [b] *Yang et al. (2017).*

TABLE 2 | Photovoltaic parameters of OSCs based on DRTB-FT:F-2Cl and DRTB-T:F-2Cl.

Donor	Treatment	V_{oc} (V)	J_{sc} (mA cm^{-2})	FF	PCE (%)
DRTB-FT	As cast	1.098	10.77	0.478	5.65 (5.51)[a]
	TA	1.070	13.46	0.532	7.66 (7.45)[a]
DRTB-T	SVA	0.969	17.24	0.64	10.76[b]

[a] *Average PCE values obtained from 20 devices are shown in parentheses;* [b] *Wang et al. (2018b).*

Optical and Electrochemical Properties

The UV-vis absorption spectra of DRTB-FT obtained in chloroform solution and in solid state are shown in **Figure 1D**. In chloroform solution, DRTB-FT exhibits an absorption maximum at 547 nm, and it shows a bathochromic-shifted and broadened absorption in the solid state ranging from 300 to 630 nm, which is well complementary to that of F-2Cl film. The optical bandgap (E_g^{opt}) obtained from DRTB-FT film absorption onset (622 nm) is 1.99 eV. Moreover, a stronger shoulder peak was observed in film absorption spectrum in comparison to the non-fluorinated counterpart DRTB-T, which reveals the stronger intermolecular stacking and π-π interactions in DRTB-FT solid film. The electrochemical behavior of DRTB-FT was investigated by CV experiments. As shown in **Figure S5**, the estimated reduction and oxidation potentials of DRTB-FT are −1.17V and 0.84V (vs Fc/Fc^+), respectively. Therefore, the first oxidation event of DRTB-FT occurs at a higher oxidation potential compared with DRTB-T, leading to a deeper HOMO of −5.64 eV, which is in favor of obtaining a higher V_{oc} in the devices when combined with appropriate acceptor. The optical and electrochemical data of DRTB-FT and DRTB-T are listed in **Table 1**.

Photovoltaic Properties

ASM-OSC devices with a conventional structure of ITO/PEDOT:PSS/active layer/PDINO/Al were fabricated. The devices performance were optimized by varying the donor to acceptor weight ratio (D/A, w/w) in the active layer, applying solvent vapor annealing (SVA) and thermal annealing (TA) treatment and etc. The detailed device parameters are provided in **Tables S1**–**S3**. The photovoltaic parameters of the as-cast and optimal devices are listed in **Table 2** and the corresponding J-V characteristics are shown in **Figure 2A**. For the as-cast device,

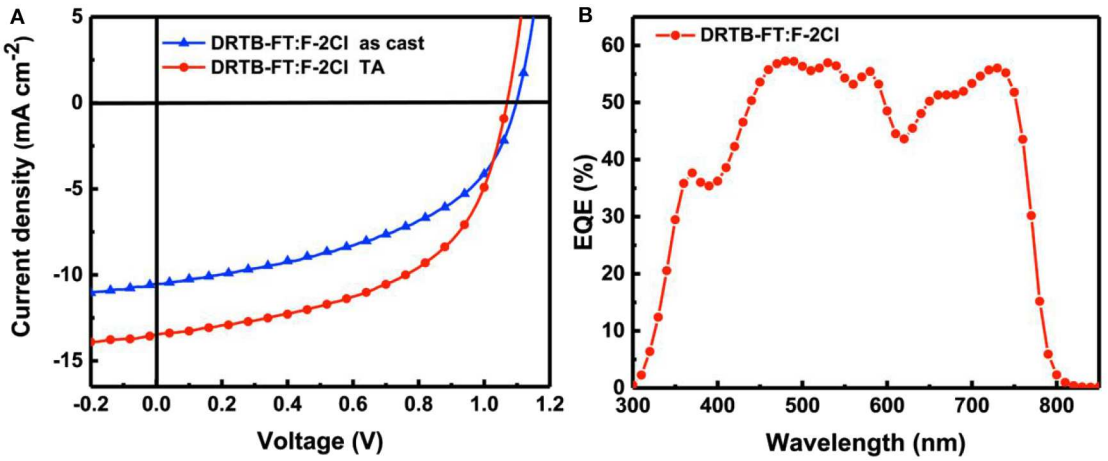

FIGURE 2 | (A) Current density-voltage (*J-V*) curves of BHJ devices and **(B)** EQE curves of the optimal BHJ device based on DRTB-FT:F-2Cl.

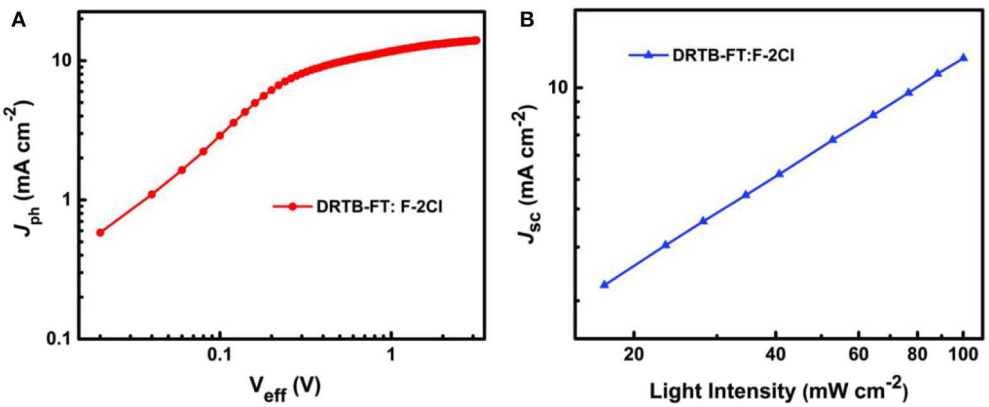

FIGURE 3 | (A) Photocurrent density vs. effective voltage (J_{ph}-V_{eff}) and **(B)** double logarithmic plots of J_{sc} as a function of incident light intensity for the optimal device based on DRTB-FT:F-2Cl.

a PCE of 5.72% with a high V_{oc} of 1.10 V was obtained. An improved photovoltaic performance with a PCE of 7.66% and a high V_{oc} of 1.07 V was achieved after TA treatment at 100°C for 10 min, and the corresponding E_{loss} is as low as 0.47 eV calculated via the equation $E_{loss} = E_g^{opt}$-eV_{oc}, where E_g^{opt} is the optical bandgap of F-2Cl film (1.54 eV). As expected, OSCs based on DRTB-FT:F-2Cl demonstrated a high V_{oc} owing to the low-lying HOMO energy level of the DRTB-FT donor. In contrast, the DRTB-T:F-2Cl based device has a V_{oc} of 0.969 V. However, limited by the low J_{sc} (13.46 mA cm^{-2}) and FF (0.532), the optimized device based on DRTB-FT:F-2Cl gave a moderate PCE (7.66%). The unsatisfactory device performance can be ascribed to the unfavorable active layer morphology and unmatched charge carrier mobilities, as will be discussed in the following section.

The EQE spectrum of the optimal device is presented in **Figure 2B**, which exhibits a broad photo-to-current response from 300 to 790 nm. However, the maximum efficiency is only 58% at 471 nm, indicating a lower photoelectron conversion process in comparison to that of DRTB-T based device (Wang et al., 2018b). The calculated J_{sc} value obtained from the integration of the EQE curve is 13.01 mA cm^{-2}, which is in good agreement with the J_{sc} value from the corresponding *J-V* curve with about 3% mismatch.

To explore the reason for lower J_{sc} and FF of the ASM-OSC, the exciton dissociation and extraction process in the active layer of optimal device was investigated. **Figure 3A** shows the relation between photocurrent density J_{ph} ($J_{ph} = J_L - J_D$) and effective voltage V_{eff} ($V_{eff} = V_0 - V_a$), where J_L, J_D, V_0, and V_a are the light current density, the dark current density, the voltage at $J_{ph} = 0$ and the applied voltage, respectively. It can be seen that the J_{ph} curve of DRTB-FT:F-2Cl based device is hard to reach the saturation current density (J_{sat}) even at a high V_{eff}. Lower J_{ph}/J_{sat} values of 85.9% and 61.0% were obtained under the short-circuit and maximal output power conditions, respectively, which demonstrated a poor exciton dissociation and charge extraction processes and limited J_{sc} and FF. For further study, the bimolecular recombination degree in active layer was

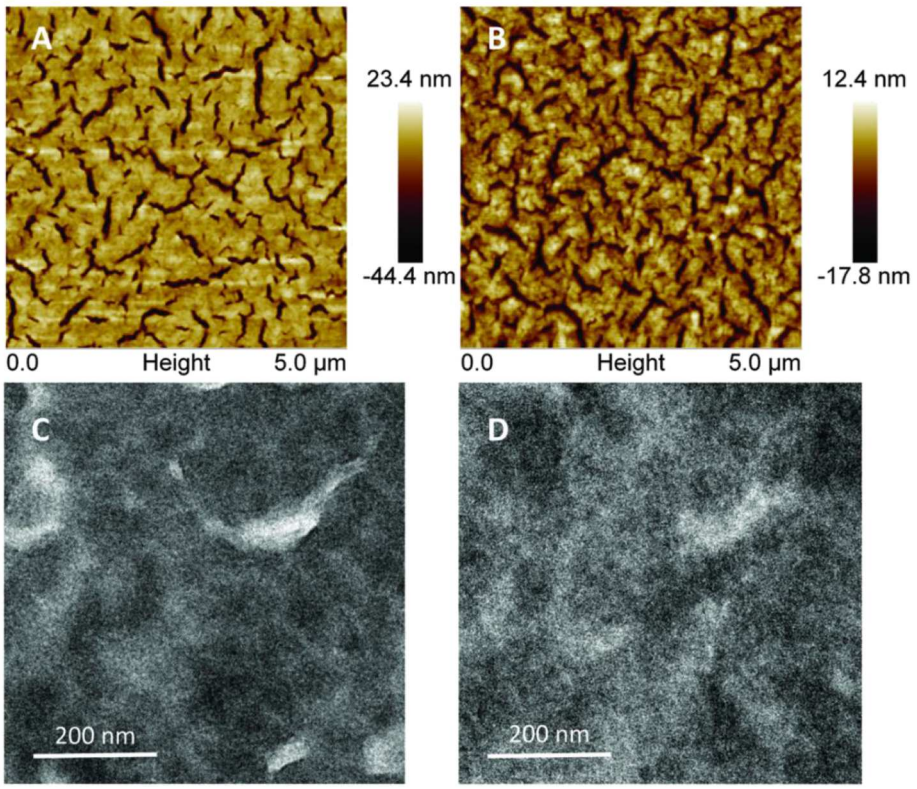

FIGURE 4 | Tapping-mode AFM height images of the active layers of the **(A)** as-cast and **(B)** optimal DRTB-FT:F-2Cl blend films. TEM images of the **(C)** as-cast and **(D)** optimal DRTB-FT:F-2Cl blend films.

estimated on the basis of the formula of $J_{sc} \propto P^{\alpha}$, where α is the exponential factor. When α value was closer to 1, the less bimolecular recombination in blend film. The fitted slope (α) is calculated to be 0.964 for the devices based on DRTB-FT as shown in **Figure 3B**, which is relatively lower compared with that of DRTB-T based device (0.985) (Wang et al., 2018b), indicating more bimolecular recombination in DRTB-FT:F-2Cl active layer.

The influence of active layer morphology on device performance was investigated by AFM and TEM technology. **Figure 4A** shows that the surface topography of the as-cast DRTB-FT:F-2Cl blend film is relatively rough in terms of the large root-mean-square (RMS) roughness (9.2 nm), which reveals the existence of excessive aggregation in the as-cast film due to the strong stacking and crystallinity of donor molecules. For the optimal blend film (**Figure 4B**), a relatively smaller RMS roughness of 4.4 nm was observed, which is beneficial to form better contact between the film and the electrode, and thus to promote charge extraction. TEM images are in consistent with the AFM, from **Figure 4C**, it can be seen that an oversized phase separation and more defects in the as-cast blend film, and the morphology becomes better obviously after TA treatment (**Figure 4D**). However, there was still no clear fiber structure or suitable phase separation in the optimized blend film, which might account for the low J_{sc} and FF.

To investigate the charge-transporting behavior of the studied devices, the electron and hole mobilities (μ_e and μ_h) were measured by the SCLC method as described in experimental section. According to **Figure S6**, the electron mobility of μ_e=2.11 × 10^{-4} $cm^{-2}V^{-1}s^{-1}$ and hole mobility of μ_h = 4.51 × 10^{-5} $cm^{-2}V^{-1}s^{-1}$ were obtained for the as-cast device. After TA treatment, the charge mobilities were raised to μ_e= 4.12 × 10^{-4} $cm^{-2}V^{-1}s^{-1}$ and μ_h = 8.56× 10^{-5} $cm^{-2}V^{-1}s^{-1}$, respectively. The relatively lower and unbalanced hole and electron mobilities could lead to more charge recombination, thus the lower FF and J_{sc}.

CONCLUSION

In summary, we have designed and synthesized a new small molecule and A-D-A type donor named DRTB-FT, taking the fluorothienyl-substituted benzodithiophene as the central unit. The introduction of fluorine atoms enables DRTB-FT to get a low HOMO of −5.64 eV. When combined with an acceptor F-2Cl, the optimal ASM-OSC device gave a PCE of 7.66%, especially a high V_{oc} of 1.070 V and a low E_{loss} of 0.47 eV. The results indicate that high V_{oc} of ASM-OSCs can be obtained through careful donor molecular optimization. On the other hand, morphology control also plays a critical role in ASM-OSCs. In this case, the low J_{sc} and FF are caused by the

unfavorable active layer morphology with large aggregation of small molecule donors. It is believed that high performance ASM-OSCs will be achieved through synergistic study of molecular design with complementary absorption, matched energy levels and morphology control.

DATA AVAILABILITY STATEMENT

All datasets generated for this study are included in the article/**Supplementary Material**.

AUTHOR CONTRIBUTIONS

CLiu synthesized the DRTB-FT and measured the optical-electric properties of DRTB-T and DRTB-FT. NQ fabricated and optimized the devices, and wrote the manuscript. YS contributed to the morphology characterization. XK ran the calculations of DRTB-FT, HZ, CLi, XW, and YC conceived and directed the project. All authors contributed to the whole work.

ACKNOWLEDGMENTS

The authors acknowledge the support from the NSFC of China (51773095), the Research Fund of Jining University (2019BSZX01), and the Young Innovative Talents Introduction & Cultivation Program for Colleges and Universities of Shandong Province: Innovative Research Team on Optoelectronic Functional Materials.

SUPPLEMENTARY MATERIAL

The Supplementary Material for this article can be found online at: https://www.frontiersin.org/articles/10.3389/fchem.2020.00329/full#supplementary-material

REFERENCES

An, Q., Ma, X., Gao, J., and Zhang, F. (2019). Solvent additive-free ternary polymer solar cells with 16.27% efficiency. *Sci. Bull.* 64, 504–506. doi: 10.1016/j.scib.2019.03.024

Badgujar, S., Song, C. E., Oh, S., Shin, W. S., Moon, S.-J., Lee, J.-C., et al. (2016). Highly efficient and thermally stable fullerene-free organic solar cells based on a small molecule donor and acceptor. *J. Mater. Chem. A* 4, 16335–16340. doi: 10.1039/C6TA06367E

Bin, H., Yao, J., Yang, Y., Angunawela, I., Sun, C., Gao, L., et al. (2018). High-efficiency all-small-molecule organic solar cells based on an organic molecule donor with alkylsilyl-thienyl conjugated side chains. *Adv. Mater.* 30:e1706361. doi: 10.1002/adma.201706361

Chen, H., Hu, D., Yang, Q., Gao, J., Fu, J., Yang, K., et al. (2019). All-small-molecule organic solar cells with an ordered liquid crystalline donor. *Joule* 3, 3034–3047. doi: 10.1016/j.joule.2019.09.009

Chen, Y., Wan, X., and Long, G. (2013). High performance photovoltaic applications using solution-processed small molecules. *Acc. Chem. Res.* 46, 2645–2655. doi: 10.1021/ar400088c

Cheng, P., Li, G., Zhan, X., and Yang, Y. (2018). Next-generation organic photovoltaics based on non-fullerene acceptors. *Nat. Photon.* 12, 131–142. doi: 10.1038/s41566-018-0104-9

Cheng, X., Li, M., Guo, Z., Yu, J., Lu, G., Bu, L., et al. (2019). "Twisted" conjugated molecules as donor materials for efficient all-small-molecule organic solar cells processed with tetrahydrofuran. *J. Mater. Chem. A* 7, 23008–23018. doi: 10.1039/C9TA07760J

Cui, Y., Yao, H., Hong, L., Zhang, T., Xu, Y., Xian, K., et al. (2019). Achieving over 15% efficiency in organic photovoltaic cells via copolymer design. *Adv. Mater.* 31:e1808356. doi: 10.1002/adma.201808356

Duan, T., Tang, H., Liang, R.-Z., Lv, J., Kan, Z., Singh, R., et al. (2019). Terminal group engineering for small-molecule donors boosts the performance of nonfullerene organic solar cells. *J. Mater. Chem. A* 7, 2541–2546. doi: 10.1039/C8TA11420J

Fan, B., Zhang, D., Li, M., Zhong, W., Zeng, Z., Ying, L., et al. (2019). Achieving over 16% efficiency for single-junction organic solar cells. *Sci. China Chem.* 62, 746–752. doi: 10.1007/s11426-019-9457-5

Frisch, M. J., Trucks, G. W., Schlegel, H. B., Scuseria, G. E., Robb, M. A., Cheeseman, J. R., et al. (2016). *Gaussian 16 rev. B.01*. Wallingford, CT: Gaussian, Inc.

Gao, K., Jo, S. B., Shi, X., Nian, L., Zhang, M., Kan, Y., et al. (2019). Over 12% efficiency nonfullerene all-small-molecule organic solar cells with sequentially evolved multilength scale morphologies. *Adv. Mater.* 31:e1807842. doi: 10.1002/adma.201807842

Ge, J., Xie, L., Peng, R., Fanady, B., Huang, J., Song, W., et al. (2019). 13.34 % efficiency non-fullerene all-small-molecule organic solar cells enabled by modulating the crystallinity of donors via a fluorination strategy. *Angew. Chem. Int. Ed. Engl.* 59, 2808–2815. doi: 10.1002/anie.201910297

He, Z., Xiao, B., Liu, F., Wu, H., Yang, Y., Xiao, S., et al. (2015). Single-junction polymer solar cells with high efficiency and photovoltage. *Nat. Photonics* 9, 174–179. doi: 10.1038/nphoton.2015.6

Heeger, A. J. (2010). Semiconducting polymers: the third generation. *Chem. Soc. Rev.* 39, 2354–2371. doi: 10.1039/b914956m

Jiang, K., Wei, Q., Lai, J. Y. L., Peng, Z., Kim, H. K., Yuan, J., et al. (2019). Alkyl chain tuning of small molecule acceptors for efficient organic solar cells. *Joule* 3, 3020–3033. doi: 10.1016/j.joule.2019.09.010

Kan, B., Li, M., Zhang, Q., Liu, F., Wan, X., Wang, Y., et al. (2015). A series of simple oligomer-like small molecules based on oligothiophenes for solution-processed solar cells with high efficiency. *J. Am. Chem. Soc.* 137, 3886–3893. doi: 10.1021/jacs.5b00305

Lee, C., Yang, W., and Parr, R. G. (1988). Development of the colle-salvetti correlation-energy formula into a functional of the electron density. *Phys. Rev. B* 37, 785–789. doi: 10.1103/PhysRevB.37.785

Li, T., Dai, S., Ke, Z., Yang, L., Wang, J., Yan, C., et al. (2018). Fused tris(thienothiophene)-based electron acceptor with strong near-infrared absorption for high-performance as-cast solar cells. *Adv. Mater.* 30:1705969. doi: 10.1002/adma.201705969

Li, W., Ye, L., Li, S., Yao, H., Ade, H., and Hou, J. (2018). A high-efficiency organic solar cell enabled by the strong intramolecular electron push-pull effect of the nonfullerene acceptor. *Adv. Mater.* 30:e1707170. doi: 10.1002/adma.201707170

Li, Y., Xu, G., Cui, C., and Li, Y. (2018). Flexible and semitransparent organic solar cells. *Adv. Energ. Mater.* 8:1701791. doi: 10.1002/aenm.201701791

Lin, Y., Adilbekova, B., Firdaus, Y., Yengel, E., Faber, H., Sajjad, M., et al. (2019). 17% efficient organic solar cells based on liquid exfoliated ws_2 as a replacement for pedot:Pss. *Adv. Mater.* 31:e1902965. doi: 10.1002/adma.201902965

Lin, Y., He, Q., Zhao, F., Huo, L., Mai, J., Lu, X., et al. (2016). A facile planar fused-ring electron acceptor for as-cast polymer solar cells with 8.71% efficiency. *J. Am. Chem. Soc.* 138, 2973–2976. doi: 10.1021/jacs.6b00853

Meng, L., Zhang, Y., Wan, X., Li, C., Zhang, X., Wang, Y., et al. (2018). Organic and solution-processed tandem solar cells with 17.3% efficiency. *Science* 361, 1094–1098. doi: 10.1126/science.aat2612

Privado, M., de la Cruz, P., Biswas, S., Singhal, R., Sharma, G. D., and Langa, F. (2018). A non-fullerene all small molecule solar cell constructed with a diketopyrrolopyrrole-based acceptor having a power conversion efficiency higher than 9% and an energy loss of 0.54 ev. *J. Mater. Chem. A* 6, 11714–11724. doi: 10.1039/C8TA02633E

Qiu, N., Zhang, H., Wan, X., Li, C., Ke, X., Feng, H., et al. (2017). A new nonfullerene electron acceptor with a ladder type backbone

for high-performance organic solar cells. *Adv. Mater.* 29:1604964. doi: 10.1002/adma.201604964

Sun, H., Liu, T., Yu, J., Lau, T.-K., Zhang, G., Zhang, Y., et al. (2019). A monothiophene unit incorporating both fluoro and ester substitution enabling high-performance donor polymers for non-fullerene solar cells with 16.4% efficiency. *Energy Environ. Sci.* 12, 3328–3337. doi: 10.1039/C9EE01890E

Sun, Y., Chang, M., Meng, L., Wan, X., Gao, H., Zhang, Y., et al. (2019). Flexible organic photovoltaics based on water-processed silver nanowire electrodes. *Nat. Electron.* 2, 513–520. doi: 10.1038/s41928-019-0315-1

Tang, A., Song, W., Xiao, B., Guo, J., Min, J., Ge, Z., et al. (2019). Benzotriazole-based acceptor and donors, coupled with chlorination, achieve a high voc of 1.24 v and an efficiency of 10.5% in fullerene-free organic solar cells. *Chem. Mater.* 31, 3941–3947. doi: 10.1021/acs.chemmater.8b05316

Tang, A., Xiao, B., Chen, F., Zhang, J., Wei, Z., and Zhou, E. (2018). The introduction of fluorine and sulfur atoms into benzotriazole-based p-type polymers to match with a benzotriazole-containing n-type small molecule: "The same-acceptor-strategy" to realize high open-circuit voltage. *Adv. Energy Mater.* 8:1801582. doi: 10.1002/aenm.201801582

Tang, A., Xiao, B., Wang, Y., Gao, F., Tajima, K., Bin, H., et al. (2017). Simultaneously achieved high open-circuit voltage and efficient charge generation by fine-tuning charge-transfer driving force in nonfullerene polymer solar cells. *Adv. Funct. Mater.* 28:1704507. doi: 10.1002/adfm.201704507

Wang, Y., Chang, M., Kan, B., Wan, X., Li, C., and Chen, Y. (2018a). All-small-molecule organic solar cells based on pentathiophene donor and alkylated indacenodithiophene-based acceptors with efficiency over 8%. *ACS Appl. Mater. Interfaces* 1, 2150–2156. doi: 10.1021/acsaem.8b00205

Wang, Y., Wang, Y., Kan, B., Ke, X., Wan, X., Li, C., et al. (2018b). High-performance all-small-molecule solar cells based on a new type of small molecule acceptors with chlorinated end groups. *Adv. Energy Mater.* 8:1802021. doi: 10.1002/aenm.201802021

Wu, H., Yue, Q., Zhou, Z., Chen, S., Zhang, D., Xu, S., et al. (2019). Cathode interfacial layer-free all small-molecule solar cells with efficiency over 12%. *J. Mater. Chem. A* 7, 15944–15950. doi: 10.1039/C9TA05023J

Wu, Y., Zheng, Y., Yang, H., Sun, C., Dong, Y., Cui, C., et al. (2019). Rationally pairing photoactive materials for high-performance polymer solar cells with efficiency of 16.53%. *Sci. China Chem.* 53, 1–7. doi: 10.1007/s11426-019-9599-1

Xiong, J., Jin, K., Jiang, Y., Qin, J., Wang, T., Liu, J., et al. (2019). Thiolactone copolymer donor gifts organic solar cells a 16.72% efficiency. *Sci. Bull.* 64, 1573–1576. doi: 10.1016/j.scib.2019.10.002

Yan, T., Song, W., Huang, J., Peng, R., Huang, L., and Ge, Z. (2019). 16.67% rigid and 14.06% flexible organic solar cells enabled by ternary heterojunction strategy. *Adv. Mater.* 31:e1902210. doi: 10.1002/adma.201902210

Yang, L., Zhang, S., He, C., Zhang, J., Yao, H., Yang, Y., et al. (2017). New wide band gap donor for efficient fullerene-free all-small-molecule organic solar cells. *J. Am. Chem. Soc.* 139, 1958–1966. doi: 10.1021/jacs.6b11612

Yuan, J., Zhang, Y., Zhou, L., Zhang, G., Yip, H.-L., Lau, T.-K., et al. (2019). Single-junction organic solar cell with over 15% efficiency using fused-ring acceptor with electron-deficient core. *Joule* 3, 1140–1151. doi: 10.1016/j.joule.2019.01.004

Yue, Q., Wu, H., Zhou, Z., Zhang, M., Liu, F., and Zhu, X. (2019). 13.7% efficiency small-molecule solar cells enabled by a combination of material and morphology optimization. *Adv. Mater.* 31:e1904283. doi: 10.1002/adma.201904283

Zhang, H., Yao, H., Hou, J., Zhu, J., Zhang, J., Li, W., et al. (2018). Over 14% efficiency in organic solar cells enabled by chlorinated nonfullerene small-molecule acceptors. *Adv. Mater.* 30:e1800613. doi: 10.1002/adma.201800613

Zhang, Q., Kan, B., Liu, F., Long, G., Wan, X., Chen, X., et al. (2014). Small-molecule solar cells with efficiency over 9%. *Nat. Photonics* 9, 35–41. doi: 10.1038/nphoton.2014.269

Zhang, Z.-G., and Li, Y. (2014). Side-chain engineering of high-efficiency conjugated polymer photovoltaic materials. *Sci. China Chem.* 58, 192–209. doi: 10.1007/s11426-014-5260-2

Zhang, Z.-G., Qi, B., Jin, Z., Chi, D., Qi, Z., Li, Y., et al. (2014). Perylene diimides: a thickness-insensitive cathode interlayer for high performance polymer solar cells. *Energy Environ. Sci.* 7, 1966–1973. doi: 10.1039/c4ee00022f

Zhao, F., Dai, S., Wu, Y., Zhang, Q., Wang, J., Jiang, L., et al. (2017). Single-junction binary-blend nonfullerene polymer solar cells with 12.1% efficiency. *Adv. Mater.* 29:1700144. doi: 10.1002/adma.201700144

Zhao, W., Li, S., Yao, H., Zhang, S., Zhang, Y., Yang, B., et al. (2017). Molecular optimization enables over 13% efficiency in organic solar cells. *J. Am. Chem. Soc.* 139, 7148–7151. doi: 10.1021/jacs.7b02677

Zhou, R., Jiang, Z., Yang, C., Yu, J., Feng, J., Adil, M. A., et al. (2019). All-small-molecule organic solar cells with over 14% efficiency by optimizing hierarchical morphologies. *Nat. Commun.* 10:5393. doi: 10.1038/s41467-019-13292-1

Conflict of Interest: The authors declare that the research was conducted in the absence of any commercial or financial relationships that could be construed as a potential conflict of interest.

frontiers in Chemistry

ORIGINAL RESEARCH
published: 28 April 2020
doi: 10.3389/fchem.2020.00310

Introducing Porphyrin Units by Random Copolymerization Into NDI-Based Acceptor for All Polymer Solar Cells

Jinliang Liu[1], Mengzhen Li[1], Dong Chen[1], Bin Huang[1], Qiannan He[1], Shanshan Ding[1], Wenquan Xie[1], Feiyan Wu[1], Lie Chen[1]* and Yiwang Chen[1,2]*

[1] College of Chemistry, Institute of Polymers and Energy Chemistry (IPEC), Nanchang University, Nanchang, China, [2] Institute of Advanced Scientific Research (IASR), Jiangxi Normal University, Nanchang, China

Naphthalene diimide (NDI)-based polymer N2200 is a promising organic polymer acceptor for all-polymer solar cells (all-PSCs), but its inherent shortcomings like poor extinction coefficient and strong aggregation limit further performance optimization of all-PSCs. Here, a series of random copolymers, PNDI-Px, were designed and synthesized by introducing porphyrin unit into NDI-based polymer as acceptors for all-PSCs. These random copolymers show a higher absorption coefficient and raised the lowest unoccupied molecular orbital (LUMO) energy levels compared to N2200. The crystallinity can also be fine-tuned by regulation of the content of porphyrin unit. The random copolymers are matched with polymer donor PBDB-T for the application in all-polymer solar cells. The best power conversion efficiency (PCE) of these PNDI-Px-based devices is 5.93%, ascribed to the overall enhanced device parameters compared with the N2200-based device. These results indicate that introducing porphyrin unit into polymer is a useful way to fine-tune the photoelectric performance for efficient all-PSCs.

Keywords: all-polymer solar cells, porphyrin, naphthalene diimide, random copolymerization, device performance

OPEN ACCESS

Edited by:
Kui Zhao,
Shaanxi Normal University, China

Reviewed by:
Wei M. A.,
Xi'an Jiaotong University, China
Chuandong Dou,
Changchun Institute of Applied Chemistry (CAS), China

***Correspondence:**
Feiyan Wu
feiywu@ncu.edu.cn
Lie Chen
chenlie@ncu.edu.cn

Specialty section:
This article was submitted to Physical Chemistry and Chemical Physics, a section of the journal Frontiers in Chemistry

Received: *28 January 2020*
Accepted: *27 March 2020*
Published: *28 April 2020*

Citation:
Liu J, Li M, Chen D, Huang B, He Q, Ding S, Xie W, Wu F, Chen L and Chen Y (2020) Introducing Porphyrin Units by Random Copolymerization Into NDI-Based Acceptor for All Polymer Solar Cells. Front. Chem. 8:310. doi: 10.3389/fchem.2020.00310

INTRODUCTION

Organic solar cells (OSCs) have caused substantial research attributed to their remarkable features such as wide sources of materials, flexibility, light weight, solution processing, high-throughput preparation, and so on (Li, 2012; Søndergaard et al., 2012; Su et al., 2012; Cui, 2018). Very recently, the power conversion efficiencies (PCEs) of OSCs based on non-fullerene small-molecule acceptors have exceeded 16% (Cui et al., 2019; Fan et al., 2019; Jiang et al., 2019; Xiong et al., 2019; Xu et al., 2019; Yuan et al., 2019; Liu et al., 2020). Among various types of OSCs, all-polymer solar cells (all-PSCs) with active layer composed of a p-type polymer donor and an n-type polymer acceptor have attracted consistently increasing interest and research. The main reasons are their unparalleled advantages of optical and electronic properties, tunability, eminent mechanical flexibility, and excellent device stability (Diao et al., 2015; Kim et al., 2015; Kang et al., 2016; Liu et al., 2018; Zhang et al., 2018; Zhou and Facchetti, 2018), which is propitious to practical applications such as large-area flexible and stable devices. With the renewal of materials and the optimization of device processing technology, the PCE of all-PSCs have reached a value over 11% (Li et al., 2019a,b; Meng et al., 2019; Wu et al., 2019; Zhu et al., 2019). Even so, the efficiency of all-PSCs is still in arrears

compared to the OSCs based on small molecule, due to the insufficient high-performance n-type polymer materials.

Generally, the high-quality n-type polymer materials are primarily based on the functionalized arenes of imides, e.g., diketopyrrolopyrrole (DPP) (Li et al., 2014, 2015; Zhang and Jin, 2019), naphthalene diimide (NDI) (Bhosale et al., 2008), perylene diimide (PDI) (Seo et al., 2011), bithiophene imide (BTI) (Wang et al., 2017), and double B←N (boron–nitrogen coordination bond) bridged bipyridine (BNBP) (Dou et al., 2016). In these various n-type organic semiconductors materials, NDI-based copolymers, especially poly(2,7-bis(2-octyldodecyl)benzo[lmn][3,8]phenanthroline-1,3,6,8(2H,7H)-tetraone-4,9-diyl)([2,2′]bithiophenyl-5,5′-diyl) (N2200), are the most outstanding one as all-PSC acceptor because of its good solubility and high electron mobility (Yan et al., 2009; Gao et al., 2016). Nevertheless, its inherent shortcomings such as poor extinction coefficient and strong aggregation limit the advancement of short circuit current (J_{SC}) and fill factor (FF), further limiting the PCE of all-PSCs (Schubert et al., 2012; Kang et al., 2016). In recent years, many research groups have been successful in introducing the third unit to regulate the photovoltaic performance of polymer acceptors through random copolymerization (Li et al., 2016; Chen et al., 2018; Liu et al., 2018; Xu et al., 2018; Kolhe et al., 2019). For most random copolymer-based systems, the morphology of the active layer can be fine-tuned through regulation of the crystallinity of the random copolymers.

Apart from optimizing the morphology of the bulk-heterojunction, the strong and broadened light absorption of polymer acceptor is also critical to optimize the performance of all-PSCs. Recently, our group introduced the dye group, 2-(1, 1′-dicyanomethylene)-4-(3-thienylmethylene) rhodanine (TR), into the NDI-based acceptor, obtaining improved extinction coefficient, raised the lowest unoccupied molecular orbital (LUMO) energy levels, and reduced crystallization (Chen et al., 2018). Inspired by this strategy, we are interested in introducing other chromophores into terpolymers to improve the absorption of polymers. Porphyrin as a type of chromophore has many remarkable features, like excellent light harvesters, easily fine-tuning optical and electronic properties and efficient electron transfer (Lee et al., 2018; Mahmood et al., 2018), which is in favor of polymer material performance improvement. Li and

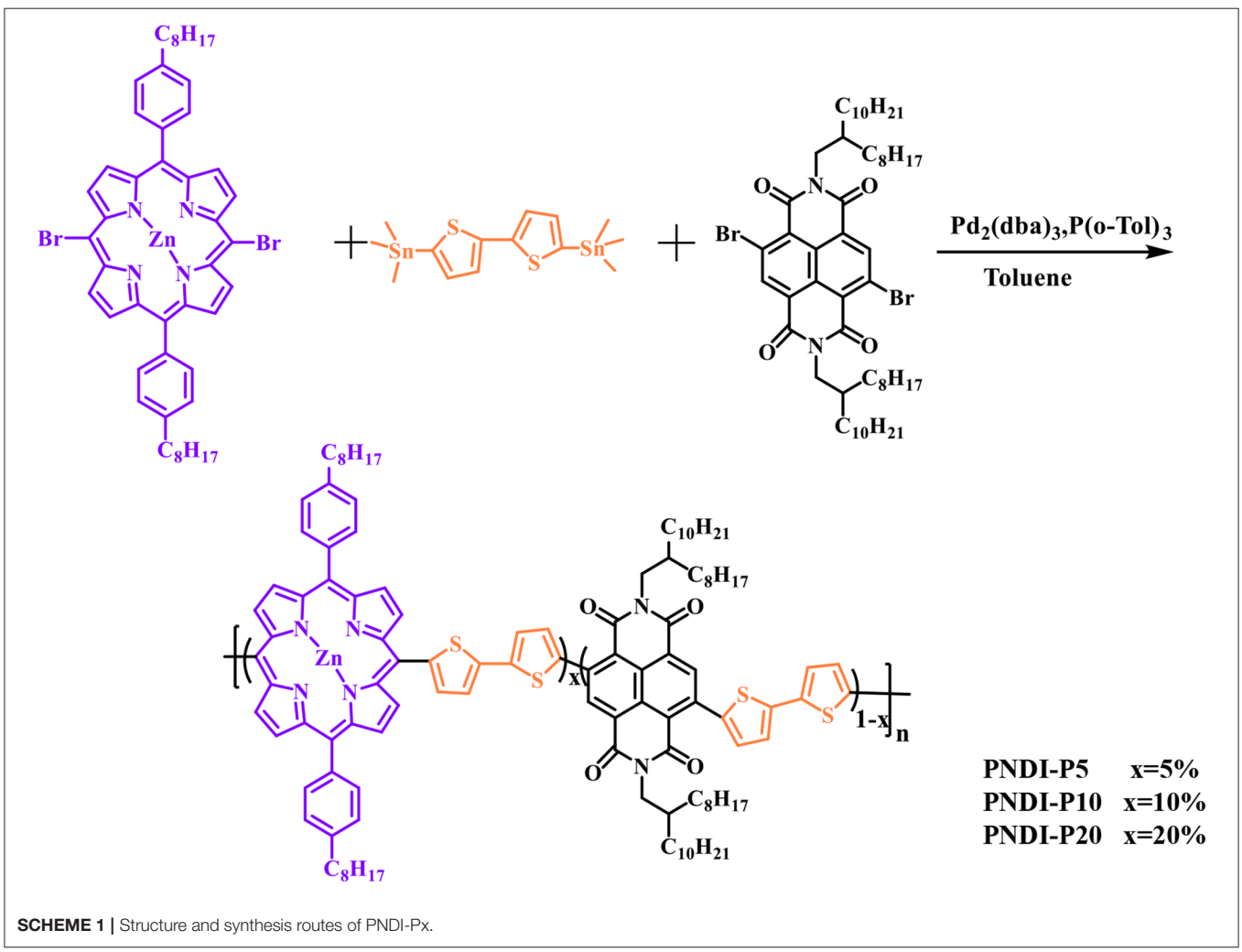

SCHEME 1 | Structure and synthesis routes of PNDI-Px.

coworkers successfully combined porphyrin group with perylene bisimides to obtain efficient small-molecule acceptors (SMAs) with high extinction coefficient (over 2.0×10^5 cm^{-1}) for OSCs (Zhang et al., 2017; Guo et al., 2018). These results motivated us to introduce porphyrin units into polymer acceptor which is rarely reported.

Herein, we introduced 5,15-dibromo-10,20-bis(4-octylphenyl) porphyrin Zinc block as the third unit into N2200 to partly replace the 2,2-bithiophene blocks by random polymerization, obtaining a series of random copolymer PNDI-Px [x represents the percentage of porphyrin (P) fusion ring relative to total acceptor units]. We systematically studied the absorption, energy levels, and crystallinity of polymer PNDI-Px. Ma and co-workers have previously reported that PBDB-T:N2200 has high tolerance to blend ratios (Zhang et al., 2018), and in view of the principle of complementary absorption and energy level matching, solar cells were prepared utilizing PBDB-T as donor and PNDI-Px as acceptor in the active layer. We compared the light harvesting, film morphology, exciton dissociation, charge transport, and the resulting photovoltaic performance of PBDB-T:PNDI-Px and PBDB-T:N2200 blends. With appropriate loadings of the porphyrin unit, the random copolymers have stronger absorption coefficient, up-shifted LUMO energy levels, more flexible main chain, and lower aggregation. Eventually, the device constructed from a PBDB-T:PNDI-P10 blend film generated an improved PCE (5.93%), with overall improved device parameters including open-circuit voltage (V_{OC}) = 0.86 V, J_{SC} = 12.84 mA/cm^2, and FF = 54.34%, compared with N2200-based device.

TABLE 1 | Molecular weight, thermal transition, and optical properties of polymer PNDI-P(x) and N2200.

Polymer	Mn (kDa)	PDI	T_m (°C)	T_c (°C)	λ_{max} (nm)	E_g^{opt} (eV)
N2200	_	_	330.04	298.46	706	1.50
PNDI-P5	265.4	2.12	319.25	293.11	707	1.46
PNDI-P10	250.4	2.32	320.78	291.58	695	1.47
PNDI-P20	284.7	2.29	345.40	314.25	683	1.47

RESULTS AND DISCUSSION

Material Synthesis and Characterization

The new random copolymers PNDI-Px were synthesized by stille coupling polymerization of three monomers, 4,9-Dibromo-2,7-bis(2-octyldodecyl)benzo[lmn][3,8]phenanthroline-1,3,6,8(2H,7H)-tetraone ($NDIBr_2$), 5,15-dibromo-10,20-bis(4-octylphenyl)porphyrin zinc, and 5,5′-bis(trimethylstannyl)-2,2′-bithiophene (**Scheme 1**). The detailed procedures are summarized in the supporting information. All the novel random polymers dissolve well in common organic solvents like tetrahydrofuran (THF), chlorobenzene (CB), o-dichlorobenzene (o-DCB) as well as chloroform (CF). The NMR spectra were used to confirm the structures of the copolymers (**Figures S1–S3**, Supporting Information). Thermogravimetric analysis (TGA) shows that the thermal decomposition temperature (T_d) of N2200 and PNDI-Px is about 420°C at a weight loss of 5% (**Figure S4**), which indicates that the polymers have sufficient thermal stability in future electronic device applications. The number average molecular weights (Mn) of the polymers were measured by the Waters gel permeation chromatography with THF as solvent, as shown in **Figure S5** and **Table 1**. The Mn values of PNDI-P5, PNDI-P10, and PNDI-P20 are 265.4, 250.4, and 284.7 kDa with the corresponding polydispersity index (PDI) of 2.12, 2.32, and 2.29, respectively.

The solid-state transition state of the polymers was characterized by differential scanning calorimetry (DSC) and depicted in **Figure 1A** and **Table 1**. All the new acceptor copolymers show only one melting transition on heating and one crystallization transition on cooling processing, confirming that these copolymers are random copolymers but not the block copolymers or the mixture of two alternative copolymers. N2200 has a melting temperature (T_m) of up to 330°C, which is relatively high in conjugated polymers. The new random copolymers of PNDI-P5 and PNDI-P10 clearly present the reduced Tm and crystallization temperature (T_c). It is because introducing third units into the polymer backbone by random copolymerization often reduces the ordering of the crystallinity of resulting copolymers (Li et al., 2016). However, for PNDI-P20, too many porphyrin units included

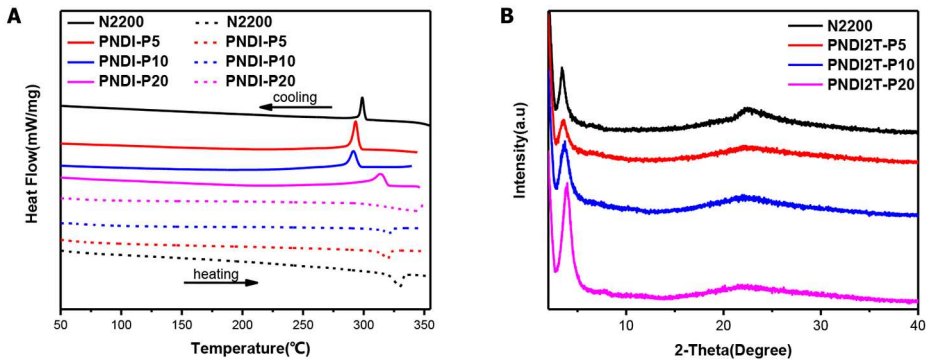

FIGURE 1 | (A) DSC thermograms of neat PNDI-Px and N2200, measured with a scan rate of 10°C per minute. **(B)** X-ray diffraction patterns of the polymer PNDI-Px and N2200 in film.

in the backbone results in the slightly improved T_m and T_c, probably caused by the stronger intramolecular interactions from the large conjugate plane of porphyrin. So as to deeply study the molecular packing and crystallization of new random copolymer PNDI-Px, X-ray diffraction (XRD) was employed (**Figure 1B**). It can be clearly seen from the XRD plot that as the amount of porphyrin units increases, the diffraction peak of the PNDI-Px film decreases first and then increases at low angles, implying that crystallinity of the PNDI-Px also decreases first and then increases. It reveals that random copolymerization of small loadings of the porphyrin group into the backbone can reduce regularity of molecular chains and obtain more flexible backbone, which facilitate the interface contact between donor and acceptor and, consequently, optimization of morphology, whereas the loading of excessive porphyrin leads to greater crystallization, probably due to the large conjugate plane of the porphyrin itself. This phenomenon is in accordance with the DSC observation.

The UV-Vis absorption spectra described the optical absorption properties of N2200 and PNDI-Px in CF solutions and thin films (**Figure 2A, Figure S6**). In solution and film, the absorption curves of PNDI-P5, PNDI-P10, and PNDI-P20 are similar to N2200, with two different absorption bands centered at 320–420 and 570–780 nm, which is caused by the excitations

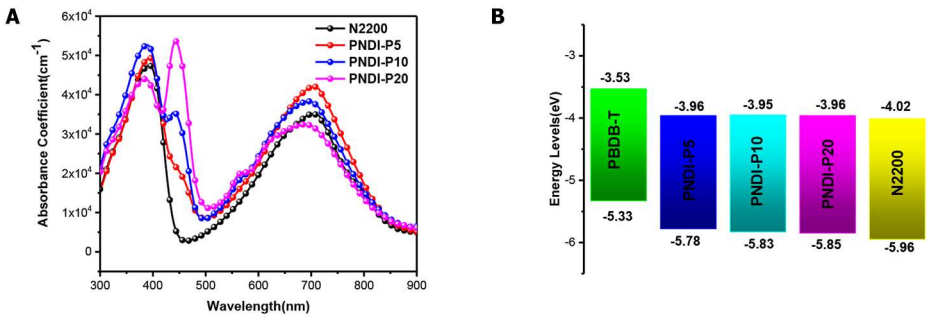

FIGURE 2 | (A) Absorption coefficients of polymer PNDI-Px and N2200 in thin film. **(B)** Energy levels of PBDB-T, PNDI-Px and N2200.

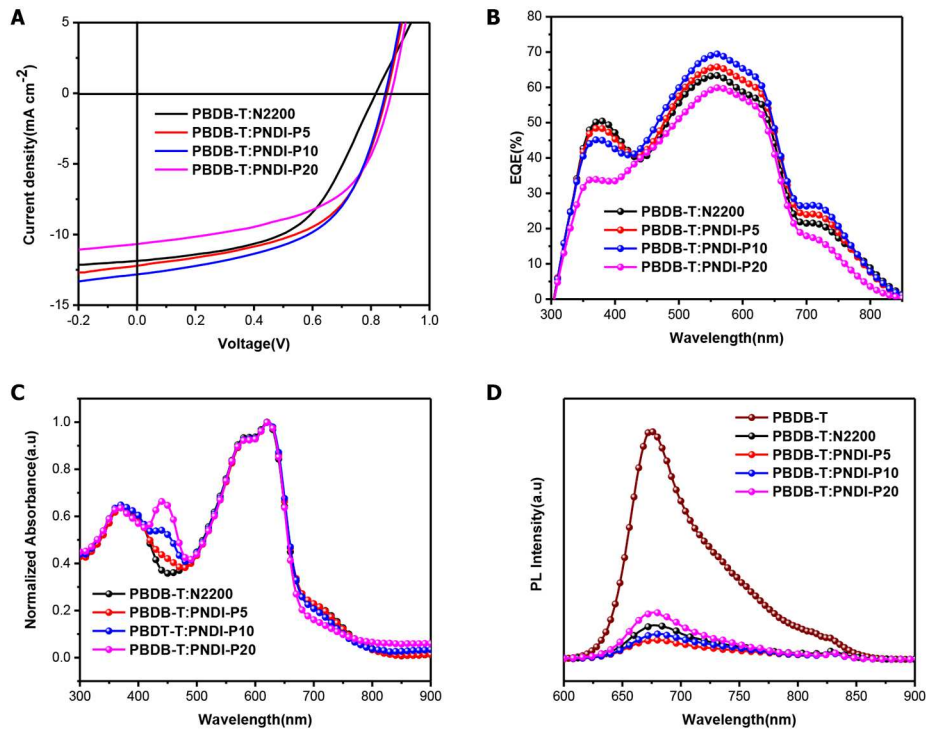

FIGURE 3 | (A) J–V curves of PBDB-T:PNDI-P(x) (2:1 w:w) and PBDB-T:N2200 (2:1 w:w) solar cells. **(B)** EQE spectrograms for the optimal PBDB-T: PNDI-Px all-polymer solar cells. **(C)** Normalized optical absorption of PBDB-T:PNDI-P(x) (2:1 w:w) and PBDBT:N2200 (2:1 w:w) blend films. **(D)** PL emission spectra (580 nm excitation) of neat PBDB-T donor film and PBDB-T:PNDI-P(x) blend films.

with the π-π* manifolds of local NDI and intramolecular charge transfer (ICT) character, respectively. Strikingly, as the content of porphyrin incorporation increases, the absorption peak (absorption bands centered at 420–470 nm) of porphyrin fusion ring becomes more and more obvious. The absorption intensity of PNDI-P20 at 420–470 nm is most pronounced, proving the highest loading of porphyrin. In addition, the absorption intensity at 570–780 nm of copolymer PNDI-P5 and PNDI-P10 is also enhanced compared with the N2200. Therefore, incorporation of the third porphyrin unit by random copolymerization is a useful way to increase the light-harvesting of the NDI-based polymer acceptor. Compared with N2200, the absorption intensity of PNDI-P20 at 570–780 nm is slightly decreased, which is mainly due to the increase of molecular disorder and decrease of intramolecular interaction caused by the introduction of porphyrin. As shown in **Figure 2A**, with the increase of porphyrin content, the absorption coefficient of PNDI-Px film gradually improved in comparison to N2200. The absorption coefficients for N2200, PNDI-P5, PNDI-P10, and PNDI-P20 film are 4.7×10^4, 5.0×10^4, 5.3×10^4, and 5.4×10^4 cm^{-1}, respectively. Similarly, the absorption coefficients for N2200, PNDI-P5, PNDI-P10, and PNDI-P20 solution are 28.8, 35.1, 35.6, and 38.1 L $g^{-1} \cdot cm^{-1}$, respectively, showing the same tendency to those of films (**Figure S6**). In the light of the film absorption onsets, the optical bandgaps (Eg) of N2200, PNDI-P5, PNDI-P10, and PNDI-P20 are estimated to be 1.44, 1.53, 1.55, and 1.56 eV, respectively (**Table 1**).

The LUMO and highest occupied molecular orbital (HOMO) energy levels of PNDI-Px, N2200, and ferrocene were evaluated by cyclic voltammetry (CV). As depicted in the energy level diagrams (**Figure 2B, Figure S7**), the values of LUMO energy level for N2200, PNDI-P5, PNDI-P10, and PNDI-P20 are −4.01, −3.96, −3.95, and −3.96 eV, respectively. The values of HOMO energy level for N2200, PNDI-P5, PNDI-P10, and PNDI-P20 are −5.95, −5.78, −5.83, and −5.85 eV, respectively, showing that introduction of porphyrin units into the NDI-based copolymer can effectively raise LUMO and HOMO energy levels. The raised LUMO energy levels would be conducive to realize high V_{OC} in the OSC device.

Photovoltaic Properties

All-PSCs is prepared to characterize the photovoltaic properties of novel terpolymer acceptors. The photovoltaic devices based on PBDB-T:PNDI-Px and PBDB-T:N2200 have the conventional construction of indium tin oxide (ITO)/ZnO/PBDB-T:acceptor/MoO_3/Ag fabricated with CB as the processing solvent. The active layer of PBDB-T:PNDI-Px and PBDB-T:N2200 was fabricated with the ratio 2:1 (wt:wt) and annealed at 150°C for 10 min without using any solvent additives or other special treatments. The current density–voltage (J–V) curves of the all-PSCs are depicted in **Figure 3A** and the corresponding parameters are presented in **Table 2**. The

TABLE 2 | Photovoltaic properties of thermally annealed (150°C for 10 min) PBDB-T: N2200 (2:1 wt/wt) and PBDB-T: PNDI-P(x) (2:1 wt/wt) all-polymer solar cells.

Active layer	V_{OC} [V]	J_{SC} [mA cm^{-1}]	FF [%]	PCE [%]
PBDB-T: N2200	0.82	11.87 [11.32][a]	54.16	5.27 [5.15][b]
PBDB-T: PNDI-P5	0.86	12.21 [11.79]	55.99	5.86 [5.77]
PBDB-T: PNDI-P10	0.85	12.84 [12.32]	54.34	5.93 [5.86]
PBDB-T: PNDI-P20	0.87	10.67 [10.09]	54.31	5.04 [4.92]

[a] *The J_{SC} integrated from the EQE spectrum.*
[b] *The values in the square brackets stand for the average PCEs from the 10 devices.*

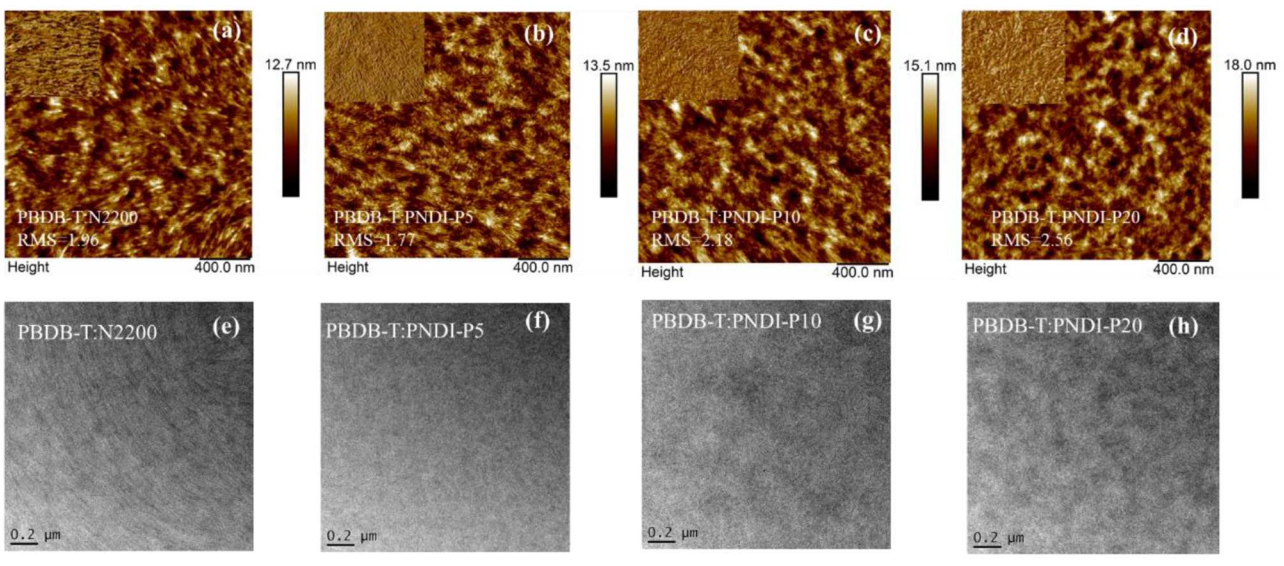

FIGURE 4 | (a–d) AFM images of PBDB-T:PNDI-P(x) (2:1 w:w) and PBDBT:N2200 (2:1 w:w) blend films. **(e–h)** TEM images of PBDB-T:PNDI-P(x) (2:1 w:w) and PBDB-T:N2200 (2:1 w:w) blended films on the actual optimum devices.

PBDB-T:N2200 solar cell exhibits a PCE of 5.27% with a V_{OC} of 0.82 V, a J_{SC} of 11.87 mA/cm^2, and a *FF* of 54.16%, which is well-consistent with the devices we reported previously (Chen et al., 2018). The PBDB-T:PNDI-P5 solar cell presents overall improved device parameters in comparison to PBDB-T:N2200 cells, including a superior PCE of 5.86%, a higher J_{SC} of 12.21 mA/cm^2, a higher V_{OC} of 0.86, and a higher *FF* of 55.99%. The overall enhanced device parameters of J_{SC}, V_{OC}, and *FF* can be attributed to improved extinction coefficient, raised LUMO level and reduced crystallization, respectively. Furthermore, the device performance based on PNDI-P10 is further improved and the best device is obtained, which is mainly due to the further improvement of the absorption coefficient of PNDI-P10. The champion device with the PBDB-T:PNDI-P10 active layer shows a PCE of 5.93% with a J_{SC} of 12.84 mA/cm^2, a V_{OC} of 0.85 V, and a *FF* of 54.34%. Besides, the PNDI-P20-based device also exhibits a higher V_{OC} and *FF*, but J_{SC} dropped significantly, which is ascribed to the increased crystallinity of PBDB-T:PNDI-P20 blended films.

The external quantum efficiency (EQE) spectrograms of the all-PSCs are plotted in **Figure 3B**. Similar to the blend film UV results (**Figure 3C**), the EQE curves of the PBDB-T:PNDI-Px-based cells exhibit response over the region between 300 and 850 nm. The PBDB-T:PNDI-P5-based and the PBDB-T:PNDI-P10-based devices show significant enhancement over the entire spectral response range relative to PBDB-T:N2200 cells, while the PBDB-T:PNDI-P20-based cell presents the weaker EQE response. As shown in **Table 2**, the integral J_{SC} values of EQE curve are in keeping with the values from J–V curves with mismatch <6%.

The photoluminescence (PL) quenching of the blend film was tested by 580 nm excitation light to quantitatively investigate the degree of exciton dissociation in the active layer. As dropped in **Figure 3D** and integrated in **Table S1**, the PL quenching efficiency (ΔPL) of PBDB-T blends is 85% for N2200, 92% for PNDI-P5, 89% for PNDI-P10, and 79% for PNDI-P20. These results indicate that the porphyrin-introduced PNDI-Px-based random copolymer semiconductor can effectively promote exciton dissociation and charge transfer. Meanwhile, the lower ΔPL in the PBDB-T:PNDI-P20 blend illustrates inefficient exciton diffusion and dissociation, which can partly explain its highest light absorption but with the lowest J_{SC} value.

Morphology Characterization

To deeply understand the influence of the porphyrin-incorporated polymer acceptors on the morphology of bulk heterojunctions, the surface morphology of the PBDB-T:N2200 and PBDB-T:PNDI-Px blend films were investigated by atomic force microscopy (AFM) and transmission electron microscopy (TEM). As plotted in **Figures 4a–d**, all the blend films exhibit smooth surfaces with similar RMS roughness values between 1.77 and 2.56 nm. Among these blend films, PBDB-T:PNDI-P5 possesses the most uniform fibril nanophase separation with a suitable phase separation size, which explained its best *FF*. The PBDB-T:PNDI-P10 blended film shows fibril nanophase separation in comparison to PBDB-T:N2200 blended film, in favor of the exciton dissociation, charge transport, and collection. The morphology of PBDB-T:PNDI-P20 blended film presents a slightly bigger aggregation, leading to the reduced *FF* and J_{SC}. As shown in **Figures 4e–h**, this morphological evolution can also be obviously detected by TEM observation. It can be deduced that a proper reduction in the crystallinity of N2200 can boost donor penetration of the acceptor, form an interpenetrating network structure, and have a more suitable domain size and phase separation.

CONCLUSIONS

To sum up, we designed and synthesized a series of novel random copolymers of PNDI-Px that introduce porphyrin into the NDI-based acceptor by random polymerization. Compared with N2200, the new polymer acceptors yield significantly higher absorbance coefficient, up-lying LUMO energy levels, lower crystallinity, and improved film morphology, accompanied by higher J_{SC} and V_{OC} values in solar cells. The polymer PNDI-P10 matched with the donor PBDB-T exhibits champion performance with a PCE of 5.93% with a J_{SC} of 12.84 mA/cm^2, a V_{OC} of 0.85 V, and a *FF* of 54.34%, which are higher than the N2200-based device. These results demonstrate that the incorporation of the third component porphyrin with excellent light harvester ability in the polymer acceptor has great potential in adjusting light absorption coefficient, crystallinity, and phase separation size of all-PSCs.

DATA AVAILABILITY STATEMENT

All datasets generated for this study are included in the article and/or the **Supplementary Material**.

AUTHOR CONTRIBUTIONS

JL and DC designed, synthesized, and characterized polymeric acceptors. ML, BH, and QH fabricated and characterized all-PSCs devices. SD and WX characterized the morphology of active layer. LC, FW, and YC guided material synthesis, device preparation, and characterization. JL and LC wrote the manuscript. All authors were responsible for discussing the results.

ACKNOWLEDGMENTS

LC thanks the National Natural Science Foundation of China (NSFC) (51673092, 51973087, and 21762029) for financial support.

SUPPLEMENTARY MATERIAL

The Supplementary Material for this article can be found online at: https://www.frontiersin.org/articles/10.3389/fchem.2020.00310/full#supplementary-material

REFERENCES

Bhosale, S. V., Jani, C. H., and Langford, S. J. (2008). Chemistry of naphthalene diimides. *Chem. Soc. Rev.* 37, 331–342. doi: 10.1039/b615857a

Chen, D., Yao, J., Chen, L., Yin, J., Lv, R., Huang, B., et al. (2018). Dye-incorporated polynaphthalenediimide acceptor for additive-free high-performance all-polymer solar cells. *Angew. Chem. Int. Ed.* 57, 4580–4584. doi: 10.1002/anie.201800035

Cui, C. (2018). Recent progress in fused-ring based nonfullerene acceptors for polymer solar cells. *Front. Chem.* 6:404. doi: 10.3389/fchem.2018.00404

Cui, Y., Yao, H., Zhang, J., Zhang, T., Wang, Y., Hong, L., et al. (2019). Over 16% efficiency organic photovoltaic cells enabled by a chlorinated acceptor with increased open-circuit voltages. *Nat. Commun.* 10:2515. doi: 10.1038/s41467-019-10351-5

Diao, Y., Zhou, Y., Kurosawa, T., Shaw, L., Wang, C., Park, S., et al. (2015). Flow-enhanced solution printing of all-polymer solar cells. *Nat. Commun.* 6:7955. doi: 10.1038/ncomms8955

Dou, C., Long, X., Ding, Z., Xie, Z., Liu, J., Wang L., et al. (2016). An electron-deficient building block based on the b? n unit: an electron acceptor for all-polymer solar cells. *Angew. Chem. Int. Ed.* 55, 1436–1440. doi: 10.1002/anie.201508482

Fan, B., Zhang, D., Li, M., Zhong, W., Zeng, Z., Ying, L., et al. (2019). Achieving over 16% efficiency for single-junction organic solar cells. *Sci. China Chem.* 62, 746–752. doi: 10.1007/s11426-019-9457-5

Gao, L., Zhang, Z. G., Xue, L., Min, J., Zhang, J., Wei, Z., et al. (2016). All-polymer solar cells based on absorption-complementary polymer donor and acceptor with high power conversion efficiency of 8.27%. *Adv. Mater.* 28, 1884–1890. doi: 10.1002/adma.201504629

Guo, Y., Liu, Y., Zhu, Q., Li, C., Jin, Y., Puttisong, Y., and Li, W. (2018). Effect of side groups on the photovoltaic performance based on porphyrin–perylene bisimide electron acceptors. *ACS Appl. Mater. Inter.* 10, 32454–32461. doi: 10.1021/acsami.8b10955

Jiang, K., Wei, Q., Lai, J. Y. L., Peng, Z., Kim, H. K., Yuan, J., et al. (2019). Alkyl chain tuning of small molecule acceptors for efficient organic solar cells. *Joule* 3, 3020–3033. doi: 10.1016/j.joule.2019.09.010

Kang, H., Lee, W., Oh, J., Kim, T., Lee, C., Kim B. J., et al. (2016). From fullerene–polymer to all-polymer solar cells: The importance of molecular packing, orientation, and morphology control. *Accounts Chem. Res.* 49, 2424–2434. doi: 10.1021/acs.accounts.6b00347

Kim, T., Kim, J. H., Kang, T. E., Lee, C., Kang, H., Shin, M., et al. (2015). Flexible, highly efficient all-polymer solar cells. *Nat. Commun.* 6:8547. doi: 10.1038/ncomms9547

Kolhe, N. B., Tran, D. K., Lee, H., Kuzuhara, D., Yoshimoto, N., Koganezawa, T., et al. (2019). New random copolymer acceptors enable additive-free processing of 10.1% efficient all-polymer solar cells with near-unity internal quantum efficiency. *ACS Energy Lett.* 4, 1162–1170. doi: 10.1021/acsenergylett.9b00460

Lee, U. H., Hadmojo, W. T., Kim, J., Eom, S. H., Yoon, S. C., Jang, S. Y., et al. (2018). Development of n-type porphyrin acceptors for panchromatic light-harvesting fullerene-free organic solar cells. *Front. Chem.* 6:473. doi: 10.3389/fchem.2018.00473

Li, W., An, Y., Wienk, M. M., and Janssen, R. A. (2015). Polymer–polymer solar cells with a near-infrared spectral response. *J. Mater. Chem. A* 3, 6756–6760. doi: 10.1039/C5TA01042J

Li, W., Roelofs, W. C., Turbiez, M., Wienk, M. M., Janssen, R. J., et al. (2014). Polymer solar cells with diketopyrrolopyrrole conjugated polymers as the electron donor and electron acceptor. *Adv. Mater.* 26, 3304–3309. doi: 10.1002/adma.201305910

Li, Y. (2012). Molecular design of photovoltaic materials for polymer solar cells: toward suitable electronic energy levels and broad absorption. *Acc. Chem. Res.* 45, 723–733. doi: 10.1021/ar2002446

Li, Z., Xu, X., Zhang, W., Meng, X., Ma, W., Yartsev, A., et al. (2016). High performance all-polymer solar cells by synergistic effects of fine-tuned crystallinity and solvent annealing. *J. Am. Chem. Soc.* 138, 10935–10944. doi: 10.1021/jacs.6b04822

Li, Z., Ying, L., Zhu, P., Zhong, W., Li, N., Liu, F., et al. (2019a). A generic green solvent concept boosting the power conversion efficiency of all-polymer solar cells to 11%. *Energy Environ. Sci.* 12, 157–163. doi: 10.1039/C8EE02863J

Li, Z., Zhong, W., Ying, L., Liu, F., Li, N., Huang, F., et al. (2019b). Morphology optimization via molecular weight tuning of donor polymer enables all-polymer solar cells with simultaneously improved performance and stability. *Nano Energy* 64:103931. doi: 10.1016/j.nanoen.2019.103931

Liu, X., Zhang, C., Duan, C., Li, M., Hu, Z., Wang, J., et al. (2018). Morphology optimization via side chain engineering enables all-polymer solar cells with excellent fill factor and stability. *J. Am. Chem. Soc.* 140, 8934–8943. doi: 10.1021/jacs.8b05038

Liu, Q., Jiang, Y., Jin, K., Qin, J., Xu, J., Li, W., et al. (2020). 18% efficiency organic solar cells. *Sci. Bull.* 65, 272–275. doi: 10.1016/j.scib.2020.01.001

Mahmood, A., Hu, J. Y., Xiao, B., Tang, A., Wang, X., and Zhou, E. (2018). Recent progress in porphyrin-based materials for organic solar cells. *J. Mater. Chem. A* 6, 16769–16797. doi: 10.1039/C8TA06392C

Meng, Y., Wu, J., Guo, X., Su, W., Zhu, L., Fang, J., et al. (2019). 11.2% Efficiency all-polymer solar cells with high open-circuit voltage. *Sci. China Chem.* 62, 845–850. doi: 10.1007/s11426-019-9466-6

Schubert, M., Dolfen, D., Frisch, J., Roland, S., Steyrleuthner, R., Stiller, B., et al. (2012). Influence of aggregation on the performance of all-polymer solar cells containing low-bandgap naphthalenediimide copolymers. *Adv. Energy Mater.* 2, 369–380. doi: 10.1002/aenm.201100601

Seo, J. H., Gutacker, A., Sun, Y., Wu, H., Huang, F., Cao, Y., et al. (2011). Improved high-efficiency organic solar cells via incorporation of a conjugated polyelectrolyte interlayer. *J. Am. Chem. Soc.* 133, 8416–8419. doi: 10.1021/ja2037673

Søndergaard, R., Hösel, M., Angmo, D., Larsen-Olsen, T. T., and Krebs, F. C. (2012). Roll-to-roll fabrication of polymer solar cells. *Mater. Today* 15, 36–49. doi: 10.1016/S1369-7021(12)70019-6

Su, Y. W., Lan, S. C., and Wei, K. H. (2012). Organic photovoltaics. *Mater. Today* 15, 554–562. doi: 10.1016/S1369-7021(13)70013-0

Wang, Y., Yan, Z., Guo, H., Uddin, M. A., Ling, S., Zhou, X., et al. (2017). Effects of bithiophene imide fusion on the device performance of organic thin-film transistors and all-polymer solar cells. *Angew. Chem. Int. Ed.* 56, 15304–15308. doi: 10.1002/anie.201708421

Wu, J., Meng, Y., Guo, X., Zhu, L., and Liu, F. (2019). All-polymer solar cells based on a novel narrow-bandgap polymer acceptor with power conversion efficiency over 10%. *J. Mater. Chem. A* 7, 16190–16196. doi: 10.1039/C9TA04611A

Xiong, J., Jin, K., Jiang, Y., Qin, J., Wang, T., Liu, J., et al. (2019). Thiolactone copolymer donor gifts organic solar cells a 16.72% efficiency. *Sci. Bull.* 64, 1573–1576. doi: 10.1016/j.scib.2019.10.002

Xu, X., Feng, K., Bi, Z., Ma, W., Zhang, G., and Peng, Q. (2019). Single-junction polymer solar cells with 16.35% efficiency enabled by a platinum (II) complexation strategy. *Adv. Mater.* 31:1901872. doi: 10.1002/adma.201901872

Xu, X., Li, Z., Wang, J., Lin, B., Ma, W., Xia, Y., et al. (2018). High-performance all-polymer solar cells based on fluorinated naphthalene diimide acceptor polymers with fine-tuned crystallinity and enhanced dielectric constants. *Nano Energy* 45, 368–379. doi: 10.1016/j.nanoen.2018.01.012

Yan, H., Chen, Z., Zheng, Y., Newman, C., Quinn, J. R., and Dötz, F. (2009). A high-mobility electron-transporting polymer for printed transistors. *Nature* 457, 679–686. doi: 10.1038/nature07727

Yuan, J., Zhang, Y., Zhou, L., Zhang, G., Yip, H. L., Lau, T. K., et al. (2019). Single-junction organic solar cell with over 15% efficiency using fused-ring acceptor with electron-deficient core. *Joule* 3, 1140–1151. doi: 10.1016/j.joule.2019.01.004

Zhang, A., Li, C., Yang, F., Zhang, J., Wang, Z., Wei, Z., and Li, W. (2017). An electron acceptor with porphyrin and perylene bisimides for efficient non-fullerene solar cells. *Angew. Chem. Int. Ed.* 56, 2694–2698. doi: 10.1002/anie.201612090

Zhang, X., and Jin, R. (2019). Rational design of low-band gap star-shaped molecules with 2, 4, 6-triphenyl-1, 3, 5-triazine as core and diketopyrrolopyrrole derivatives as arms for organic solar cells applications. *Front. Chem.* 7:122. doi: 10.3389/fchem.2019.00122

Zhang, Y., Xu, Y., Ford, M. J., Li, F., Sun, J., Ling, X., et al. (2018). Thermally stable all-polymer solar cells with high tolerance on blend ratios. *Adv. Energy Mater.* 8:1800029. doi: 10.1002/aenm.201800029

Zhou, N., and Facchetti, A. (2018). Naphthalenediimide (NDI) polymers for all-polymer photovoltaics. *Mater. Today* 21, 377–390. doi: 10.1016/j.mattod.2018.02.003

Zhu, L., Zhong, W., Qiu, C., Lyu, B., Zhou, Z., Zhang, M., et al. (2019). Aggregation-induced multilength scaled morphology enabling 11.76% efficiency in all-polymer solar cells using printing fabrication. *Adv. Mater.* 31:1902899. doi: 10.1002/adma.201902899

Conflict of Interest: The authors declare that the research was conducted in the absence of any commercial or financial relationships that could be construed as a potential conflict of interest.

frontiers in Chemistry

ORIGINAL RESEARCH
published: 28 April 2020
doi: 10.3389/fchem.2020.00255

An Alternating D1-A-D2-A Conjugated Ternary Copolymer Containing [1,2,5]selenadiazolo[3,4-c]pyridine Unit With Photocurrent Response Up to 1,100 nm

Xuelong Huang[1]*, *Ning Lan*[1], *Yunnan Yan*[1], *Xin Hu*[1] and *Shengjian Liu*[2]*

[1] Department of Pharmaceutical Engineering, College of Pharmacy, Gannan Medical University, Ganzhou, China,
[2] Guangzhou Key Laboratory of Materials for Energy Conversion and Storage, Guangdong Provincial Engineering Technology Research Center for Materials for Energy Conversion and Storage, School of Chemistry, South China Normal University, Guangzhou, China

OPEN ACCESS

Edited by:
Jiangang Liu,
Shantou University, China

Reviewed by:
Baofeng Zhao,
Xi'an Modern Chemistry Research Institute, China
Biao Xiao,
Jianghan University, China

***Correspondence:**
Xuelong Huang
huangxuelong1988@126.com
Shengjian Liu
shengjian.liu@m.scnu.edu.cn

Specialty section:
This article was submitted to Physical Chemistry and Chemical Physics, a section of the journal Frontiers in Chemistry

Received: 11 February 2020
Accepted: 17 March 2020
Published: 28 April 2020

Citation:
Huang X, Lan N, Yan Y, Hu X and Liu S (2020) An Alternating D1-A-D2-A Conjugated Ternary Copolymer Containing [1,2,5]selenadiazolo[3,4-c]pyridine Unit With Photocurrent Response Up to 1,100 nm. Front. Chem. 8:255. doi: 10.3389/fchem.2020.00255

Two narrow band gap conjugated ternary copolymers comprising two electron-rich (donor, D) and one electron-deficient (acceptor, A) moieties regularly alternating along the polymer backbone were designed and synthesized. The polymers with the repeating unit in a D1-A-D2-A manner were constructed by copolymerizing a bisstannyled-D1 (D1 = n-alkyl-substituted cyclopentadithiophene) and a dibromo-monomer (Br-A-D2-A-Br, D2 = branched-alkyl-substituted cyclopentadithiophene, A =[1,2,5]selenadiazolo[3,4-c]pyridine or 5-fluorobenzo[c][1,2,5]selenadiazole) through a palladium-catalyzed Stille polymerization. This approach that enables variations in the donor fragment substituents can not only control the polymer regiochemistry but also the solubility. Two ternary copolymers exhibited absorbance up to near-infrared region along with relatively narrow band gap in the range of 1.02–1.26 eV. The polymeric photovoltaic cells based on CDTPSE/$PC_{61}BM$ show the short circuit density of 1.45 mA cm^{-2}, open current voltage of 0.53 V, and photocurrent spectra response from 300 to 1,150 nm under AM 1.5 simulator (100 mW cm^{-2}). It is indicated that it can be potentially applied to near infrared photodetectors.

Keywords: D1-A-D2-A, [1,2,5]selenadiazolo[3,4-c]pyridine, polymer photodetectors, near-infrared absorption, ternary copolymer

HIGHLIGHTS

- Two novel D2-A-D1-A type copolymers containing [1,2,5]selenadiazolo[3,4-c]pyridine or 5-fluorobenzo[c][1,2,5]selenadiazole were synthesized.
- The D2-A-D1-A structure made control over the polymer regiochemistry and solubility possible.
- Broad photocurrent response up to 1,100 nm was realized.

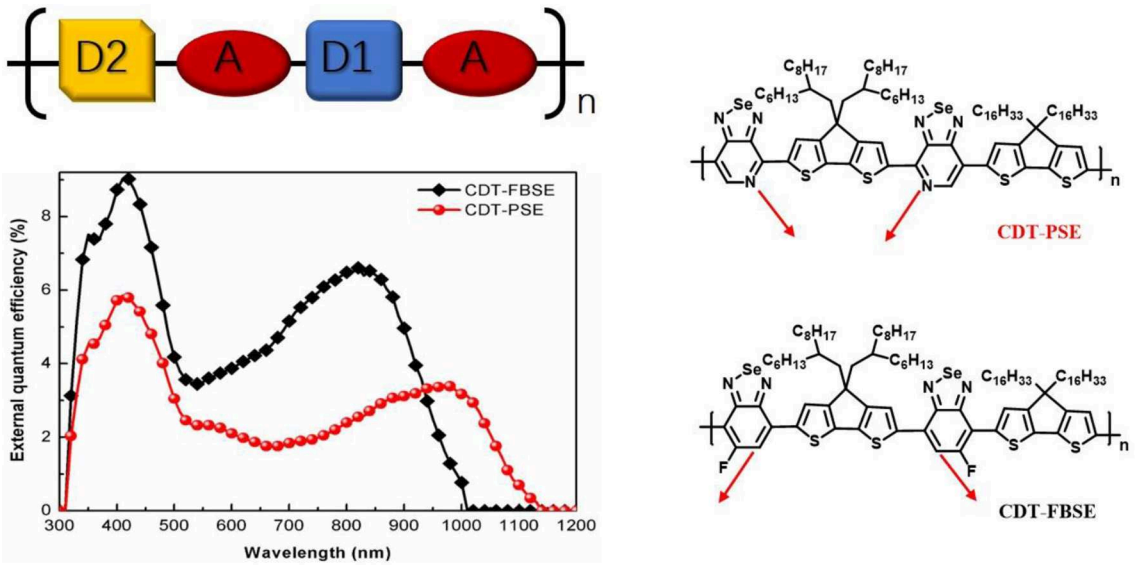

GRAPHICAL ABSTRACT | The D1-A-D2-A structure ternary copolymers and the external quantum efficiency.

INTRODUCTION

Conjugated polymers have attracted both industrial and academic interests due to the potential for large-area, flexible, and low-cost applications in recent years. Great progress has been made in related research areas based on conjugated polymers including polymer light-emitting diode (PLED), polymeric field-effect transistor (PFET), polymer solar cell (PSC) (Zhao et al., 2016). The conjugated polymers with narrow band gap are promising for the development of polymer photodetectors (PPDs) due to the broad absorption and photoresponse (Gong et al., 2009). Photodetectors from the ultraviolet (UV) to near-infrared (NIR) wavelength is critical for multi-functional applications including chemical/biological sensing, image sensing, environmental monitoring, remote control (Chen et al., 2016). Conventional photodectors exhibited limited absorption ranges through inorganic materials including GaN, Si, InGaAs (Hu et al., 2013). Polymer photodetectors (PPDs) achieve broad spectral response and high sensitivity through photoinduced electron transfer from donor materials (conjugated polymers) to acceptor materials (fullerene derivatives) (Chen and Cao, 2009). For polymer photodetectors applications, donor materials with a narrow band gap are desirable because of their contribution to obtaining photocurrent at long wavelength including NIR region (Hendriks et al., 2014). The common methods to reduce the band gap of conjugated polymers such as extension of conjugation length or introduction of strong donor and acceptor groups can often lead to a rise in the highest occupied molecular orbital (HOMO) energy level (Dong et al., 2013). High-lying highest occupied molecular orbital (HOMO) energy level of conjugated copolymers is essentially unfavorable for ambient stability of devices (Miao et al., 2018). The open circuit voltage (V_{oc}) of OPVs including photodetectors is directly related to the bang gap between the HOMO of donor materials (conjugated polymers) and the lowest unoccupied molecular orbital (LUMO) energies of the acceptor (fullerene). To promote the V_{oc}, the D-A type of conjugated copolymers containing weak donor unit (D, donor) and strong acceptor (A, acceptor) along polymer backbone are synthesized (Han et al., 2017). The "weak donor-strong acceptor" strategy which is widely used in the synthesis of donor materials in OPVs can not only maintain low-lying HOMO energy levels to promote the V_{oc} but also effectively reduce band gap through intramolecular charge transfer (ICT) (Zhou et al., 2010). It is difficult to balance between selecting weak donor to promote the V_{oc} value and selecting strong donor to broad spectral range to the NIR. Bazan et al. reported a conjugated polymer containing pyridyl[2,1,3]thiadiazole (PT) acceptor unit with very low E_g-eV_{oc} loss in OPVs by controlling conjugated polymer regioregularity (Wang et al., 2014). It is possible to fabricate promising PPDs materials with strong donor unit in conjugated polymer by controlling the precise orientation of the donor or acceptor units relative to the backbone vector (Qin et al., 2014).

Compared with pyridyl[2,1,3]thiadiazole (PT), [1,2,5]selenadiazolo[3,4-c]pyridine (PSe) has lower band gaps and the wavelength region has longer in near-infrared (NIR) wavelength than the sulfur based analogs (Hou et al., 2008). In fact, some Se-containing electron-acceptor building blocks, such 2,1,3-benzoselenadiazole and the derivatives are generally poorly soluble. In order to overcome the poor solubility and improve the regularity of the polymer, we proposed regular conjugated ternary copolymers consisting of ternary components with the repeating units denoted as D1–A–D2–A (Huang et al., 2015). This means that the solubility of the D1–A–D2–A structure polymer can be altered by changing of the solubilizing groups on D1 or D2 fragment, respectively. Compared with other well-known donor units, the CDT unit

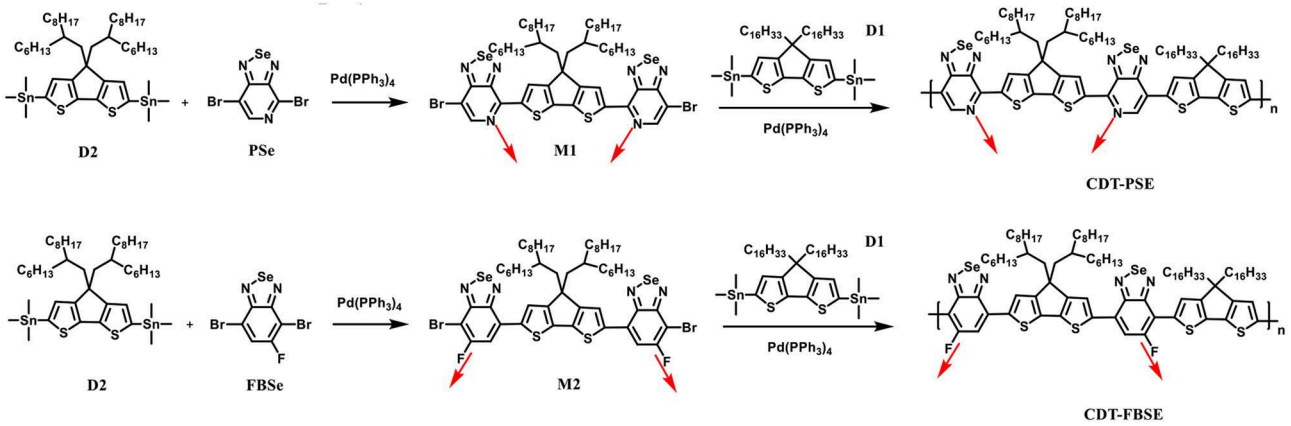

SCHEME 1 | Synthetic route of D1-A-D2-A ternary copolymers.

as a strong donor can provide an easy way to incorporate solubilizing substituents (Zhou et al., 2012). For the acceptor fragment, [1,2,5]selenadiazolo[3,4-c]pyridine (PSe) and 5-fluorobenzo[c][1,2,5]selenadiazole (FBSe) are selected due to the similar property to the S-containing analog, which demonstrates asymmetric reactivity between ortho- and meta-positions (Sun et al., 2012).

RESULTS AND DISCUSSION

Synthesis and Characterization

A stepwise synthetic strategy is required for the preparation of the D1-A-D2-A polymers, see **Scheme 1**. First, the palladium catalyzed Stille coupling reaction of two equivalents of 4,7-dibromo-[1,2,5]selenadiazolo[3,4-c]pyridine with (4,4-bis(2-hexyldecyl)-4H-cyclopenta[2,1-b:3,4-b′]dithiophene-2,6-diyl)bis(trimethylstannane) (D2) provided 4,4′-(4,4-bis(2-hexyldecyl)-4H-cyclopenta[2,1-b:3,4-b′]dithiophene-2,6-diyl)bis(7-bromo-[1,2,5]selenadiazolo[3,4-c]pyridine) (M1). The palladium catalyzed Stille coupling reaction of the D2 with 2 equivalents of 4,7-dibromo-5-fluorobenzo[c][1,2,5]selenadiazole (FBSe) gave the dibromointermediate of 7,7′-(4,4-bis(2-hexyldecyl)-4H-cyclopenta[2,1-b:3,4-b′]dithiophene-2,6-diyl)bis(4-bromo-5-fluorobenzo[c][1,2,5]selenadiazole), which was denoted as M2 (**Supplementary Figures 1–7**).

The asymmetric nature of PSe allows for monofunctionalization resulting in strictly organized PSe orientations, such that the pyridyl nitrogen atoms point toward the CDT fragment in M1 intermediate. For another acceptor fragment, FBSe has the asymmetric reactivity in meta-position, in which the fluorine atoms are far from the CDT fragment in M2 intermediate. M1 and M2 are subsequently polymerized with (4,4-dihexadecyl-4H-cyclopenta[2,1-b:3,4-b′]dithiophene-2,6-diyl)bis(trimethylstannane) (D1) under microwave heating in anhydrous toluene to yield two regioregular, D1-A-D2-A polymers CDT-PSE and CDT-FBSE.

The two polymers were purified by Soxhlet extraction by using methanol, acetone, and hexane successively to remove the oligomer and catalyst. The number-average molecular weight (M_n) and polydispersity index (PDI) of the two polymers were determined by gel permeation chromatography (GPC) at 150°C using 1,2,4-trichlorobenzene as the eluent and polystyrene standards. The number-average molecular weight (M_n) was determined to be 21.9 and 46.1 kDa for CDT-PSE, CDT-FBSE, respectively, with PDI values of 2.7 and 2.3, respectively. Thermal properties of the two polymers were detected by differential scanning calorimetry (DSC) and thermogravimetric analysis (TGA) measurements. No discernable phase transition was realized in DSC characteristics up to 300°C. TGA measurements demonstrated that the decomposition temperatures (corresponding to 5% weight-loss temperatures) were 354.3 and 365.2°C for CDT-PSE and CDTF-BSE, respectively, implying good thermal stabilities of the two polymers (**Supplementary Figure 8**).

Optical Properties

Absorption spectra in the 300–1,400 nm region of CDT-PSE and CDT-FBSE in *o*-dichlorobenzene solution with concentration of ca. 1×10^{-5} g mL^{-1} as well as in thin films are shown in **Figure 1**. Two polymers show two absorption bands. The high energy absorbance band located in the range of 300–500 nm can be attributed to the π-π* transition of D1–A–D2–A backbones in dilute solutions, while the low energy absorbance peak displayed typical dual band features of D–A copolymers with the intramolecular charge transfer (ICT) effects between the donors and the acceptor moieties located at long wavelength up to NIR regions. Broader and further red-shifted bands arise in the solid-state absorption spectra. The maximum absorption edge of CDT-PSE and CDT-FBSE was at 1,200 and 1,000 nm, respectively. Relative to CDT-FBSE, the absorption peak of CDT-PSE as a thin film was broader in width, which is consistent with the greater degree of structural order due to the PSe nitrogen atoms. The optical band gaps (*E*opt g) of the two D1–A–D2–A polymers as estimated from the onset of the absorbance of solid films are in the range of 1.02–1.26 eV.

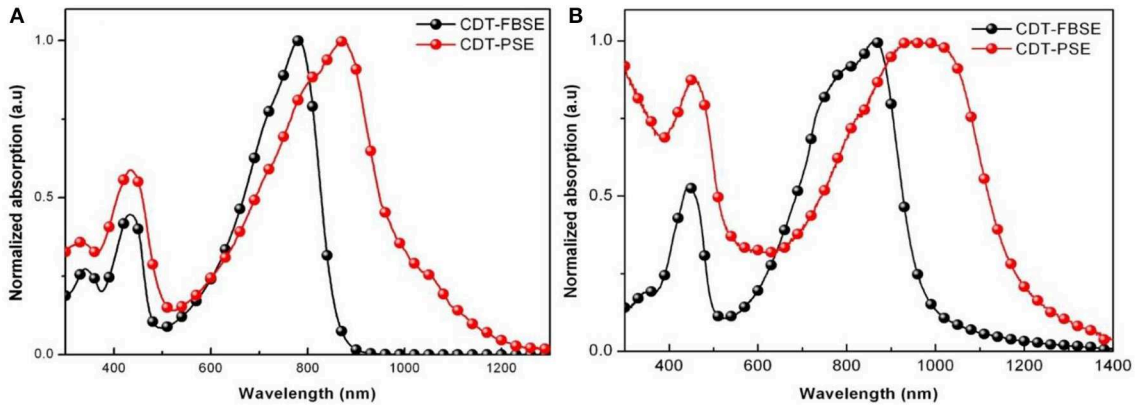

FIGURE 1 | Normalized UV-vis absorption spectra of D2-A-D1-A polymers in *o*-DCB solution **(A)** and in thin films **(B)**.

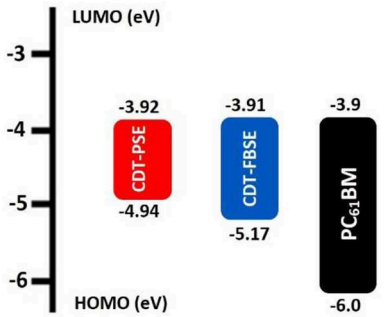

FIGURE 2 | Schematic energy level diagrams of ternary copolymers.

TABLE 1 | Electrochemical properties and molecular weight of the polymers.

	E_{HOMO}[a](ev)	E_{LUMO}[a](ev)	E_g^{opt}[b](ev)	M_n(kDa)	PDI	T_d (°C)
CDT-PSE	−4.94	−3.92	1.02	21.9	2.7	354.3
CDT-FBSE	−5.17	−3.91	1.26	46.1	2.3	365.2

[a]The E_{HOMO} is determined by cyclic voltammetry, E_{LUMO} = -E_{HOMO} + E_g^{opt}. [b]Optical band-gap estimated from the absorption onset as thin films.

Electrochemical Properties

To investigate the influence of regioregularity on the frontier energy levels of the D1–A–D2–A structure polymer, cyclic voltammetry (CV) measurements were performed. The measurement was carried out in tetra(*n*-butyl)ammonium hexafluorophosphate (n-Bu_4NPF_6, 0.1 M in acetonitrile) solution by using a ITO glass electrode as working electrode and saturated calomel electrode (SCE) as a reference electrode at a scan rate of 50 mV s^{-1}. The films of CDT-PSE and CDT-FBSE were cast from *o*-DCB solution with a concentration of 10 mg mL^{-1} and all measurements were performed under an inert atmosphere. The CV characteristics of two polymers are demonstrated in **Figure 2**. It is assumed that the redox potential of Fc/Fc+ was measured as a standard, which has an absolute energy level of −4.80 eV to vacuum. The onset of oxidation (E_{ox}) of the two polymers was estimated to be 0.14, and 0.37 eV for CDT-PSE and CDT-FBSE in the same experimental conditions, respectively (**Supplementary Figure 9**).

Therefore, the highest occupied molecular orbitals (E_{HOMO}) of the two polymers were calculated according to the following equation of E_{HOMO} = −e(E_{ox}+4.80) (eV). Consequently, the HOMO values are −4.94 and −5.17 eV for CDT-PSE and CDT-FBSE, respectively. According to the equation of E_{LUMO} =-E_{HOMO} + Eopt g, the E_{LUMO} are calculated to be −3.92 and −3.91 eV for CDT-PSE and CDT-FBSE, respectively. Detailed electrochemical data are summarized in **Table 1** and **Figure 2**.

Photovoltaic Properties

The photovoltaic properties of the two polymers were investigated by fabricating solar cells with an inverted device structure of ITO/poly[9,9-bis(60-(*N*, *N*-diethylamino)hexyl)fluorene-alt-9,9-bis(3-ethyl(oxetane-3-ethyloxy)hexyl)fluorene] (PFN-OX)/polymer:$PC_{61}BM$/MoO_3/Al. The PFN layer (∼5 nm) was deposited on the top of photoactive layer before deposition of cathode, since it can facilitate electrons extraction from photoactive layer and reduce the work function of ITO. The thickness of MoO_3 layer is about 10 nm and Al electrode thickness is about 80 nm. The photoactive layer of the polymer:$PC_{61}BM$ was fabricated by spin coating from *o*-dichlorobenzene (*o*-DCB) solution. The current density vs. voltage (*J*–*V*) characteristics of the solar cell devices under AM 1.5 G at 100 mW m^{-2} conditions was shown in **Figure 3**. CDT-PSE was achieved a power conversion efficiency (PCE) of 0.24% with an open circuit voltage (V_{oc}) of 0.53 V, a short-circuit current density (J_{sc}) of 1.45 mA cm^{-2}, and a fill factor (FF) of 0.30. The better device performance was achieved based on CDT-FBSE:$PC_{61}BM$ as the photoactive layer, which showed a moderate PCE = 0.49% (V_{oc} =0.63 V, J_{sc} = 2.37 mA cm^{-2}, and FF = 33.2%). We speculated that the moderate value in V_{oc} can be attributed to the decreased HOMO level. The decreased short circuit current (J_{sc}) in CDT-PSE can be attributed to the lack of driving force for the charge separation in the interface of polymer and $PC_{61}BM$ due to the relatively low-lying LUMO energy level of CDT-PSE. The external quantum efficiency (EQE) curves are shown in **Figure 4**.

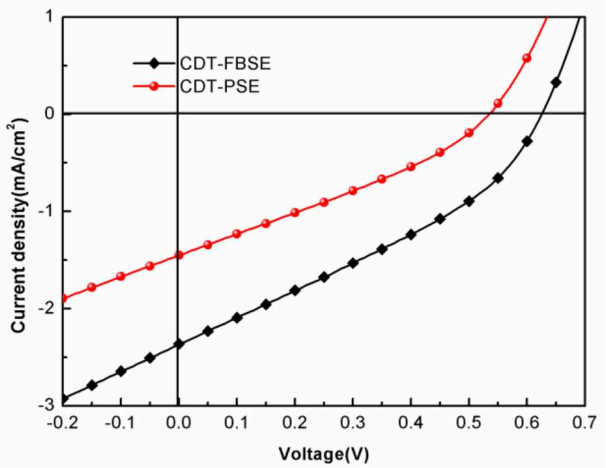

FIGURE 3 | *J-V* characteristics of the devices with the structure of ITO/PFN-OX/polymer: $PC_{61}BM$ (1: 1, wt:wt)/MoO_3/Al under AM 1.5G irradiation (100 mW cm^{-2}).

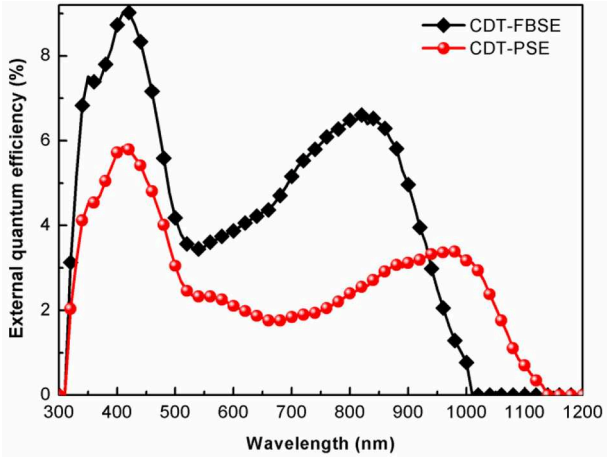

FIGURE 4 | EQE of the photovoltaic devices with configuration of ITO/PFN-OX/polymer: $PC_{61}BM$(1: 1, wt:wt)/MoO_3/Al.

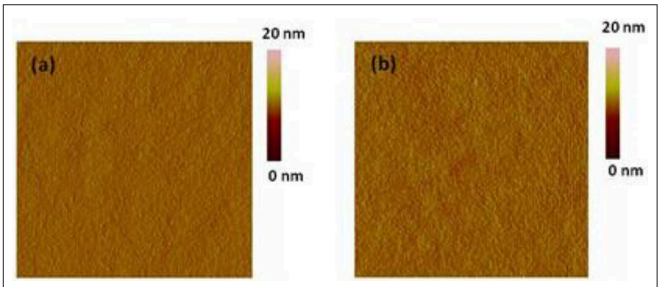

FIGURE 5 | AFM height images of polymer: $PC_{61}BM$ blend films (1:1, wt:wt): CDT-PSE **(A)**, CDT-FBSE **(B)**. All the images are in the size of 5 × 5 μm.

Both the polymers show a broad EQE response from 300 nm to NIR region. The photosensitivity response of CDT-FBSE is higher over a wide range compared to CDT-PSE. But it is worth noting that CDT-PSE exhibits prolonged response beyond 1,100 nm, which reveals its great potential for the application in NIR photodetector.

Morphology

Tapping mode atomic force microscopy (AFM) was investigated the surface topography of the bulk heterojunction polymer: $PC_{61}BM$ (1:1 in wt:wt) blend films (**Figure 5**). The blend film of CDT-PSE: $PC_{61}BM$ showed comparatively smooth surface topography with a root-mean-square roughness (RMS) value of 0.47 nm. From **Figure 5B** one can clearly observe the rough morphology of CDT-FBSE: $PC_{61}BM$ with a root-mean-square (RMS) roughness of 0.42 nm. The smooth surface topography of the polymer/$PC_{61}BM$ components may give rise to this non-optimal nanostructure, which is essentially not favorable for charge carrier transporting to the corresponding electrodes and would lead to relatively low J_{sc} of the device.

CONCLUSION

In conclusion, two novel D1-A-D2-A ternary copolymers containing asymmetric reactivity unit ([1,2,5]selenadiazolo[3,4-c]pyridine or 5-fluorobenzo[c][1,2,5]selenadiazole) was synthesized by stepwise approach. Incorporating the branched-alkyl-substituted cyclopentadithiophene (D2) to the A-D-A intermediates is of great benefit to solubility and purification of the PSe or FBSe units. We have shown that the D1-A-D2-A repeating structure can control the regiochemistry of the polymer backbone and indicate a much lower E_g-eV_{oc} loss than the D-A analogs. We have presented the n-alkyl-substituted cyclopentadithiophene (D1) to enhance the intermolecular π-stacking interactions. The polymers CDT-PSE and CDT-FBSE show wide light absorption ranges of 300–1,000 and 300–1,100 nm in solid thin film, respectively. The photoresponse wavelengths of the CDT-PSE based on CDT-PSE/$PC_{61}BM$ blends extend to about 1,100 nm, illustrating its great potential for the application in NIR photodetector.

EXPERIMENTAL SECTION

Materials

All reagents were purchased from commercial sources such as from Aldrich, Acros and TCI Chemical Co. The ^1H and ^{13}C NMR spectra were measured on a Bruker AV-300 (300 MHz) in a deuterated chloroform solution with tetramethylsilane(TMS) as the internal standard. Compound 4H-cyclopenta[2,1-b:3,4-b′]dithiophene (2), 4,4-dihexadecyl-4H-cyclopenta[2,1-b:3,4-b′]dithiophene (3),(4,4-dihexadecyl-4H-cyclopenta[2,1-b:3,4-b′]dithiophene-2,6-diyl)bis(trimethylstannane) (D1), (4,4-bis(2-hexyldecyl)-4H-cyclopenta[2,1-b:3,4-b′]dithiophene-2,6-diyl)bis(trimethylstannane) (D2), 5-fluorobenzo[c][1,2,5]thiadiazole(5), 4,7-dibromo-5-fluorobenzo[c][1,2,5]thiadiazole (6) were synthesized according to the reported procedures.

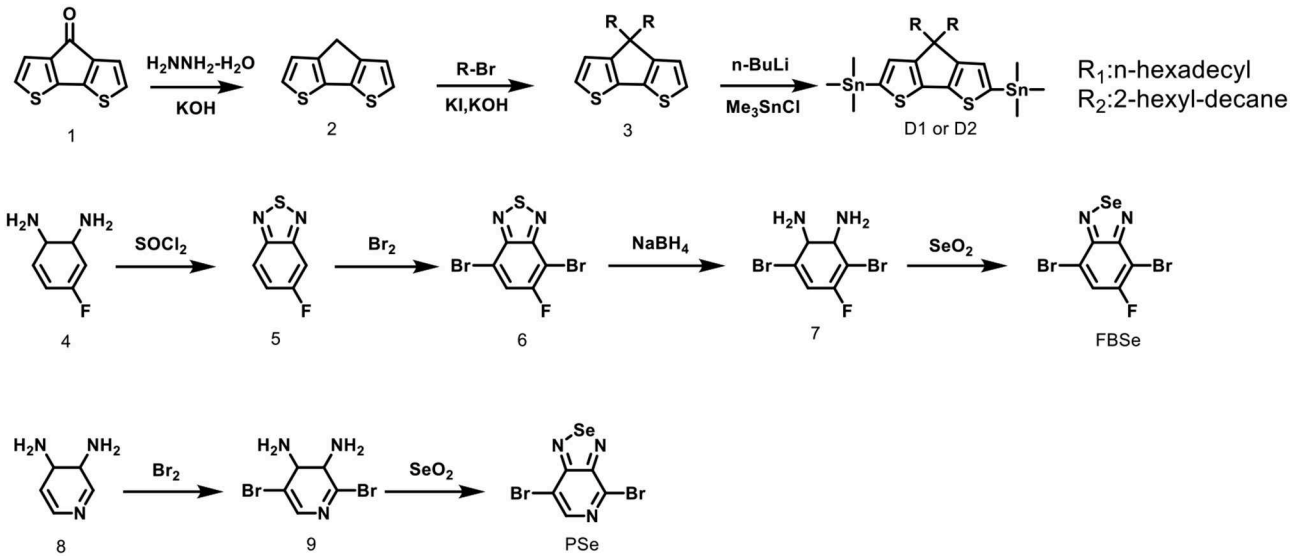

FIGURE 6 | Synthetic routes of monomers.

Synthesis of Intermediates

Compound 3,6-dibromo-4-fluorocyclohexa-3,5-diene-1,2-diamine (7)

Compound 7 was synthesized through the reduction of compound 6 with sodium borohydride in ethanol (**Figure 6**). Compound 6 (5 g, 16 mmol) and ethanol (100 mL) were added to a two-necked round-bottom flask and cooled to 0°C. After sodium borohydride (12.1 g, 320 mmol) was slowly added, the reaction mixture was stirred for 20 h at room temperature. The ethanol was evaporated and the extract was concentrated to obtain pale-yellow compound 7 in 90% yield. ^{1}H NMR (300 MHz, $CDCl_3$, TMS) (ppm): 6.35 (s, 1H); 5.11 (dd, 4H).

Compound 4,7-dibromo-5-fluorobenzo[c][1,2,5]selenadiazole (FBSe)

Compound 7 (0.76 g, 2.67 mmol) and ethanol (60 mL) were added to a two-necked round-bottom flask and heated to refluxing with stirring. After a solution of selenium dioxide (0.312 g, 2.8 mmol) in hot water (5 mL) was slowly added, the reaction mixture was refluxed for 3 h and cooled to room temperature. Then, the precipitate was filtrated, recrystallized from ethyl acetate, and dried. Compound FBSe was obtained as a golden-yellow needle crystal in 87% yield. ^{1}H NMR (300 MHz, $CDCl_3$, TMS) (ppm): 7.85 (d, 1H).

Compound 2,5-dibromo-3,4-dihydropyridine-3,4-diamine (9)

Compound 9 was synthesized through the reaction of compound 8 (9.8 g, 90 mmol) and bromine in hydrobromic acid (48%). The bromine (15 mL) was added dropwise to the vigorously stirred solution at room temperature and the mixture was refluxed for 5 h. Finally, the reaction mixture was cooled to room temperature and filtrated, washed with saturated aqueous sodium thiosulfate solution and distilled water, recrystallized from methanol. Finally, compound 9, the yellow needle crystal was obtained in 51% yield. ^{1}H NMR (300 MHz, $CDCl_3$, TMS) (ppm): 7.52 (s, 1H); 5.97 (d, 2H); 5,03 (d, 2H).

Compound 4,7-dibromo-[1,2,5]selenadiazolo[3,4-c]pyridine (PSe)

Compound 7 (8 g, 30 mmol) and ethanol (120 mL) were added to a two-necked round-bottom flask and heated to refluxing with stirring. After a solution of selenium dioxide (3.34 g, 30 mmol) in hot water (5 mL) was slowly added, the reaction mixture was refluxed for 3 h and cooled to room temperature. Then, the precipitate was filtrated, recrystallized from ethyl acetate, and dried. Compound PSe was obtained as a golden-yellow needle crystal in 90% yield. ^{1}H NMR (300 MHz, $CDCl_3$, TMS) (ppm): 8.74 (s, 1H).

Measurement and Characterization

^{1}H and ^{13}C NMR spectra were measured on Bruker AVANCE Digital 300 MHz NMR workstation or Bruker AVANCE Digital 400 MHz NMR workstation. The number-average molecular weights (*M*n) were determined by Polymer Laboratories PL220 Chromatograph (150°C in 1,2,4-trichlorobenzene) with linear polystyrene as the standard. Cyclic voltammograms (CV) were recorded on CHI 600D electrochemical workstation at a scan rate of 50 mV s^{-1}. The tapping-mode atomic force microscopy images were performed on a Nano-Scope NS3A system (Digital Instrument) to observe the surface morphologies of the ITO-coated glass substrates. UV-vis spectra were obtained by a HP 8453 spectrophotometer. Thermogravimetric analyses (TGA) measurements were carried out with a NETZSCH TG 209 under a heating rate of 10°C min^{-1} and a N_2 flow rate of 20 mL min^{-1}. Differential scanning calorimetry (DSC) were conducted on a Netzsch DSC 204 under N_2 flow at heating and cooling rates of 10°C min^{-1}.

SOLAR CELL DEVICE FABRICATION AND CHARACTERIZATION

PSCs were fabricated with an inverted device structure of ITO/PFN-OX/polymer:$PC_{61}BM$/MoO_3/Al. ITO-coated glass substrates were cleaned in ultrasonic baths by sequentially immersing the substrates in detergent, deionized water, acetone and isopropyl alcohol and dried under a nitrogen stream, followed by a UV-ozone treatment. A 5 nm thin film of polymer PFN-OX (0.5 mg mL^{-1}) was spin-casted on the pre-cleaned ITO substrates, and the PFN-OX films were thermally annealed at 150°C for 20 min. The polymer: $PC_{61}BM$ active blend layer with a thickness of ∼90 nm was prepared by spin-coating the 1,2-dichlorobenzene solution on top of the PFN-OX layer. Finally, 10 nm molybdenum oxide (MoO_3) and 100 nm aluminum were deposited by thermal evaporation under vacuum (∼10^{-6} mbar) in glovebox to complete device fabrication. The characteristic current-voltage (J–V) curves of the resulting PSCs were measured using a Keithley 236 source meter under 100 mW cm^{-2} (1 sun, AM 1.5G spectra, calibrated using a standard Si solar cell and simulator provided by Oriel model 91192). The external quantum efficiency (EQE) measurements were performed by using a QE-R3011 system. A calibrated Si photodiode was used to determine the photosensitivity.

DATA AVAILABILITY STATEMENT

The raw data supporting the conclusions of this article will be made available by the authors, without undue reservation, to any qualified researcher.

AUTHOR CONTRIBUTIONS

XHua: investigation, data curation, and writing-original draft. NL: writing-review & editing. YY: investigation. XHu: data curation. SL: project administration.

FUNDING

This work was financially supported by Natural Science Foundation of Jiangxi Provincial Education Department (no. GJJ190817), the Open Project Fund of Key Laboratory of Radioactive and Rare Scattered Minerals, Ministry of Land and Resources (no. RRSM-KF2018-05) and The Ph.D. Start-up Fund of Gannan Medical University (no. QD201907).

SUPPLEMENTARY MATERIAL

The Supplementary Material for this article can be found online at: https://www.frontiersin.org/articles/10.3389/fchem.2020.00255/full#supplementary-material

REFERENCES

Chen, J., and Cao, Y. (2009). Development of novel conjugated donor polymers for high-efficiency bulk-heterojunction photovoltaic devices. *Acc. Chem. Res.* 42, 1709–1718. doi: 10.1021/ar900061z

Chen, S., Teng, C., Zhang, M., Li, Y., Xie, D., and Shi, G. (2016). A flexible UV–Vis–NIR photodetector based on a perovskite/conjugated-polymer composite. *Adv. Mater.* 28, 5969–5974. doi: 10.1002/adma.201600468

Dong, Y., Cai, W., Wang, M., Li, Q., Ying, L., Huang, F., et al. (2013). [1,2,5]Thiadiazolo[3,4-f]benzotriazole based narrow band gap conjugated polymers with photocurrent response up to 1.1μm. *Org. Electron.* 14, 2459–2467. doi: 10.1016/j.orgel.2013.06.002

Gong, X., Tong, M., Xia, Y., Cai, W., Moon, J. S., Cao, Y., et al. (2009). High-detectivity polymer photodetectors with spectral response from 300 nm to 1450 nm. *Science* 325, 1665–1667. doi: 10.1126/science.1176706

Han, J., Qi, J., Zheng, X., Wang, Y., Hu, L., Guo, C., et al. (2017). Low-bandgap donor-acceptor polymers for photodetectors with photoresponsivity from 300 nm to 1600 nm. *J. Mater. Chem. C* 5, 159–165. doi: 10.1039/c6tc05031j

Hendriks, K. H., Li, W., Wienk, M. M., and Janssen, R. A. J. (2014). Small-bandgap semiconducting polymers with high near-infrared photoresponse. *J. Am. Chem. Soc.* 136, 12130–12136. doi: 10.1021/ja506265h

Hou, J., Park, M.-H., Zhang, S., Yao, Y., Chen, L.-M., Li, J.-H., et al. (2008). Bandgap and molecular energy level control of conjugated polymer photovoltaic materials based on Benzo[1,2-b:4,5-b′]dithiophene. *Macromolecules* 41, 6012–6018. doi: 10.1021/ma800820r

Hu, X., Dong, Y., Huang, F., Gong, X., and Cao, Y. (2013). Solution-processed high-detectivity near-infrared polymer photodetectors fabricated by a novel low-bandgap semiconducting polymer. *J. Phys. Chem. C* 117, 6537–6543. doi: 10.1021/jp4001237

Huang, X., Zhang, G., Zhou, C., Liu, L., Jin, Y., Liu, S., et al. (2015). Dithienosilole-benzothiadiazole-based ternary copolymers with a D1–A–D2–A structure for polymer solar cells. *Polym. Chem.* 6, 4154–4161. doi: 10.1039/C5PY00201J

Miao, J., Zhang, F., Du, M., Wang, W., and Fang, Y. (2018). Photomultiplication type organic photodetectors with broadband and narrowband response ability. *Adv. Opt. Mater.* 6:1800001. doi: 10.1002/adom.201800001

Qin, T., Zajaczkowski, W., Pisula, W., Baumgarten, M., Chen, M., Gao, M., et al. (2014). Tailored donor–acceptor polymers with an A–D1–A–D2 structure: controlling intermolecular interactions to enable enhanced polymer photovoltaic devices. *J. Am. Chem. Soc.* 136, 6049–6055. doi: 10.1021/ja500935d

Sun, Y., Welch, G. C., Leong, W. L., Takacs, C. J., Bazan, G. C., and Heeger, A. J. (2012). Solution-processed small-molecule solar cells with 6.7% efficiency. *Nat. Mater.* 11, 44–48. doi: 10.1038/nmat3160

Wang, M., Wang, H., Yokoyama, T., Liu, X., Huang, Y., Zhang, Y., et al. (2014). High open circuit voltage in regioregular narrow band gap polymer solar cells. *J. Am. Chem. Soc.* 136, 12576–12579. doi: 10.1021/ja506785w

Zhao, J., Li, Y., Yang, G., Jiang, K., Lin, H., Ade, H., et al. (2016). Efficient organic solar cells processed from hydrocarbon solvents. *Nat. Energy* 1:15027. doi: 10.1038/nenergy.2015.27

Zhou, H., Yang, L., Price, S. C., Knight, K. J., and You, W. (2010). Enhanced photovoltaic performance of low-bandgap polymers with deep LUMO levels. *Angew. Chem.* 122, 8164–8167. doi: 10.1002/ange.201003357

Zhou, H., Yang, L., and You, W. (2012). Rational design of high performance conjugated polymers for organic solar cells. *Macromolecules* 45, 607–632. doi: 10.1021/ma201648t

Conflict of Interest: The authors declare that the research was conducted in the absence of any commercial or financial relationships that could be construed as a potential conflict of interest.

frontiers in Chemistry

ORIGINAL RESEARCH
published: 29 April 2020
doi: 10.3389/fchem.2020.00350

Propeller-Like All-Fused Perylene Diimide Based Electron Acceptors With Chalcogen Linkage for Efficient Polymer Solar Cells

Ying Li, Yufei Gong, Yongjie Che, Xiaopeng Xu, Liyang Yu and Qiang Peng**

Key Laboratory of Green Chemistry and Technology of Ministry of Education, College of Chemistry and State Key Laboratory of Polymer Materials Engineering, Sichuan University, Chengdu, China

OPEN ACCESS

Edited by:
Kui Zhao,
Shaanxi Normal University, China

Reviewed by:
Junfeng Fang,
East China Normal University, China
Zhu Xunjin,
Hong Kong Baptist University, Hong Kong

***Correspondence:**
Liyang Yu
liyangyu@scu.edu.cn
Qiang Peng
qiangpengjohnny@yahoo.com

Specialty section:
This article was submitted to Physical Chemistry and Chemical Physics, a section of the journal Frontiers in Chemistry

Received: *20 March 2020*
Accepted: *03 April 2020*
Published: *29 April 2020*

Citation:
Li Y, Gong Y, Che Y, Xu X, Yu L and Peng Q (2020) Propeller-Like All-Fused Perylene Diimide Based Electron Acceptors With Chalcogen Linkage for Efficient Polymer Solar Cells. Front. Chem. 8:350. doi: 10.3389/fchem.2020.00350

Perylene diimide (PDI) is a widely explored chromophore for constructing non-fullerene acceptors (NFAs) for polymer solar cells (PSCs). The advantage of using PDI derivatives lies in the readily availability of PDI unit which largely reduces the synthesis cost and improves material stability. Indeed, the recent development of high performance NFAs shed light on the feasibility of the commercialization, but the complex synthesis and poor stability of the top performing NFAs cast a shadow on this bright future. Our previous work has demonstrated a propeller-like structure with three PDIs lined to a benzene center core with a C-C bond which prevented the PDIs to aggregate into undesired large crystals. In this work, we designed and synthesized three new propeller-like PDI derivatives with extra chalcogen linkages between the PDIs and the center core to form all-fused rigid structures. These molecules showed more suitable absorption range than that of their unfused counterparts when blend with donor polymer PTB7-Th. Comparing between the molecules with extra oxygen, sulfur or selenium linkages, the sulfur-based BTT-PDI outperformed the others due to its higher photon absorption and charge transport abilities. This work demonstrated the great potential of PDI derivatives for PSC applications and explored the influences of linkage type on the fused PDI derivatives, which provided a useful tuning knob for molecular design of PDI-based NFAs in the future.

Keywords: polymer solar cells, non-fullerene acceptor, perylene diimide, propeller-like, all fused molecular structure

INTRODUCTION

Polymer solar cell (PSC) is widely considered as a viable alternative for solar energy harvesting for its relatively low manufacturing cost and intrinsic characteristics such as light weight and flexibility (Inganäs, 2018). The recent development of non-fullerenes acceptor (NFA) molecules has promoted this technology by delivering largely increased power conversion efficiency (PCE)

of the PSCs (Cheng et al., 2018; Hou et al., 2018; Yan et al., 2018; Zhang G. et al., 2018; Xu et al., 2019a). Top performing devices using NFAs have exceed 16% in PCE, which demonstrate a bright future for this technology maturing into commercialization (Cui et al., 2019; Sun et al., 2019; Xu et al., 2019b, 2020; Yan et al., 2019; Yu et al., 2019).

On the other hand of the fast rising top PCEs lies a reality that the used NFAs are often with complex and costly synthesis routes. The high synthesis cost, which impaired the full exploration of the low-cost advantage of PSCs, was mainly raised because each of the component chromophores needed to be bottom-up synthesized. Hence, the utilization of readily available chromophores has drawn increasing attention as the potential of commercialization emerges. PDI and its derivatives are long explored candidates for NFAs (Duan et al., 2017a; Hou et al., 2018; Yan et al., 2018; Zhang G. et al., 2018; Zhang J. et al., 2018; Genene et al., 2019), because the PDI chromophore is relatively inexpensive and with high electron mobilities. However, the flat PDI molecules are well-known for strong aggregation (Hartnett et al., 2014). Large crystals of PDI derivatives delivered outstanding performances for N-type transistors (Zhan et al., 2011) but deviated the PSC nanostructure far from the optimized phase separation scale, which limits the PCE (Zhan et al., 2011).

Connecting a few PDI molecules was a method widely explored to disturb the crystallization of PDI derivatives. In comparison with connecting the PDIs heat to tail (Ye et al., 2015; Liang et al., 2016; Eastham et al., 2017), a more widely adopted method was to connect the PDIs at the bay positions. Connecting two or more PDI side by side by either ridged (Zhong et al., 2014, 2015, 2016; Eastham et al., 2017; Sisto et al., 2017; Wang et al., 2020) or flexible (Yan et al., 2013; Zhang et al., 2013; Liu et al., 2016; Meng et al., 2016a; Wu et al., 2018; Kim et al., 2019) linkages at the bay positions have been demonstrated to optimize the nanostructure of PSCs. These linked PDI molecules were found to be twisted with chromophores not positioned in the same plane, which was a cause for the reduction in crystallization tendency. A propeller-like structure connecting three or four PDI molecules with a center core through a flexible linkage have also been demonstrated with success (Lin et al., 2014, 2016; Lee et al., 2016; Duan et al., 2017b; Sun et al., 2017; Bian et al., 2019; Tang et al., 2019; Weng et al., 2019; Zhang et al., 2019; Ding et al., 2020; Wang et al., 2020). Strong steric hindrance effect twisted the molecules sharply and large coplanar angles where found between these PDIs and the center core. The 3D structure largely reduced the aggregation tendency of PDIs and thin films containing these molecules were often found to be amorphous. Fusing the PDIs on the center core can reduce the coplanar angle between them (Meng et al., 2016b; Wang et al., 2019; Wu et al., 2019). Hence fused rigid propeller-like structure were found with both improved intra- and intermolecular charge transport (Meng et al., 2016b; Wang et al., 2019; Wu et al., 2019).

Particularly, triperylene hexaimides (TPH) with PDI molecules simply fused together by a benzene ring was a successful example of fused propeller-like structure with three PDI units delivering high PCE (Meng et al., 2016b). The small center core unit dramatized the steric hindrance effect and the molecule was found with an extremely twisted structure. In this work, we elegantly separated the three PDIs of the TPH with an additional planar five-membered heterocyclic ring between the PDIs and the benzene ring at the center. This design was in hope to further extend the conjugation length and reduce the molecule torsion. The choice of the additional five-membered heterocyclic ring was also investigated. Furan (BTO-PDI), thiophene (BTT-PDI), or selenophene (BTSe-PDI) were added between the PDIs and the center benzene ring by introducing additional oxygen, sulfur, or selenium linkages to the flexible linked Ph-PDI molecule we reported previously (Duan et al., 2017b). The chemical structures and the synthesis routes of these three NFAs are presented in **Scheme 1**. In fact, chalcogens were often used to decorate the bay position of the PDIs to influence their optoelectronic properties (Li et al., 2019, 2020). Differences in size and electron withdrawing ability of the three chalcogen elements shall influence both the molecular conformations, energetic structures, and device performances of these PDIs (Heeney et al., 2007; Chen et al., 2010; Das and Zade, 2010; Jahnke et al., 2013). The molecules developed in this work shows more delocalized and deeper HOMO level than TPH (Meng et al., 2016b) and Ph-DPI (Duan et al., 2017b). The larger band gap caused by the deeper HOMO level formed an improved complimentary absorption of these three new NFAs incorporated with the donor polymer PBT7-Th comparing with TPH and Ph-PDI. The highest performances were observed with BTT-PDI for its high photon absorption and charge transport mobility.

RESULTS AND DISCUSSIONS

Thermal Study

Thermal stabilities of the three NFAs were examined by thermogravimetry analysis (TGA, **Figure 1A**). All the three materials showed a single weight loss as a step function. The temperatures reaching 5% weight loss were recorded for BTO-PDI, BTT-PDI, and BTSe-PDI at 368, 376, and 381°C, respectively, as the decomposition temperature. Hence, all the three molecules could be considered thermally stable for PSC application. Differential scanning calorimetry (DSC, **Figure 1B**) scans of the three NFAs were also performed to look for thermal transitions. However, no endo- or exothermal transition was observed between 50 and 300°C for any of the three molecules during heating and cooling at rate of 10°C/min suggesting no melting, phase transformation or other secondary transitions in this temperature range for all the three NFAs.

Optical Property

UV-vis absorption spectroscopy was conducted on the three NFAs to characterize their photon absorption abilities as well as band structures. Strong absorptions of the three molecules in chloroform solution were found in 300–400 nm region and 420–550 nm region with distinguishable vibronic structures as shown in **Figure 2A**. The maximum extinction coefficient of

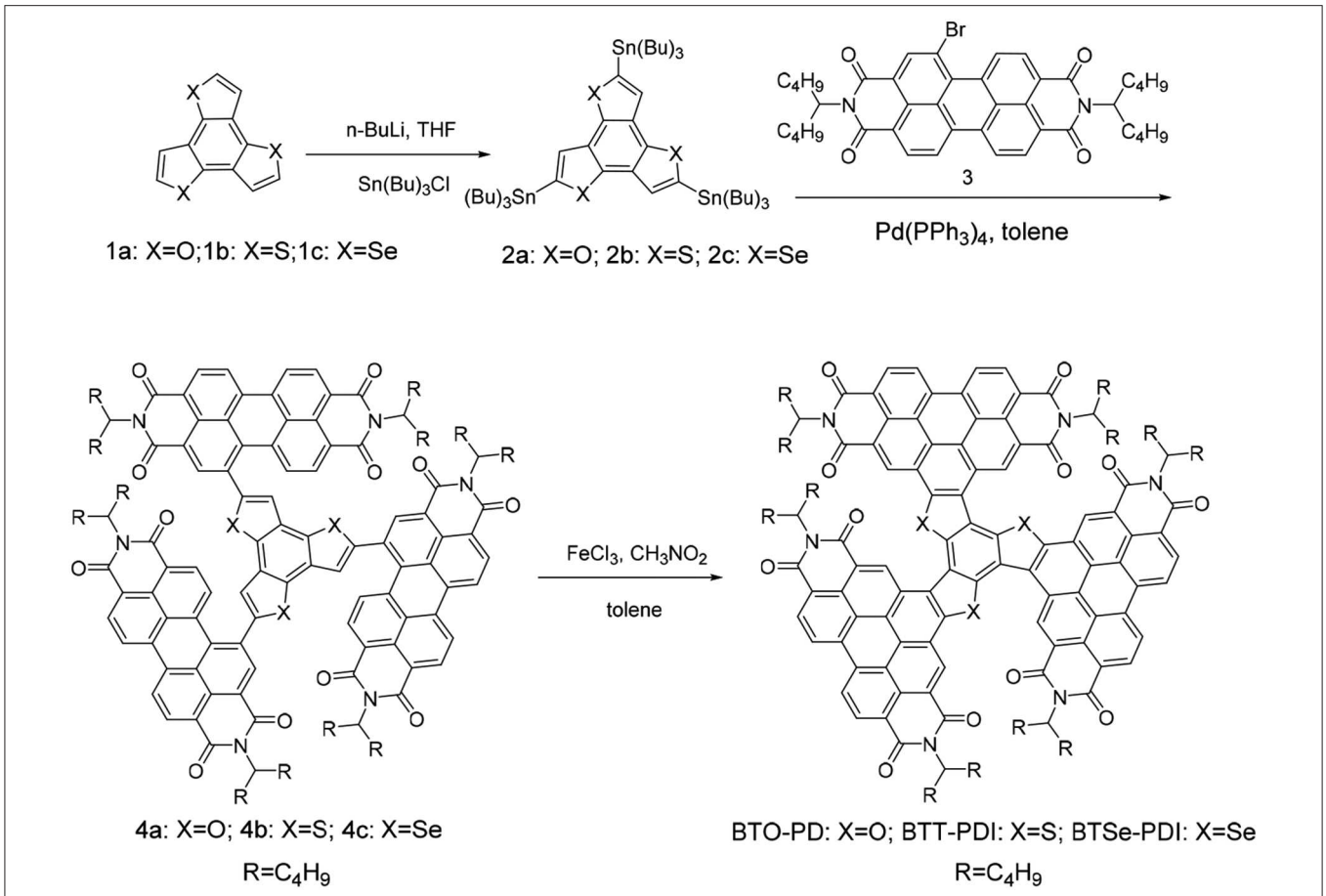

SCHEME 1 | Synthesis routes for the NFAs presented in this work.

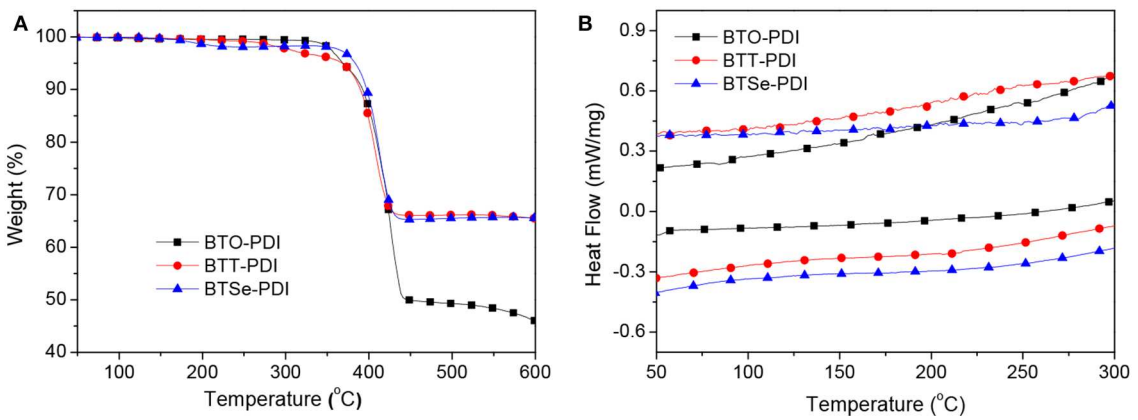

FIGURE 1 | TGA **(A)** and DSC **(B)** thermograms of the three NFAs.

the BTO-PDI, BTT-PDI, and BTSe-PDI in 300–400 nm region reached 5.8 × 10^4 M^{-1} cm^{-1}(at 330 nm), 8.9 × 10^4 M^{-1} cm^{-1} (at 376 nm), 6.6 × 10^4 M^{-1} cm^{-1} (at 381 nm), respectively. In the 420–550 nm region, maximum extinction coefficient for BTO-PDI, BTT-PDI, and BTSe-PDI were found to be 6.5 × 10^4 M^{-1} cm^{-1} (at 490 nm), 6.3 × 10^4 M^{-1} cm^{-1} (at 516 nm), 4.2 × 10^4 M^{-1} cm^{-1} (at 518 nm), respectively. BTT-PDI absorbed significantly more at the low wavelength

region. However, BTO-PDI show slightly higher maximum extinction coefficient than BTT-PDI in the high wavelength region. Additionally, the maximum absorption edge was found to be red shifted as the linking chalcogen getting heavier. This agreed with the observation in most conjugated molecular systems containing chalcogens that heavier chalcogen atoms provides poorer electron withdrawing strength and larger distortion of the five-membered ring both of which favor the extension of conjugation (Heeney et al., 2007; Chen et al., 2010; Das and Zade, 2010; Jahnke et al., 2013). Because the absorption range of BTT-PDI extended to significantly (46 nm) higher wavelengths than BTO-PDI, the BTT-PDI was found with stronger absorption in the high wavelength region as well. In a contrast, the absorption of BTSe-PDI was found to be relatively low in both regions. Absorption spectra of thin films containing neat NFAs and the donor polymer were presented in **Figure 2B**. The vibronic structures of the absorption spectra for the three molecules were all found to be similar and slightly red shifts comparing with their solutions suggesting that the aggregation of molecules in solid-state was weak. The largest red shift of 15 nm was found for BTT-PDI indicating its strongest inter-molecular aggregation and interaction among the three (Brown et al., 2003; Spano and Silva, 2014). The maximum absorption wavelength (λ_{onset}) of the three molecules were used to extract the optical bandgap (E_g^{opt}) using equation $E_g^{opt} = 1{,}240/\lambda_{onset}$. The E_g^{opt} for BTO-PDI, BTT-PDI, and BTSe-PDI were found at 2.25, 2.20, 2.20 eV, respectively. Compared with the TPH (Meng et al., 2016b) with a simple benzene core or the unfused Ph-PDI (Duan et al., 2017b), the absorption of these three NFAs overlaps less with the absorption of the donor polymer PTB7-Th, suggesting an improved complimentary absorption.

Electrochemical Study

Electrochemical analysis was carried out using cyclic voltammetry (CV, **Figure 3A**) to measure the highest occupied molecular orbital (HOMO) and lowest unoccupied molecular orbital (LUMO) levels of the NFAs. The energy levels of these

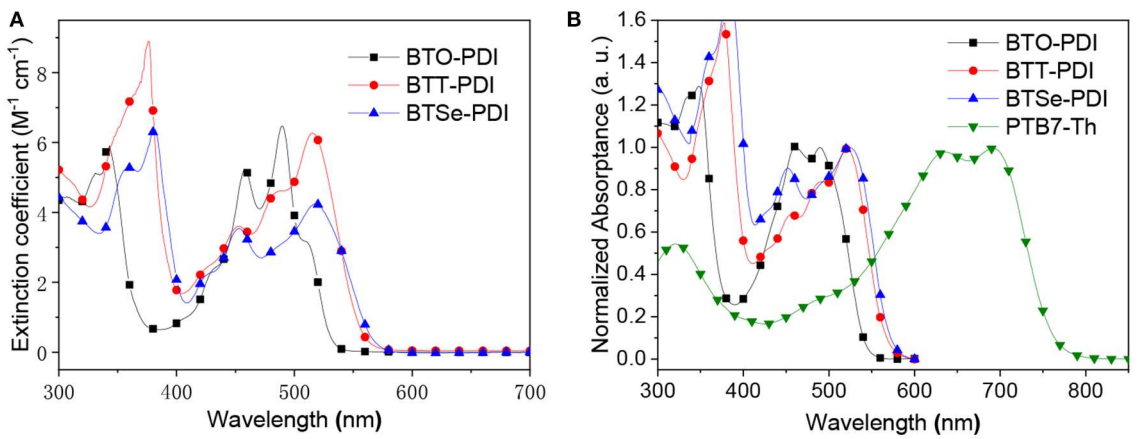

FIGURE 2 | UV-vis absorption spectra of chloroform solution containing the acceptors **(A)** and thin films of the donor and acceptor materials used in this work (**B**, normalized).

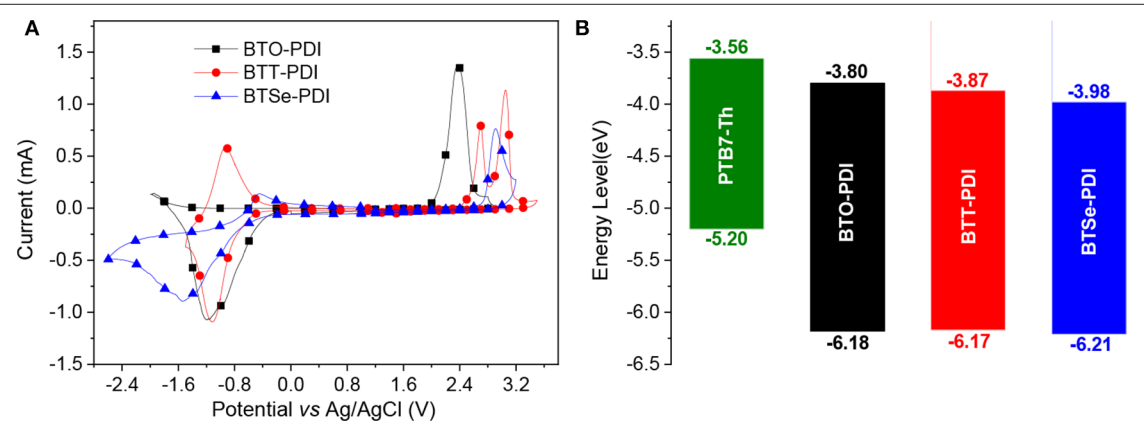

FIGURE 3 | (A) Cyclic voltammograms (CV) of the three NFAs, **(B)** energy diagrams of the three NFAs in comparison with the donor polymer PTB7-Th.

TABLE 1 | Photonic and electrochemical properties of the acceptors.

Material	Solution		Film	E_g^{opt} (eV)	HOMO (eV)	LUMO (eV)	E_g^{cv} (eV)
	λ_{max} (nm)	ε (M^{-1} cm^{-1})	λ_{max} (nm)				
BTO-PDI	490	6.5×10^4	348	2.25	−3.80	−6.18	2.38
BTT-PDI	376	8.9×10^4	387	2.20	−3.87	−6.17	2.30
BTSe-PDI	381	6.6×10^4	393	2.20	−3.98	−6.21	2.23

frontier orbitals were summarized in **Table 1** and compared with the donor polymer in **Figure 3B**. The energy levels of the frontier orbitals (HOMO/LUMO) of BTO-PDI, BTT-PDI, and BTSe-PDI were found at −6.18/−3.80, −6.17/−3.87 and, −6.21/−3.98 eV, with extracted bandgap of 2.38, 2.30, and 2.23 eV, respectively. Deeper LUMO levels were found for the molecules with heavier chalcogens while the HOMO levels were hardly affected leading to a clear reduction in bandgap agreeing with the red shifted UV-vis absorption. A lower LUMO level of the acceptor molecule can lead to reduced open circuit voltage (V_{oc}) of the PSC devices for molecules with heavier chalcogens linkage. The HOMO level of these NFAs were significantly deeper than that of the TPH (E_{HOMO} = 6.02 eV) (Meng et al., 2016b) or the Ph-PDI (E_{HOMO} = 6.02 eV) (Duan et al., 2017b) suggesting that it was strongly affected by the linkage type of the PDI units to the center core while the LUMO level remained within proximity.

Molecular Simulations

To obtain further insight on the molecular conformation and the frontier orbitals, molecular simulation based on density function theory (DFT, B3LYP/6-31G(d) level) were carried out for these three NFAs. The molecular conformations were clearly less twisted comparing with the benzene core TPH (Meng et al., 2016b) and unfused Ph-PDI (Duan et al., 2017b). From the calculated frontier orbital distribution displayed in **Figure 4**, the HOMO of all three NFAs were found to be largely delocalized over more than one PDI unit while the LUMOs were almost localized to one or two isolated PDI units. Hence, the HOMO levels were more sensitive to the connection between the PDI units and the center core, which explained the more significant deeper HOMO levels of these NFAs than the TPH and the Ph-PDI. The calculated frontier orbital energy levels (HOMO/LUMO) for BTO-PDI, BTT-PDI, and BTSe-PDI were −6.04/−3.29, −6.10/−3.36, −6.13/−3.39 eV, respectively. The increasing trend in the HOMO levels and LUMO levels within an approximate range agreed with optical and CV measurements.

Photovoltaic Performances

The PSC devices containing the three NFAs were fabricated in an inverted architecture. The *J*-*V* characteristics of top performing devices were presented in **Figure 5A** and the extracted figure-of-merits were summarized in **Table 2**. The V_{oc} of devices containing BTO-PDI, BTT-PDI, and BTSe-PDI were found at 0.924, 0.910, and 0.876 V, respectively. The decreasing of V_{oc} as the linking chalcogen getting heavier agreed with the decreasing LUMO levels of the NFAs. In a contrast, higher J_{sc} and the fill factors (FF) were found for devices containing BTT-PDI (J_{sc} = 13.91 mA/cm^2, FF = 62.22%). BTO-PDI delivered lower J_{sc} (12.06 mA/cm^2) and FF (60.74%) yielding an overall PCE of 6.77% which was lower than that of BTT-PDI (PCE = 7.87%). All figure-of-merits of photovoltaic performances of devices containing BTSe-PDI were lower than those of the other two NFAs with J_{sc} = 11.35 mA/cm^2, FF = 54.17% and PCE = 5.39%.

External quantum efficiencies (EQE) were measured for these devices to obtain understanding on the J_{sc} differences. The EQE responses of these PSC devices were displayed in **Figure 5B**. In the 300–400 nm region, BTT-PDI generated high EQE up to 70% while the other two materials delivered EQE under 50% within this range. A sharp drop of EQE around 400 nm for BTO-PDI was noticed, which agreed with its low extinction coefficient at this wavelength. In a contrast, BTO-PDI delivered high maximum EQE in the 420–550 nm region due to its relatively high extinction coefficient in this range. Above 550 nm, the EQE responses were mainly generated from the photons absorbed by the donor polymer PTB7-Th. Interestingly, BTT-PDI provided higher EQE response than the other two NFAs. Hence, there are additional causes for the differences in J_{sc} other than the photon absorption ability of the NFAs. The total integrated J_{EQE} were found to be similar to the J_{sc} of the devices.

Charge Carrier Mobilities

The charge carrier mobilities of the PTB7-Th/acceptor blends were measured using space charge limited conductivity (SCLC, **Figure 6**) method (Malliaras et al., 1998) to further understand the origin for the differences in J_{sc} and FF. The SCLC measurements were conducted in hole only and electron only devices to obtain hole mobility (μ_h) and electron mobility (μ_e) separately. The extracted charge carrier mobilities (μ_h/μ_e)of PTB7-Th in blend with BTO-PDI, BTT-PDI, and BTSe-PDI were found to be $4.51 \times 10^{-4}/2.79 \times 10^{-4}$, $6.43 \times 10^{-4}/4.44 \times 10^{-4}$, and $3.98 \times 10^{-4}/2.49 \times 10^{-4}$ cm^2 V^{-1} s^{-1} with μ_h/μ_e ratio of 1.62, 1.45, and 1.60, respectively. The significantly higher μ_e from the BTT-PDI agrees with its strongest red shift between its thin film and solution. The higher μ_e and the relatively more balanced μ_h/μ_e ratio could lead to a more efficient charge transferring process and higher J_{sc} and FF (Andersson et al., 2011).

Crystallinity and Blend Morphology

The crystallinity of the NFAs and nano phase separations of the corresponding blend films were characterized by using X-ray diffraction (XRD) and atomic force microscopy (AFM) techniques. The three XRD diffractograms of thin films containing the PTB7-Th/acceptor blends in **Figure 7** show similar features with two diffraction peaks one around 5° and the other around 22.5° in 2θ. The two diffractions were corresponding to a lamellar packing distance of 17.7 Å and a π stacking distance of 3.9 Å from the PTB7-Th. Hence, the PDI derivatives remained predominantly amorphous in the thin films. The 3D fused propeller-like structure indeed largely prevented the generation of large crystals of PDI which was a source for the high performances. AFM images of thin films containing PTB7-Th/acceptor blends all showed homogeneously

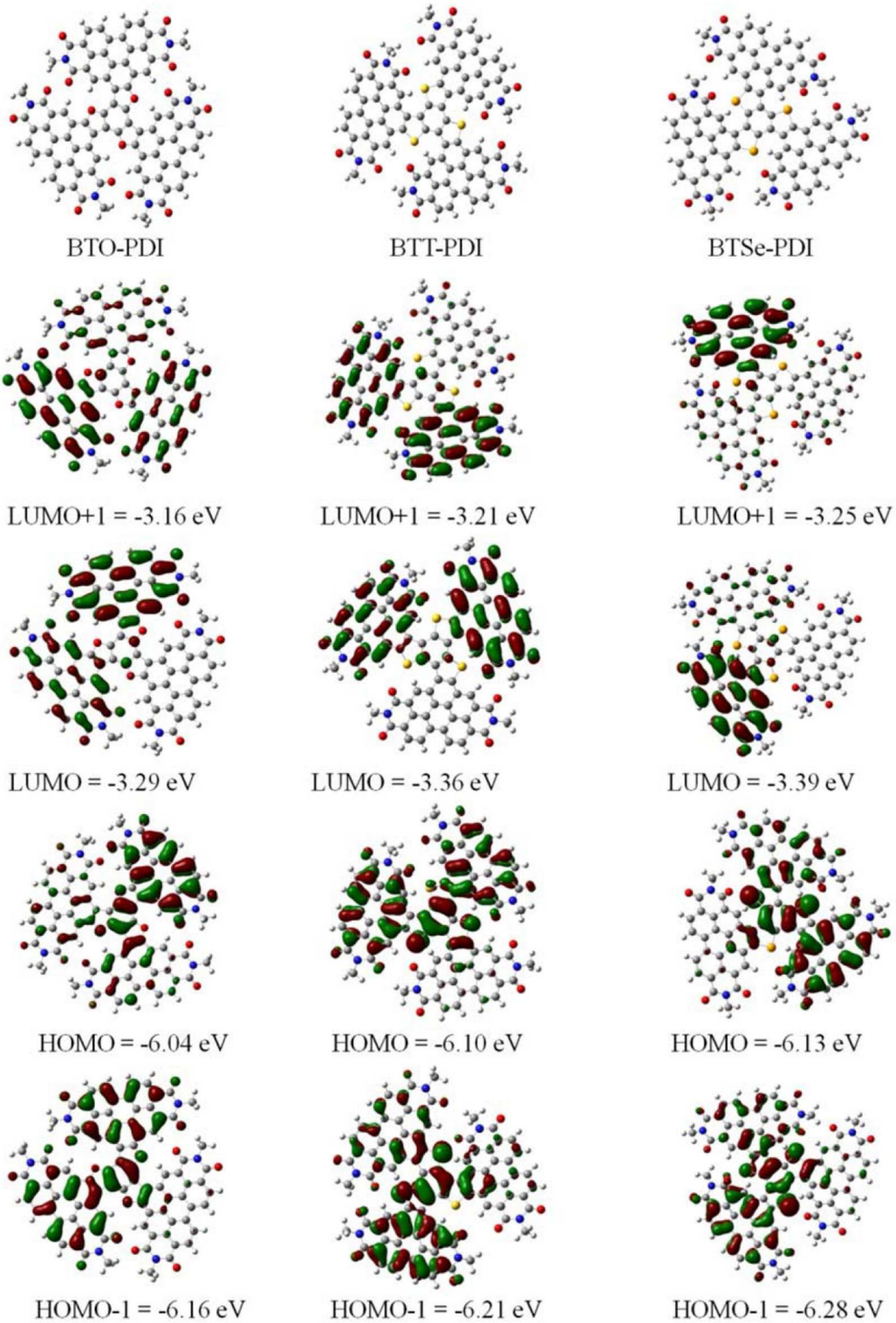

FIGURE 4 | Calculated distribution and energy levels of the frontier orbitals of the three NFAs based on the density function theory (DFT).

distributed sub-micrometer features in both height and phase images (**Figure 8**). The root mean square (RMS) of the height of thin films containing BTO-PDI, BTT-PDI, and BTSe-PDI were found to be 3.23, 2.65, and 4.55 nm, respectively. The smooth films also excluded the existence of micrometer sized crystals often found in conventional PDI based PSCs.

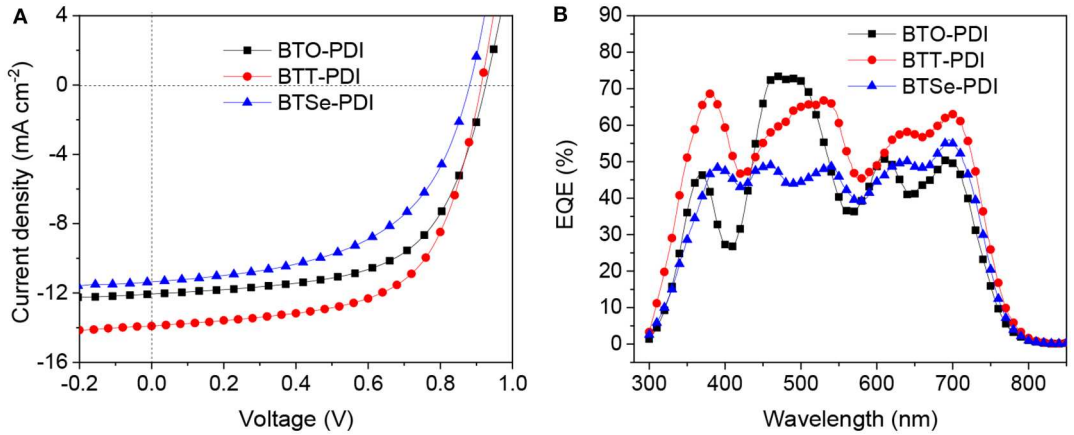

FIGURE 5 | *J-V* characteristics **(A)** and EQE responses **(B)** of the top performing PSC devices, the acceptor used in each PSC was noted in the figures.

TABLE 2 | Photovoltaic performance of the PSC devices.

Active layer	V_{oc}^{a} (V)	J_{sc} (mA/cm^2)	FF (%)	PCE (%)
PTB7-Th:BTO-PDI	0.919 ± 0.006 (0.924)	11.88 ± 0.31 (12.06)	60.01 ± 0.95 (60.74)	6.55 ± 0.35 (6.77)
PTB7-Th:BTT-PDI	0.907 ± 0.005 (0.910)	13.79 ± 0.35 (13.91)	61.65 ± 0.76 (62.22)	7.71 ± 0.21 (7.87)
PTB7-Th:BTSe-PDI	0.873 ± 0.005 (0.876)	11.11 ± 0.32 (11.35)	52.97 ± 1.44 (54.17)	5.14 ± 0.36 (5.39)

[a]*Averaged parameters were calculated from 10 devices.*

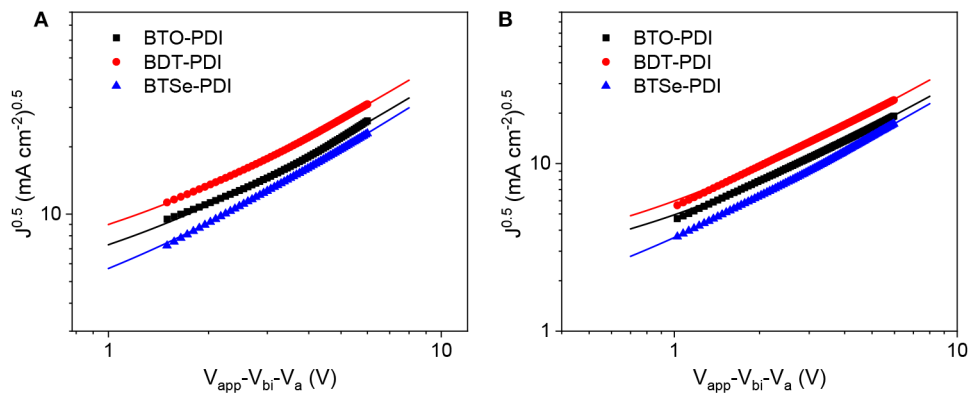

FIGURE 6 | SCLC measurements for extracting hole **(A)** and electron **(B)** transport mobility for thin films containing PTB7-Th in blend with each of the three NF ninety-nine noted in the figures).

EXPERIMENTAL

Materials

All chemicals used for synthesis and device fabrications were purchased from Aladdin and Chron Chemicals without further purification. Compound **1a**, **1b**, **1c**, **2b,** and **3** were synthesized according to the previously reported procedures (Sonoda et al., 2001; Nicolas et al., 2004; Tsuji et al., 2014; Viswanath et al., 2014).

Material Synthesis

Synthesis of Compound 2a

An *n*-butyllithium solution (1.62 mL, 4.04 mmol, 2.50 M in hexane) was added into a solution of compound **1a** (0.20 g, 1.01 mmol) in anhydrous tetrahydrofuran (30 mL) at 0°C and stirred for 1 h at room temperature under argon protection. After that, tributyltin chloride (1.90 mL, 4.10 mmol) was added into the mixture and stirred for 8 h at room temperature under argon protection. The obtained mixture was poured into deionized water, extracted by dichloromethane, dried with $MgSO_4$ and filtered. The solvent was removed *via* rotary evaporation. The crude product was purified by column chromatography with petroleum ether as eluent to get the compound **2a** as a colorless oil (0.97 g, 89.56%). ^{1}H NMR (400 MHz, $CDCl_3$, δ/ppm): 7.32 (s, 3H), 1.68–1.60 (m, 18H), 1.41–1.34 (m, 18H), 1.24–1.17 (m, 18H), 0.95–0.91 (m, 27H). ^{13}C NMR (100 MHz, $CDCl_3$, δ/ppm): 137.10, 135.74, 132.72, 132.52, 130.77, 130.65, 130.54,

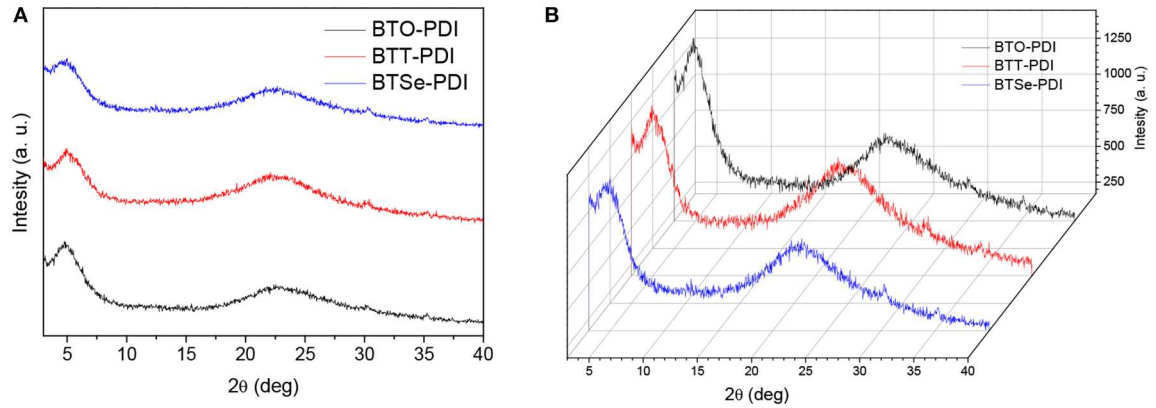

FIGURE 7 | Strength ratio **(A)** and Watrefall **(B)** XRD diffractograms of thin films containing PTB7-Th in blend with each of the three NFAs (noted in the figures).

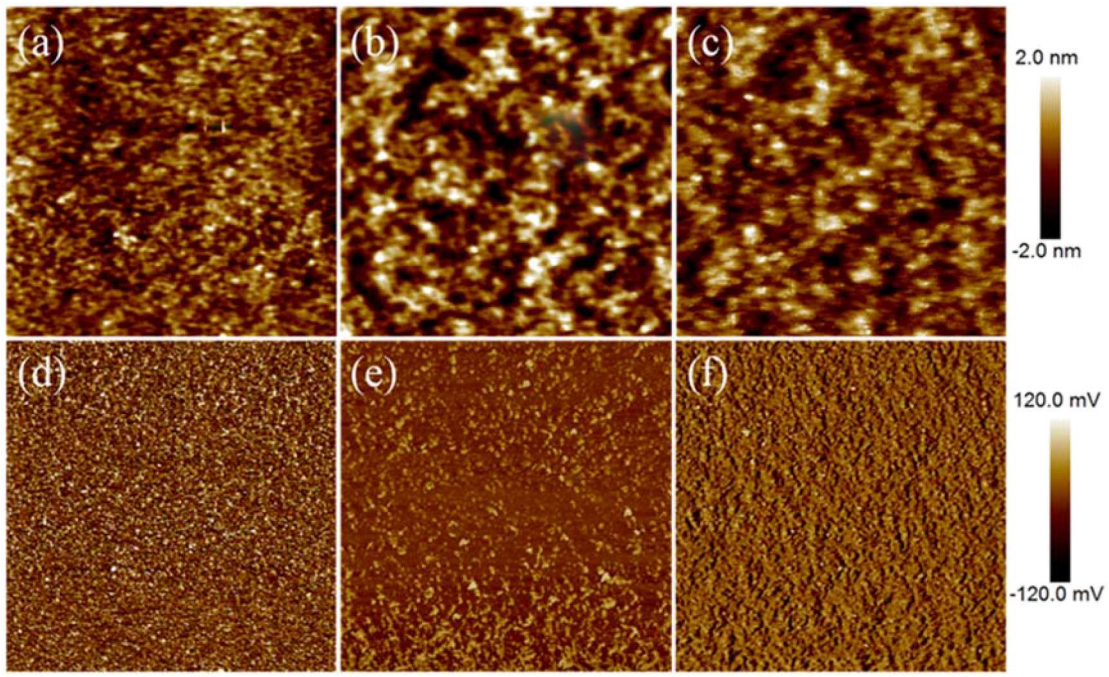

FIGURE 8 | AFM height **(a–c)** and phase **(d–f)** images of thin films containing PBT-7-Th in blend with BTO-PDI **(a,d)**, BTT-PDI **(b,e)**, and BTSe-PDI **(c,f)**.

77.36, 77.24, 77.04, 76.72, 29.75, 29.15, 29.04, 28.94, 27.62, 27.33, 27.03, 13.72, 12.73, 12.65, 11.79, 10.96, 9.27. Anal. calcd for ($C_{48}H_{84}O_3Sn_3$) (%): C, 54.12; H, 7.95. Found (%): C, 53.72; H, 8.37.

Synthesis of Compound 2c

An *n*-butyllithium solution (6.40 mL, 10.20 mmol, 2.50 M in hexane) was added into a solution of compound **1c** (0.66 g, 1.70 mmol) in anhydrous tetrahydrofuran (50 mL) at 0°C and stirred for 2 h at room temperature under argon protection. After that, tributyltin chloride (3.0 mL, 11.10 mmol) was added into the mixture and stirred at room temperature for 12 h under argon protection. The obtained mixture was poured into deionized water, extracted by dichloromethane, dried with $MgSO_4$ and filtered. The solvent was removed *via* rotary evaporation. The crude product was purified by column chromatography with petroleum ether as eluent to get the compound **2c** as a light-yellow oil (1.89 g, 87.40%). ^{1}H NMR (400 MHz, $CDCl_3$, δ/ppm): 7.86 (s, 3H), 1.69–1.60 (m, 18H), 1.39–1.32 (m, 18H), 1.25–1.17 (m, 18H), 0.95–0.89 (m, 27H). ^{13}C NMR (100 MHz, $CDCl_3$, δ/ppm): 141.16, 141.10, 138.67, 138.17, 137.94, 137.72, 136.20, 136.11, 135.21, 130.61, 130.55, 77.41, 77.30, 77.09, 76.78, 29.80, 29.23, 29.04, 28.94, 28.60, 27.56, 27.34, 27.22, 13.94, 13.78, 12.65, 12.57, 11.29. Anal. calcd for

($C_{48}H_{84}Se_3Sn_3$) (%): C, 45.97; H, 6.75. Found (%): C, 45.78; H, 6.81.

Synthesis of Compound 4a

A mixture of compound **3** (0.49 g, 0.68 mmol), compound **2a** (0.18 g, 0.17 mmol), degassed toluene (30 mL), and $Pd(PPh_3)_4$ (4% mol) was stirred for 20 h at 100°C under argon protection. The obtained mixture was poured into deionized water, extracted by dichloromethane, dried with $MgSO_4$ and filtered. The solvent was removed *via* rotary evaporation. The crude product was purified by column chromatography with petroleum ether/dichloromethane (1:3) as eluent to get the compound **4a** as a dark red solid (0.124 g, 34.42%). ^{1}H NMR (400 MHz, $CDCl_3$, ppm): 8.89 (s, 3H), 8.71–8.65 (m, 12H), 8.34 (s, 3H), 8.03–8.01 (m, 3H), 7.49 (s, 3H), 5.23–5.11 (m, 6H), 2.27–2.17 (m, 12H), 1.84–1.82 (m, 12H), 1.33–1.25 (m, 48H), 0.86–0.75 (m, 36H). ^{13}C NMR (100 MHz, $CDCl_3$, ppm): 164.67, 163.54, 155.79, 146.89, 137.14, 135.02, 134.14, 133.50, 131.06, 129.25, 129.18, 128.92, 128.12, 128.03, 127.32, 126.25, 126.00, 124.15, 123.74, 123.45, 123.02, 119.69,111.72, 103.76, 77.27, 77.26, 77.05, 76.74, 54.76, 54.65, 32.94, 29.10, 22.62, 22.57, 14.05, 13.98. Anal. calcd for ($C_{138}H_{138}N_6O_{15}$) (%): C, 78.16; H, 6.56; N, 3.96. Found (%): C, 77.56; H, 6.96; N, 4.27.

Synthesis of Compound 4b

A mixture of compound **3** (0.5 g, 0.7 mmol), compound **2b** (0.19 g, 0.17 mmol), degassed toluene (30 mL), and $Pd(PPh_3)_4$ (4% mol) was stirred for 20 h at 100°C under argon protection. The obtained mixture was poured into deionized water, extracted by dichloromethane, dried with $MgSO_4$ and filtered. The solvent was removed *via* rotary evaporation. The crude product was purified by column chromatography with petroleum ether/dichloromethane (1:3) as eluent to get the compound **4b** as a dark red solid (0.14 g, 38.00%). ^{1}H NMR (400 MHz, $CDCl_3$, δ/ppm): 8.85 (s, 3H), 8.74–8.67 (m, 12H), 8.57 (s, 3H), 8.45–8.39 (m, 3H), 7.94 (s, 3H), 5.20–5.16 (m, 6H), 2.34–2.22 (m, 12H), 1.90–1.78 (m, 12H), 1.39–1.16 (m, 48H), 0.94–0.79 (m, 36H). ^{13}C NMR (100 MHz, $CDCl_3$, δ/ppm): 164.49, 164.15, 163.26, 152.14, 145.69, 144.36, 143.47, 138.35, 137.24, 135.46, 134.13, 132.35, 129.01, 125.89, 123.45, 122.11, 119.67, 117.89, 55.83, 45.37, 42.70, 33.14, 32.03, 31.73, 30.47, 29.36, 26.47, 22.91, 21.79, 14.45, 13.34. Anal. calcd for ($C_{138}H_{138}N_6O_{12}S_3$) (%): C, 76.42; H, 6.41; N, 3.87. Found (%): C, 76.36, H, 6.62, N, 3.92.

Synthesis of Compound 4c

A mixture of compound **3** (0.5 g, 0.7 mmol), compound **2c** (0.21 g, 0.17 mmol) degassed toluene (30 mL), and $Pd(PPh_3)_4$ (4% mol) was stirred for 20 h at 100°C under argon protection. The obtained mixture was poured into deionized water, extracted by dichloromethane, dried with $MgSO_4$ and filtered. The solvent was removed *via* rotary evaporation. The crude product was purified by column chromatography with petroleum ether/dichloromethane (1:3) as eluent to get the compound **4c** as a red solid (0.14 g, 36.12%). ^{1}H NMR (400 MHz, $CDCl_3$, δ/ppm): 8.88–8.85 (m, 6H), 8.81–8.68 (m, 12H), 8.48 (s, 3H), 8.03 (s, 3H), 5.23–5.16 (m, 6H), 2.28–2.20 (m, 12H), 1.87–1.81 (m, 12H), 1.32–1.23 (m, 48H), 0.86–0.80 (m, 36H). ^{13}C NMR (100 MHz, $CDCl_3$, δ/ppm): 164.66, 163.53, 148.99, 137.82, 136.36, 134.90, 134.15, 133.45, 131.63, 129.13, 128.04, 127.35, 123.78, 123.06, 77.37, 77.26, 77.06, 76.74, 54.79, 54.72, 32.08, 29.72, 29.11, 22.63, 22.38, 14.07, 14.05. Anal. calcd for ($C_{138}H_{138}N_6O_{12}Se_3$) (%): C, 71.77; H, 6.02; N, 3.64. Found (%): C, 70.56; H, 6.93; N, 3.87.

Synthesis of BTO-PDI

A mixture of compound **4a** (0.42 g, 0.20 mmol), degassed toluene (30 mL), anhydrous ferric chloride (1.62 g, 10 mmol), and nitromethane (5 mL) was stirred for 12 h at 100°C under argon protection. The obtained mixture was poured into deionized water, extracted by dichloromethane for three times, dried with $MgSO_4$ and filtered. The solvent was removed *via* rotary evaporation. The crude product was purified by column chromatography with petroleum ether/dichloromethane (1:3) as eluent to get the compound **BTO-PDI** as a red solid (0.38 g, 90.52%). ^{1}H NMR (400 MHz, $CDCl_3$, δ/ppm): 11.64 (s, 3H), 10.81 (s, 3H), 9.49–9.36 (m, 6H), 9.29–9.05 (m, 6H), 5.82–5.39 (m, 6H), 2.49–2.33 (m, 12H), 2.10–2.00 (m, 12H), 1.42–1.34 (m, 48H), 0.86–0.82 (m, 36H). ^{13}C NMR (100 MHz, $CDCl_3$, δ/ppm): 166.38, 165.27, 163.93, 151.92, 150.81, 135.46, 133.90, 130.79, 129.68, 128.79, 127.45, 125.01, 123.67, 122.56, 120.56, 119.67, 109.21, 103.76, 55.38, 42.04, 32.69, 29.14, 23.35, 22.46, 14.01, 13.87. Anal. calcd for ($C_{138}H_{132}N_6O_{15}$) (%): C, 78.38; H, 6.29; N, 3.97. Found (%): C, 77.86; H, 7.26; N, 4.12. MS (MALDI-TOF-MS):$[M]^+$: Calcd: 2113.97; Found: 2113.96.

Synthesis of BTT-PDT

A mixture of compound **4b** (0.43 g, 0.20 mmol), degassed toluene (30 mL), anhydrous ferric chloride (1.62 g, 10 mmol), and nitromethane (5 mL) was stirred for 12 h at 100°C under argon protection. The obtained mixture was poured into deionized water, extracted by dichloromethane, dried with $MgSO_4$ and filtered. The solvent was removed *via* rotary evaporation. The crude product was purified by column chromatography with petroleum ether/dichloromethane (1:3) as eluent to get the compound **BTT-PDT** as a red solid (0.39 g, 89.14%). ^{1}H NMR (400 MHz, $CDCl_3$, δ/ppm): 10.95 (s, 3H), 9.61–9.56 (m, 6H), 9.48–9.47 (d, $J = 7.9$ Hz, 3H), 9.32–9.28 (m, 3H), 9.15–9.13 (m, 3H), 5.37–5.25 (m, 6H), 2.41–2.37 (m, 12H), 2.29–2.27 (m, 12H), 1.34–1.25 (m, 48H), 0.84–0.81 (m, 36H). ^{13}C NMR (100 MHz, $CDCl_3$, δ/ppm): 164.61, 164.13, 138.90, 137.98, 133.45, 131.51, 129.98, 129.13, 127.36, 127.11, 125.40, 125.27, 124.55, 124.06, 123.71, 123.21, 55.02, 54.67, 32.10, 29.71, 29.24, 29.07, 22.64, 22.49, 14.04, 14.01. Anal. calcd for ($C_{138}H_{132}N_6O_{12}S_3$) (%): C, 76.64; H, 6.15; N, 3.89. Found (%): C, 75.56; H, 6.83; N, 4.37. MS (MALDI-TOF-MS):$[M]^+$: Calcd: 2161.90; Found: 2161.89.

Synthesis of BTSe-PDT

A mixture of compound **4c** (0.46 g, 0.20 mmol), degassed toluene (30 mL), anhydrous ferric chloride (1.62 g, 10 mmol), and nitromethane (5 mL) was stirred for 12 h at 100°C under argon protection. The obtained mixture was poured into deionized water, extracted by dichloromethane, dried with $MgSO_4$ and filtered. The solvent was removed *via* rotary evaporation. The crude product was purified by column chromatography with petroleum ether/dichloromethane (1:3) as eluent to get the compound **BTSe-PDT** as a red solid (0.41 g, 88.31%). ^{1}H NMR (400 MHz, $CDCl_3$, δ/ppm): 10.67 (s, 3H), 9.56–9.50 (m, 6H),

9.48–9.45 (d, 3H), 9.32–9.28 (m, 3H), 9.15–9.13 (m, 3H), 5.37–5.25 (m, 6H), 2.41–2.31 (m, 12H), 2.12–1.73 (m, 12H), 1.89–1.25 (m, 48H), 0.90–0.86 (m, 36H). ^{13}C NMR (100 MHz, $CDCl_3$, δ/ppm): 164.57, 163.97, 142.16, 141.15, 137.42, 135.34, 133.66, 133.11, 131.08, 130.07, 127.52, 127.16, 125.94, 124.72, 124.64, 124.09, 123.71, 122.84, 77.37, 77.25, 77.05, 76.73, 54.99, 32.16, 31.94, 29.72, 29.38, 29.14, 22.49, 22.48, 14.14, 14.03. Anal. calcd for ($C_{138}H_{132}N_6O_{12}Se_3$) (%): C, 71.96; H, 5.78; N, 3.65. Found (%): C, 71.56; H, 5.83; N, 3.74. MS (MALDI-TOF-MS):$[M]^+$: Calcd: 2303.74; Found: 2303.73.

Materials Characterization and Methods

^{1}H and ^{13}C NMR spectra were recorded on a Bruker Avance-400 spectrometer with *d*-chloroform ($CDCl_3$) or *d*-dimethyl sulfoxide [$(CD_3)_2SO$] as the solvents and tetramethylsilane (TMS) as internal standard. Thermalgravimetric analysis (TGA) and differential scanning calorimetry (DSC) analysis were carried out using a TA TGA Q500 and a Netzsch DSC 200, respectively, under N_2 protective gas. The heating and cooling rates for thermal analysis were kept at 10°C/min. UV-vis absorption spectra were collected using a Persee TU1901 spectrometer. Cyclic voltammetry (CV) measurements were conducted using a CHI660 potentiostat/galvanostat electrochemical workstation at a scanning rate of 50 mV s^{-1}. A platinum wire was used as the counter electrode and the reference electrode was Ag/AgCl with its energy level calibrated by a ferrocene/ferrocenium (Fc/Fc^+) redox couple to be −4.34 eV. X-ray diffraction (XRD) was measured with a Philips X'pert X-ray diffractometer. Atomic force microscopy (AFM) images were recorded using a Bruker Innova Atomic Force Microscope in tapping mode.

Device Fabrication and Measurements

PSC devices were fabricated with an inverted configuration (ITO/ZnO/active layer/MoO_3/Al). Thirty nanometer thick ZnO layer was prepared with a Sol-Gel method on ITO glass substrates. The active layer of thickness around 100 nm containing PTB7-Th and the acceptor molecules (1:1.5 wt%) were spin coated onto the substrate from a chlorobenzene solution with total concentration of 25 mg/mL and 1% 1,8-diiodooctane as additive. MoO_3 (10 nm) and Al (80 nm) layers were deposited onto the active layer *via* thermal evaporation. The device area was exactly fixed to 4.00 mm^2

The *I-V* characteristics of the PSC devices were obtained by placing the PSCs under an AM 1.5G (100 mW cm^{-2}) illumination created by a solar simulator (XES-70S1, SAN-EI, calibrated with a Konica Minolta AK-200 standard Si solar cell) and measuring using a Keithley 2400 Source Measure Unit.

The EQE curves were measured with a Newport QE Test Model during illumination with monochromatic light from a xenon lamp. The fabrication of PSC devices for *I-V* and EQE characteristic as well as the *I-V* measurements were conducted in a high purity argon filled glove box (<0.1 ppm O_2 and H_2O). EQE characteristics were performed in air on devices shortly removed from the glove box.

Charge Transport Characterization

The charge carrier mobilities presented in this work were obtained using the space-charge limited conductivity (SCLC) method. Hole only (ITO/PEDOT:PSS/active layer/Mo_3O/Au) and electron only (Al/active layer/Al) devices were fabricated similar to the PSC devices. The dark *J-V* current was collected by a Keithley 2400 Source Measure Unit and fitted to equation: $J = 9\varepsilon_0\varepsilon_r\mu V^2/8L^3$, where J is the current density, L is the active layer thickness, μ is the charge transport mobility, ε_r and ε_0 are the relative and free space (8.85×10^{-12} F m^{-1}) permittivity, V is the internal voltage in device deduced from: $V = V_{appl} - V_{bi} - V_a$, where V_{appl} is the applied voltage, V_{bi} is the built-in voltage and V_a is the voltage drop.

CONCLUSIONS

In this work, we designed and synthesized three fused propeller-like PDI derivatives namely BTO-PDI, BTT-PDI, and BTSe-PDI by introduce an additional chalcogen (oxygen, sulfur, and selenium, respectively) linkage to our previously reported Ph-PDI molecule to form rigid fused linkages. The fused PDI derivatives show flatter molecular conformation and more delocalized HOMO with deeper HOMO energy levels. The larger band gaps provide blue shifted absorption which was beneficial for the complimentary absorption incorporated with the donor polymer PTB7-Th. The propeller-like structure largely prevented the formation of large PDI crystals. In comparison between the three NFAs introduced in this work, heavier chalcogen linkage reduced the LOMO energy level and the V_{oc} of the devices. Highest PSC performances was found with the BTT-PDI which combines high absorption with high electron transport mobility. Our work demonstrated the great potential of PDI derivatives for PSC application and explored the influences of linkage type on the fused PDI derivatives which provide a useful tuning knob for molecular design of NFAs.

DATA AVAILABILITY STATEMENT

The original contributions presented in the study are included in the article/supplementary materials, further inquiries can be directed to the corresponding author/s.

AUTHOR CONTRIBUTIONS

YL: design and synthesis of the materials. YG: synthesis of the materials. YC: characterization of the materials. XX: fabrication and characterization of the devices. LY: analysis of the results and organization of the manuscript. QP: affording the idea, directing this work and organization of the manuscript.

FUNDING

This work was supported by the National Natural Science Foundation of China (NSFC, 21825502, 51573107, 91633301, and 21905185) and the Foundation of State Key Laboratory of Polymer Materials Engineering (SKLPME 2017-2-04) and the Fundamental Research Funds for the Central Universities (YJ201957).

REFERENCES

Andersson, L. M., Mü, C., Badada, B., Zhang, F., Würfel, U., and Inganas, O. (2011). Mobility and fill factor correlation in geminate recombination limited solar cells. *J. Appl. Phys*. 110:024509. doi: 10.1063/1.3609079

Bian, G.-F., Zhao, F., Ki, L. T., Sheng, C., Liu, X., Du, H., et al. (2019). Simply planarizing nonfused perylene diimide based acceptors toward promising non-fullerene solar cells. *J. Mater. Chem. C* 7, 8092–8100. doi: 10.1039/C9TC02013F

Brown, P. J., Thomas, D. S., Köhler, A., Wilson, J. S., Kim, J.-S., Ramsdale, C. M., et al. (2003). Effect of interchain interactions on the absorption and emission of poly(3-hexylthiophene). *Phys. Rev. B* 67:064203. doi: 10.1103/PhysRevB.67.064203

Chen, Z., Lemke, H., Albert-Seifried, S., Caironi, M., Nielsen, M. M., Heeney, M., et al. (2010). High mobility ambipolar charge transport in polyselenophene conjugated polymers. *Adv. Mater*. 22, 2371–2375. doi: 10.1002/adma.200903711

Cheng, P., Li, G., Zhan, X., and Yang, Y. (2018). Next-generation organic photovoltaics based on non-fullerene acceptors. *Nat. Photonics* 12, 131–142. doi: 10.1038/s41566-018-0104-9

Cui, Y., Yao, H., Zhang, J., Zhang, T., Wang, Y., Hong, L., et al. (2019). Over 16% efficiency organic photovoltaic cells enabled by a chlorinated acceptor with increased open-circuit voltages. *Nat. Commun*. 10:2515. doi: 10.1038/s41467-019-10351-5

Das, S., and Zade, S. S. (2010). Poly(cyclopenta[c]selenophene): a new polyselenophene. *Chem. Commun*. 46:1168. doi: 10.1039/b915826j

Ding, K., Wang, Y., Shan, T., Xu, J., Bao, Q., Liu, F., et al. (2020). Propeller-like acceptors with difluoride perylene diimides for organic solar cells. *Org. Electron*. 78:105569. doi: 10.1016/j.orgel.2019.105569

Duan, Y., Xu, X., Li, Y., and Peng, Q. (2017a). Recent development of perylene diimide-based small molecular non-fullerene acceptors in organic solar cells. *Chin. Chem. Lett*. 28, 2105–2115. doi: 10.1016/j.cclet.2017.08.025

Duan, Y., Xu, X., Yan, H., Wu, W., Li, Z., and Peng, Q. (2017b). Pronounced effects of a triazine core on photovoltaic performance-efficient organic solar cells enabled by a PDI trimer-based small molecular acceptor. *Adv. Mater*. 29, 1–6. doi: 10.1002/adma.201605115

Eastham, N. D., Dudnik, A. S., Aldrich, T. J., Manley, E. F., Fauvell, T. J., Hartnett, P. E., et al. (2017). Small molecule acceptor and polymer donor crystallinity and aggregation effects on microstructure templating: understanding photovoltaic response in fullerene-free solar cells. *Chem. Mater*. 29, 4432–4444. doi: 10.1021/acs.chemmater.7b00964

Genene, Z., Mammo, W., Wang, E., and Andersson, M. R. (2019). Recent advances in n-type polymers for all-polymer solar cells. *Adv. Mater*. 31:1807275. doi: 10.1002/adma.201807275

Hartnett, P. E., Timalsina, A., Matte, H. S., Zhou, N., Guo, X., Zhao, W., et al. (2014). Slip-stacked perylenediimides as an alternative strategy for high efficiency nonfullerene acceptors in organic photovoltaics. *J. Am. Chem. Soc*. 136, 16345–16356. doi: 10.1021/ja508814z

Heeney, M., Zhang, W., Crouch, D. J., Chabinyc, M. L., Gordeyev, S., Hamilton, R., et al. (2007). Regioregular poly(3-hexyl)selenophene: a low band gap organic hole transporting polymer. *Chem. Commun*. 5061–5063. doi: 10.1039/b712398a

Hou, J., Inganäs, O., Friend, R. H., and Gao, F. (2018). Organic solar cells based on non-fullerene acceptors. *Nat. Mater*. 17, 119–128. doi: 10.1038/nmat5063

Inganäs, O. (2018). Organic photovoltaics over three decades. *Adv. Mater*. 30:1800388. doi: 10.1002/adma.201800388

Jahnke, A. A., Djukic, B., McCormick, T. M., Buchaca Domingo, E., Hellmann, C., Lee, Y., et al. (2013). Poly(3-alkyltellurophene)s are solution-processable polyheterocycles. *J. Am. Chem. Soc*. 135, 951–954. doi: 10.1021/ja309404j

Kim, H. S., Park, H. J., Lee, S. K., Shin, W. S., Song, C. E., Hwang, D.-H., et al. (2019). Effects of the core unit on perylene-diimide-based molecular acceptors in fullerene-free organic solar cells. *Org. Electron*. 71, 238–245. doi: 10.1016/j.orgel.2019.05.029

Lee, J., Singh, R., Sin, D. H., Kim, H. G., Song, K. C., and Cho, K. (2016). A Nonfullerene small molecule acceptor with 3D interlocking geometry enabling efficient organic solar cells. *Adv. Mater*. 28, 69–76. doi: 10.1002/adma.201504010

Li, G., Wang, S., Li, D., Liu, T., Yan, C., Li, J., et al. (2020). Chalcogen-fused perylene diimides-based nonfullerene acceptors for high-performance organic solar cells: insight into the effect of O, S, and Se. *Sol. RRL* 4:1900453. doi: 10.1002/solr.201900453

Li, G., Yang, S., Liu, T., Li, J., Yang, W., Luo, Z., et al. (2019). Functionalizing tetraphenylpyrazine with perylene diimides (PDIs) as high-performance nonfullerene acceptors. *J. Mater. Chem. C* 7, 14563–14570. doi: 10.1039/C9TC05643B

Liang, N., Sun, K., Zheng, Z., Yao, H., Gao, G., Meng, X., et al. (2016). Perylene diimide trimers based bulk heterojunction organic solar cells with efficiency over 7%. *Adv. Energy Mater*. 6:1600060. doi: 10.1002/aenm.201600060

Lin, H., Chen, S., Hu, H., Zhang, L., Ma, T., Lai, J. Y., et al. (2016). Reduced intramolecular twisting improves the performance of 3D molecular acceptors in non-fullerene organic solar cells. *Adv. Mater*. 28, 8546–8551. doi: 10.1002/adma.201600997

Lin, Y., Wang, Y., Wang, J., Hou, J., Li, Y., Zhu, D., et al. (2014). A star-shaped perylene diimide electron acceptor for high-performance organic solar cells. *Adv. Mater*. 26, 5137–5142. doi: 10.1002/adma.201400525

Liu, J., Chen, S., Qian, D., Gautam, B., Yang, G., Zhao, J., et al. (2016). Fast charge separation in a non-fullerene organic solar cell with a small driving force. *Nat. Energy* 1:16089. doi: 10.1038/nenergy.2016.89

Malliaras, G. G., Salem, J. R., Brock, P. J., and Scott, C. (1998). Electrical characteristics and efficiency of single-layer organic light-emitting diodes. *Phys. Rev. B* 58, R13411–R13414. doi: 10.1103/PhysRevB.58.R13411

Meng, D., Fu, H., Xiao, C., Meng, X., Winands, T., Ma, W., et al. (2016b). Three-bladed rylene propellers with three-dimensional network assembly for organic electronics. *J. Am. Chem. Soc*. 138, 10184–10190. doi: 10.1021/jacs.6b04368

Meng, D., Sun, D., Zhong, C., Liu, T., Fan, B., Huo, L., et al. (2016a). High-performance solution-processed non-fullerene organic solar cells based on selenophene-containing perylene bisimide acceptor. *J. Am. Chem. Soc*. 138, 375–380. doi: 10.1021/jacs.5b11149

Nicolas, Y., Blanchard, P., Levillain, E., Allain, M., Mercier, N., and Roncali, J. (2004). Planarized star-shaped oligothiophenes with enhanced π-electron delocalization. *Org. Lett*. 6, 273–276. doi: 10.1021/ol0362764

Sisto, T. J., Zhong, Y., Zhang, B., Trinh, M. T., Miyata, K., Zhong, X., et al. (2017). Long, atomically precise donor-acceptor cove-edge nanoribbons as electron acceptors. *J. Am. Chem. Soc*. 139, 5648–5651. doi: 10.1021/jacs.6b13093

Sonoda, M., Inaba, A., Itahashi, K., and Tobe, Y. (2001). Synthesis of differentially substituted hexaethynylbenzenes based on tandem sonogashira and negishi cross-coupling reactions. *Org. Lett*. 3, 2419–2421. doi: 10.1021/ol016274o

Spano, F. C., and Silva, C. (2014). H- and J-aggregate behavior in polymeric semiconductors. *Annu. Rev. Phys. Chem*. 65, 477–500. doi: 10.1146/annurev-physchem-040513-103639

Sun, H., Liu, T., Yu, J., Ki, L. T., Zhang, G., Zhang, Y., et al. (2019). A monothiophene unit incorporating both fluoro and ester substitution enabling high-performance donor polymers for non-fullerene solar cells with 16.4% efficiency. *Energy Environ. Sci*. 12, 3328–3337. doi: 10.1039/C9EE01890E

Sun, H., Song, X., Xie, J., Sun, P., Gu, P., Liu, C., et al. (2017). PDI derivative through fine-tuning the molecular structure for fullerene-free organic solar cells. *ACS Appl. Mater. Interfaces* 9, 29924–29931. doi: 10.1021/acsami.7b08282

Tang, F., Wu, K., Zhou, Z., Wang, G., Zhao, B., and Tan, S. (2019). Alkynyl-functionalized pyrene-cored perylene diimide electron acceptors for efficient nonfullerene organic solar cells. *ACS Appl. Energy Mater*. 2, 3918–3926. doi: 10.1021/acsaem.9b00611

Tsuji, H., Cantagrel, G., Ueda, Y., Chen, T., Wan, L. J., and Nakamura, E. (2014). Synthesis of benzotrifuran and benzotripyrrole derivatives and molecular orientations on the surface and in the solid state. *Chem. Asian J*. 8, 2377–2382. doi: 10.1002/asia.201300106

Viswanath, L., Shirtcliff, L. D., Krishnan, S., Handa, N. V., and Darrell Berlin, K. (2014). Synthesis, photophysical and electrochemical properties of bay-axial perylene diimide-subphthalocyanine dyads. *Tetrahed. Lett*. 55, 4199–4202. doi: 10.1016/j.tetlet.2014.05.120

Wang, K., Xia, P., Wang, K., You, X., Wu, M., Huang, H., et al. (2020). π-extension, selenium incorporation, and trimerization: "three in one" for efficient perylene diimide oligomer-based organic solar cells. *ACS Appl. Mater. Interfaces* 12, 9528–9536. doi: 10.1021/acsami.9b21929

Wang, R., Jiang, K., Yu, H., Wu, F., Zhu, L., and Yan, H. (2019). Efficient inverted perovskite solar cells with truxene-bridged PDI trimers as electron transporting materials. *Mater. Chem. Front*. 3, 2137–2142. doi: 10.1039/C9QM00329K

Weng, K., Li, C., Bi, P., Ryu, H., Guo, Y., Hao, X., et al. (2019). Ternary organic solar cells based on two compatible PDI-based acceptors with an enhanced power conversion efficiency. *J. Mater. Chem. A* 7, 3552–3557. doi: 10.1039/C8TA12034J

Wu, J., Li, X., Liu, X., Wu, S., Lai, W., and Zheng, Y. (2018). Effects of conjugated bridges on the photovoltaic properties of ortho -functionalized perylene diimides for non-fullerene polymer solar cells. *J. Mater. Chem. C* 6, 13171–13178. doi: 10.1039/C8TC03303J

Wu, M., Yi, J., Hu, J., Xia, P., Wang, H., Chen, F., et al. (2019). Ring fusion attenuates the device performance: star-shaped long helical perylene diimide based non-fullerene acceptors. *J. Mater. Chem. C* 7, 9564–9572. doi: 10.1039/C9TC02150G

Xu, X., Feng, K., Bi, Z., Ma, W., Zhang, G., and Peng, Q. (2019b). Single-junction polymer solar cells with 16.35% efficiency enabled by a Platinum(II) complexation strategy. *Adv. Mater*. 31:1901872. doi: 10.1002/adma.201901872

Xu, X., Feng, K., Lee, Y. W., Woo, H. Y., Zhang, G., and Peng, Q. (2020). Subtle polymer donor and molecular acceptor design enable efficient polymer solar cells with a very small energy loss. *Adv. Funct. Mater*. 30:1907570. doi: 10.1002/adfm.201907570

Xu, X., Zhang, G., Li, Y., and Peng, Q. (2019a). The recent progress of wide bandgap donor polymers towards non-fullerene organic solar cells. *Chinese Chem. Lett*. 30, 809–825. doi: 10.1016/j.cclet.2019.02.030

Yan, C., Barlow, S., Wang, Z., Yan, H., Jen, A. K.-Y., Marder, S. R., et al. (2018). Non-fullerene acceptors for organic solar cells. *Nat. Rev. Mater*. 3:18003. doi: 10.1038/natrevmats.2018.3

Yan, Q., Zhou, Y., Zheng, Y. Q., Pei, J., and Zhao, D. (2013). Towards rational design of organic electron acceptors for photovoltaics: a study based on perylenediimide derivatives. *Chem. Sci*. 4:4389. doi: 10.1039/c3sc51841h

Yan, T., Song, W., Huang, J., Peng, R., Huang, L., and Ge, Z. (2019). 16.67% rigid and 14.06% flexible organic solar cells enabled by ternary heterojunction strategy. *Adv. Mater*. 31:1902210. doi: 10.1002/adma.201902210

Ye, L., Sun, K., Jiang, W., Zhang, S., Zhao, W., Yao, H., et al. (2015). Enhanced efficiency in fullerene-free polymer solar cell by incorporating fine-designed donor and acceptor materials. *ACS Appl. Mater. Interfaces* 7, 9274–9280. doi: 10.1021/acsami.5b02012

Yu, R., Yao, H., Cui, Y., Hong, L., He, C., and Hou, J. (2019). Improved charge transport and reduced nonradiative energy loss enable over 16% efficiency in ternary polymer solar cells. *Adv. Mater*. 31:1902302. doi: 10.1002/adma.201902302

Zhan, X., Facchetti, A., Barlow, S., Marks, T. J., Ratner, M. A., Wasielewski, M. R., et al. (2011). Rylene and related diimides for organic electronics. *Adv. Mater*. 23, 268–284. doi: 10.1002/adma.201001402

Zhang, G., Xu, X., Lee, Y. W., Woo, H. Y., Li, Y., and Peng, Q. (2019). Achieving a high fill factor and stability in perylene diimide-based polymer solar cells using the molecular lock effect between 4,4′-Bipyridine and a Tri(8-hydroxyquinoline)aluminum(III) core. *Adv. Funct. Mater*. 29:1902079. doi: 10.1002/adfm.201902079

Zhang, G., Zhao, J., Chow, P. C. Y., Jiang, K., Zhang, J., Zhu, Z., et al. (2018). Nonfullerene acceptor molecules for bulk heterojunction organic solar cells. *Chem. Rev*. 118, 3447–3507. doi: 10.1021/acs.chemrev.7b00535

Zhang, J., Tan, H. S., Guo, X., Facchetti, A., and Yan, H. (2018). Material insights and challenges for non-fullerene organic solar cells based on small molecular acceptors. *Nat. Energy* 3, 720–731. doi: 10.1038/s41560-018-0181-5

Zhang, X., Lu, Z., Ye, L., Zhan, C., Hou, J., Zhang, S., et al. (2013). A potential perylene diimide dimer-based acceptor material for highly efficient solution-processed non-fullerene organic solar cells with 4.03% efficiency. *Adv. Mater*. 25, 5791–5797. doi: 10.1002/adma.201300897

Zhong, H., Wu, C. H., Li, C. Z., Carpenter, J., Chueh, C. C., Chen, J. Y., et al. (2016). Rigidifying nonplanar perylene diimides by ring fusion toward geometry-tunable acceptors for high-performance fullerene-free solar cells. *Adv. Mater*. 28, 951–958. doi: 10.1002/adma.201504120

Zhong, Y., Trinh, M. T., Chen, R., Purdum, G. E., Khlyabich, P. P., Sezen, M., et al. (2015). Molecular helices as electron acceptors in high-performance bulk heterojunction solar cells. *Nat. Commun*. 6:8242. doi: 10.1038/ncomms9242

Zhong, Y., Trinh, M. T., Chen, R., Wang, W., Khlyabich, P. P., Kumar, B., et al. (2014). Efficient organic solar cells with helical perylene diimide electron acceptors. *J. Am. Chem. Soc*. 136, 15215–15221. doi: 10.1021/ja5092613

Conflict of Interest: The authors declare that the research was conducted in the absence of any commercial or financial relationships that could be construed as a potential conflict of interest.

frontiers in Chemistry

ORIGINAL RESEARCH
published: 20 May 2020
doi: 10.3389/fchem.2020.00394

Increasing N2200 Charge Transport Mobility to Improve Performance of All Polymer Solar Cells by Forming a Percolation Network Structure

Ye Yan[1,2], *Yadi Liu*[1,2], *Qiang Zhang*[1]* and *Yanchun Han*[1,2]*

[1] State Key Laboratory of Polymer Physics and Chemistry, Changchun Institute of Applied Chemistry, Chinese Academy of Sciences, Changchun, China, [2] School of Applied Chemistry and Engineering, University of Science and Technology of China, Hefei, China

The poor electron transport ability of the polymer acceptor is one of the factors restricting the performance of all-polymer solar cells. The percolation network of conjugated polymers can promote its charge transfer. Hence, we aim to find out the critical molecular weight (MW) of N2200 on the forming of the percolation network and to improve its charge mobility and thus photovoltaic performance of J51:N2200 blend. Detailed measurements demonstrate that when the MW of N2200 is larger than 96k, a percolation network structure is formed due to the chain tangled and multi-chain aggregations. Analysis of kinetic experiments reveals that it is the memory of the N2200 long chain conformation and the extent of aggregation in solution are carried into cast films for the formation of the percolation network. Thus, the electron mobility increases from 5.58 $\times$ 10^{-6} $cm^2V^{-1}s^{-1}$ ($N2200_{17k}$) to 9.03 $\times$ 10^{-5} $cm^2V^{-1}s^{-1}$ when the MW of N2200 is >96k. It led to a balance between hole and electron mobility. The μ_h/μ_e decrease from 16.9 to 1.53, causing a significant enhancement in the PCEs, from 5.87 to 8.28% without additives.

Keywords: molecular weight, charge transport, percolation network, solution aggregation, all-polymer solar cells, chain conformation

OPEN ACCESS

Edited by:
Kui Zhao,
Shaanxi Normal University, China

Reviewed by:
Hin-Lap Yip,
South China University of Technology, China
Erjun Zhou,
National Center for Nanoscience and Technology (CAS), China

***Correspondence:**
Qiang Zhang
zhqawh@ciac.ac.cn
Yanchun Han
ychan@ciac.ac.cn

Specialty section:
This article was submitted to Physical Chemistry and Chemical Physics, a section of the journal Frontiers in Chemistry

Received: *10 March 2020*
Accepted: *15 April 2020*
Published: *20 May 2020*

Citation:
Yan Y, Liu Y, Zhang Q and Han Y (2020) Increasing N2200 Charge Transport Mobility to Improve Performance of All Polymer Solar Cells by Forming a Percolation Network Structure. Front. Chem. 8:394. doi: 10.3389/fchem.2020.00394

INTRODUCTION

All-polymer solar cells (all-PSCs) have attracted widespread attention due to their unique advantages, such as good morphological stability and outstanding mechanical properties (Zhou et al., 2014; Kim et al., 2015; Zhang et al., 2018; Xu et al., 2019; Yang et al., 2019a,b; Zheng et al., 2019). However, their efficient uses still cannot compete with the polymer–small molecules system (Zhu et al., 2019; Liu et al., 2020). One of the main factors restricting its performance is the poor electron transport capacity of the polymeric acceptor (Holcombe et al., 2009; Mori et al., 2011; Wetzelaer et al., 2012).

The mobility of conjugated polymers mostly increases with the increase of molecular weights, and this usually promotes PCE improvement (Bartelt et al., 2014; Fan et al., 2017; Khan et al., 2019; Li et al., 2019; Yin et al., 2019; Zhang Z. et al., 2019). Jung et al. found the tendency of face-to-face stacking to increase with an increase in the the MW of N2200 in PTB7-Th:N2200 blends (Jung et al., 2016). This stacking facilitated the free charge carrier generation, and the PCE was up to 6.14%. Marks and collaborators investigated the molecular weight effect of both PTPD3T and N2200 (Zhou et al., 2016). They found that the blend with the intermediary molecular weight

of PTPD3T and N2200 can get an optimal morphology. The blend morphology, having ordered crystalline to promote charge transport, and good miscibility, provides a sufficient interface for exciton separation. Kolhe et al. (2018). produced the PNDIBS with different MWs (28.4 kDa, 57.3 kDa) and blended it with the donor PBDB-T. They found the electron mobility in the high MW blends is nearly an order of magnitude higher compared to the low MW blends. The power conversion efficiency (PCE) achieved 9.4% in all-PSCs with high-molecular-weight PNDIBS. Hoefler et al. used a different MWs PTB7-Th blend with O-IDTBR to investigate the effect of MW on the device performance (Hoefler et al., 2018). They assigned the enhanced J_{sc} values to the improvement of hole mobility with the increasing molecular weight of PTB7-Th. The hole mobility increased from 6.2×10^{-3} cm^2 V^{-1} s^{-1} (50 kDa) to 1.05×10^{-2} cm^2 V^{-1} s^{-1} (200 kDa), and the PCE increased from 8.44 to 9.57%. This kind of behavior is also described in some studies to generally originate from a higher effective conjugation length and extended interconnectivity between ordered polymer aggregates (Kline and McGehee, 2006; Gu et al., 2018; McBride et al., 2018). When the chain is long enough that it is beyond a critical MW, the interconnectivity chain can form a percolated network for supporting macroscopic charge transport. This percolation network structure can not only improve the electrical properties but also enhance the mechanical properties (Choi et al., 2019). However, this critical MW or percolation threshold has varied from study to study caused by molecular characteristics of polymers. For example, the critical MW of P3HT exists normally in the region of 20–30 kDa, and the FTAZ is below 30 kDa (Chang et al., 2006; Koch et al., 2013; Balar et al., 2019).

N2200 is one of the most studied n-type polymeric semiconductors and is broadly used as the polymer acceptor in all-polymer solar cells. Despite extensive research focused on improvements on the device performance front (Osaka et al., 2012), however, it remains a challenge to understand the mechanism of how processes can lead to efficient electronic charge transport in all-polymer solar cells (Vacha and Habuchi, 2010; Jackson et al., 2015). Within the current body of the manuscript, we have aimed at understanding how long the N2200 chain can realize the percolation network structure to optimal charge transfer pathways. The difference in the characteristic is related to the difference between the different MWs of N2200. Finally, we have correlated the evolution of such microstructures to the evolution of electronic properties in devices. The MW of N2200 used in this experiment was calculated: the number-average molecular weight of 17, 28, 57, 96, and 110 kDa, denoted as $N2200_{17k}$, $N2200_{28k}$, $N2200_{57k}$, $N2200_{96k}$, and $N2200_{110k}$, respectively. Through a detailed study of the intrinsic feature of the N2200, we revealed the mechanism behind the N2200 percolation network structure. Thus, the relationship between the structure–property paradigms is constructed. The prepared high-performance devices have shown the importance of reasonable molecular weight selecting for performance optimization.

MATERIALS AND METHODS

Materials

J51 (M_n = 23 kDa, PDI = 2.1) and N2200 with different molecular weights (M_n = 17 kDa, PDI = 2.2; M_n = 28 kDa, PDI = 2.0; M_n = 57 kDa, PDI = 3.0; M_n = 96 kDa, PDI = 2.0; M_n = 110 kDa, PDI = 2.0) were acquired from 1-Materials company, as displayed in **Scheme 1B**. Solvent chloroform was purchased from Beijing Chemical Plant.

Devices Fabrication

All-polymer solar cells were fabricated with a conventional structure of ITO/PEDOT:PSS/J51:N2200/PFN-Br/Ag, as shown in **Scheme 1A**. The ITO substrate was sonicated and treated in a UV ozone etching machine. The solutions were prepared by blending J51 and N2200 (2:1 w/w) in chloroform with a total concentration of 12 mg ml^{-1}, stirring overnight to ensure the polymer soluble. The PBDB-T:N2200 blend system based on different MWs of N2200 is fabrication in the same condition. The active layers were spun-coated on the PEDOT:PSS-based ITO. Then, a ≈100 nm film was formed and thermally annealed at 130°C for 10 min. Lastly, a 5 nm PFN-Br and 95 nm thickness of Ag were sequentially deposited below the vacuum level of 1×10^{-4} Pa. The device area is 0.072 cm^2.

Space-Charge-Limited Current (SCLC) Measurement

The mobility is tested by the space-limited charge (SCLC) method. The structures for electron-only and hole-only were ITO/ZnO/active layer/PFN-Br/Ag and ITO/PEDOT:PSS/active layer/MoO_3/Ag, respectively. The thickness of the active layers was ∼100 nm. The film thermal annealed at 130°C for 10 min. Current–voltage (J–V) characteristics of the SCLC devices were tested by utilizing a Keithley 2400 SMU under dark condition

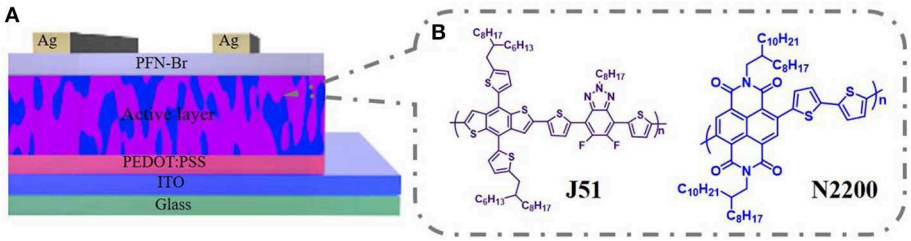

SCHEME 1 | (A) The conventional device architecture. **(B)** The chemical structures of polymers.

in glove box filling nitrogen. The carrier mobility was extracted according to the equation of Mott–Gurney (Equation 1):

$$J = \frac{9}{8}\varepsilon_r\varepsilon_0\mu\frac{V^2}{d^3} \quad (1)$$

Where J is the current density, ε_0 and ε_r is the free space and relative permittivity, respectively. The μ is the zero-field mobility, V is the effective voltage ($V = V_{applied}$-V_{bi}-V_{series}), and d is the thickness of the film.

Characterization

The film morphology was measured by atomic force microscopy (AFM) and a transmission electron microscope (TEM). Sessile-drop measurements were done on the pure N2200 films with different MWs for water drops by using a contact angle goniometer (KRUSS GmbH Germany DO3021 Mk1). The molecular weights were tested by the gel permeation chromatography (GPC) of high-temperature in trichlorobenzene (TCB) with polystyrene as the calibration standard. The viscosities of the N2200 solutions (4 mg ml^{-1}) were measured utilizing a cone-plate rheometer (BROOKFIELD DV-III ULTRA). The measurement was carried out at a constant rotor speed is 120 rpm min^{-1} at room temperature. DSC curves were tested using DSC Q2000. The heating and cooling rate is 3°C min^{-1} under nitrogen filling atmosphere. The melting enthalpy and melting temperature are read from the second heating curve, and the crystallization temperature is read from the first cycles of the cooling curve. The UV-vis absorption spectra were measured by applying a Lambda 750 absorption spectrum (Perkin-Elmer, Wellesley, MA). The instrument used for PL spectroscopy was a Jobin Yvon LabRAM HR spectrometer. The solution concentration was 0.1 mg ml^{-1}. The GIXRD data were got on a Bruker D8 Discover reflector.

We tested the J–V characteristics curves of the devices under simulated AM 1.5G solar irradiation (100 MW cm^{-2}, Keithley 2400 SMU) at a nitrogen filling glove box. The EQE results were obtained applying a QE-R 3011 instrument (Enli Tech.Co) at an ambient atmosphere.

RESULTS

Photovoltaic Performance

To explore how the molecular weight of N2200 in blends of J51:N2200 affects the device performance, conventional-type PSCs were fabricated. The devices were processed by thermal annealing at 130°C for 10 min without solvent additives. The current density–voltage (J–V) curves of the devices were tested under simulated AM 1.5G, 100MW cm^{-2} illumination, as illustrated in **Figure 1A**. The correlative photovoltaic parameters are shown in **Table 1**. The J51:N2200$_{17k}$ and J51:N2200$_{28k}$ showed lower PCEs of 5.87 and 6.38%, respectively, with a close J_{sc} of about 12.8 mA cm^{-2}. With the increase of the molecular weight of N2200, the J_{sc} and FF values increased. The V_{oc} value was almost unchanged (0.81–0.82 V). The J_{sc} and FF values of N2200$_{110k}$ improved significantly from 12.70 mA cm^{-2} and 56.18% for J51:N2200$_{17k}$, to 15.61 mA cm^{-2} and 64.88%. Then, a peak PCE of 8.28% was achieved, which is a 41% enhancement. External quantum efficiency (EQE) spectra of the all-PSCs are presented in **Figure 1B**. The J_{sc} got from

TABLE 1 | Summary of photovoltaic performance for J51:N2200 and relevant parameters of carrier mobility for blend film.

Donor: acceptor	V_{oc} (V)	J_{sc} (mA cm^{-2})	FF (%)	PCE (%)	μ_h (cm^{2}V^{-1}s^{-1})	μ_e (cm^{2}V^{-1}s^{-1})	μ_h/μ_e
J51:N2200$_{17k}$	0.82	12.70	56.18	5.87	9.43×10^{-5}	5.58×10^{-6}	16.9
J51:N2200$_{28k}$	0.82	12.82	60.80	6.38	1.14×10^{-4}	7.55×10^{-6}	15.1
J51:N2200$_{57k}$	0.81	13.85	62.56	7.02	4.67×10^{-5}	1.64×10^{-5}	2.85
J51:N2200$_{96k}$	0.81	14.01	61.62	7.22	6.07×10^{-5}	2.85×10^{-5}	2.13
J51:N2200$_{110k}$	0.82	15.61	64.88	8.28	1.38×10^{-4}	9.03×10^{-5}	1.53

(Average values are obtained from 10 devices).

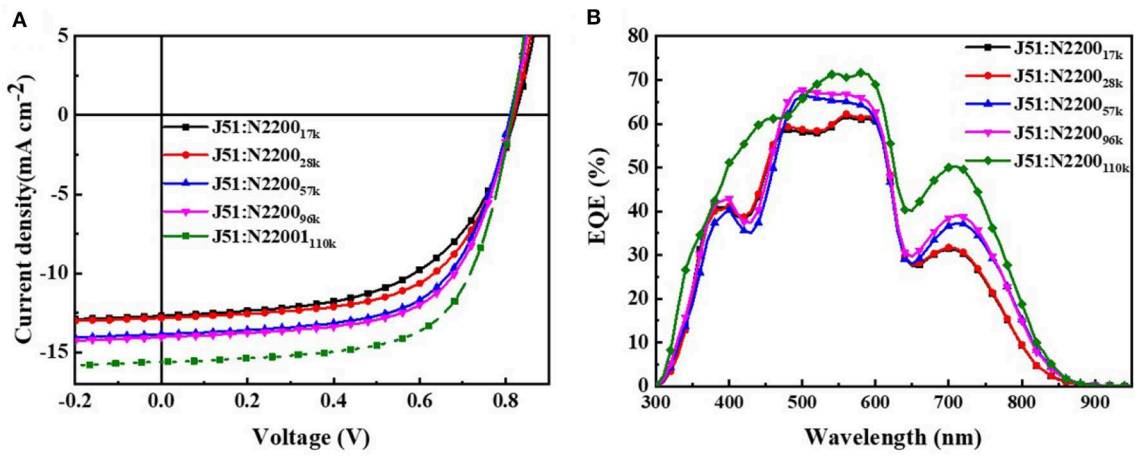

FIGURE 1 | (A) *J-V* curves **(B)** EQE curves for J51:N2200 films based on different N2200 MWs.

the EQE spectra were consistent with those obtained from *J*–*V* measurements. The variations between them were below 6%. All the devices had a broad EQE response from 300 to 900 nm. The EQE values gradually increased with the increasing MW of N2200, particularly in the long-wavelength band of 700–900 nm assigned to N2200. The J51:$N2200_{110k}$ blend exhibited a higher EQE response than other lower N2200 MW blend, 71%, located at 580 nm. We also fabricated the device of PBDB-T:N2200 in the same condition as shown in **Figure S1** and **Table S1**. The same trend can found in PBDB-T:N2200 system. A peak PCE of 7.98% was achieved for PBDB-T:$N2200_{110k}$. It is much larger than 5.74% for PBDB-T:$N2200_{17k}$. The J_{sc} values improved significantly from 10.55 mA cm^{-2} for PBDB-T:$N2200_{17k}$ to 16.17 mA cm^{-2} for PBDB-T:$N2200_{110k}$. Hence, the J_{sc} is a strong N2200 molecular weight dependent, increasing with N2200 MWs.

Charge Transport Ability

To further study the cause of the enhanced J_{sc} in the devices, we tested the ability of charge transport. The mobility is examined by the space charge-limited current (SCLC) method, as illustrated in **Figure S2**. The detailed parameters are listed in **Table 1**. The increase of MW of N2200 improved the electron mobility (μ_e) values of the PSCs, as displayed in **Figure 2A**. The μ_e was 16 times larger in the $N2200_{110k}$ blends. As the MW of N2200 increases, the mobility of electrons and holes is more balanced, and the ratio between hole mobility (μ_h) and μ_e decreases from 16.9 to 1.53, as shown in **Figure 2B**. The results of the SCLC mobility indicated the enhanced PCEs of the blend devices with different MWs of N2200 are due to improving the ability of charge transport. We speculated that high MW of N2200 molecules is sufficient to form percolation pathways to facilitate electron transport. To prove our conjecture, the μ_e and μ_h of the pure components were measured (**Figure 2C**, **Figure S3**). As with the blend system, the hole mobility of J51 is 2.29 × 10^{-4} $cm^2V^{-1}s^{-1}$, which is higher than the electron mobility of different MWs of N2200 in this work. Meanwhile, the μ_e increases with the N2200 MW increasing. The μ_e was 1.89 × 10^{-4} $cm^2V^{-1}s^{-1}$ in $N2200_{110k}$ devices, which is 32 times the improvement compared to $N2200_{17k}$. The electron mobility of pure N2200 is gradually increased when increasing the MWs, getting closer to the pure J51. The mobility data of pure component provide a solid support for the high MW N2200 forming a percolation network structure to improve the ability of charge transport.

A Percolation Network Phase Separation Structure

We compared the morphology of the blend films as a function of MW of N2200 **Figure 3A**. As the MW increased, the surface roughness of the film gradually reduced from 0.87 to 0.63 nm. The phase separation size of J51:$N2200_{17k}$ and J51:$N2200_{28k}$ are significantly larger than the high-molecular-weight blend system. Furthermore, the fiber structure can be observed obviously in both J51:$N2200_{110k}$ blend and the pure $N2200_{110k}$ (**Figure S4**). The crystallinity of the blend system is shown in **Figure 3B**. With the increase of the MW of N2200, the intensity of the (100) peak of N2200 at 3.75° in the blended film gradually weakened,

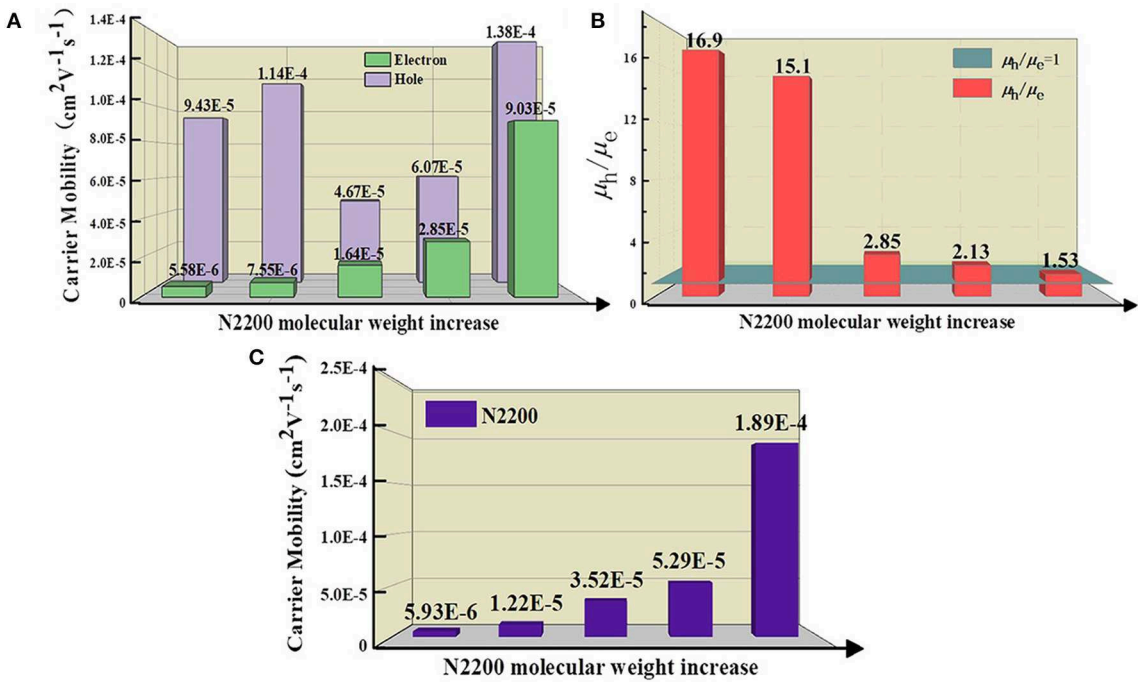

FIGURE 2 | (A) The hole and electron mobility **(B)** The ratio value of hole and electron mobility for J51:N2200 films based on different N2200 MWs. **(C)** The electron mobility of pure N2200 with different MWs.

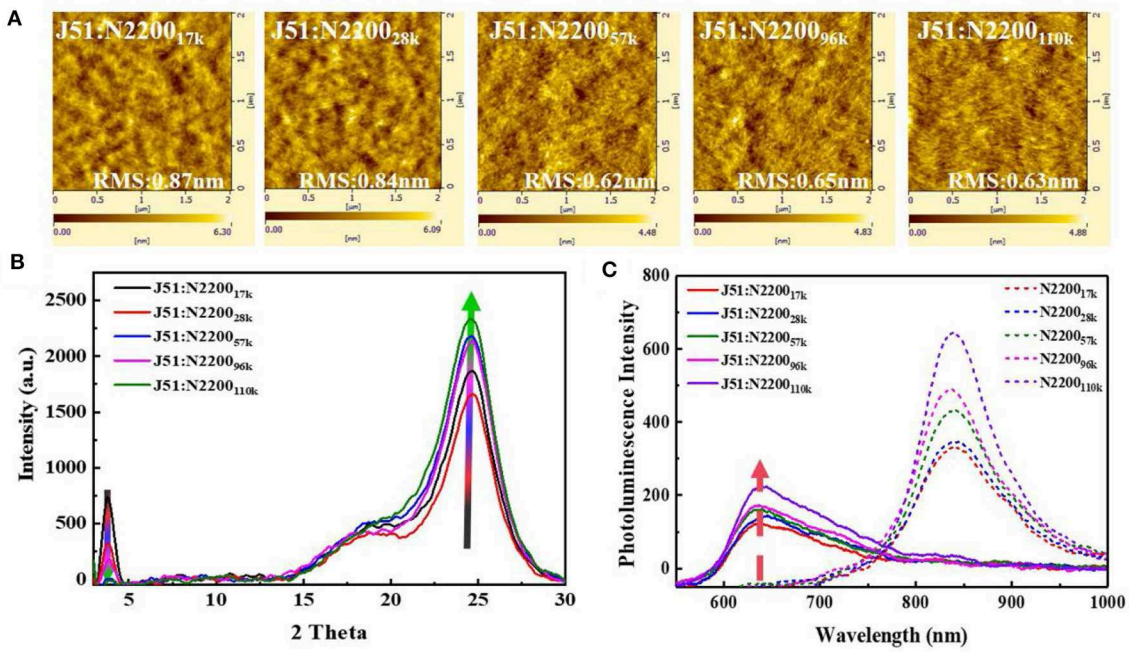

FIGURE 3 | (A) The AFM height images **(B)** GIXRD spectra of J51:N2200 films with different N2200 MWs. **(C)** PL spectra of the film (excited at 532 nm), where the solid line representative blend films, dash line representative pure films of N2200.

while the π-π stacking direction of (010) both N2200 at 22.5° and J51 at 24.5° was enhanced (Gao et al., 2016). This result indicates that the blend is more preferentially face-on orientated when the N2200 MW increases. The fluorescence spectrum tested to compare the purity of the phase domain, as revealed in **Figure 3C**. For pure component N2200, the intensity at 838 nm increases with increasing MW. After blending with the donor J51, the fluorescence intensity decreased sharply. The intensity of J51 at 637 nm increased with the increase of N2200 MW. This means that the phase purity of J51 in the blend system is strengthened as the MW of N2200 increases.

Taken together, these results indicate that the N2200$_{110k}$ is long enough to form a percolation network structure compared to other MWs. This percolation network can produce an optimal blend morphology with smaller size of phase separation and purer phase domain purity and the stronger tendency of face-on orientation to realize both high J_{sc} and PCE.

The Memory of the Long Chain Conformation and the Extent of Aggregation in Solution Are Carried into Cast Films for the Formation of the Percolation Network

To understand why N2200$_{110k}$ can form a percolation network, the chain structural characteristics of different MWs were investigated by the following detailed measurements.

Figure 4A is the solution of the absorption spectra of different MWs of N2200. The N2200 solution concentration is 0.1 mg ml^{-1}. All samples revealed two bands: high-energy bands are ascribed to π-π* transition (nearly 390 nm), and low-energy bands are assigned to intramolecular charge transfer transition (500–800 nm). The absorption of the N2200$_{17k}$ and N2200$_{28k}$ revealed a broad and featureless band centered at about 640 nm. The appearance of the low-energy bands is indicative of the fine structure when the MWs reach 57k and 96k. In N2200$_{110k}$, the absorption spectra redshift, with a peak at 710 nm and a shoulder at ∼815 nm.

Changes of fluorescence spectra are in analogy to the absorption spectra displayed in **Figure 4B**. As the molecular weight increases from 17k to 110k, it leads to a pronounced redshift of the emission maximum. The emission spectra in the N2200$_{17k}$ and N2200$_{28k}$ are rather complex, showing distinct peaks at 760 and 820 nm. The spectrum in N2200$_{110k}$ exhibits a more structured emission, with the peak center at 843 nm. Furthermore, the lower energy band intensity increases with the increasing MWs of N2200. The one of N2200$_{110k}$ is 300% stronger than that of N2200$_{17k}$.

This pronounced changes in absorption and emission are similar to Neher and co-workers' results about the spectra of N2200 in different solvents (Schubert et al., 2012; Steyrleuthner et al., 2012). They dissolved two batches N2200 (MW = 29 and 526 kDa, convert to our experiments) in toluene (Tol), trichlorobenzene (TCB), and chloronaphthalene (CN) (Steyrleuthner et al., 2012). Notably, in CN and Tol, the spectrum was almost unchanged with MW. However, significant changes occurred in TCB as the MW changed. Therefore, we concluded that the effect of molecular weight on spectral chromophores mainly occurs in a moderately good solvent, such as chloroform

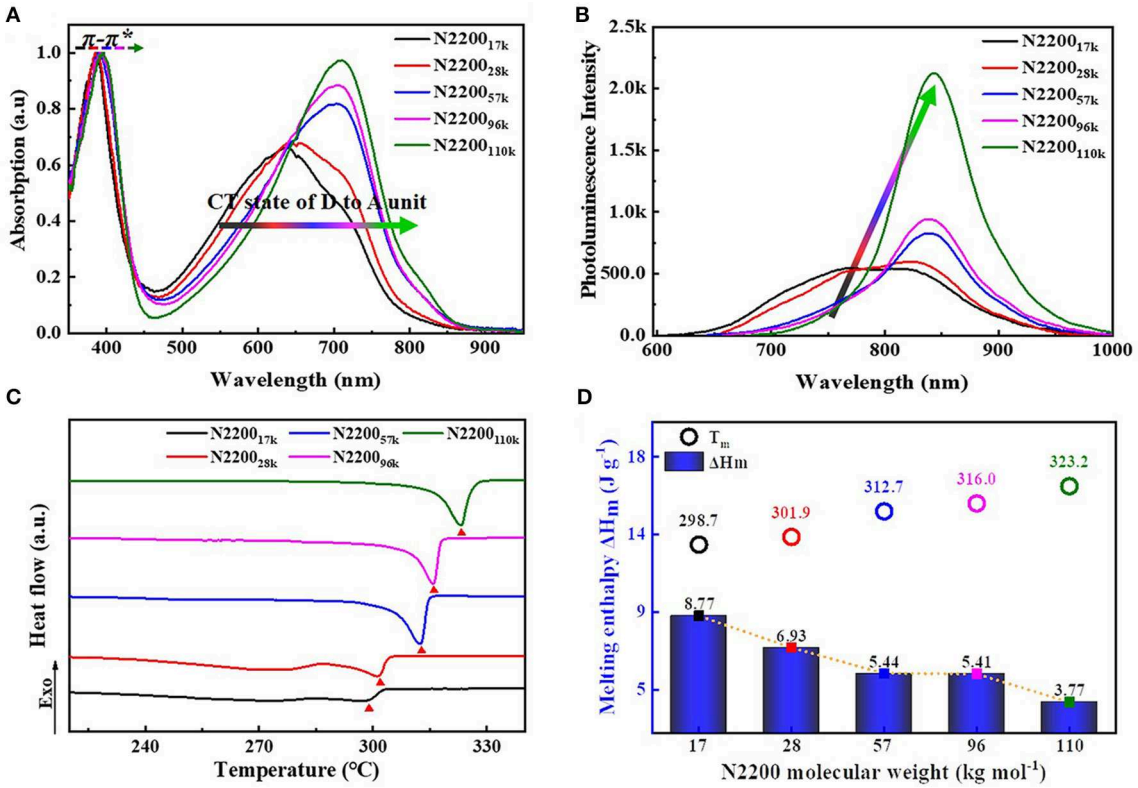

FIGURE 4 | (A) Normalized UV-vis absorption **(B)** PL spectra in chloroform solutions (0.1 mg/ml). **(C)** The second heating cycles of DSC curves **(D)** Summary of melting temperature (T_m) and melting enthalpy (ΔH_m) with different N2200 MWs.

and TCB. It is an intrachain phenomenon and related to different conformations of individual chains.

The melting temperature (T_m), melting enthalpy (ΔH_m), and crystallization temperature (T_c) of N2200 with different MWs were characterized by thermal analysis DSC (summarized in **Table 2**, **Figure S5**). The second heating curve of DSC was selected for the measurement of melting temperature, as shown in **Figure 4C**. The changes of T_m and ΔH_m as a function of MW are shown in **Figure 4D**. As the molecular weight increased from 17k to 110k, the T_m increased from 298.7 to 323.2°C. The ΔH_m also has a molecular weight dependence. The ΔH_m decreases from 8.77 to 3.77 J g^{-1} with an increase of MW. It is because that N2200$_{17k}$ has a shorter chain length, forming a chain extend crystals with less entangled structure. The entanglements happen in a longer chain of N2200$_{110k}$, hindering the crystallization process and resulting in a reduced crystallinity.

By studying the basic properties of different MWs N2200, we found that the chain conformation plays a key role in determining the phase separation structure. Though a direct and quantitative characterization of chain conformation remains a challenge, prediction of the backbone planarity and rigidity can provide the key steps to help our understanding of the chain conformation characteristic. Here, we hoped to utilize a power law relationship that exists between the intrinsic viscosity and the molecular weight to obtain information of chain conformation.

TABLE 2 | Characteristics of N2200 with different MWs.

	Mn (kDa)	PDI	λ_{max} (nm)	T_m (°C)	T_c (°C)	ΔH_m (J/g)
N2200$_{17k}$	17	2.2	636	298.7	281.6	8.77
N2200$_{28k}$	28	2.0	652	301.9	285.5	6.93
N2200$_{57k}$	57	3.0	705	312.7	295.2	5.44
N2200$_{96k}$	96	2.0	705	316.0	298.6	5.41
N2200$_{110k}$	110	2.0	710	323.2	300.9	3.77

The corresponding viscosity values are summarized in **Table S2**. The viscosity of the solvent chloroform was 0.61 mPa S, and the deviation from the conventional value was 8%. This discrepancy could be attributed to different test methods. **Figure 5A** shows the change of relative viscosity and specific viscosity with N2200 number-average molecular weight. In chloroform, the η_{sp} of the N2200 increased from 0.05 to 1.48 when the MW increase from 17k to 96k. Strikingly, the η_{sp} dramatically increased when the molecular weight reached 110k. Though the Mn of N2200$_{110k}$ increase merely 6-fold than the N2200$_{17k}$, the η_{sp} yielded a 97-fold increase. The η_r values follow the same trend. The marked increase in solution viscosity is caused by polymer chains entangling when the MW achieved the critical molecular weight (Na et al., 2019). The critical molecular weight range is consistent

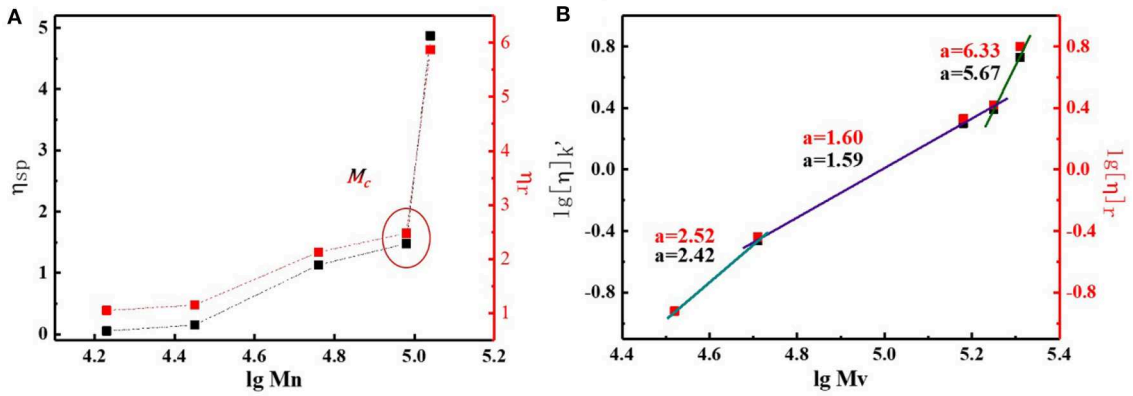

FIGURE 5 | (A) The change of relative viscosity and specific viscosity with N2200 number-average molecular weights. **(B)** Change of intrinsic viscosity with viscosity-average molecular weights.

with the literature (Choi et al., 2019). According to the Mark–Houwink formula where $[\eta] = KM\eta^a$, in a certain molecular weight range, the values of the index can reflect the chain conformation. Here, we used the relative viscosity (Equation 2) and specific viscosity (Equation 3) to calculate the intrinsic viscosity of the solution. The change of intrinsic viscosity with the viscosity-average molecular weight (M_v) is plotted in **Figure 5B**. The k' in Equation 3 is the interaction parameter between N2200 and chloroform, and its value is shown in **Figure S6**. The slope of the curve is a, which is obtained by taking the logarithm of the molecular weight and the intrinsic viscosity.

$$[\eta] = 0.25(\eta_r - 1 + 3\ln\eta_r/c \quad (2)$$

$$\eta_{sp}/c = [\eta] + k'[\eta]^2 c \quad (3)$$

The value obtained by the two methods are basically the same. The slope of the curve can be divided into three molecular weight intervals. At $N2200_{17k}$ and $N2200_{28k}$, the value of a is about 2.4. For rigid polymers, the value of a is close to 2. Therefore, the chain behaved as a rigid short rod-like structure in MWs 17k∼28k. The value of a decrease to 1.6, when the molecular weight increases to 57k and 96k. The polymer chain is a rigid chain structure. It is worth noting that the value of a is about six at $N2200_{110k}$, which is far away from the theoretical value of a. In the same polymer-solvent system, the longer polymer chain is, the greater the tendency is to bend and entangle in solution. The chain may form a cylindrical conformation (Hu et al., 2000; Adachi et al., 2010). The range of a with molecular weight is consistent with the spectrum. It firmly proves that the conformation change is the main reason for the change of spectrum. Meanwhile, the $N2200_{110k}$ has arrived at a critical MW.

The chain conformations greatly impact the aggregation behavior, which is important for charge transport in conjugated polymers (Liu et al., 2019; Zhang Q. et al., 2019). For this reason, we next analyzed in detail the aggregate behavior caused by conformation changes in the solution and film formation. The aggregation is a temperature-controlled process that is driven by a thermodynamic order–disorder transition (Kohler et al., 2012; Panzer et al., 2014, 2017; Reichenberger et al., 2018). Here, we used temperature-dependent absorption spectroscopy to study this order–disorder transition with different N2200 MWs. The low-energy band redshifted, and intensity grew alongside the reduction in temperature, as shown in **Figure 6A**. All samples gave rise to an isosbestic point. The isosbestic point indicates an equilibrium between two components in the solution: one corresponds to the planar structure of the chain with a longer and ordered conjugation length and another a disordered phase. The position of the isosbestic point is plotted as a function of MWs, as illustrated in **Figure 6B**. The conformational degree of freedom reduced with the reduction of temperature, causing the enthalpy upon planarization to become dominant, and the entropy contributed decreased. We therefore interpret from the data shown in **Figure 6B** that the isosbestic point gradually redshifted with an increase in the MW, and chain backbones tended to be more planar, causing effective electronic delocalization. Meanwhile, the solution contained larger multi-chain aggregates with an increase in the MW. These aggregates were more thermodynamically advantageous, owing to the lower the energy between the transform ordered and disordered phases.

To comprehensively understand the effect of aggregation from solution to film state, we subsequently tested the absorption spectra of films of different N2200 MWs. Using the Franck–Condon analysis of the absorption (Ho et al., 2001), the contribution of the solution state in the film is subtracted to obtain the aggregation during film formation (Jiao et al., 2019). Taking $N2200_{17k}$ as an example (**Figure 6C**), the data of other MWs are listed in **Figure S7**. The aggregation during film formation with different N2200 molecular weights is shown in **Figure 6D**. As the MW increases from 17k to 110k, the spectral intensity gradually decreases in the entire absorption range. The intensity of the π-π * transition decreases, and this is accompanied by the peak position being redshifted from 409 to 420 nm. Meanwhile, the CT state transition peak at 710 nm showed a dramatic decline with MW increases. These changes indicate the ordered structures have existed in solution and are preserved during the drying process. It has only a few rearrangements of polymer chains in the process of drying in

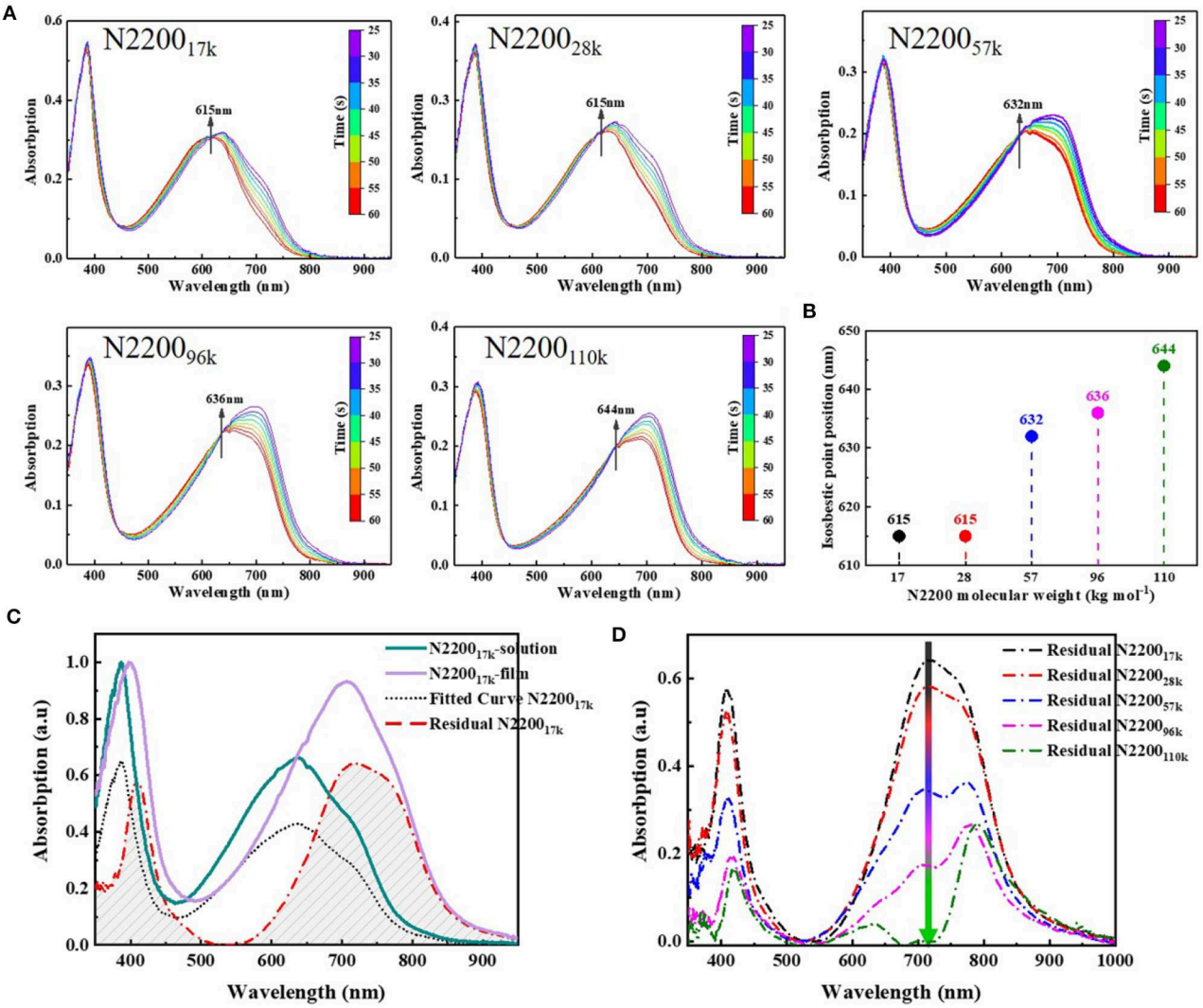

FIGURE 6 | (A) Variable-temperature UV-Vis absorption spectra of N2200 with different MWs. **(B)** Plot of isobestic point peak position vs. N2200 MWs. **(C)** Processing of film and solution absorption spectra, the green solid line is the normalized pristine solution spectra of $N2200_{17k}$, the purple solid line is the normalized pristine film spectra of $N2200_{17k}$, the black dot line is solution spectra after fitting pristine solution spectra to film spectra and the red dotted line is the spectra film spectra subtracted the fitted solution spectra. **(D)** Summary of the contribution of aggregation during film formation at different N2200 MWs.

high MW N2200, whereas the lower MW chains transform from solution to film happens chain aggregation within some coils or agglomerates. We interpreted from this data that the high-molecular-weight N2200 has longer active repeat units (Fauvell et al., 2016), and the longer chain length leads to a slow chain movement rate with the chain rearrangement appearing insufficient.

The detailed information obtained was used to form a complete and consistent picture of the chain conformation and aggregates characteristics vary as a function of N2200 molecular weights.

Next, to verify whether the structural characteristics of the molecular chain of N2200 still exists in the blend system, we characterized the aggregation of the blend solution and the film-forming drying process. We aimed to build a complete image of the chain structure and device performance.

The normalized solution absorption spectrum of different N2200 MWs and J51 blend system, as shown in **Figure 7A**. The two absorption peaks of J51 for 545 nm and 585 nm in the different MWs N2200 blend systems are coincident. However, the π-π* and the CT state transition peak of N2200 have strong molecular weight dependence. The π-π* transition peak increased with increasing MW of N2200, and the peak position was redshifted from 380 to 391 nm. By enlarging the absorption wavelength of **Figure 7A** from 650 to 900 nm, we can see that the CT state transition peak intensity of N2200 at 710 nm gradually increases with the increase of the MW of N2200. It corresponds to the improved charge transfer

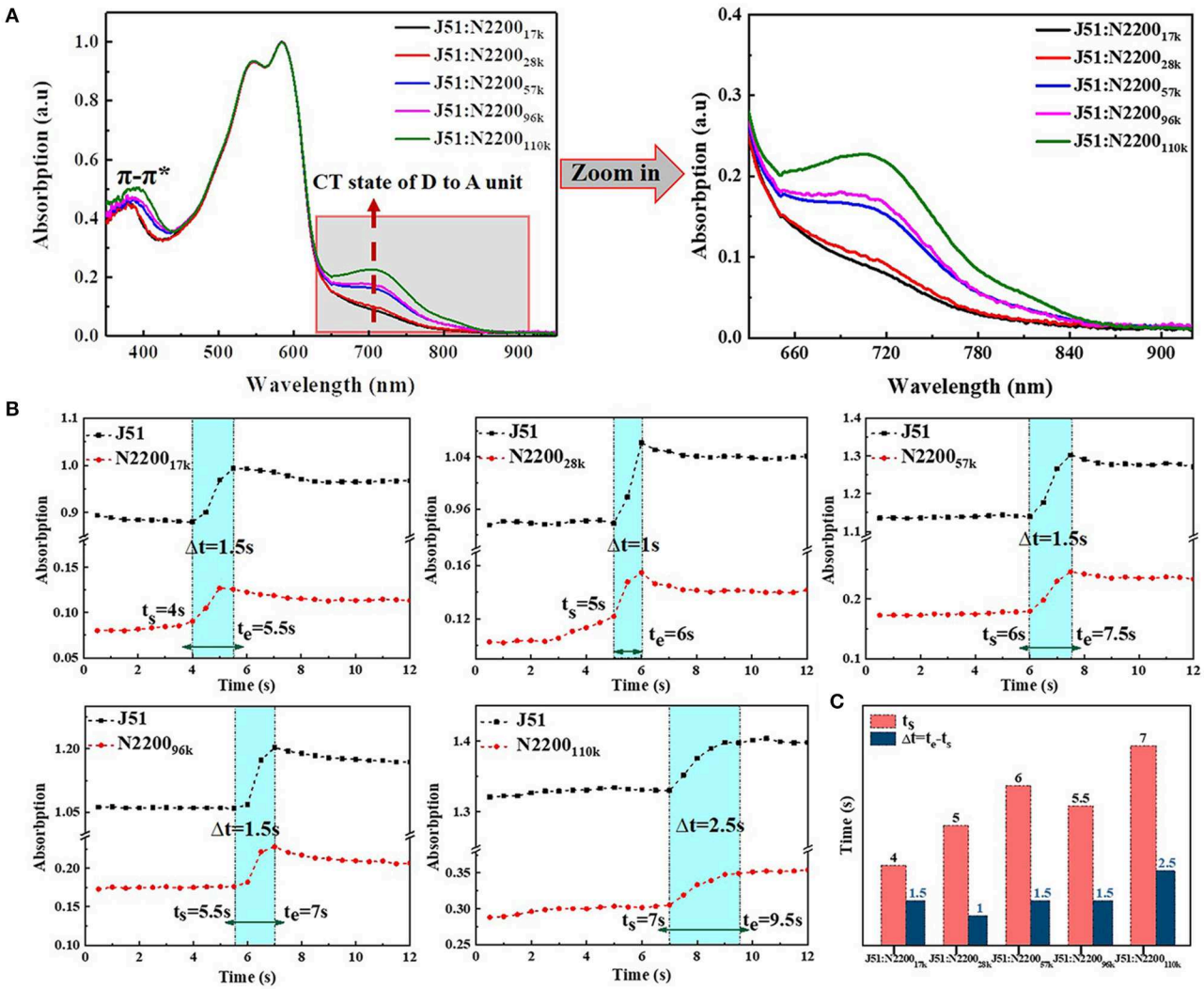

FIGURE 7 | (A) Normalized UV-vis absorption spectra of blend in chloroform solution (concentration is 0.1 mg/ml). **(B)** The absorption intensity at 596 and 710 nm change with time at different N2200 MWs blend systems. **(C)** Summary of the start time (t_s) and the entire time ($\Delta t = t_e$-t_s) of the second stage in solvent evaporation.

between adjacent electron-donating NDI and the electron-withdrawing T2 unit. This reflects that the aggregates increase in solution when the molecular weight of N2200 increases. The change region of MW in the blend solution absorption intensity is in good agreement with the aforementioned chain conformation and aggregates. We thus concluded that the properties of N2200 in the pure component can hold in the blended solution.

The non-equilibrium assembly occurs during the fabrication process, which is critical to determining thin film morphology across the length scale (Patel and Diao, 2018). We therefore used *in situ* time-dependent absorption spectroscopy to study the effect of aggregation on the solution drying process. The original data are shown in **Figure S8**. The position of aggregation of J51 at 596 nm and the CT state transition of N2200 at 710 nm was plotted as a function of time with different N2200 MWs, shown in **Figure 7B**. The solvent evaporation in the film formation process is mainly divided into three periods in the spectra (Wang et al., 2010; van Franeker et al., 2015; Engmann et al., 2016; Yan et al., 2019). The first stage (dissolved state) is where the solvent molecules evaporate rapidly, and the spectral intensity remains unchanged. The second stage (nucleation and growth) is where the solvent content decreases, and the evaporate rate slows. The solution concentration increases to reach saturated solubility, and the polymer chain begins nucleation and growth. The spectral intensity gradually increases. The rate of solvent evaporates is related to the size and shape of the polymer molecule in this stage. The third stage (film formation complete) is where the solvent is completely evaporated, the film formation process is over, and the spectral intensity remains unchanged. We compared the start time (t_s) and the entire time ($\Delta t = t_e$-t_s) of the second stage in solvent

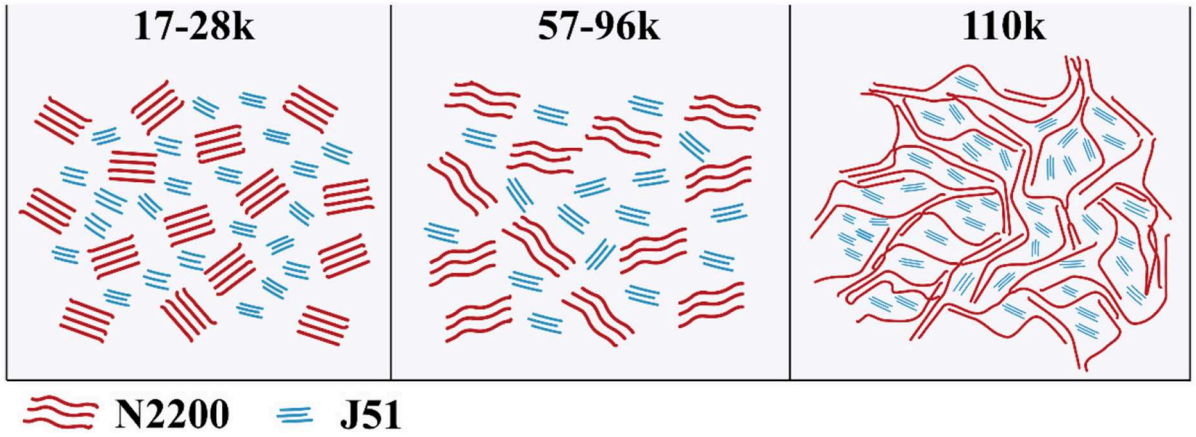

FIGURE 8 | Illustration of the chain behavior effects on the resulting morphologies of J51:N2200 films with different molecular weights, low MW **(Left)**, medium MW **(Middle)**, and high MW **(Right)**.

evaporation of blend system with different MWs N2200, as shown in **Figure 7C**. The t_s increased from 4 s at 17k to 7 s at 110k. This phenomenon is due to the difference in the viscosity of different MWs N2200. The low viscosity N2200 accelerates the chloroform solvent evaporation on the film surface, while the high-molecular-weight N2200 has a large viscosity. The slow convection rate with air makes the solvent evaporation rate slow. Furthermore, the Δt is almost the same when the MW <110k, and the Δt increased from 1.5 to 2.5 s when MW reached 110k. The Δt of a molecular weight reaching the critical MW is stronger than other MWs; the slower solution drying kinetics were explained by the slow diffusion rate of multi-chain aggregates. The data provided strong support for the formation of an effective percolation network in the $N2200_{110k}$ blend system.

From the above, we can entirely understand the complete picture of the relationship between the structure of the MW of N2200 and the property of J51:N2200. The chain conformation depends strongly upon the MW because of the effect MW has on the chain contour length. According to the value of the power index, which we retrieved from the viscosity test in **Figure 5**, we can divide the conformation into three regions. As shown in **Figure 8** (left), the persistence length resulted in a highly rigid backbone, which behaved rigid and rod-like in the low molecular weight polymer (17k−28k for N2200). Though the extended chain improves the crystallinity for low MW of N2200, the short chain makes for poor connectivity between adjacent crystalizes. Furthermore, there is good solubility and the high degree freedom of chain movement in film formation; this resulted in overmixing between donor and acceptor. The blended films form a poor domain purity. The insufficient charge transport and overmuch mixed domain lead to a low power conversion efficiency. In the region of medium MW (57k−96k for N2200), the contour length of the chain increases, and this is presented as a coil-like rod as shown in **Figure 8** (middle). The solution aggregation increases with the decrease in solubility. It enhances the probability of intermolecular collision among individual polymer chains. The intermolecular interaction of N2200 therefore increases. The slightly higher domain purity makes a middle the power conversion efficiency. Strikingly, the polymer of $N2200_{110k}$ shows greater flexibility, as shown in **Figure 8** (right). From the high viscosity value for $N2200_{110k}$, it is not a surprise that 110k reaches a threshold forming a percolation network. The solution has a strong aggregation tendency in $N2200_{110k}$. Combined with the film formation kinetics experiment, we believe that the pre-aggregation caused by the N2200 network in solution acts as a pristine crystal nucleus. The network structure of N2200 furthers collapse and self-assembly in the process of film formation. Hence, high sufficient connectivity between crystallizes enhances the electron transport. Finally, an 8.28% PCE was realized.

CONCLUSION

By studying the characteristics of N2200 materials with different MWs, we found that, as the chain length increases, the chain conformation of N2200 can be divided into three ranges. The chain behaves like a rigid-rod structure for $N2200_{17k}$ and $N2200_{28k}$. The molecular rigidity is weakened, and a rigid chain structure is observed for $N2200_{57k}$ and $N2200_{96k}$. When MW is at $N2200_{110k}$, which is larger than the critical MW, the molecular chains are tangled. Multi-chain aggregations appear when the MW is larger than the critical one, which providing opportunities for the formation of percolation networks. This structure can effectively decrease the size of phase separation and improve the purity of the phase domain and the tendency of face-on orientation. It leads to an effective charge transport pathway. Thus, the charge transport between electron and hole mobility is more balanced. The power conversion efficiency is increased

from 5.87% for J51:N2200$_{17k}$ to 8.28% for J51:N2200$_{110k}$. This research can guide for the fabrication of high-performance all-polymer solar cells by choosing the suitable MW of polymer, which is distinguishable from a small molecule, to achieve percolation network structure.

AUTHOR CONTRIBUTIONS

YY conceived and performed the experiments and wrote the manuscript. YL helped to test the performances of the device. QZ discussed the experimental details. YH directed this work and revised the manuscript.

FUNDING

This work was supported by the National Key Research and Development Program of China (Grand No. 2019YFA0705900) funded by MOST and the National Natural Science Foundation of China (51933010, 91833306).

SUPPLEMENTARY MATERIAL

The Supplementary Material for this article can be found online at: https://www.frontiersin.org/articles/10.3389/fchem.2020.00394/full#supplementary-material

REFERENCES

Adachi, T., Brazard, J., Chokshi, P., Bolinger, J. C., Ganesan, V., and Barbara, P. F. (2010). Highly ordered single conjugated polymer chain rod morphologies. *J. Phys. Chem. C* 114, 20896–20902. doi: 10.1021/jp108546w

Balar, N., Rech, J. J., Henry, R., Ye, L., Ade, H., You, W., et al. (2019). The importance of entanglements in optimizing the mechanical and electrical performance of all-polymer solar cells. *Chem. Mater.* 31, 5124–5132. doi: 10.1021/acs.chemmater.9b01011

Bartelt, J. A., Douglas, J. D., Mateker, W. R., Labban, A. E., Tassone, C. J., Toney, M. F., et al. (2014). Controlling solution-phase polymer aggregation with molecular weight and solvent additives to optimize polymer-fullerene bulk heterojunction solar cells. *Adv. Energy Mater.* 4:1301733. doi: 10.1002/aenm.201301733

Chang, J.-F., Clark, J., Zhao, N., Sirringhaus, H., Breiby, D. W., Andreasen, J. W., et al. (2006). Molecular-weight dependence of interchain polaron delocalization and exciton bandwidth in high-mobility conjugated polymers. *Phys. Rev, B.*74:115318. doi: 10.1103/PhysRevB.74.115318

Choi, J., Kim, W., Kim, D., Kim, S., Chae, J., Choi, S. Q., et al. (2019). Importance of critical molecular weight of semicrystalline n-type polymers for mechanically robust, efficient electroactive thin films. *Chem. Mater.* 31, 3163–3173. doi: 10.1021/acs.chemmater.8b05114

Engmann, S., Bokel, F. A., Ro, H. W., DeLongchamp, D. M., and Richter, L. J. (2016). Real-time photoluminescence studies of structure evolution in organic solar cells. *Adv. Energy Mater.*6:1502011. doi: 10.1002/aenm.201502011

Fan, B., Ying, L., Wang, Z., He, B., Jiang, X. F., Huang, F., et al. (2017). Optimisation of processing solvent and molecular weight for the production of green-solvent-processed all-polymer solar cells with a power conversion efficiency over 9%. *Energy Environ. Sci.*10, 1243–1251. doi: 10.1039/c7ee00619e

Fauvell, T. J., Zheng, T., Jackson, N. E., Ratner, M. A., Yu, L., and Chen, L. X. (2016). Photophysical and morphological implications of single-strand conjugated polymer folding in solution. *Chem. Mater.* 28, 2814–2822. doi: 10.1021/acs.chemmater.6b00734

Gao, L., Zhang, Z. G., Xue, L., Min, J., Zhang, J., Wei, Z., et al. (2016). All-polymer solar cells based on absorption-complementary polymer donor and acceptor with high power conversion efficiency of 8.27%. *Adv. Mater.* 28, 1884–1890. doi: 10.1002/adma.201504629

Gu, K.,Snyder, C. R.,Onorato, J., Luscombe, C. K., Bosse, A. W., and Loo, Y. L. (2018). Assessing the huang–brown description of tie chains for charge transport in conjugated polymers. *ACS Macro Lett.* 7, 1333–1338. doi: 10.1021/acsmacrolett.8b00626

Ho, P. K. H.,Kim, J.-S.,Tessler, N., and Friend, R. H. (2001). Photoluminescence of poly(p-phenylenevinylene)–silica nanocomposites: evidence for dual emission by Franck–Condon analysis. *J. Chem. Phys.* 115, 2709–2720. doi: 10.1063/1.1372508

Hoefler, S. F., Rath, T., Pastukhova, N., Pavlica, E., Scheunemann, D., Wilken, S., et al. (2018). The effect of polymer molecular weight on the performance of PTB7-Th: O-IDTBR non-fullerene organic solar cells. *J. Mater. Chem. A* 6, 9506–9516. doi: 10.1039/C8TA02467G

Holcombe, T. W., Woo, C. H., Kavulak, D. F. J., Thompson, B. C., and Fréchet, J. M. (2009). All-polymer photovoltaic devices of Poly(3-(4-n-octyl)-phenylthiophene) from Grignard Metathesis (GRIM) polymerization. *J. Am. Chem. Soc.* 131, 14160–14161. doi: 10.1021/ja9059359

Hu, D., Yu, J., Wong, K., Bagchi, B., Rossky, P. J., and Barbara, P. F. (2000). Collapse of stiff conjugated polymers with chemical defects into ordered, cylindrical conformations. *Nature* 405, 1030–1033. doi: 10.1038/35016520

Jackson, N. E., Kohlstedt, K. L., Savoie, B. M., Olvera de la Cruz, M., Schatz, G. C., Chen, L. X., et al. (2015). Conformational order in aggregates of conjugated polymers. *J. Am. Chem. Soc.* 137, 6254–6262. doi: 10.1021/jacs.5b00493

Jiao, X., Wang, C., and McNeill, C. R. (2019). Detecting the onset of molecular reorganization in conjugated polymer thin films using an easily accessible optical method. *Macromolecules* 52, 4646–4654. doi: 10.1021/acs.macromol.9b00606

Jung, J., Lee, W., Lee, C., Ahn, H., and Kim, B. J. (2016). Controlling molecular orientation of naphthalenediimide-based polymer acceptors for high performance all-polymer solar cells. *Adv. Energy Mater.* 6:1600504. doi: 10.1002/aenm.201600504

Khan, J. I., Ashraf, R. S., Alamoudi, M. A., Nabi, M. N., Mohammed, H. N., Wadsworth, A., et al. (2019). P3HT molecular weight determines the performance of P3HT:O-IDTBR solar cells. *Solar RRL* 3:1900023. doi: 10.1002/solr.201900023

Kim, T., Kim, J. H., Kang, T. E., Lee, C., Kang, H., Shin, M., et al. (2015). Flexible, highly efficient all-polymer solar cells. *Nat. Commun.* 6, 1–7. doi: 10.1038/ncomms9547

Kline, R. J., and McGehee, M. D. (2006). Morphology and charge transport in conjugated polymers. *J. Macromol. Sci. C* 46, 27–45. doi: 10.1080/15321790500471194

Koch, F. P. V., Rivnay, J., Foster, S., Müller, C., Downing, J. M., Buchaca-Domingo, E., et al. (2013). The impact of molecular weight on microstructure and charge transport in semicrystalline polymer semiconductors–poly(3-hexylthiophene), a model study. *Prog. Polym. Sci.* 38, 1978–1989. doi: 10.1016/j.progpolymsci.2013.07.009

Kohler, A., Hoffmann, S. T., and Bassler, H. (2012). An order-disorder transition in the conjugated polymer MEH-PPV. *J. Am. Chem. Soc.* 134, 11594–11601. doi: 10.1021/ja302408a

Kolhe, N. B., Lee, H., Kuzuhara, D., Yoshimoto, N., Koganezawa, T., and Jenekhe, S. A. (2018). All-polymer solar cells with 9.4% efficiency from naphthalene diimide-biselenophene copolymer acceptor. *Chem. Mater.* 30, 6540–6548. doi: 10.1021/acs.chemmater.8b03229

Li, Z., Zhong, W., Ying, L., Liu, F., Li, N., Huang, F., et al. (2019). Morphology optimization via molecular weight tuning of donor polymer enables all-polymer solar cells with simultaneously improved performance and stability. *Nano Energy* 64:103931. doi: 10.1016/j.nanoen.2019.103931

Liu, Q., Jiang, Y., Jin, K., Qin, J., Xu, J., Li, W., et al. (2020). 18% Efficiency organic solar cells. *Sci. Bulletin 65, 272–275.* doi: 10.1016/j.scib.2020.01.001

Liu, Y.-D., Zhang, Q., Yu, X.-H., Liu, J. G., and Han, Y. C. (2019). Increasing the content of β phase of poly(9,9-dioctylfluorene) by synergistically controlling solution aggregation and extending film-forming time. *Chinese J. Polymer Sci.* 37, 664–673. doi: 10.1007/s10118-019-2259-3

McBride, M., Persson, N., Keane, D., Bacardi, G., Reichmanis, E., and Grover, M. A. (2018). A polymer blend approach for creation of effective conjugated polymer charge transport pathways. *ACS Appl Mater Interfaces* 10, 36464–36474. doi: 10.1021/acsami.8b13255

Mori, D., Benten, H., Kosaka, J., Ohkita, H., Ito, S., and Miyake, K. (2011). Polymer/Polymer blend solar cells with 2.0% efficiency developed by thermal purification of nanoscale-phase-separated morphology. *ACS Appl. Mater. Interfaces* 3, 2924–2927. doi: 10.1021/am200624s

Na, J. Y., Kang, B., and Park, Y. D. (2019). Influence of molecular weight on the solidification of a semiconducting polymer during time-controlled spin-coating. *J. Phys. Chem. C* 123, 17102–17111. doi: 10.1021/acs.jpcc.9b03203

Osaka, I., Saito, M., Mori, H., Koganezawa, T., and Takimiya, K. (2012). Drastic change of molecular orientation in a thiazolothiazole copolymer by molecular-weight control and blending with PC61BM leads to high efficiencies in solar cells. *Adv. Mater. Weinheim*. 24, 425–430. doi: 10.1002/adma.201103065

Panzer, F., Bassler, H., and Kohler, A. (2017). Temperature induced order-disorder transition in solutions of conjugated polymers probed by optical spectroscopy. *J. Phys. Chem. Lett*. 8, 114–125. doi: 10.1021/acs.jpclett.6b01641

Panzer, F., Bässler, H., Lohwasser, R., Thelakkat, M., and Köhler, A. (2014). The impact of polydispersity and molecular weight on the order-disorder transition in poly(3-hexylthiophene). *J. Phys. Chem. Lett*. 5, 2742–2747. doi: 10.1021/jz5009938

Patel, B. B., and Diao, Y. (2018). Multiscale assembly of solution-processed organic electronics: the critical roles of confinement, fluid flow, and interfaces. *Nanotechnology* 29:044004. doi: 10.1088/1361-6528/aa9d7c

Reichenberger, M., Kroh, D., Matrone, G. M., Schötz, K., Pröller, S., Filonik, O., et al. (2018). Controlling aggregate formation in conjugated polymers by spin-coating below the critical temperature of the disorder-order transition. *J. Polymer Sci. Part B* 56, 532–542. doi: 10.1002/polb.24562

Schubert, M., Dolfen, D., Frisch, J., Roland, S., Steyrleuthner, R., Stiller, B., et al. (2012). Influence of aggregation on the performance of all-polymer solar cells containing low-bandgap naphthalenediimide copolymers. *Adv. Energy Mater*. 2, 369–380. doi: 10.1002/aenm.201100601

Steyrleuthner, R., Schubert, M., Howard, I., Klaumünzer, B., Schilling, K., Chen, Z., et al. (2012). Aggregation in a high-mobility n-type low-bandgap copolymer with implications on semicrystalline morphology. *J. Am. Chem. Soc*. 134, 18303–18317. doi: 10.1021/ja306844f

Vacha, M., and Habuchi, S. (2010). Conformation and physics of polymer chains: a single-molecule perspective. *NPG Asia Mater*. 2, 134–142. doi: 10.1038/asiamat.2010.135

van Franeker, J. J., Turbiez, M., Li, W., Wienk, M. M., and Janssen, R. A. (2015). A real-time study of the benefits of co-solvents in polymer solar cell processing. *Nat. Commun*. 6:6229. doi: 10.1038/ncomms7229

Wang, T., Dunbar, A. D., Staniec, P. A., Pearson, A. J., Hopkinson, P. E., MacDonald, J. E., et al. (2010). The development of nanoscale morphology in polymer:fullerene photovoltaic blends during solvent casting. *Soft Matter*. 6:4128. doi: 10.1039/c0sm00343c

Wetzelaer, G. J. A., Kuik, M., Olivier, Y., Lemaur, V., Cornil, J., Fabiano, S., et al. (2012). Asymmetric electron and hole transport in a high-mobility n-type conjugated polymer. *Phys. Rev. B*.86:165203. doi: 10.1103/PhysRevB.86.165203

Xu, Y., Yuan, J., Zhou, S., Seifrid, M., Ying, L., Li, B., et al. (2019). Ambient processable and stable all-polymer organic solar cells. *Adv. Funct. Mater*. 29:1806747. doi: 10.1002/adfm.201806747

Yan, Y., Zhang, R., Liang, Q., Liu, J., and Han, Y. (2019). Control the interplay of crystallization and phase separation of conjugated polymer blends by the relative rate of nucleation and growth. *Polymer* 182:121827. doi: 10.1016/j.polymer.2019.121827

Yang, J., An, N., Sun, S., Sun, X., Nakano, M., Takimiya, K., et al. (2019b). The effect of alkyl chain branching positions on the electron mobility and photovoltaic performance of naphthodithiophene diimide (NDTI)-based polymers. *Sci China Chem*. 62, 1649–1655. doi: 10.1007/s11426-019-9645-1

Yang, J., Xiao, B., Tang, A., Li, J., Wang, X., and Zhou, E. (2019a). Aromatic-diimide-based n-type conjugated polymers for all-polymer solar cell applications. *Adv Mater*. 31:e1804699. doi: 10.1002/adma.201804699

Yin, H., Yan, J., Ho, J. K. W., Liu, D., Bi, P., Ho, C. H. Y., et al. (2019). Observing electron transport and percolation in selected bulk heterojunctions bearing fullerene derivatives, non-fullerene small molecules, and polymeric acceptors. *Nano Energy* 64:103950. doi: 10.1016/j.nanoen.2019.103950

Zhang, Q.,Liu, J.,Yu, X., and Han, Y. (2019). Design optimized intermixed phase by tuning polymer-fullerene intercalation for free charge generation. *Chinese Chem. Letters* 30, 1405–1409. doi: 10.1016/j.cclet.2019.04.004

Zhang, Y., Xu, Y., Ford, M. J., Li, F., Sun, J., Ling, X., et al. (2018). Thermally stable all-polymer solar cells with high tolerance on blend ratios. *Adv. Energy Mater*. 8:1800029. doi: 10.1002/aenm.201800029

Zhang, Z., Wang, T., Ding, Z., Miao, J., Wang, J., Dou, C., et al. (2019). Small molecular donor/polymer acceptor type organic solar cells: effect of molecular weight on active layer morphology. *Macromolecules* 52, 8682–8689. doi: 10.1021/acs.macromol.9b01666

Zheng, N., Mahmood, K., Zhong, W., Liu, F., Zhu, P., Wang, Z., et al. (2019). Improving the efficiency and stability of non-fullerene polymer solar cells by using N2200 as the additive. *Nano Energy* 58, 724–731. doi: 10.1016/j.nanoen.2019.01.082

Zhou, E., Nakano, M., Izawa, S., Cong, J., Osaka, I., Takimiya, K., et al. (2014). All-polymer solar cell with high near-infrared response based on a naphthodithiophene diimide (NDTI) copolymer. *ACS Macro Lett*. 3, 872–875. doi: 10.1021/mz5004272

Zhou, N., Dudnik, A. S., Li, T. I., Manley, E. F., Aldrich, T. J., Guo, P., et al. (2016). All-polymer solar cell performance optimized via systematic molecular weight tuning of both donor and acceptor polymers. *J. Am. Chem. Soc*. 138, 1240–1251. doi: 10.1021/jacs.5b10735

Zhu, L., Zhong, W., Qiu, C., Lyu, B., Zhou, Z., Zhang, M., et al. (2019). Aggregation-induced multilength scaled morphology enabling 11.76% efficiency in all-polymer solar cells using printing fabrication. *Adv. Mater. Weinheim* 31:e1902899. doi: 10.1002/adma.201902899

Conflict of Interest: The authors declare that the research was conducted in the absence of any commercial or financial relationships that could be construed as a potential conflict of interest.

Advantages of publishing in Frontiers

OPEN ACCESS
Articles are free to read for greatest visibility and readership

FAST PUBLICATION
Around 90 days from submission to decision

HIGH QUALITY PEER-REVIEW
Rigorous, collaborative, and constructive peer-review

TRANSPARENT PEER-REVIEW
Editors and reviewers acknowledged by name on published articles

Frontiers
Avenue du Tribunal-Fédéral 34
1005 Lausanne | Switzerland

Visit us: www.frontiersin.org
Contact us: info@frontiersin.org | +41 21 510 17 00

REPRODUCIBILITY OF RESEARCH
Support open data and methods to enhance research reproducibility

DIGITAL PUBLISHING
Articles designed for optimal readership across devices

FOLLOW US
@frontiersin

IMPACT METRICS
Advanced article metrics track visibility across digital media

EXTENSIVE PROMOTION
Marketing and promotion of impactful research

LOOP RESEARCH NETWORK
Our network increases your article's readership